Flinders
UNIVERSITY
ADELAIDE · SOUTH AUSTRALIA

Understanding the vortex fluidic device through the development of a theoretical model and the application of neutron techniques

by

Timothy Samuel Elling Solheim

Thesis
Submitted to Flinders University
for the degree of

Doctor of Philosophy
College of Science and Engineering
21 March 2019

Understanding the vortex fluidic device through the development of a theoretical model and the application of neutron techniques

Timothy Samuel Elling Solheim

BSc. (Hons)

Supervised by Professor Colin Raston AO

Declaration

I certify that this thesis does not incorporate without acknowledgement any material previously submitted for a degree or diploma in any university; and that to the best of my knowledge and belief, it does not contain any material previously published or written by another person.

Signed:

[redacted] 20/11/2018

Dedication

To Bestemor and Bestefar

Summary

The vortex fluidic device (VFD) is a thin film continuous flow processing platform with a wide range of useful capabilities enabling the environmentally friendly processing of compounds. These capabilities include the refolding of misfolded proteins, the biphasic performance of clean oxidations using bleach, and the performance of chemical reactions using more environmentally friendly reagents. The VFD has also demonstrated the ability to prepare a range of materials, including carbon nanorings from carbon nanotubes, the silica-based material SBA-15, and carbon nano-onions coated with Pt or Pd nanodots. Despite these wide-ranging capabilities, minimal work has been performed investigating the behaviour of fluid within the VFD.

This thesis involved the development of a mathematical model predicting the shape of the thin liquid film within the VFD, along with the generation of a number of useful formulae enabling the calculation of the residence time of liquid within the device, the maximum volume the device can hold, and conditions which generate the thickest film. These equations were shown to be consistent with equations relating to other related systems, and were applied to previous work within the VFD, providing additional insights.

The shape of the thin film within the VFD was investigated using neutron imaging performed at the OPAL nuclear reactor. Images acquired using short acquisition times showed that the thin film within the VFD usually reaches stability within 5 seconds, and showed that the behaviour of water in the VFD is consistent with the behaviour predicted by the mathematical model. Subsequent high resolution images demonstrated that the model accurately predicts the behaviour of toluene, but not the behaviour of more viscous liquids such as glycerol and propylene glycol. Despite this deviation between experimental and predicted behaviour, an effective method was demonstrated for adjusting the mathematical model using experimental data, enabling the accurate prediction of the shape of the film for more viscous liquids. The behaviour of water when interacting with a hydrophobic surface was shown to not be accurately predicted by the model, likely because liquid-surface interactions are not considered by the mathematical model. Investigations into the behaviour of biphasic systems revealed that at present, neutron imaging is unable to provide significant useful information about the behaviour of biphasic systems in the VFD.

A method for performing Small Angle Neutron Scattering *in situ* with the VFD was developed, and a preliminary investigation into the behaviour of Pluronic P-123 micelles in the VFD was conducted. The results suggest that the VFD may be influencing the interactions between Pluronic P-123 micelles and water. The potential that the VFD may be influencing solvent-substrate interactions is a hypothesis that has been generated previously on several occasions. Lastly, the mathematical model was successfully used to design scaled-up versions of previous methods for preparing imines and amides within the VFD, increasing production rates up to twenty-fold. Overall, the development of this mathematical model and the demonstration of its accuracy and utility will enable the better understanding of future work within the VFD and the more intelligent design of reaction conditions.

Acknowledgements

Firstly, I would like to thank my supervisor, Colin Raston. I have thoroughly enjoyed working with you these past five years, and I have learnt a lot about science and the scientific process, and about questioning everything. Even my supervisor! Thank you. It has been an awesome journey, and I hope I am fortunate enough to work with you again in the future.

I would like to thank Andrew Dunn from Flinders Technical Services Unit. Your help over the years and willingness to design new versions of the VFD has been very helpful. Without your help, many parts of my project would have been much more difficult, or outright impossible. I would like to thank everyone in the Raston Research Group for their help throughout my PhD, particularly those who visited ANSTO with me: Nikita Joseph, Scott Pye, Xuan Luo, Jessica Philips, Dr Kasturi Vimalanathan, David Harvey and Emily Crawley. I also want to thank Dr Daniel Mangos for being such a great role model and helping me deal with the many frustrations of a PhD and working in such a cluttered lab. I also want to thank Ahmed al-Antaki for friendship and many funny stories in the laboratory. I would like to thank Sandra Marshall, Dr Melissa Schlein and Jacqui Hull for their kindness and support. I also want to thank the various academics who have inspired me throughout both my PhD and my undergraduate degree. Professor Claire Lenehan, Professor Jamie Quinton and Professor Paul Kirkbride, you have all inspired me to be the best I can and taught me that science is amazing.

I would like to thank the various instrument scientists at ANSTO who have taught me so much about neutron science and provided immense help on my visits to ANSTO: Dr Andrew Whitten, Dr Elliot Gilbert, Dr Floriana Salvemini, Dr Jitendra Mata and Dr Chris Garvey. I would also like to thank Norman Booth for helping arrange equipment that we need at ANSTO, as well as Ferdi Franceschini for his help with writing the DINGO program to automate movement of the sample stage. I would like to thank Professor Greg Weiss from University of California, Irvine, and Professor Stuart Dalziel and Jenny Leivadarou from Cambridge University. Your help and advice throughout my PhD has been greatly appreciated. I would also like to acknowledge the support provided by an Australian Government Research Training Program Scholarship.

I would also like to thank my family, Helen Solheim, Erik Solheim, and Kristin Solheim for encouraging me to follow whatever path I want and supporting me along the way. I would also like to thank my friends, Connor, Ruby, Adam, Nathan, Kelly-Anne, Amanda, Jo, (Dr) Tristan, and Callum. Friday night board games is one of the things that has helped keep me sane over the years. Thank you all for your friendship and understanding the many frustrations of a PhD.

The person I want to thank both last and most is my fiancée Jennie. You have provided a tremendous amount of support while I've been doing my PhD. The frequent reassurance, encouragement and words of wisdom have helped me enormously. Thank you. I promise I'll give you as much support and tolerance as you approach the final year of your own PhD, as you have provided me.

Contents Page

Figure list

Scheme list

Table list

Abbreviation list

2-MeTHF	2-methyltetrahydrofuran
ACC	Amorphous calcium carbonate
ANSTO	Australian Nuclear Science and Technology Organisation
BHC	Boots-Hoechts Celanese
BZP	*N*-Benzylpiperazine
CBA	Continuous Bubble Reactor
C-PC	c-phycocyanin
CSTR	Continuous stirred tank reactor
DBP	*N*,*N*-dibenzylpiperazine
DIBALH	Diisobutylaluminium hydride
DMAP	Dimethylaminopyridine
DMF	Dimethylformamide
FSR	film shear reactor
HEWL	Hen egg white lysozyme
IMAC	immobilised metal affinity column
MJOD	multi-jet oscillating disc
NMP	N-methyl-2-pyrrolidone
NMR	Nuclear Magnetic Resonance
OPAL	Open Pool Australian Lightwater (Reactor)
PEO	Poly(ethylene oxide)
PPO	Poly(propylene oxide)
SANS	Small angle neutron scattering
SDP	Spinning disc processor
SLD	Scattering length density
STT	Spinning tube-in-tube reactor
SWCNT	Single walled carbon nanotubes
TBAB	Tetrabutylammonium bromide
TfOH	Trifluoromethanesulfonic acid, or triflic acid
TMOS	Tetramethyl orthosilicate
USANS	Ultra-small angle neutron scattering
VFD	Vortex Fluidic Device

Symbol list

A	$\frac{g\cos\theta}{\omega^2}$
a	A correction factor to convert rotational speed to effective rotational speed
a_1	The volume fraction of polymer in the core of a Pluronic P123 micelle
a_2	The volume fraction of polymer in the shell of a Pluronic P123 micelle
B	$-\frac{2g\sin\theta}{\omega^2}k$. Alternatively, the background factor used in the analysis of small angle neutron scattering data
b	A correction factor to convert rotational speed to effective rotational speed
c	The concentration of Pluronic P123 in samples analysed by small angle neutron scattering
c_{CMC}	The critical micelle concentration of Pluronic P123
d_1	The horizontal distance travelled by a beam of light from one thin film to another thin film
d_2	The horizontal distance travelled by a beam of light whilst travelling through a second thin film
d_3	The horizontal distance travelled by a beam of light whilst travelling through the second glass or quartz wall of a VFD tube
$\vec{F}$	Net force (vector) experienced by the liquid in the VFD
$\overrightarrow{F_c}$	Centripetal force (vector) experienced by the liquid in the VFD
$\overrightarrow{F_g}$	Gravitational force (vector) experienced by the liquid in the VFD
f_0	The film thickness at $h = 0$
f_1	The film thickness at the height at which a beam of light enters a VFD tube
f_m	The minimum film thickness as a function of ϕ for considering the case where surface tension causes the film to not smoothly reach zero thickness
f_t	Film thickness
G	A term used in modelling small angle neutron scattering data
g	Gravitational acceleration on Earth
g_m	Gravitational acceleration giving the greatest film thickness for a particular height
H	Height of the VFD tube
h	Position along the axis of the VFD tube
h_0	The height at which a beam of light enters the VFD tube
h_m	Maximum height of the film (h where $f_t = 0$)

h_r	The height of the liquid relative to the height of the liquid in the absence of rotation
$I(q)$	The intensity of scattering of a neutron by a nucleus, as a function of q
K	Fraction of residence time in the bottom section of the tube
$\mathbf{k}$	The momentum of a neutron travelling towards a nucleus
$\mathbf{k'}$	The momentum of a neutron after being scattered by a nucleus
k	Distance from the base of the VFD tube to the height where $r = 0$
K_m	The minimum fraction of residence time in the lower part of a tube for a given h_2
L	The distance travelled by a beam of light whilst travelling from one thin film to another thin film
L_G	The thickness of the glass/quartz wall of a VFD tube
m	A scale factor used in the analysis of small angle neutron scattering data
N	The number of molecules per micelle (aggregation number) in a Pluronic P123 micelle
$\vec{n}$	Vector normal to the surface of the VFD film
n_1	The refractive index of the liquid inside the VFD
n_2	The refractive index of air
n_3	The refractive index of the glass/quartz VFD tube
$P(q)$	The form factor of the scattering of a neutron by a nucleus as a function of q
Q	Flow rate
$\mathbf{q}$	The change in momentum of a neutron caused resulting from scattering by a nucleus
q	The magnitude of $\mathbf{q}$
R	Radius
R^2	Square of the R correlation coefficient
R_c	The radius of the core of a Pluronic P123 micelle
R_m	The radius of a Pluronic P123 micelle
R_s	The thickness of the shell of a Pluronic P123 micelle
r	Distance from the centre of the VFD tube to the film
r_i	r for the height $h = 0$
t_s	The thickness of the shell of a Pluronic P123 micelle
$S(q)$	The structure factor of the scattering of a neutron by a nucleus as a function of q
T	Temperature
V	Volume
V_E	Volume in the VFD system external to the tube
V_{PEO}	The volume of poly(ethylene oxide) in a Pluronic P123 molecule
V_{PPO}	The volume of poly(propylene oxide) in a Pluronic P213 molecule

θ	Tilt angle of the VFD. Alternatively, half the angle at which a neutron scatters after interacting with a nucleus
θ_1	The angle between the surface of the VFD thin film and the horizontal plane
θ_2	The acute angle between the surface of the VFD thin film and the path of a beam of light exiting the film (after refraction)
θ_3	The acute angle between the surface of the VFD thin film and the path of a beam of light entering the film (before refraction)
θ_4	The acute angle between the surface of the VFD thin film and the path of a beam of light entering the film (after refraction)
θ_5	The acute angle between the wall of the VFD tube and the path of a beam of light entering the tube (before refraction)
θ_6	The acute angle between the wall of the VFD tube and the path of a beam of light entering the tube (after refraction)
θ_m	Tilt angle of the VFD giving the greatest film thickness for a particular height
λ	The wavelength of a neutron
ρ	Density. Alternatively, scattering length density
ρ_c	The scattering length density of the core of a Pluronic P123 micelle
ρ_{PEO}	The scattering length density of poly(ethylene oxide)
ρ_{PPO}	The scattering length density of poly(propylene oxide)
ρ_s	The scattering length density of the shell of a Pluronic P123 micelle
ρ_{solv}	The scattering length density of the solvent
τ	Residence time
ϕ	Radial position around the VFD tube. Alternatively, a term used in modelling small angle neutron scattering data
ω	Rotational speed
ω_e	Effective rotational speed
ω_m	The rotational speed giving the greatest film thickness for a particular height

Chapter 1

Continuous flow organic synthesis and its applications in green chemistry

The environmental impact of human civilisation has become of increasing global concern over the past 20 years,[1-5] as evidenced by the Paris Climate Agreement,[6-8] regional efforts to reduce greenhouse gas production,[9-11] and the significant growth in green chemistry research.[5,12] Efforts to reduce our environmental impact include the imposition of government regulations, the growing focus on renewable sources of energy, and the development of a wide range of new chemicals[13-15] and methodologies to reduce the environmental impact of current chemical processes.[16-18] One of the many approaches to reducing our environmental footprint is the development of green and sustainable processes for the production and purification of chemicals. These approaches include the development of new methodology to substitute green chemicals for toxic chemicals, and the development of new compounds where suitable alternatives are currently unavailable. Approaches to new methodology include the use of supercritical CO_2,[19-21] ionic liquids,[22-24] and continuous flow processing platforms,[25-27] whilst the development of new compounds includes new catalysts,[13,15,28] solvents,[14,29,30] and enzymes.[31-33]

In 1998, Paul Anastas and John Warner published what are now known as the 12 Principles of Green Chemistry.[34] These principles can be summarised as follows: 1) reduce waste, 2) increase atom economy, 3) use less hazardous chemicals, 4) produce inherently safer chemicals, 5) reduce solvent and auxiliary substance usage, 6) perform reactions near ambient conditions, 7) use renewable raw materials, 8) reduce the number of synthetic steps, 9) use catalysts instead of stoichiometric reagents, 10) use chemical products that degrade into non-toxic compounds, 11) use real-time in-line monitoring of processes, and 12) use safer reagents.[34] Continuous flow processing has advantages over traditional batch processing that address a number of these principles. Continuous processes often allow the reduction of waste produced (1),[35-37] the safe use of chemicals such as ozone in increasing the atom economy (2),[38-40] the avoidance of auxiliary substances, particularly phase transfer catalysts (5),[41-43] more efficient heat transfer, allowing reactions to be performed at closer to ambient temperature (6), the use of packed-bed catalysts (9),[44,45] and real-time analysis of processes (11).[46,47] Some of these advantages relate to technology that can, in principle, be developed for any continuous flow system, such as real-time analysis. In contrast, other advantages relate to the fine control over processing conditions afforded by flow processing, affording greater selectivity and reducing the build-up of potentially dangerous intermediates.[18,24,48,49] Advantages relating to fine control over processing are more likely to be system-dependent, and it cannot be reasonably assumed that individual flow systems are capable of these advantages merely because other flow systems are.

A variety of plug-flow continuous flow processing platforms exist, including microfluidic chips, coiled tubing, and the H-Cube and X-Cube.[26,50,51] In addition to these reactors where liquid behaves under plug flow, a variety of high-shear flow systems exist, including the Film-Shear Reactor,[27,38,52] the Multi-Jet Oscillating Disc,[53-56] and the Vortex Fluidic Device (VFD).[25,57,58] Understanding the fluid behaviour is important for all flow systems, particularly for the development of reactions where the advantages are afforded by fine control over operating conditions. Fluid behaviour in plug flow systems is relatively well understood, whilst it is much less understood in high-shear flow systems. Amongst these high-shear flow systems, the Vortex Fluidic Device is almost unique in that in addition to the presence of a liquid-solid interface, there is a liquid-air interface. This significantly complicates the fluid behaviour and causes difficulty in predicting which advantages and disadvantages of existing flow systems apply to the VFD. The focus of this project is to better understand fluid behaviour in the Vortex Fluidic Device, and through this understanding, gain insight into how the capabilities and challenges of flow synthesis in the VFD align with the advantages and challenges that conventional flow systems have over batch processing.

Chapter 1.1 – Advantages, Challenges, and Approaches to Continuous Flow Synthesis

Although the advantages of continuous organic synthesis are numerous, continuous flow processing does come with its own set of challenges. Many of these advantages and challenges are exemplified by the different approaches taken to the continuous synthesis of various pharmaceuticals, including imatinib, ibuprofen, lidocaine and methylphenidate (Ritalin), as well as their comparison to batch procedures.

Ibuprofen is a common over-the-counter pain-killer that has been prepared using a variety of approaches in batch[59-63] and under continuous flow.[64,65] The original Boots synthesis of ibuprofen involved 6 steps and produced a significant amount of waste, leading to the development of the Hoechts method (Scheme 1.1.1, also known as the Boots-Hoechts-Celanese method, or BHC method), as a greener alternative that produced minimal unrecycled waste.[61] Despite this, the batch process converted into flow is that reported by Tamura in 1985 (Scheme 1.1.2).[63] The Hoechts synthesis involves a Friedel-Crafts acylation of isobutylbenzene using acetic anhydride and hydrofluoric acid, followed by reduction of the ketone to an alcohol using Raney nickel and hydrogen, with the final product formed through palladium-catalysed CO insertion.[61] The Tamura procedure similarly involves a Friedel-Crafts acylation, however it instead uses 1 equivalent of aluminium chloride with propionyl chloride, followed by $PhI(OAc)_2$-induced aryl migration to give the methyl ester, and hydrolysis to give ibuprofen.[63]

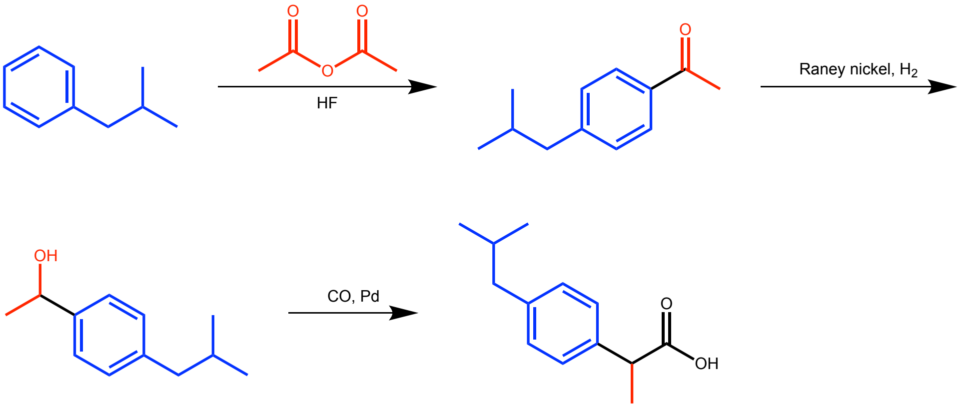

Scheme 1.1.1: The Hoechts synthesis of ibuprofen.[61]

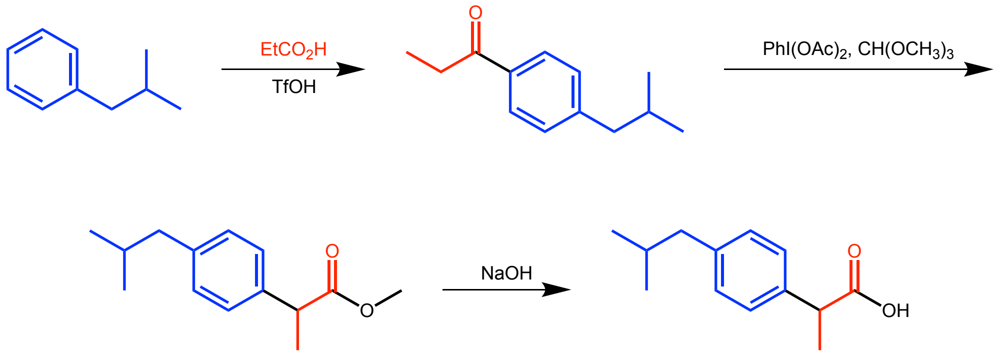

Scheme 1.1.2: The Tamura synthesis of ibuprofen,[63] adapted to continuous flow by the Jamison Group[65] and the McQuade Group.[64]

A significant difference between the Tamura method and the McQuade method is the latter's avoidance of aluminium chloride, which results in clogging of the reactor and is incompatible with downstream reagents. Instead, five equivalents of trifluoromethanesulfonic acid (triflic acid, TfOH) was used for the acylation. Continuous flow operation allowed the usage of TfOH for both the acylation and migration, however, it necessitated the usage of significant equivalents of NaOH for the hydrolysis to quench the TfOH still in the system. Despite the significantly greater quantities of reagents used in the continuous process, it reduced the synthesis time from 15 hours to 10 minutes,[a] which represents a significant achievement.[64] The Jamison group improved this synthesis through the replacement of TfOH with aluminium chloride, preventing downstream reactor clogging through an in-line acidic quench to dissolve the aluminium oxides/hydroxides, and using a membrane separator to afford the acylated product neat.[65] The Jamison group also replaced $PhI(OAc)_2$ with iodine monochloride with the intention of developing a more economical synthesis ($963/mol for $PhI(OAc)_2$ compared to $249/mol for ICl).[66,67] One challenge encountered by this group was coupling the aryl migration step to the hydrolysis. The use of iodine monochloride necessitated a subsequent quench to prevent oxidative destruction of the gold spring they used in their back-pressure regulator. However, quenching the ICl with acetone generated iodoacetone and chloroacetone, thereby preventing the transfer of the methyl ester intermediate into the aqueous phase used for the hydrolysis. Instead, mercaptoethanol was used as a quenching reagent, and 25% methanol was added to the aqueous sodium hydroxide solution to facilitate phase mixing, giving ibuprofen in the form of its sodium carboxylate salt. Ultimately, the Jamison Group developed a more

---

[a] 10 minutes is the total time within the reaction zones under flow, and does not include the time required to transfer liquid between reaction zones under flow.

economical continuous synthesis of ibuprofen based on McQuade's methodology, also increasing the yield (83% from 51%) and decreasing the processing time (3 min from 10 min).[65]

The third continuous method involved using a photo-Favorskii Rearrangement (Scheme 1.1.3) to replace the aryl migration and hydrolysis step, although the Baxendale Group did not couple this step to the Friedel-Crafts Acylation as their intention was to demonstrate a continuous procedure for the photo-Favorskii Rearrangement. Although none of the typical continuous flow challenges were faced, the ability to perform photochemical reactions under flow is a noteworthy demonstration.[68] The advantages of continuous flow processing utilised by the Jamison and McQuade research groups, as well as its challenges and solutions, are typical of such processing. The advantages are focused around the significantly reduced processing time, whilst the main challenges were to design a process that circumvented reactor clogging and ensured the compatibility of reagents with other reagents and reactor components. These challenges were solved through the use of a membrane separator and the careful selection of reagents.[65]

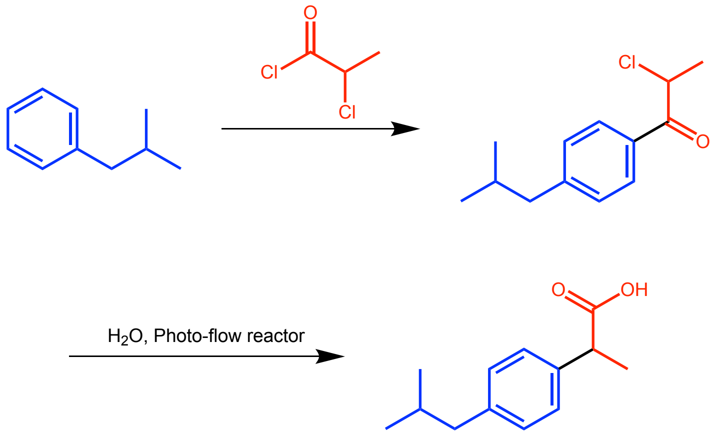

Scheme 1.1.3: The synthesis of ibuprofen using a photo-Favorskii Rearrangement under flow.[68]

Another early pharmaceutical produced under flow is imatinib (Scheme 1.1.4), a drug developed by Novartis AG for use in the treatment of chronic myeloid leukaemia.[69] The problematic batch syntheses inspired the development of the first flow synthesis, noting that under batch, all pathways involve multiple multi-hour operations, with start-to-end synthesis times ranging from 22 hours to 78 hours.[70,71] In contrast, the first flow synthesis of imatinib required only approximately 4 hours. The first step in the reaction was amide formation and involved loading the acyl chloride onto a polystyrene-supported 4-(dimethylamino)pyridine (DMAP) resin within a glass column, followed by pumping aniline through the column to form the amide. Attempts to use excess DMAP resin to scavenge any carboxylic acid produced through hydrolysis were unsuccessful, and instead a column with polymer-supported dimethylamine was used as a scavenger. Attempts to perform the reaction without preloading the acyl chloride onto a DMAP resin resulted in significantly higher variations in concentration, significantly hindering the ability to achieve a high yield for the subsequent step. Performing the amidation in sequence with S_N2 substitution of *N*-methylpiperazine posed two challenges; firstly, *N*-methylpiperazine is only slightly soluble in dichloromethane, and secondly, the use of a catch-and-release system for the amidation resulted in an output stream of inconsistent concentration, requiring the use of excess *N*-methylpiperazine, resulting in faster consumption of the relatively expensive scavenger column intended to scavenge excess *N*-methylpiperazine. The problem of inconsistent concentration was solved by monitoring the concentration of amide using in-line UV-Vis spectroscopy, which demonstrated that the first 10 mL of output contained 75% of the amide. This enabled the first 10 mL to be collected in a vial containing an appropriate stoichiometry of *N*-methylpiperazine in DMF. The problem of solubility was then solved by heating this vial at 50 °C for 30 minutes to remove the dichloromethane, before passing it into a $CaCO_3$ column at 80 °C for the S_N2 reaction. Any remaining *N*-methylpiperazine was then scavenged by an isocyanate (NCO) resin column.

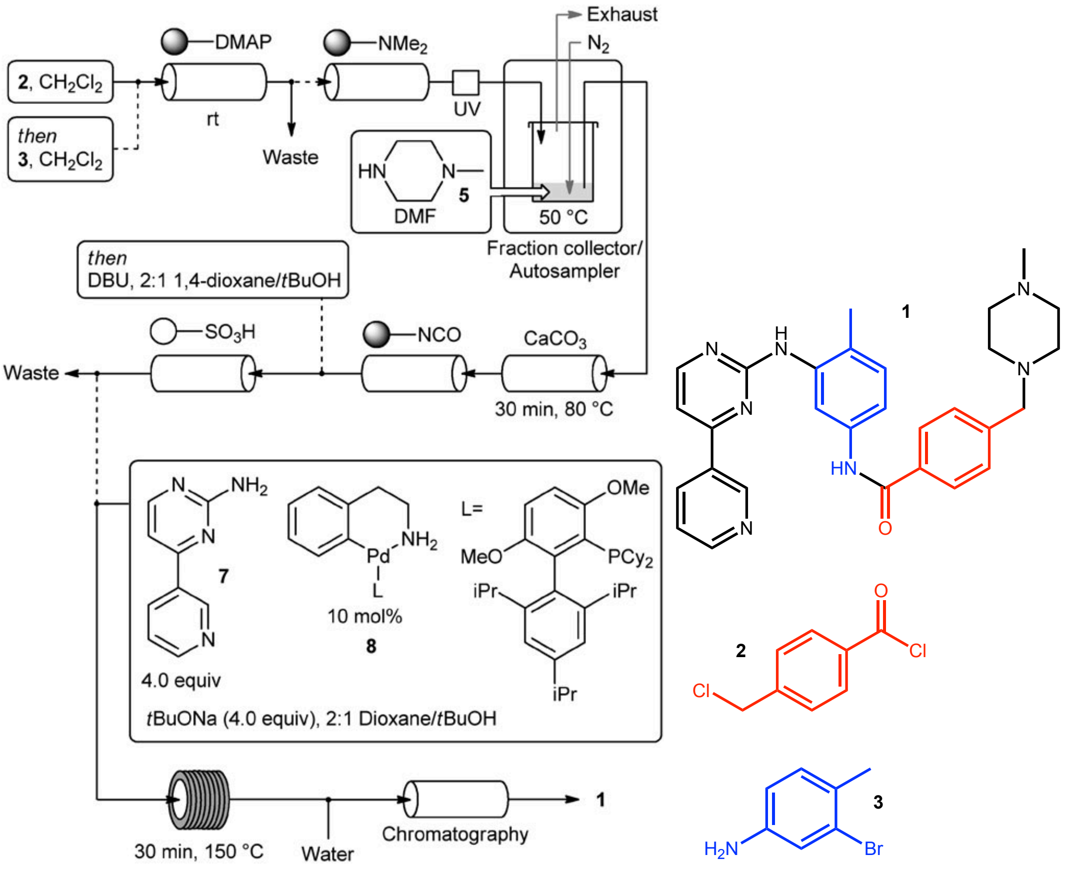

Scheme 1.1.4: The flow synthesis of imatinib as performed by the Ley group.[69]

Coupling this reaction to the final Buchwald-Hartwig coupling also resulted in problems typical of continuous flow: the conditions used previously for this reaction utilised xylenes as a solvent, whilst the reactant is not sufficiently soluble in xylenes or other typical solvents used for the coupling. Inspired by Novartis' synthesis of the related pharmaceutical Nilotinib, the authors tested a combination of $Pd_2(dba)_3$, Cs_2CO_3, and XantPhos in a dioxane-*t*-BuOH system. Unfortunately, although this system dissolved the reagents, significant amounts of precipitate of palladium black and sodium bromide were formed, which resulted in clogging of the reactor. The use of BrettPhos as an alternative precatalyst was successful at preventing the formation of Pd black, whilst the addition of a water stream post-reaction ensured the sodium bromide redissolved before it clogged the system. Overall, a yield of 32% was achieved for this challenging pharmaceutical, under semi-flow conditions.[69] The significantly reduced reaction times utilised here in comparison to batch processing are typical of flow chemistry, however, several aspects of this synthesis demonstrate its challenges. Firstly, solvent exchanges in batch processing are usually simple, however under flow they are not. The difficulty of low reactant solubility is often not a major issue for batch processing, with reactions sometimes performed solventless or without complete dissolution of reactants. Under flow, however, reagent solubility concerns can require the use of solvent switches (here, from CH_2Cl_2 to DMF), or the use of alternative reagents (here, from XantPhos to BrettPhos). A third continuous flow specific challenge observed here is the need to continuously scavenge excess reagents and by-products which are incompatible downstream, for example, the carboxylic acid produced from the acyl chloride, and excess *N*-methylpiperazine.[69]

A later synthesis of imatinib by the Buchwald Group significantly increased the yield and decreased the number of procedural steps in the synthesis.[72] Instead of utilising a catch-and-release system for the amidation, the amide was formed by mixing three reagent streams: the acyl chloride in 2-methyltetrahydrofuran (2-MeTHF), the aniline in 2-MeTHF, and aqueous potassium hydroxide. This enabled the use of all the amide product instead of only the most concentrated first portion. The substitution reaction was performed through the addition of an aqueous solution of *N*-methylpiperazine, with the mixture passed through a stainless steel packed-bed reactor, instead of the $CaCO_3$ reactor used by the Ley group. The Buchwald group determined that removal of excess *N*-methylpiperazine was unnecessary because their subsequent coupling reaction was sufficiently selective to avoid reaction with excess *N*-methylpiperazine. In the final coupling reaction, both groups used a BrettPhos Pd precatalyst, however the Ley group used *t*-BuONa in Dioxane/*t*-BuOH, whilst the Buchwald Group utilised a new solvent *N*,*N*-dimethyloctanamide as an amphiphilic catalytic solvent to encourage mixing between immiscible solvents. However, solubility concerns resulted in the use of the hydrochloride salt of 2-amino-4-(3-pyridinyl)-pyrimidine. The improved synthesis achieved a higher yield (56%) and utilised more environmentally friendly solutions to many of the difficulties encountered by the Ley group.[72] The avoidance of the catch-and-release system for the amidation allowed the use of 100% of the amide produced instead of only 75%, and careful solvent selection avoided the need for a continuous flow solvent switch, demonstrating that careful reaction design can significantly improve on previous procedures.

Atropine is a naturally occurring pharmaceutical that has been synthesised through a variety of pathways. Despite a chemical synthesis pathway being available, industry relies mainly on the isolation of atropine from its natural sources. Jamison first developed a continuous process for atropine synthesis and purification in 2015 (Scheme 1.1.5), aiming for an industrially useful process, however only achieved 7.7% yield.[73] An improved synthesis published in 2017, described a significantly better process achieving 78% yield with a focus on reducing waste. The first step in Jamison's synthesis of atropine is the esterification of tropine with phenylacetyl chloride, however the use of a stoichiometric amount of phenylacetyl chloride resulted in a yield of only 50%. It was hypothesised that phenylacetyl chloride was reacting with the tertiary amine, reducing the yield. In order to increase the yield two options were considered; the usage of the quaternary ammonium salt of tropine, or the usage of two equivalents of phenylacetyl chloride. The first option was selected to avoid the presence of unused phenylacetyl chloride that could cause problems in the later reaction steps, and was successfully used to give quantitative conversion. The second step of hydroxymethylation was challenging given the tendency of atropine to undergo elimination of the alcohol to give apoatropine. Despite these challenges, atropine could be successfully synthesised, with in-line pH adjusted extractions giving a yield of 43%, albeit with only 78% purity. The most difficult impurity to remove was the intermediate produced from the first step, a problem that was only resolved through the usage of more forcing conditions for the hydroxymethylation, resulting in a decreased yield due to the increased conversion to apoatropine. In the end, an overall yield of only 7.7% was produced. These challenges highlight the importance of considering downstream reactivity of reagents, as well as the consequences of limiting purification to in-line systems.[73]

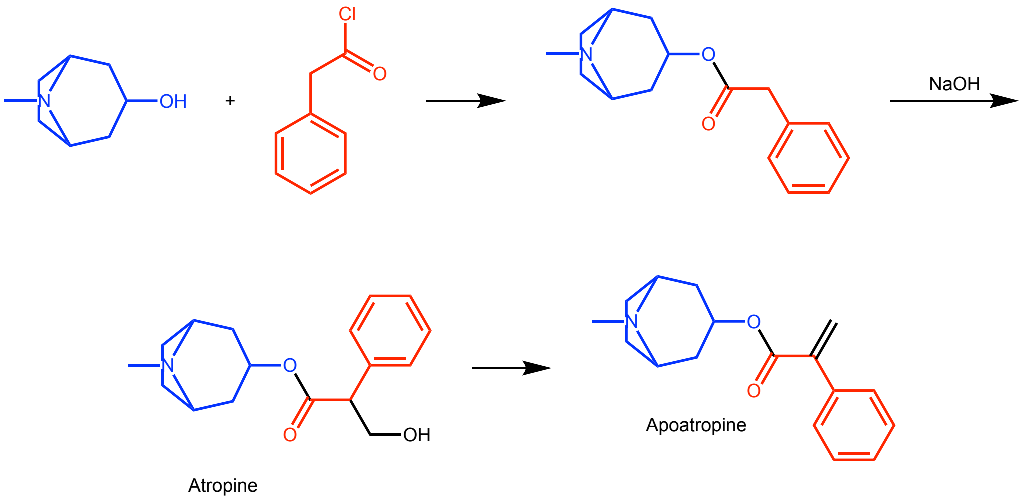

Scheme 1.1.5: The continuous flow synthesis of the pharmaceutical atropine, with degradation to apoatropine shown.[73]

The improved synthesis reported in 2017 focused on achieving a higher yield and reducing the quantity of and involved several changes to the synthesis system.[35] The first change was pumping tropine and phenylacetyl chloride into the reaction zone separately instead of from a single container, allowing the successful use of tropine instead of its hydrochloride salt. Secondly, significantly increasing the temperature of the second reaction zone allowed the use of lower concentrations of sodium hydroxide, reducing the amount of apoatropine that was produced. The in-line purification was also improved using computer software to predict the separation of the product and impurities in various solvent and pH combinations. This allowed a shorter purification process and reduced the amount of product that ended up in waste, giving an overall yield of 78%. Overall, this demonstrates the ability of continuous processing to give finer control over temperature and residence time, allowing the optimisation of conditions to give the desired product. Despite these advantages, the challenges of selecting reagents for downstream compatibility and difficulties in continuous flow purification were encountered.[35]

The continuous flow synthesis of diazepam presents an interesting example where a high-yielding relatively green process has been developed, but where an attempt to develop a greener process resulted in a lower yield. The synthesis of diazepam under flow (Scheme 1.1.6) is based on a batch process described by Sugasawa in 1979.[35,74,75] The first flow synthesis reported by the Jamison group firstly involved the amidation of 5-chloro-2-(methylamino)benzophenone with bromoacetyl chloride in NMP, followed by cyclisation with ammonia in 9:1

methanol/water. In-line purification involved the addition of sodium chloride and ethyl acetate for extraction into the organic phase to give 78% yield with an E-Factor of 36.[75] In designing a synthesis with reduced waste, it was noted that two thirds of the waste originates from the extraction with ethyl acetate, and consequently a solvent suitable for both the reaction and purification was sought. 2-MeTHF was selected, enabling a reduction in the waste produced to an E-Factor of 9.[b] Although the amidation still proceeded in excellent yield (and with the use of chloroacetyl chloride instead of bromoacetyl chloride), it was necessary to use dichloromethane to dilute the stream to prevent precipitation upon cooling. Additionally, the authors were unable to achieve high yields for the second step, presumably because of the use of 2-MeTHF/CH_2Cl_2 instead of *N*-methyl-2-pyrrolidone (NMP). Overall, the final yield was 55%, a marked decrease from the original process, however the waste stream was reduced by 75%.[35]

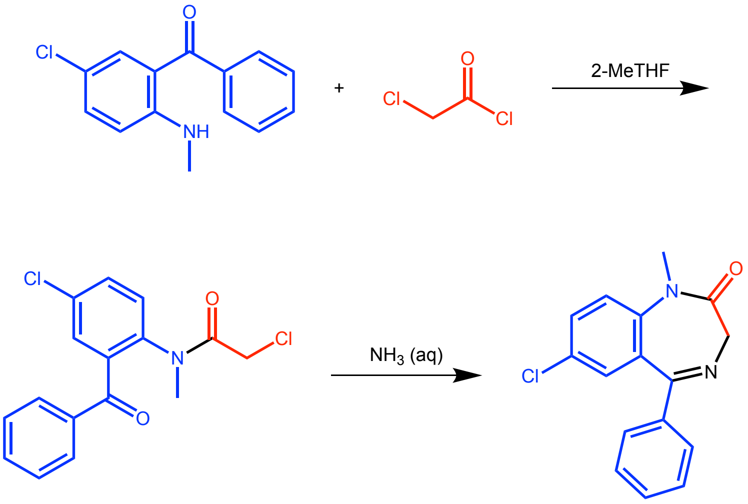

Scheme 1.1.6: The flow synthesis of diazepam as performed by the Jamison group.[35]

The synthesis of methylphenidate (Ritalin) involves the conversion of a diazo compound to the final pharmaceutical, a step which can be performed either intermolecularly (Scheme 1.1.7) or intramolecularly (Scheme 1.1.8).[76] In preparing Ritalin under flow, the Monbaliu group investigated both approaches. The intermolecular approach involved the preparation of tosyl azide under flow, initially involving sodium azide and H_2O/NMP. Although this system resulted in complete conversion in 5 minutes at 45 °C, precipitation of sodium chloride was observed after 30 minutes, resulting in clogging of the reactor. The precipitation of by-products

---

[b] The E-Factor of a reaction or sequence of reactions is the mass of waste produced divided by the mass of the product produced.

is not usually disadvantageous in batch, instead it is often advantageous because it allows easy removal of some impurities. In contrast, the occurrence of this precipitation under flow necessitated the use of an alternative reagent, in this case *n*-Bu_4NN_3. Telescoping this reaction with the diazo transfer to prepare methylphenyldiazoacetate encountered no significant issues. Performing the carbene insertion separately under flow using $Rh_2(oct)_4$ failed to produce yields of the product above 38%, which is likely due to dimerization of the diazo compound. Sequential performance of the previous reactions and the carbene insertion (with an intermediate liquid-liquid extraction using hexane) resulted in a lower yield of 19%, a result hypothesised to be caused by the presence of NMP and trace amounts of water which were not present in the non-sequential performance of the reaction. The final step was boc-deprotection, but this was not carried out under flow.

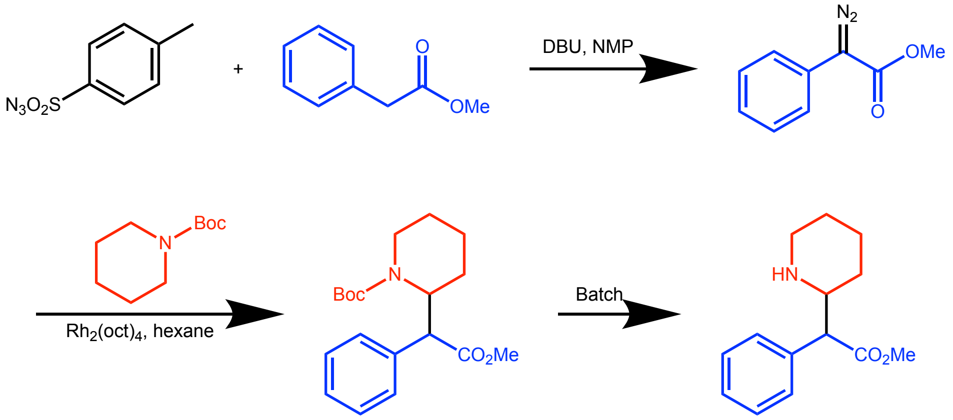

Scheme 1.1.7: Intermolecular flow synthesis of Ritalin.[76]

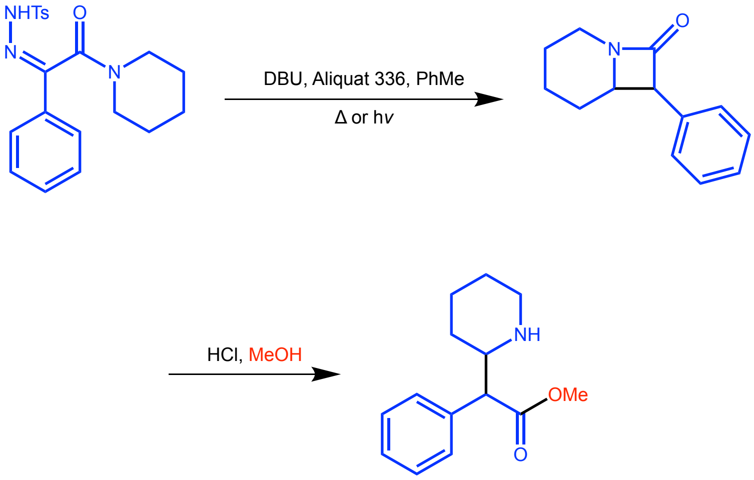

Scheme 1.1.8: Intramolecular synthesis of Ritalin.[76]

In comparison, formation of the diazo compound required for the intramolecular synthesis was significantly more challenging. Direct formation of the diazo compound using tosyl azide was unsuccessful, whilst formation of the tosyl hydrazone in batch required 15 hours at 90 °C. The first continuous flow step in this procedure was the fused-ring-forming degradation of the tosyl hydrazone, a process which resulted in high yields of the product at either high temperatures with short residence times (180 °C/5 min and 150 °C/10 min), or near ambient temperature while irradiated with high-powered LEDs (395 nm) for 60 minutes. Unfortunately, solutions of the DBU salt of the tosylhydrazone in toluene are not stable over extended periods of time, and it was necessary to add 10 mol% of Aliquat 336 (a tertiary ammonium salt) to ensure the salt did not decompose or precipitate over the course of several hours. This was then connected to the methanolysis of the amide to produce methylphenidate, affording the product in over 70% isolated yield. Both processes required off-line processing for reactions with lengthy times, a capability of continuous flow that has not yet been developed. The intramolecular strategy was clearly shown to be superior, not only through the significantly higher isolated yield of the product, but also because the cost per gram of product was much lower at 4.13 €/g, compared to 59.43 €/g for the intermolecular strategy.[76] Important considerations here were the long-term stability of reactant solutions, which is not a factor for batch processes, where reactant solutions which lack long-term stability can be used immediately upon preparation.

The synthesis of Lidocaine (Scheme 1.1.9) has been performed under continuous flow by two groups: the Raston group using the vortex fluidic device (VFD),[57] and the Myerson group using coiled tubing.[77] The synthesis in the VFD was performed in two manners: two steps in non-sequential VFDs, and two steps in a single VFD tube. The sequential process involved the addition of 2,6-dimethylaniline and chloroacetyl chloride, both in $NEt_3/CHCl_3$, to a glass tube in the VFD rotating at 6950 rpm. After collection, the crude mixture was then passed into the VFD again at 60 °C, with addition of neat diethylamine and neat DMF. This process resulted in an 85% isolated yield. Performance of the reaction in a single tube involved the addition of 2,6-dimethylaniline in $CHCl_3$ and neat chloroacetyl chloride at the base of the tube; 5 cm up the tube the tube was heated and DMF was added to induce a solvent exchange, with neat diethylamine added a further 4.5 cm up the tube. This shortened procedure resulted in a yield of only 15%.[57] The synthesis presented by Myerson uses the same synthetic approach, however utilises NMP in place of chloroform and $KOH/MeOH/H_2O$ in place of DMF. Additionally, both steps were performed at elevated temperatures (120 °C and 130 °C respectively), with the system operating at high pressure (1.7 MPa). This process produced lidocaine in 99% yield, and appears to be devoid of any challenges, with the focus of the paper on the continuous flow purification to the purity required by the US Food and Drug Administration.[77]

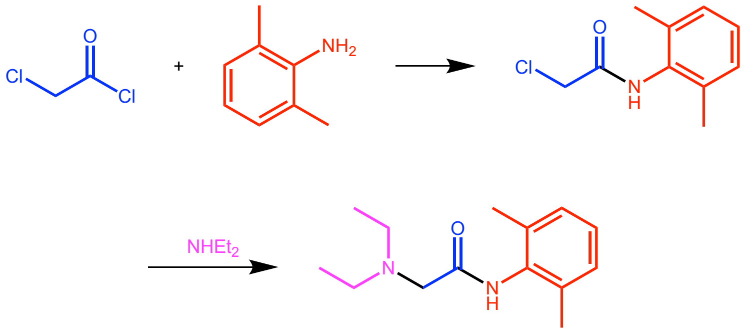

Scheme 1.1.9: Flow synthesis of Lidocaine.[57]

In summary, the use of continuous flow technology has demonstrated considerably reduced reaction times compared to batch processing, as in the cases of the synthesis of imatinib, ibuprofen and Ritalin. Disadvantages and challenges in using flow often revolved around reagent compatibility (ibuprofen, imatinib, Ritalin, atropine), as well as challenges related to solubility (imatinib), stability (Ritalin) and efficient in-line purification (diazepam).

Chapter 1.2 – Safer Flow Chemistry Through Isolation of Dangerous Intermediates

Synthetic procedures that use or produce highly reactive compounds such as hydrazoic acid,[78] diazonium salts,[78,79] and hazardous gases, are dangerous to use on large scales, where there is risk of explosion. The ability of continuous flow processing to finely control residence time and limit the build-up of any hazardous intermediates offers safer procedures for large-scale syntheses. This eliminates the necessity of using less environmentally friendly alternative reaction pathways, such as those using transition metal catalysts.[79] Additionally, the conversion to continuous flow processing often allows the use of smaller quantities of hazardous chemicals, an advantage not only for safety, but also for green chemistry in general.[80] This is an example where the specific flow system used is an important consideration, and it is not clear that the ability to use highly reactive compounds more safely is a capability that extends to all flow systems.

One process which produces diazonium salts as an intermediate is the Balz-Schiemann Reaction (Scheme 1.2.1) for the conversion of anilines to aryl fluorides.[79,81] This reaction involves the diazotization of aniline to form a diazonium salt, followed by decomposition of the salt to the aryl fluoride. Translating the process into continuous flow is not straight forward because the formation of the diazonium salt requires a polar solvent, whilst the conversion to the aryl fluoride is usually performed either under solventless conditions or using non-polar solvents which do not readily dissolve the salt. In developing a method for carrying out the Balz-Schiemann reaction under continuous flow, the Buchwald group performed the diazotization under continuous flow, and then continuously fed the reaction mixture into a stirred batch reactor, maintaining the safety advantages of a continuous flow process. The quick conversion of the diazonium salt to the aryl fluoride prevented the build-up of the dangerous intermediate, and the process could be easily converted to a fully continuous system by using a large continuous flow stirred reactor tank.[79] It is noted that Yu, et al. developed a procedure for carrying out Balz-Schiemann reactions under flow, but their process involved manual handling of the reaction mixtures, and consequently it does not achieve the safety advantage of flow processing discussed here.[81]

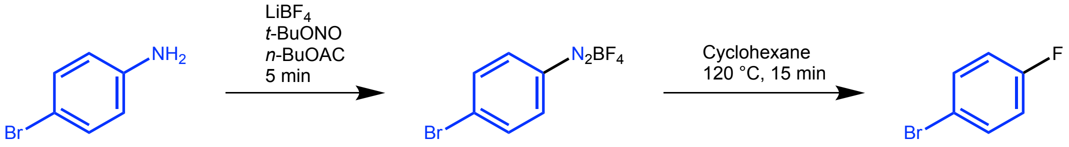

Scheme 1.2.1: The Balz-Schiemann reaction for the synthesis of aryl fluorides.[79]

The *in situ* production of hydrazoic acid during the Schmidt reaction is another example where continuous flow chemistry allowed the safer performance of a reaction. The Schmidt reaction (Scheme 1.2.2) provides a convenient synthesis of amides from ketones through the insertion of ammonia.[82] The danger with the Schmidt reaction is that when performed at room temperature, hydrazoic acid can become entrained in the nitrogen gas by-product, giving rise to gaseous hydrazoic acid, which is a significant safety concern. Performing the reaction at lower, safer temperatures, is difficult because the system becomes too viscous to be effectively mixed using a magnetic stirrer. Continuous flow processing has been used by the Jia group to prevent the entrainment of hydrazoic acid and allowing the reaction to be performed safely at temperatures up to 100 °C (although temperatures above 80 °C increase the formation of impurities), giving near quantitative yield of the product with only 5 minutes reaction time. The advantages of continuous flow processing for this system are not restricted to only improved safety, but also extends to improved green chemistry metrics, where the amount of waste produced is often reduced. When performed under batch conditions, 3 equivalents of azide are usually used because of the amount of hydrazoic acid lost by entrainment, whilst under continuous flow only 1.35 equivalents of azide is required.[82] A similar process has also been reported by the Aube group for the synthesis of alkyl azides, which is followed by intramolecular insertion to form lactams (Scheme 1.2.3). Like the Jia group, temperatures up to 100 °C were safely utilised.[83]

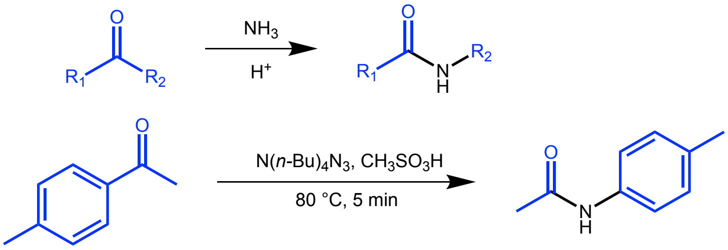

Scheme 1.2.2: The Schmidt reaction for the production of amides.[82]

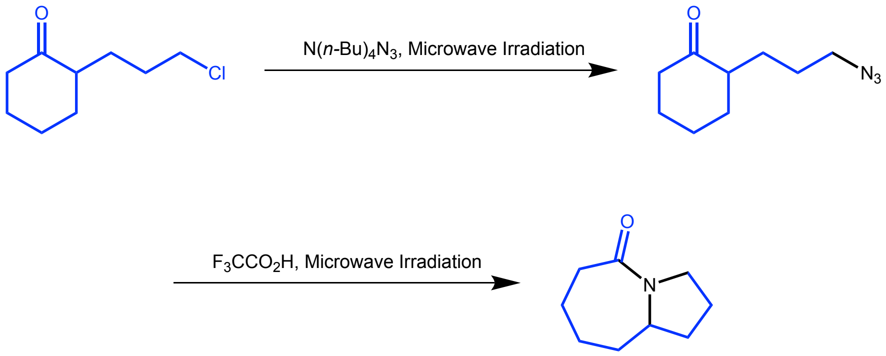

Scheme 1.2.3: Intramolecular Schmidt reaction using tetrabutylammonium azide.[83]

Carrying out Wolff-Kishner reductions under continuous flow is another example where safety and other green chemistry benefits are tied together.[80] Wolff-Kishner reductions involve the conversion of ketones, aldehydes, or esters, to hydrazones using hydrazine, followed by liberation of N_2 in the presence of a base, to form the alkane (Scheme 1.2.4). Typically, these procedures use several mole equivalent excess of hydrazine, which significantly contributes to the overall waste stream.[84-86] The Jensen group utilised a silicon carbide microreactor chip (Fig. 1.2.1) to perform the Wolff-Kishner reduction of benzophenone to diphenylmethane, whilst using only 1.5 equivalents of hydrazine, resulting in 83% yield of the product. Their substrate scope of different phenones and benzaldehydes established that the yields of the product are high, ranging from 78% to 96%, thereby demonstrating a clear ability to utilise continuous flow processing to create a safer and overall greener procedure.

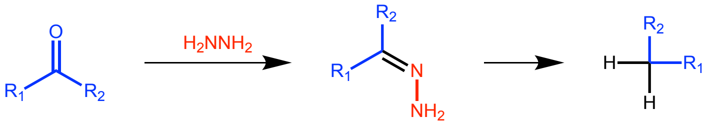

Scheme 1.2.4: Wolff-Kishner reduction.[80]

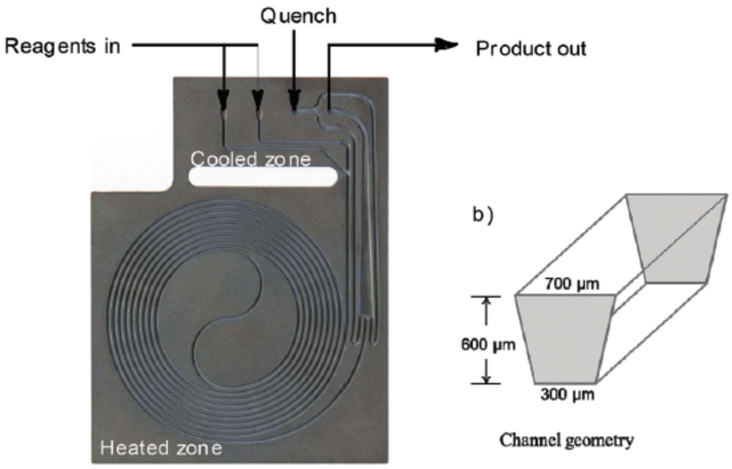

Fig. 1.2.1: Silicon Carbide Chip used for the Wolff-Kishner reduction under flow.[80]

Ozone is a useful reagent for oxidations due to the absence of the formation of by-products, however it suffers from safety concerns associated with its use. On the other hand, the use of ozone under continuous flow has been more limited, despite being used in a variety of different continuous flow systems. One common application of ozone is for the ozonolysis of alkenes and alkynes to form aldehydes or ketones (Scheme 1.2.5). The reaction proceeds by cleaving the C=C to form a 1,2,3 trioxolane (ozonide or molozonide), followed by ring cleavage and recombination to a slightly more stable 1,2,4 trioxolane, followed by reductive work-up to form aldehydes or ketones.[40] Both the 1,2,3 and 1,2,4 trioxolanes are potentially explosive when there is a build-up in a localised area, and the safe usage of ozone can be accomplished by preventing the build-up of these intermediates using a continuous flow system.[39,40] Six different processing platforms or systems have been studied in establishing the safety aspect of these reactions; a falling film microreactor demonstrated in 2007;[87] the O-Cube,[40] a Vapourtec microreactor,[39] a gas-permeable membrane,[88] and a Continuous Bubble Reactor[89] (all demonstrated in 2010-2011); and a film shear reactor demonstrated in 2016.[38] The first of these systems was the falling-film microreactor in 2007 (Fig. 1.2.2), whereby substrate dissolved in a suitable solvent falls into a thin film with ozone bubbling upwards. This system was used for the ozonolysis of acetic acid 1-vinyl-hexyl ester (Scheme 1.2.6), however, conditions which resulted in increased olefin consumption also resulted in decreased selectivity of the aldehyde over the 1,2,4 trioxolane product. The reaction temperature could be increased from -50 °C to 0 °C without negatively impacting the conversion or selectivity.[87]

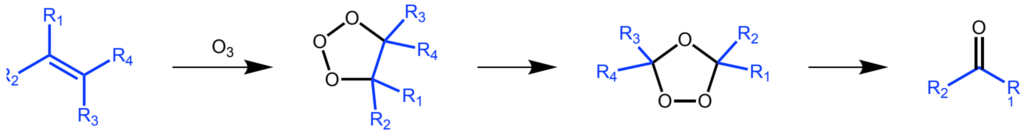

Scheme 1.2.5: Ozonolysis of alkenes.[40]

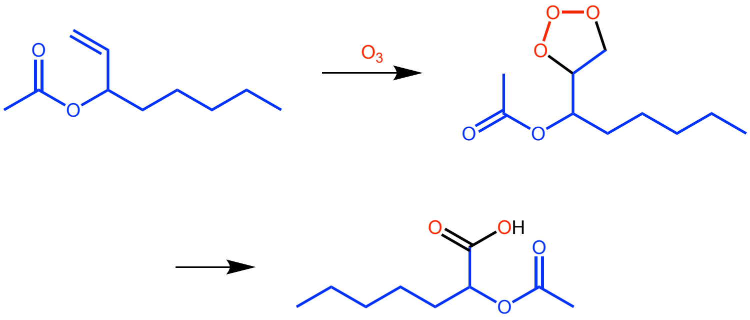

Scheme 1.2.6: Ozonolysis of 1-vinyl-hexyl ester.[87]

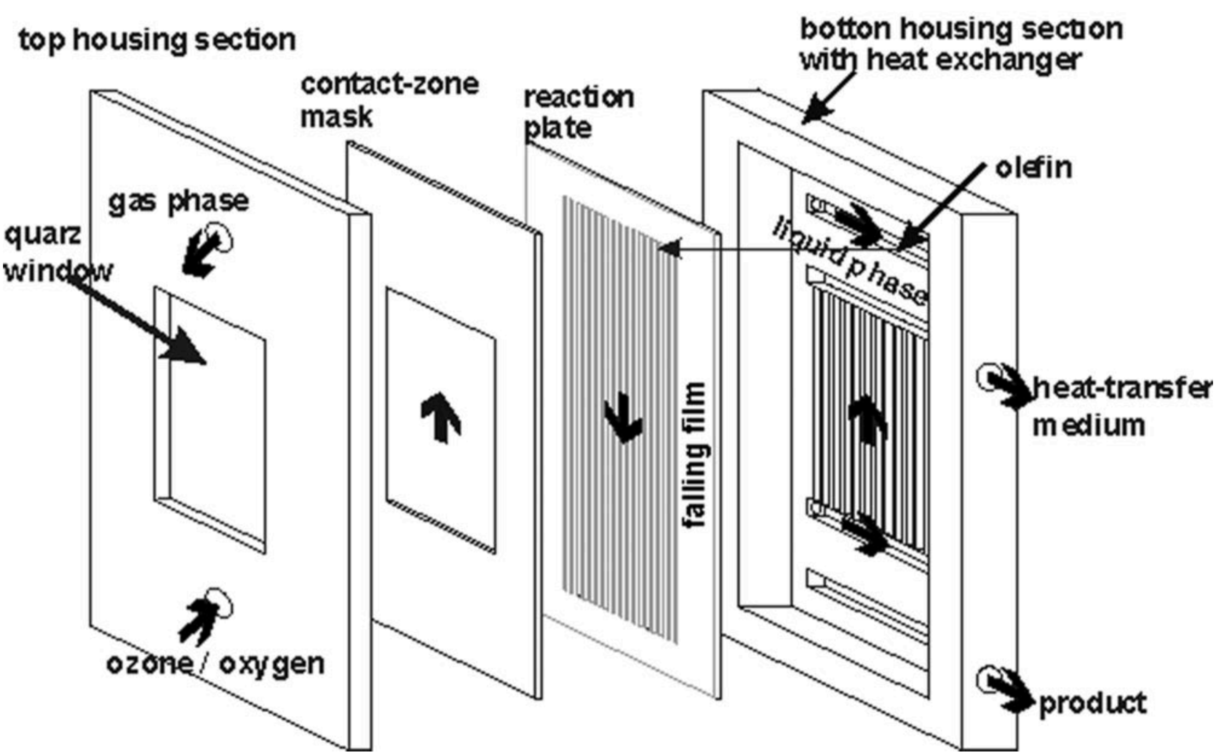

Fig. 1.2.2: The Falling Film Reactor used for continuous flow ozonolysis.[87]

In the subsequent years of 2010-2011, four alternative systems for the ozonolysis of olefins were demonstrated, all achieving yields above 70%. One of these systems is the O-Cube, which uses an O_2 cylinder to produce O_3 on-demand.[40] The ozone is then passed into Teflon tubing coiled around a refrigeration unit, in order to mix with pre-cooled dissolved substrate, forming the 1,2,4 trioxolane. The reaction mixture is then passed into a second cooled reaction loop containing 5% acetone/water or $NaBH_4$/MeOH as a quenching agent, and lastly collected in a vial, giving yields upwards of 70%. The ability to generate O_3 on small scales allowed the safe usage of ozone as an environmentally friendly, safe, synthesis.[40] The Vapourtec microreactor was similarly successfully used for ozonolysis, for dec-1-ene as the substrate and triethylphosphite as the quenching agent, resulting in a 76% yield of the product.[39] Like the O-Cube, the system was cooled to -10 °C.[39] As an alternative to the use of pure O_3, the Ley group has demonstrated the effectiveness of an O_2/O_3 mix for ozonolysis, using the mixture in conjunction with a tetrafluoroethylene/ perfluorodimethyldioxolane copolymer (Teflon AF-2400) (Fig. 1.2.3a, b, c).[88] The system functions through the feeding of substrate dissolved in a suitable solvent into the gas-permeable membrane, which is sealed inside a glass bottle. The O_2/O_3 mixture is pumped into the glass container, where it then passes into the tubing to react with the substrate. The quenching agent was triphenylphosphine, and the yields were upwards of 73% for terminal alkenes.[88] The ability to perform ozonolysis on a larger scale has been demonstrated by the Process Research and Development team at Abbott Laboratories, who built a Continuous Bubble Reactor (CBR, Fig. 1.2.3d).[89] The CBR functions by feeding in dissolved substrate at the base, which is allowed to flow out at the 2 L mark, whilst ozone is bubbled in from the bottom through a coarse frit, and allowed to escape out the top. This design allowed the production of an unspecified "isobutylene-type drug intermediate" at a rate of 80 g/hr with 99% conversion.[89] A more recent system is the film-shear reactor (Fig. 1.2.4) used by the Tyler Group for ozonolysis, whereby the substrate dissolved in ethyl acetate, O_3, and water are fed into the base of a 2.2 mL cylindrical reactor containing a rotating disc and allowed to exit at the top of the cylinder through an outlet. Despite the high shear produced by the rotating disc and the immiscible EtOAc/H_2O combination, isolated yields ranged from 35% to 81%, significantly lower than the other systems discussed.[38] Overall, the variety of continuous flow systems capable of using ozone more safely and at higher temperatures than batch procedures have been established, thereby demonstrating the ability of continuous flow systems in general to operate with improved safety and greener chemistry metrics.

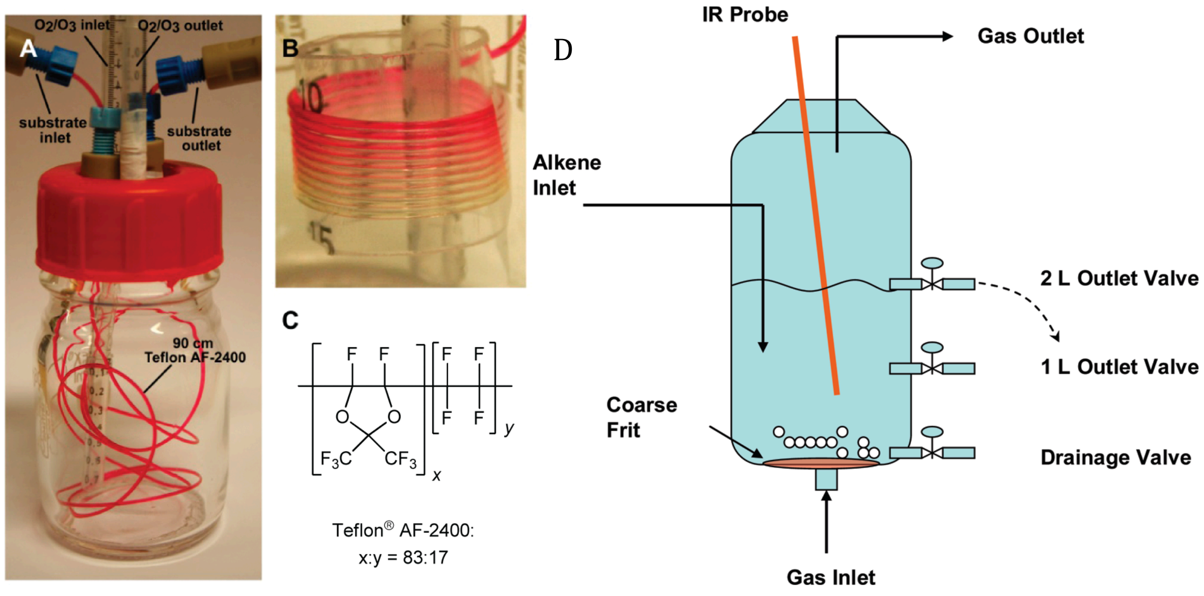

Fig. 1.2.3: a) The flow ozonolysis setup used by the Ley group for continuous flow ozonolysis. b) The gas-permeable membrane used by the Ley group (bleached with Sudan red 7B for clarity). c) The molecular formula of the gas permeable Teflon AF-2400 membrane used by the Ley Group.[88] d) The Continuous Bubble Reactor (CBR) used by Abbott Laboratories for continuous flow ozonolysis.[89]

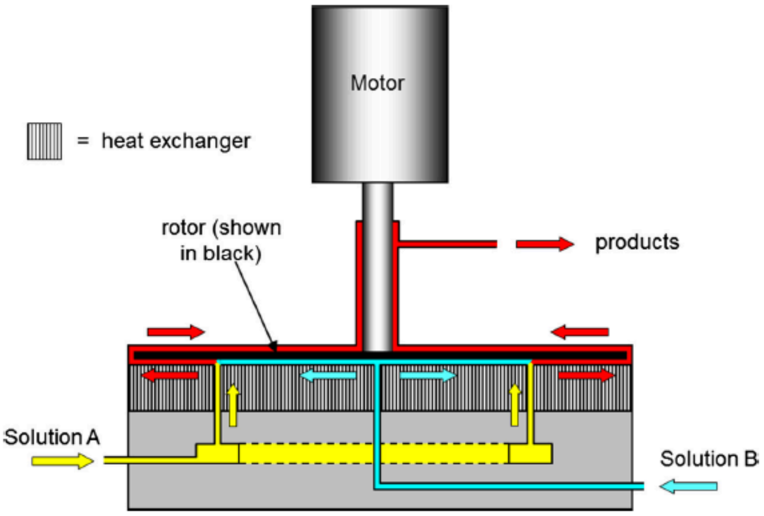

Fig. 1.2.4: The Film-Shear Reactor (FSR).[27]

Another interesting example of continuous flow reactions involving in-line gas production is hydrogenation using diazene, which can be used as an alternative to H_2 where the use of metal catalysts is problematic (Scheme 1.2.7).[90,91] The use of diazene poses the same safety issue presented by many reactions involving nitrogen, namely, pressurisation caused by the production of significant quantities of the gas. The use of diazene (generated from *N*,*O*-bistrifluoroacetylhydroxylamine and hydroxylamine) resulted in the reduction of a range of olefins, with isolated yields from 68% to 97%. The reaction system tolerated a range of functional groups, including acid-sensitive groups, despite the production of trifluoroacetic acid as a byproduct in the generation of diazene. Like the use of sodium azide above, continuous flow operation allowed a dramatic reduction in the number of equivalents of diazene required, from 10 equivalents in batch processing,[90] to 1.5 under continuous flow.[91]

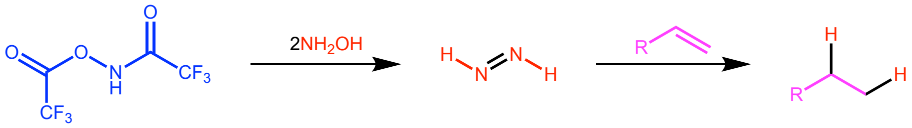

Scheme 1.2.7: Continuous flow reductions using diazene.[91]

Overall, the ability to perform dangerous reactions more safely through the isolation of hazardous intermediates is consistently demonstrated using a variety of flow systems, with the ozonolysis of alkenes being a common example.

Chapter 1.3 – Continuous flow synthesis enhancing selectivity

Continuous flow systems allow precise control over the temperature and residence time of the liquid. This fine control offers scope for increasing the selectivity of reactions by ensuring the desired product is quenched before it undergoes subsequent undesired reactions. The ability to control selectivity through parameter control significantly improves the green chemistry metrics because of the higher yield, and in some cases reducing the number of synthetic steps required and minimising the formation of byproducts. Additionally, physical control over selectivity can reduce the need for additional selectivity-controlling reagents, improving the green chemistry both by their absence and by simplifying the purification process.

Selectivity is a common concern in oxidations and reductions, where there are often a number of sites that can be oxidised or reduced to different extents. The synthesis of aldehydes from esters is desirable given the natural abundance of esters, however, the inability to avoid subsequent reduction necessitates the usual approach of deliberate reduction of the ester to the alcohol, followed by oxidation back to the aldehyde. Di-isobutylaluminium hydride (DIBALH) is capable of reducing esters to aldehydes at low temperatures (Scheme 3.1), however over-reduction to the alcohol is a problem, with some describing the procedure as capricious.[92,93] The use of a continuous flow system was effective in the controlled reduction of esters to the corresponding aldehyde, using DIBALH as a reducing agent. For a flow system operating at 78 °C, the model reaction of ethyl hydrocinnamate to hydrocinnamaldehyde gave 96% yield of the product, whilst the selectivity was reduced when the reaction was performed at room temperature, but still with a respectable yield of 80%.[93]

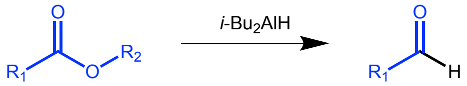

Scheme 1.3.1: The continuous flow controlled reduction of esters to aldehydes using di-isobutylaluminium hydride and coiled tubing.[93]

Like in reductions, selectivity is also an important consideration in oxidations. One consideration in using the versatile Swern oxidation reaction (Scheme 1.3.2) is the ability to form thioacetals via the Pummerer rearrangement, requiring the reactions to be typically performed below -50 °C where such rearrangement is slow. In order to avoid operating at such low temperature, the reaction can be performed under continuous flow, where the first cationic intermediate is quickly mixed with the alcohol after its production, reducing the likelihood of the Pummerer rearrangement. Yields of 75% to 95% were achieved at -20 °C under continuous flow, whilst batch processes at the same temperature resulted in yields of 11% to 49% for the same substrates. Impressively, yields of 71% to 89% were still achieved when the reaction was performed under continuous flow at room temperature. Like the use of DIBALH, the Swern oxidation is a clear example where continuous flow processing allows significant improvement in selectivity at more practical temperatures than those used in batch processing.[49]

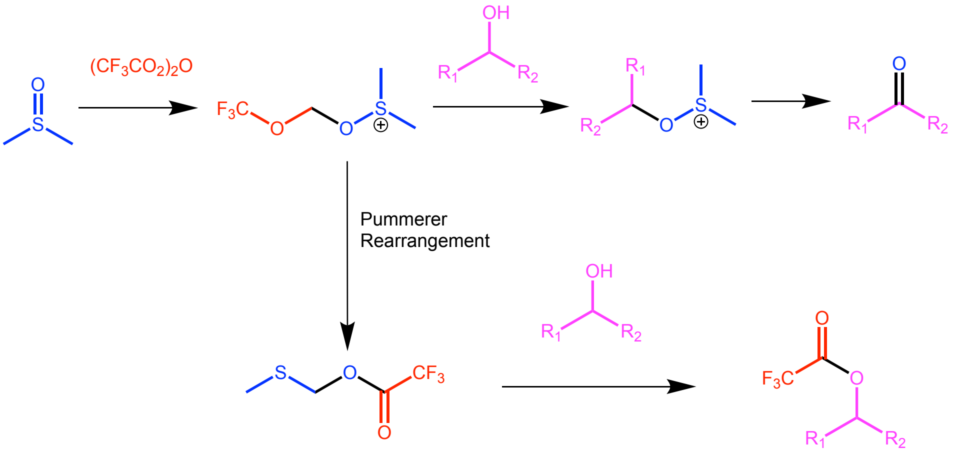

Scheme 1.3.2: Selective room temperature Swern oxidation performed using stainless steel tube reactors under flow.[49]

The selectivity enabled by using continuous flow processing is not limited to oxidations and reductions, extending to the use of organometallic reactions. One example is the carboxylation of organolithiums to produce an asymmetric ketone or carboxylic acid (Scheme 1.3.3), where the symmetric product is also possible.[94] The production of carboxylic acids and ketones occurs first through the insertion of carbon dioxide between the C-Li bond, secondly through the removal of excess carbon dioxide, thirdly through the addition of a second alkyllithium to form a dilithium salt (only when forming a ketone), and lastly by quenching the dilithium salt to form the ketone or carboxylic acid. The two major by-products usually produced are the symmetric ketone formed in the first step, and tertiary alcohols in the final step. The formation of symmetric ketones can be avoided in batch using a slow addition of the alkyllithium to dry ice, a process not convenient for continuous flow. The carboxylation of *para*-(trifluoromethyl)phenyllithium to *para*-(trifluoromethyl)benzoic acid was investigated as a test reaction, with yields of the product of 19% and 66% using 1 and 3 equivalents of carbon dioxide respectively. This is in comparison to a yield of 64% when using “massive dry ice” as cited for the literature.[95] The yield was further increased to 96% using tetrahydrofuran as the solvent, even when the amount of carbon dioxide was reduced to 1 equivalent. In all cases, most of the alkyl lithium not in the final product ended up in the generated symmetrical ketone. Yields above 75% were recorded for the majority of the products they synthesised.[94]

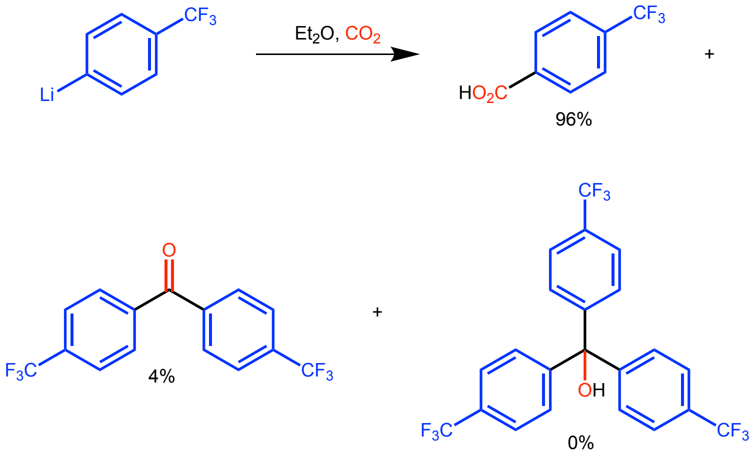

Scheme 1.3.3: Selective carboxylation using Teflon tubing under flow.[94]

Evidently, significant advantages exist for selective syntheses through the ability to finely control continuous flow processing, although it is unclear whether flow systems which operate away from plug-flow, such as the VFD, are capable of producing the same kind of selectivity.

Chapter 1.4 – The Vortex Fluidic Device

The Vortex Fluidic Device (Fig. 1.4.1 (a)) is a continuous flow processing platform developed within the Raston group and first described in 2012 (although it was briefly mentioned in 2011).[96,97] The Vortex Fluidic Device (VFD) consists of a borosilicate or quartz tube tilted at an angle and rapidly rotated at speeds up to 10000 rpm, resulting in liquid placed within the tube forming a thin liquid film against the walls. The device can operate either in confined mode, where a fixed volume is placed within the tube, or under continuous flow, where liquid is continually inserted at the base through feed-jets and collected out the top of the tube. The early prototype VFD (Fig. 1.4.1 (b)) used a tube with external diameter of 10 mm, whilst subsequent VFDs used a different design, along with a tube of external diameter 20 mm. Recent work has demonstrated that vibrations and rotational stability may be important, both factors whose dependence on rotational speed will vary greatly between the 10 mm and 20 mm VFDs due to the significant design changes that occurred between the two versions. Consequently, although the capabilities demonstrated within the 10 mm VFD should be possible in the 20 mm, the operating conditions required may be very different due to the design changes. For this reason, although the mechanisms operating in the complex fluid dynamics for the results in the 10 mm VFD are discussed here, the effect of changing operating parameters is not.

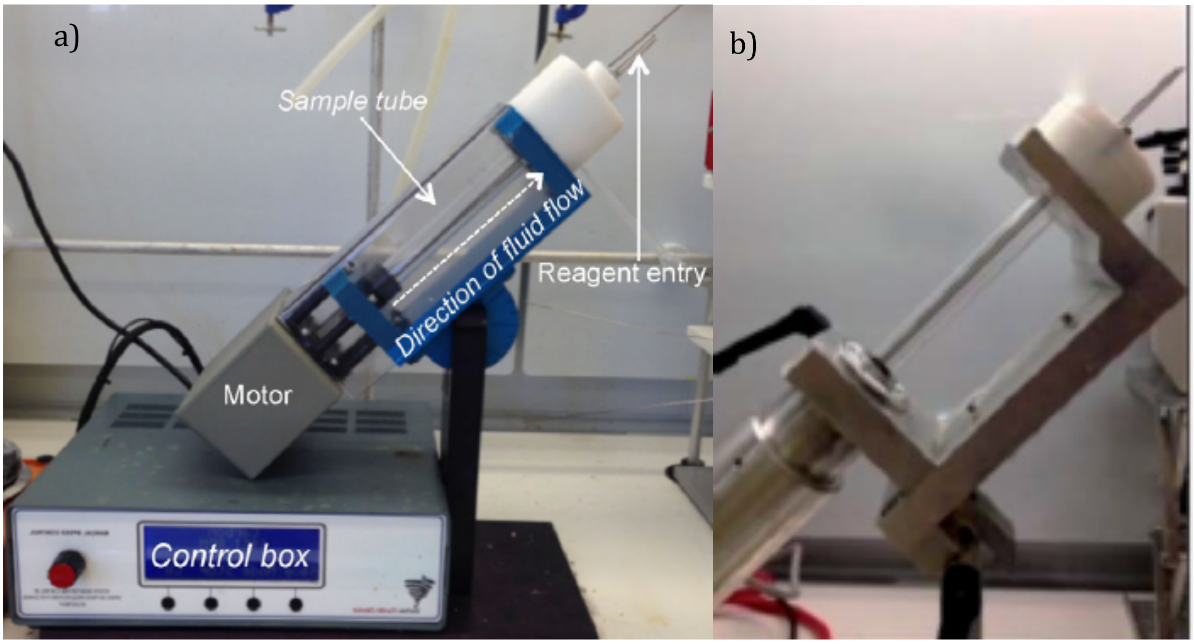

Fig. 1.4.1: a) The Vortex Fluidic Device fitted with a 20 mm external diameter tube.[58] b) An early prototype version of the VFD fitted with a 10 mm external diameter tube.[98]

Chapter 1.4.1 – VFD-mediated processing of materials

The VFD was first mentioned in 2011 when it was used to encapsulate carboplatin into *p*-phosphonic acid calix[5]arene capsules, although the term “Vortex Fluidic Device” is not used.[97] In order to encapsulate the carboplatin, the calixarene capsules must first be disassembled, a process allowed by the intense shearing that occurs within the VFD. Most later work involving materials synthesis would also attribute the capabilities of the VFD to intense shearing, although they usually used much higher rotational speeds than the 1500 rpm used to disassemble calixarene capsules.[97] Another capability demonstrated by the VFD and also attributed to the high shear forces is the ability to exfoliate graphite, resulting in graphite flakes with a reduced thickness. The proposed mechanism was that graphite was pushed against the walls of the tube, and the shear forces partially lifted layers of graphite off each other, which then slipped along the graphite shear to separate. The sheets remained separated because the surface binding energy for graphite-graphite is similar to that of graphite-NMP (the solvent used), and hence the restoring force bringing the sheets back together was very small. The same capability was also demonstrated for boron nitride.[96]

An understanding of the origin of shear forces with the VFD was further developed in controlling the growth of palladium and platinum nanoparticles onto carbon nano-onions, through the coating of H_2PdCl_4 and H_2PtCl_6 on the nano-onions, followed by their reduction, using H_2 and ascorbic acid respectively.[99-101] It was observed in both cases that the nanoparticles formed were smaller and more uniform in size under VFD processing than under batch processing. In the case of Pd, where H_2 was used as the reducing agent, these observations are attributed to the shear increasing the amount of H_2 present in the solution, increasing the number of nucleation sites for the reduction, resulting in a reduction of nanoparticle size. The shear forces are attributed to instabilities, waves, and ripples causing the breakdown of surface tension, although the origins of these instabilities are not discussed.[99]

The effect of shear forces within the VFD was further investigated through demonstrating the ability of the VFD to control the formation of different polymorphs of anhydrous calcium carbonate.[102] There are three polymorphs of calcium carbonate, which, in order of most stable to least stable (and in order of least soluble in water to most soluble), are calcite, aragonite, and vaterite. Batch synthesis of calcium carbonate using aqueous solutions of $NaHCO_3$ and $CaCl_2$ produces vaterite. Similarly, the 10 mm VFD operated at the mild conditions of room temperature and/or low shear (500 rpm) produces vaterite, whilst when operated at the harsher conditions of 80 °C and higher shear (4500 rpm), produces calcite. The ability of high shear forces to produce calcite is compared to the mechanical forces present in milling, which have been shown to induce the conversion of vaterite to calcite.[102] Further control over calcium carbonate polymorph formation was demonstrated in the formation of the amorphous hydrated phase, proto-vaterite. One challenge in synthesising amorphous calcium carbonate (ACC) is that the rapid nucleation and particle growth result in unstable particles. Consequently, additives or low temperatures are required in order to slow the nucleation process, producing stable ACC. The application of the VFD to this challenge resulted in the formation of stable ACC, using high shear forces (2000 rpm to 4000 rpm), instead of low temperatures or additives. The ability of these shear forces to enable the formation of stable ACC was hypothesised to be due to a slowing of the rate of nucleation and a hindrance of particle aggregation.[103] The ability of high shear in the VFD to hinder nucleation and aggregation has also been observed in the formation of lanthanide phosphate nanoparticles, whereby low shear produces large particles, moderate shear produces dandelion-type structures of multiple rods stemming from a single point, whilst high shear produced bundles and single rods.[104] In addition to preventing aggregation, the VFD has also shown an ability to breakdown gel networks.[105] This demonstrates that not only are the high shear forces within the VFD antithetical to the formation of larger nanoparticles, it is antithetical to the existence of pre-formed structures of the same size.

Further investigations into the capabilities of the VFD for materials processing involved the synthesis of SBA-15, a well-ordered 2D hexagonal form of mesoporous silica.[106] This synthesis typically includes a hydrothermal treatment step, whereby a solution containing tetraethyl orthosilicate and Pluronic P-123 is autoclaved for 24 to 48 hours, at temperatures ranging from 35 °C to 100 °C. This treatment often includes the use of additives, with the exact additives and autoclaving conditions controlling the mesoscopic regularity of the material. The 10 mm VFD was able to avoid this hydrothermal treatment, instead utilising the shear forces within the VFD to produce mesoporous silica. This capability is hypothesised to be caused by fast kinetics resulting from an increased collision rate caused by the shear forces. Importantly, higher shear forces typically resulted in SBA-15 with smaller pores, enabling fine-tuning of the silica properties, an ability which is without precedent.[106] The ability to reduce processing times has also been demonstrated in the VFD-mediated formation of gels from the water-condensation of tetramethyl orthosilicate (TMOS). The formation of gels from alkoxysilanes usually requires lengthy reaction times (up to 1000 hours for tetraethyl orthosilicate), in conjunction with an acid or base. These conditions are required because the very low solubility of alkoxysilanes with water results in very slow reaction. Continuous flow processing involving water and TMOS in a 20 mm VFD resulted in gelation times of 3-4 hours post VFD processing, compared to in excess of 9 hours for batch processing of the same system. VFD-processed gels also showed an increase in the degree of condensation, rising from 89% in batch-processed, to 95% for the VFD-processed samples. The ability to increase the reaction rate between TMOS and water was attributed to the shear forces overcoming the immiscibility of the two reagents, appearing to form a single phase.[107]

The behaviour of carbon nanotubes within the VFD has resulted in significant insight into the origins and effects of shear-forces within the thin film microfluidic platform. The processing of a combination of single-walled carbon nanotubes (SWCNT), water, and toluene within a 20 mm VFD affords SWCNT nanorings of 300 to 700 nm diameter, whilst processing in the 10 mm VFD afforded nanorings of 100 to 200 nm diameter (Fig. 1.4.2a). The hypothesis given for the formation of these rings is that during sonication pre-VFD processing, the toluene forms toroids in the water, with SWCNT dispersed in the toluene toroids. During VFD-processing, the shear forces within the VFD cause compaction of the toroids and intertwining of the nanorings.[108] The ability of the VFD to slice carbon-nanotubes in a water/(NMP) dispersion using a laser has also been demonstrated. The hypothesis behind this capability is that the shear forces within the VFD cause bending in the SWCNT, which, in combination with the laser, result in the rupturing of C-C bonds, slicing the carbon nanotubes.[109] The formation of C_{60} nanotubules using a water/toluene solvent system in the VFD has also been demonstrated (Fig. 1.4.2b). The proposed mechanism involves the formation of micelles from water, providing a template for the growth of the nanotubules.[110]

The VFD has been used to encapsulate various cells in a variety of materials, including graphene,[111] graphene oxide,[112,113] and a magnetic polymer matrix.[114] The vast majority of these capabilities stem from one of three effects; the ability of shear forces to reduce aggregation and disassemble or exfoliate; the ability of shear forces to increase collision rates; and effects produced through the mixing of immiscible liquids. Together, these provide a general framework describing the capabilities of the VFD.

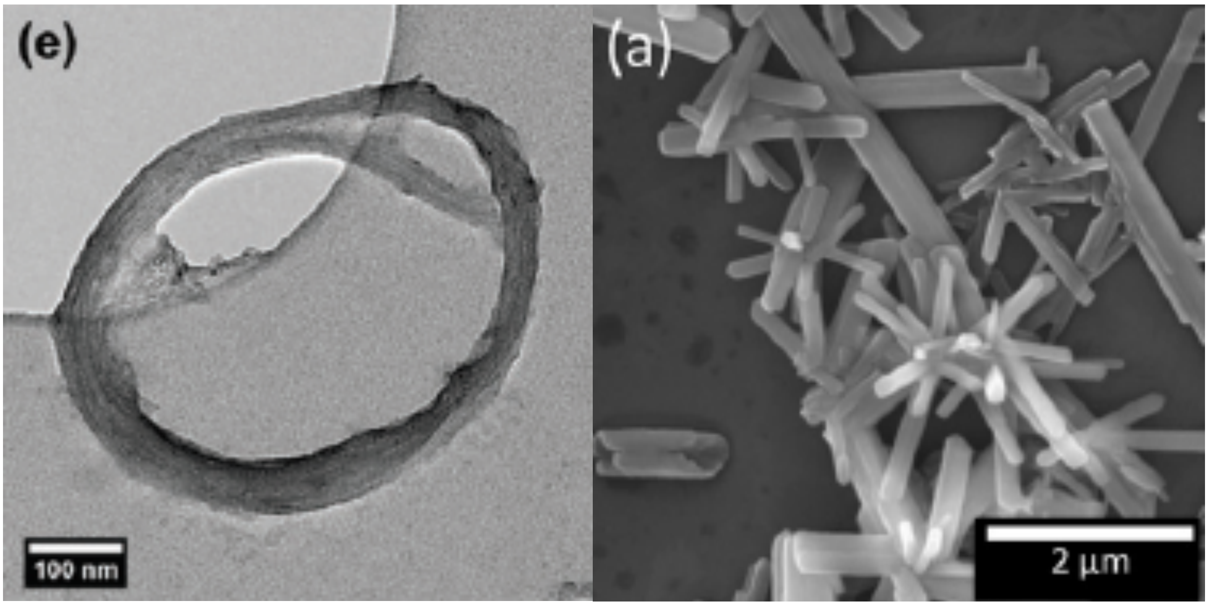

Fig. 1.4.2: a) TEM of a SWCNT nanoring prepared in the 20 mm VFD.[108] b) SEM of C_{60} nanotubules prepared in the 20 mm VFD.[110]

Chapter 1.4.2 – VFD-mediated chemical and biochemical processing

The VFD has produced interesting effects on proteins and enzymes. The processing of denatured hen egg white lysozyme (HEWL) in the VFD resulted in successful recovery of activity of the protein after 5 minutes, whilst longer processing resulted in unfolding of the protein.[115] The ability to refold denatured proteins was extended to a variant of caveolin lacking its transmembrane domain, which at 17 kDa is slightly larger than the 14 kDa of HEWL, although optimal processing time was longer at 30 minutes. Refolding of the larger cAMP-dependent protein kinase A (42 kDa) required binding of the protein to Ni^{2+}-charged immobilised metal affinity chromatography (IMAC) resin.[115] The ability to affect proteins also extends to the ability to accelerate enzymatic reactions, as demonstrated by the increase in reaction rate of esterase, β-glucosidase, alkaline phosphatase and deoxyribose-5-phosphate aldolase. The increase in reaction rate is highly rotational speed dependent (Fig. 1.4.3) and is attributed to the presence of rotational-speed dependent vibrations which result in a unique rotational landscape for each enzyme. The effect of these vibrations is hypothesised to be caused by one of three mechanisms: reduction in the active site volume caused by transient pressurisation of the active site resulting in increased turnover rates per the Van't Hoff Equation, beneficial conformational fluctuations caused by pressure fluctuations, and β- and α-relaxations caused by the pressure, resulting in small but beneficial conformational changes.[116]

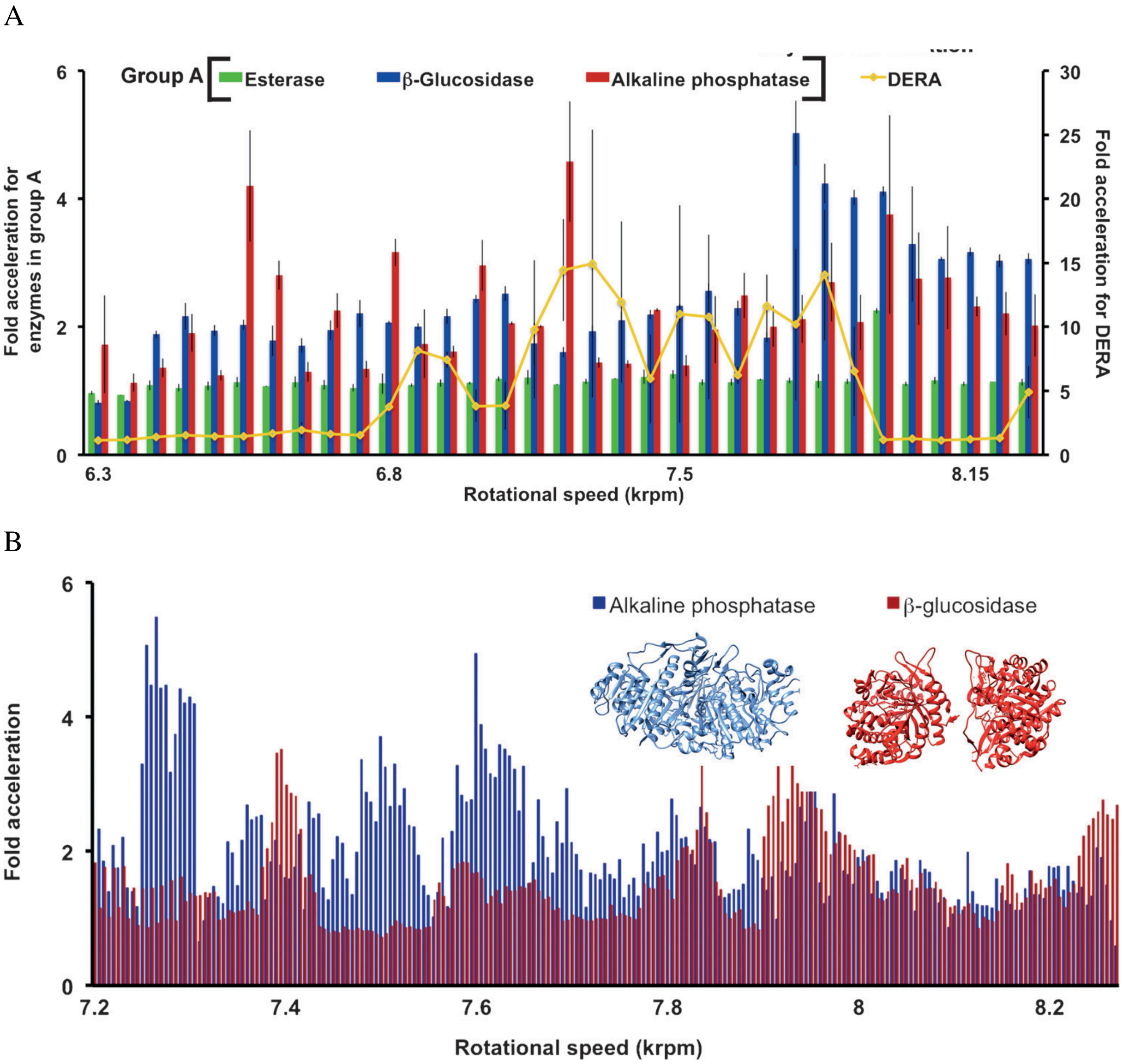

Fig. 1.4.3: Acceleration of enzymatic reactions in the VFD over the rotational speed range a) 6300 rpm to 8250 rpm, and b) 7200 rpm to 8250 rpm.[116]

The ability to accelerate reactions isn't limited to enzymatic reactions but extends to chemical reactions in general. Early work involving organic chemistry in the VFD demonstrated the ability to synthesise pyrazine-substituted amines from 2-chloropyrazine and secondary amines using aqueous bases with significantly reduced reaction times (Scheme 1.4.1).[117] The Diels-Alder dimerization of cyclopentadiene was shown to be more effective at higher tilt angles up to 45°, where a decrease was observed, followed by an increase at 90°. As before, this effect was attributed to an increase in shear forces, and introduces the concept of different shear regimes occurring at different tilt angles.[25] The acceleration of Diels-Alder reactions isn't limited to the dimerization of cyclopentadiene, extending to the reaction between substituted anthracenes and N-maleimides (Scheme 1.4.2), where higher rotational speeds result in higher yields.[118] In addition to resulting in reduced reaction times, the VFD has demonstrated an ability to accelerate reactions sufficiently to allow the avoidance of auxiliary reagents. This is demonstrated by the ability to prepare substituted pyrimidines and quinoxalines (Scheme 1.4.3), as reactions that typically require a toxic base or metal catalyst,[119] as well as the ability to synthesise esters and diesters using significantly less quantities of acid.[120,121]

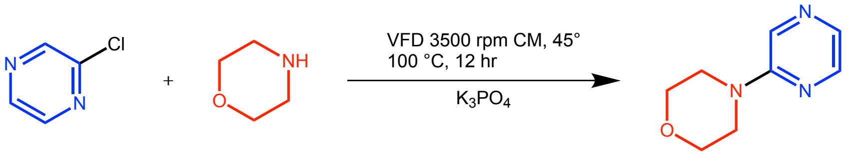

Scheme 1.4.1: The synthesis of pyrazine-substituted amines through VFD-mediated processing.[117]

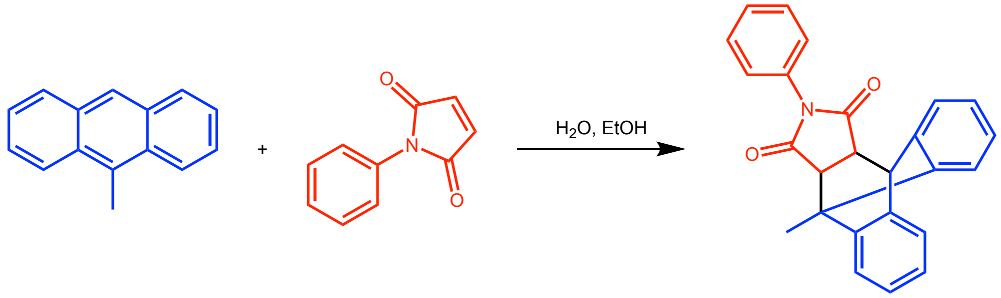

Scheme 1.4.2: The Diels-Alder reaction between 9-methylanthracene and phenylmaleimide.[118]

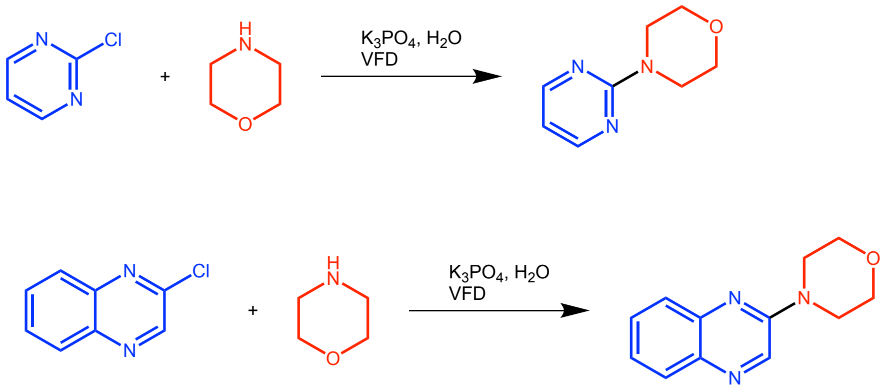

Scheme 1.4.3: Metal-free substitution of pyrimidines and quinoxalines.[119]

In addition to accelerating chemical reactions, the VFD has shown an ability to control selectivity in the synthesis of substituted pyridines. Substituted pyridines can be prepared from ammonium acetate, ketones and aldehydes (Scheme 1.4.4), however batch processing preferentially results in the formation of the Schiff base from the chalcone, in contrast to processing in the VFD, which allows the formation of the pyridine in yields ranging from 50%

to 70%.[25,122] The ability to control selectivity has also been demonstrated with the controlled synthesis of dichlorinated sulfones from allyl phenyl sulphide (Scheme 1.4.5), a product that is not produced in typical batch processing, although this capability is likely linked to the biphasic mixing afforded by the VFD.[41]

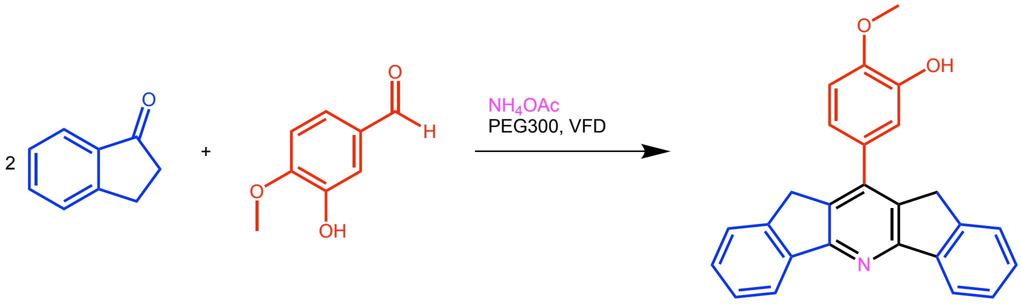

Scheme 1.4.4: The selective synthesis of pyridines.[122]

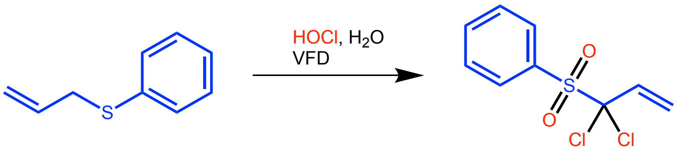

Scheme 1.4.5: The synthesis of chlorinated sulfones.[41]

Interestingly, the VFD can rapidly separate solvent mixtures that are immiscible but slow-separating, as established in the synthesis of biodiesel from sunflower oil. The production of biodiesel as such involves the conversion of oil tri-esters and methanol to fatty acid methyl esters and glycerol byproduct, in the presence of potassium hydroxide. As the mixture exits the VFD, it immediately separates into 3 layers: methanol with KOH, biodiesel, and glycerol.[98,123] In addition to this phase-separation, VFD is effective in improving the aqueous two-phase extraction of c-phycocyanin (C-PC) from *Spirulina maxima* along with rapid phase separation. Although PEG_{4000} is water-soluble, it is not soluble in high concentration in aqueous solutions of potassium phosphate. One conventional method for the extraction of C-PC involves extracting it from an aqueous potassium phosphate solution into PEG_{4000}, however, this process also extracts the contaminant protein allophycocyanin and involves long demixing times due to the small difference in densities between the two phases. Performing the extraction process in the VFD also reduced phase-separation times, as well as affording higher purity C-PC.[124] It is possible that these capabilities of the VFD are linked to the mixing of multi-phasic systems, which encourages the extraction of compounds selectively into one phase, thereby increasing the relative difference in phase density and polarity, and accelerating the separation rate of the phases.

In addition to performing single-step reactions in the VFD, the ability to couple multiple reactions together in a single tube has been demonstrated in two cases. The first involved the synthesis of Lidocaine as discussed above,[57] whilst the second was the multi-step synthesis of α-aminophosphonates. This synthesis involved the production of a Schiff base from benzaldehyde and aniline, followed by the replacement of methanol with DMF and the addition of triethylphosphite, and followed lastly by the addition of I_2 (Scheme 1.4.6). Note that although both I_2 and triethylphosphite are required for the second reaction, the I_2 must be added second, else it reacts with the Schiff base, resulting in a mixture of products.[125]

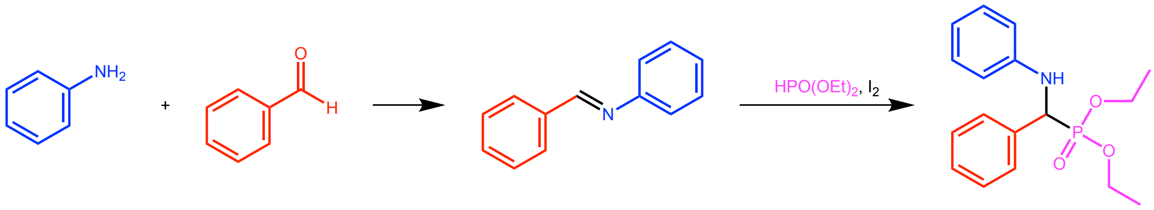

Scheme 1.4.6: The synthesis of an α-aminophosphonate in a single VFD through the formation of an imine followed by addition of diethylphosphite.[125]

Chapter 1.5 – Other Continuous Flow High-Shear Systems

A variety of other high-shear continuous flow systems have been utilised for organic synthesis, particularly for biphasic reactions. These systems include the Continuous Stirred Tank Reactor (CSTR),[42,126-128] the Film-Shear Reactor (FSR),[27,38,52] the Multi-Jet Oscillating Disc (MJOD), the Spinning Disc Processor (SDP), and the Spinning Tube-in-Tube Reactor (STT).

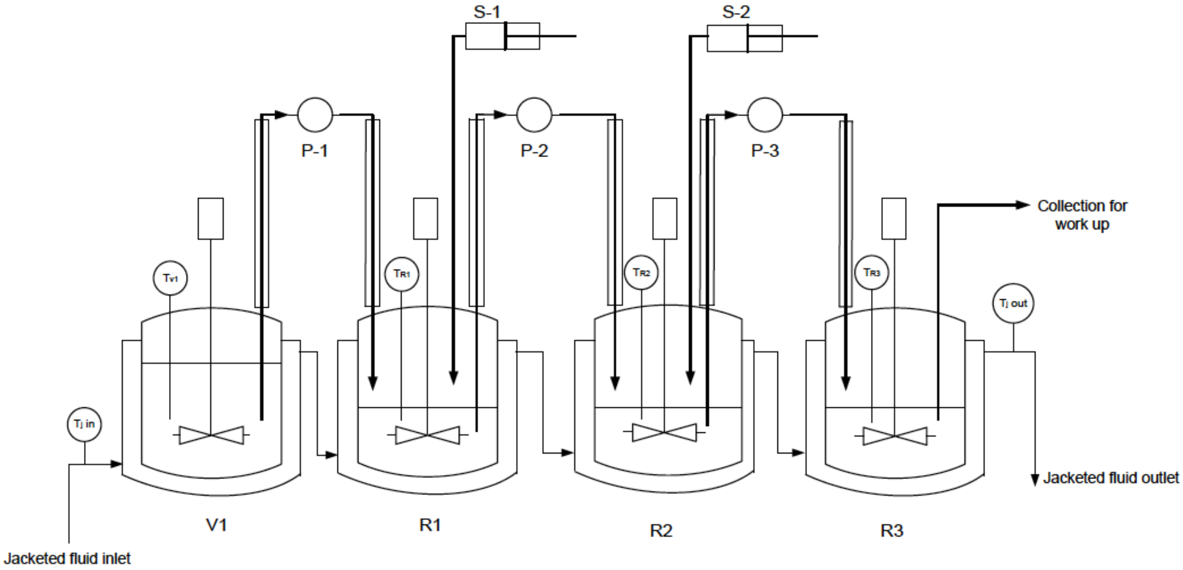

Fig. 1.5.1: Schematic of four Continuous Stirred Tank Reactors (CSTRs) connected in series.[128]

The design of the CSTR (Fig. 1.5.1) is exactly as it sounds, with reagents continuously fed into a stirred tank and extracted using a pump. An early use of the CSTR was for the final step in the synthesis of the anti-cancer agent tasisulam which involved the formation of an acyl sulphonamide under Schotten-Baumann conditions (Scheme 1.5.1a). The development of a continuous flow process was desired as a method for limiting the handling of tasisulam because of its cytotoxic properties, with the continuous flow synthesis connected to a continuous flow purification procedure. In selecting a continuous flow system, the CSTR was selected in favour of a plug flow reactor because the stirred nature of the CSTR resulted in better biphasic mixing, reducing the formation of the anhydride impurity. Additionally, the greater mixing also reduces the swing in local stoichiometry caused by fluctuations in flow rate.[42]

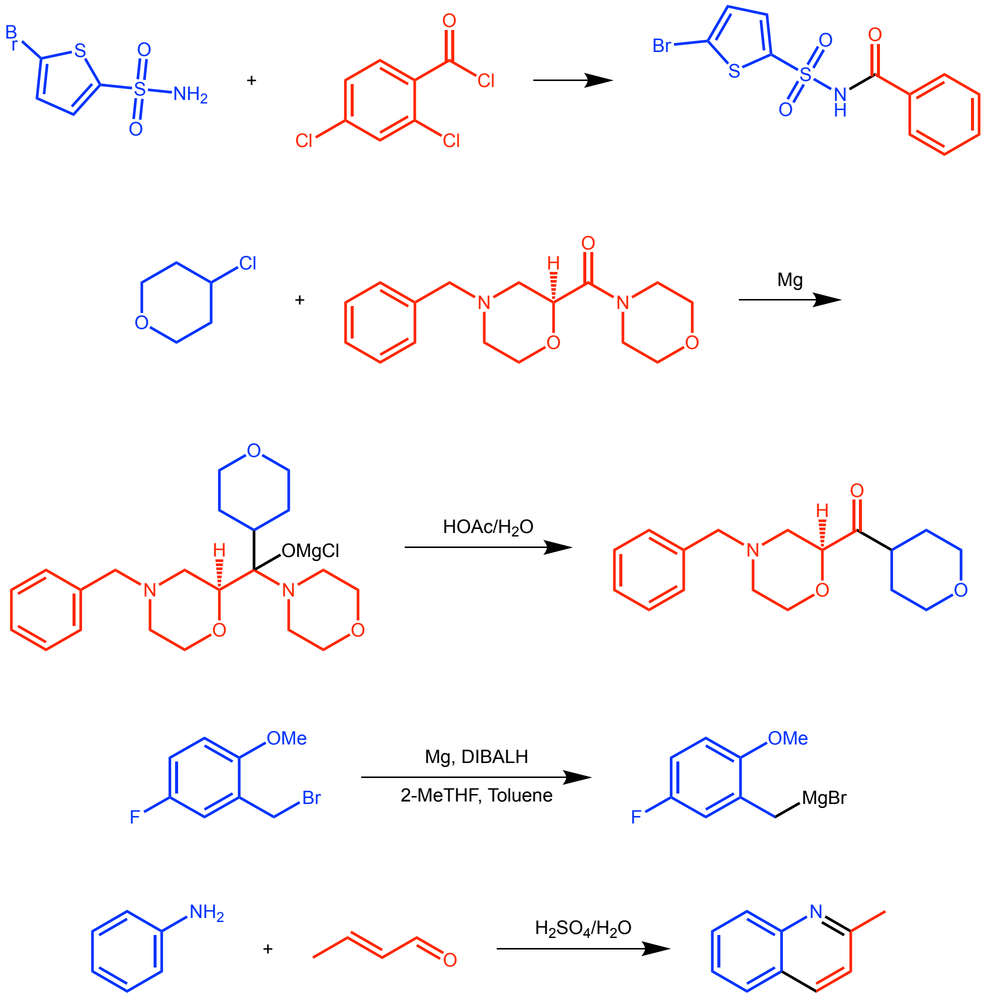

Scheme 1.5.1: Syntheses in the CSTR: a) Synthesis of tasisulam;[42] b) Barbier reaction for the replacement of a morpholine moiety with a tetrahydropyran moiety;[126] c) synthesis of a benzyl bromide Grignard reagent;[127] d) synthesis of 2-methylquinalone.[128]

The CSTR has also been applied to the Barbier reaction (Scheme 1.5.1b), a one-pot variation of the Grignard reaction for the synthesis of tertiary alcohols, resulting in an 88% yield sustained for 47 hours.[126] The CSTR has also been used for the more traditional synthesis of a Grignard reagent from a benzyl bromide (Scheme 1.5.1c).[127] The other example of organic synthesis in the CSTR is the synthesis of 2-methylquinoline from aniline, crotonaldehyde and sulfuric acid (Scheme 1.5.1d). The reaction involved heating a mixture of water, sulfuric acid and aniline to 92 °C, and pumping this mixture and crotonaldehyde into a CSTR. The reaction mixture was then pumped into a second CSTR, which was then pumped into a series of non-stirred vessels where the addition of sodium hydroxide raised the pH to 1 to encourage the precipitation of any polymerised crotonaldehyde. Continuous vacuum filtration and the addition of further NaOH increased the pH to 8, resulting in precipitation of the product.[128]

The Film-Shear Reactor (FSR) (Fig. 1.5.2) is capable of continuous processing of 2.2 mL of liquid at shear rates up to 840,000 Hz, and involves feeding reagents into a small gap (25-150 μm) between a rapidly spinning lower disc and a stationary upper disc. The very small gap and the high shear forces result in the intense mixing of the two feeds before their upwards exit in the centre of the stationary disc.[27] In addition to being used for ozonolysis as discussed above,[38] the FSR has been used for the oxidation of sulfur containing heterocyclic compounds in fuels, allowing the desulfurization of the fuels, a process termed oxidative desulfurization. This oxidative process is typically performed after conventional hydrodesulfurization, when polycyclic thiophenes are typically the only impurities remaining. Oxidation of thiophenes to sulfones using hydrogen peroxide results in their easy removal by taking advantage of their low solubility in the fuel phase. However, this is typically a slow process due to the biphasic nature of the system. As in the ozonolysis of alkenes, the FSR was applied to the challenge of accelerating biphasic reactions.[27,52] The use of 5% formic acid in 1:1 30% H_2O_2:isopropanol to oxidise a 0.5% solution of benzothiophene in decane achieved 53% desulfurization in 80 s at 10 °C, whilst conventional batch conditions required 4 hours at 80 °C to achieve 60% desulfurization.[52] The extension of this system to the removal of other thiophenes showed significantly decreased desulfurization (13%-27%), including for 2-methylbenzothiophene and 4-methylbenzothiophene, both of which are expected to be more easily oxidised than benzothiophene. No explanation for this unexpected result is provided, although they rule out the generation of both bulk and localized thermal hot spots as the cause behind the effect.[27]

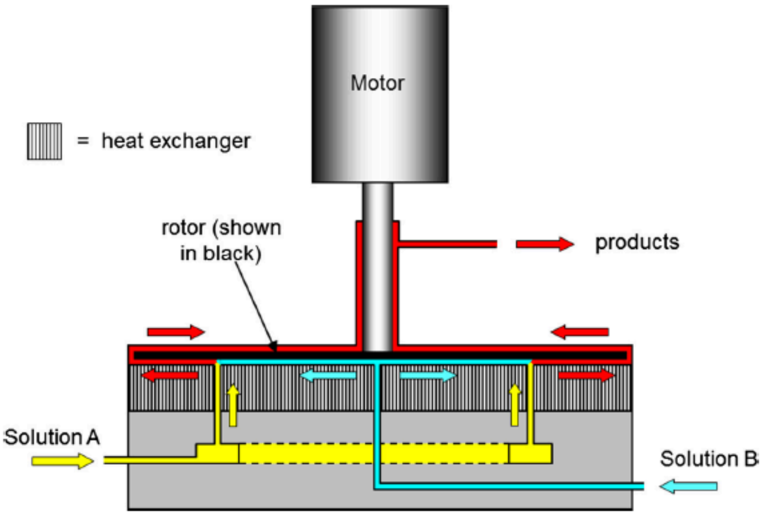

Fig. 1.5.2: The Film Shear Reactor (FSR).[27]

Like the FSR, operation of a spinning tube-in-tube reactor (STT, Fig. 1.5.3) involves the feeding of reactants into a thin gap, although for the STT the gap is annular in shape rather than flat and is slightly larger (250-380 μm) and processes a smaller volume of liquid (1.4 mL). Like the FSR, the STT has been used for biphasic reactions, specifically for the oxidation of alcohols using bleach (Scheme 1.5.4). Yields from 70% to 99% were achieved for various substrates, for speeds between 4000 rpm and 6000 rpm, although interestingly the yield was lower for speeds above or below this range.[129] The solventless synthesis of ionic liquids has also been performed in the same system (Fig. 1.5.4), where they compare commercially available STTs from two different companies. The conversion increased significantly at higher shear rates and was comparable for the two reactors at identical shear rates (Fig. 1.5.4).[130]

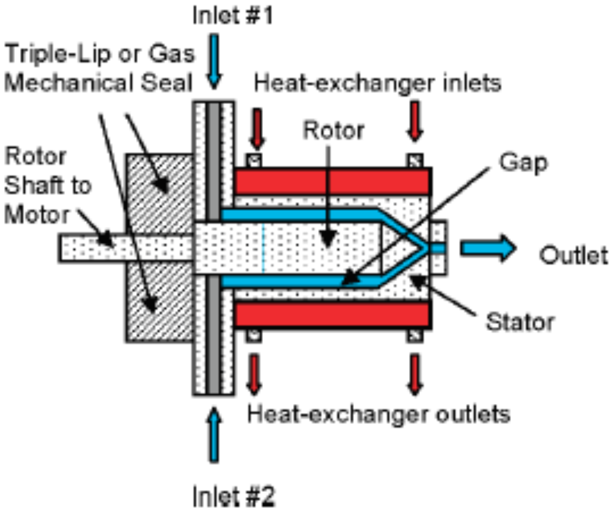

Fig. 1.5.3: The Spinning Tube-in-Tube Reactor (STT).[129]

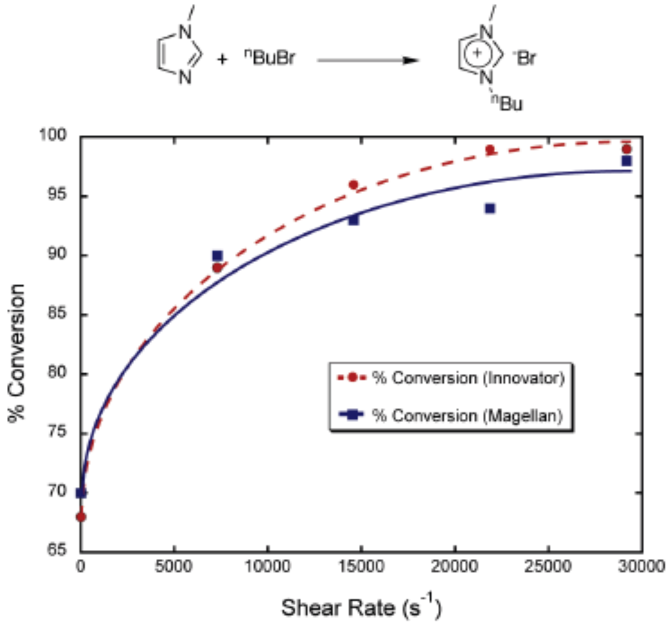

Fig. 1.5.4: The synthesis of imidazolium ionic liquids in STTs from Innovator and Magellan.[130]

An interesting non-laminar flow system is the Multi-Jet Oscillating Disc (MJOD) Reactor (Fig. 1.5.5), although the authors of the reporting papers do not discuss shear rates within the reactor. The MJOD consists of a cylindrical tube with a piston running through the centre of the tube. Attached to the piston are equally-spaced perforated discs that extend out to the walls of the reactor. The designers typically use between 60 and 100 discs, each with 4 perforations, giving cavities up to 650 μL in volume for a total volume up to 38 mL. During operation, liquid is fed into the tube and the piston oscillates rapidly in the longitudinal direction. Consequently, the liquid alternates between high velocity whilst being pushed through the perforations, and low velocity when it enters the larger cavity between the discs. This results in vortexes and exceptional mixing. Surrounding the reactor tube is an additional tube allowing for the circulation of heating and cooling fluid. The MJOD has been used for a wide variety of synthetic procedures, including the two-phase synthesis of allyloxybenzene without a phase-transfer catalyst,[54] the epoxidation of alkenes,[56] and other reactions.[53-55]

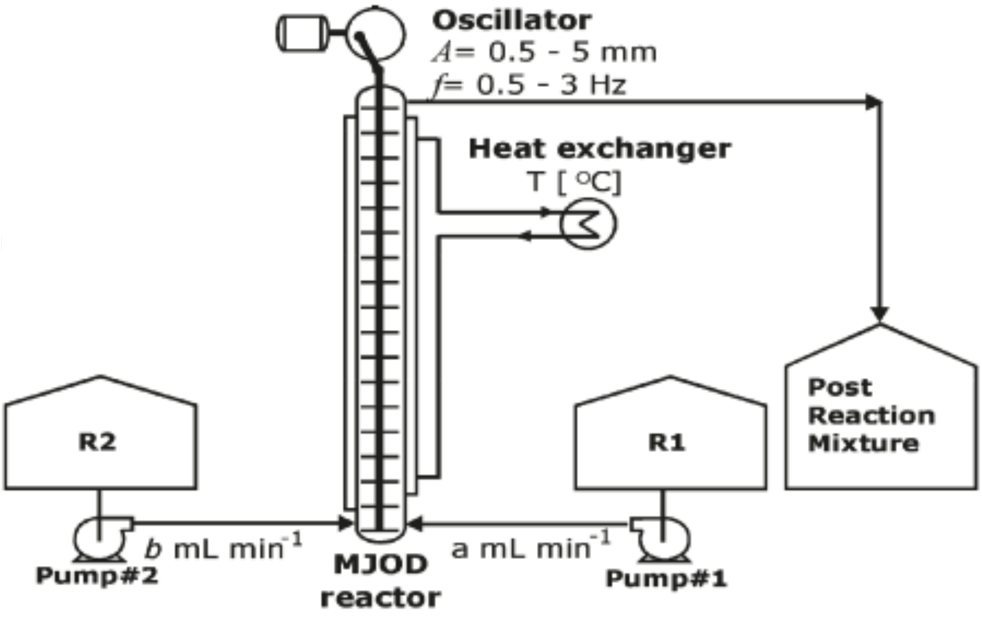

Fig. 1.5.5: The Multi-Jet Oscillating Disc (MJOD) Reactor.[54]

One of only two other non-laminar flow systems with a liquid-air interface is the spinning disc processor (SDP), which functions through the addition of liquid to the centre of a rapidly rotating disc, producing a film on the order of 1-200 μm. This system has been used for the Mizoroki-Heck Reaction.[131]

The other non-laminar flow system with a liquid-air interface is a vortex reactor recently reported by Martyn Poliakoff, which consists of a cylindrical vessel inside a cylindrical vessel with only a small gap (1 mm), with the *internal* cylinder rotated rapidly (up to 4000 rpm) (Fig. 1.5.6).[c] Like the MJOD, a heating/cooling jacket surrounds the outer tube. Typically, the top is not capped, in order to allow an air-liquid interface. Like the VFD, reagents are inserted through the top down to the bottom using feeds, exiting the system at the top. Around the cooling/heating jackets are LEDs allowing for photochemical reactions. Reactions demonstrated for this system include the photo-oxidation of furfural and phenylboronic acid, both of which were produced in higher yield at high rotational speeds.[132]

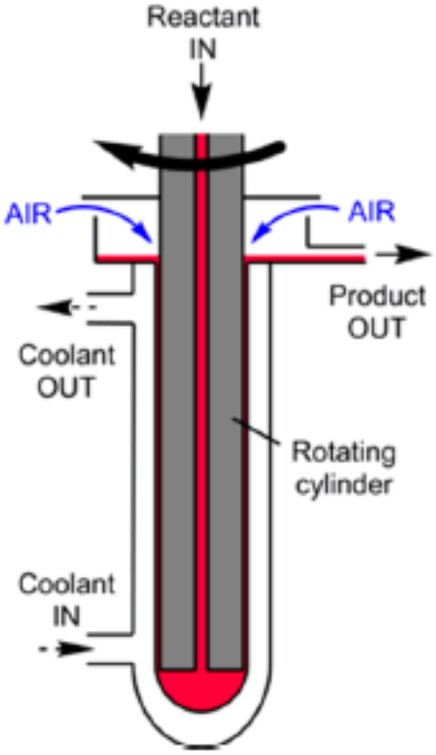

Fig. 1.5.6: The vortex reactor used for photo-oxidations.[132]

In summary, continuous flow processing has a wide range of advantages for designing more environmentally benign reactions, often allowing the reduction in processing times and the utilisation of closer-to-ambient conditions. In contrast to these advantages are challenges related to the solubility and compatibility of reactants, intermediates, products, and byproducts.

---

[c] The volume of the reactor is not stated, however, because the dimensions of the reactor are similar to those of the standard VFD design, the volume is likely to be on the order of 1-3 mL.

In addition to these system-generic capabilities, a number of specific flow systems have demonstrated the ability to finely control various operating conditions and restrict the localised accumulation of dangerous intermediates, allowing for the safer performance of greener reactions, whilst other flow systems have demonstrated the ability of high-shear systems to accelerate multi-phasic reactions. Amongst these flow systems is the Vortex Fluidic Device, which has demonstrated many useful capabilities for the synthesis of chemicals and nano-carbon materials, and for probing the structure of self-organised systems. However, the VFD has a liquid-air interface which makes understanding and predicting its capabilities, along with how it compares to other systems, inherently challenging.

To this end the overall aims of the research presented in this thesis are to develop a mathematical model predicting the shape of the thin film in the VFD, and to identify and utilise appropriate techniques to investigate the accuracy of the mathematical model. Further aims of this research are to advance the understanding of the environment within the VFD through the demonstration of Small Angle Neutron Scattering as a viable *in situ* technique for probing the environment within the VFD. A final aim of this research is to begin investigating whether the demonstrated ability of other flow systems to control selectivity through strict control of the residence time is an ability of the VFD.

Chapter 1.6 – References

1 Marion, P. *et al.* Sustainable chemistry: how to produce better and more from less? *Green Chemistry* **19**, 4973-4989, (2017).

2 Rockström, J. *et al.* A safe operating space for humanity. *Nature* **461**, 472, (2009).

3 Steffen, W. *et al.* Planetary boundaries: Guiding human development on a changing planet. *Science* **347**, 1259855, (2015).

4 Foley, J. A. *et al.* Solutions for a cultivated planet. *Nature* **478**, 337, (2011).

5 Clark, J., Sheldon, R., Raston, C., Poliakoff, M. & Leitner, W. 15 years of Green Chemistry. *Green Chemistry* **16**, 18-23, (2014).

6 Christoff, P. The promissory note: COP 21 and the Paris Climate Agreement. *Environmental Politics* **25**, 765-787, (2016).

7 Rogelj, J. *et al.* Paris Agreement climate proposals need a boost to keep warming well below 2 °C. *Nature* **534**, 631, (2016).

8 Hulme, M. 1.5 °C and climate research after the Paris Agreement. *Nature Climate Change* **6**, 222, (2016).

9 Olabisi, L. S. *et al.* Reducing Greenhouse Gas Emissions for Climate Stabilization: Framing Regional Options. *Environmental Science & Technology* **43**, 1696-1703, (2009).

10 Lutsey, N. & Sperling, D. America's bottom-up climate change mitigation policy. *Energy Policy* **36**, 673-685, (2008).

11 Reese, A. Blackouts cast Australia's green energy in dim light. *Science* **355**, 1001, (2017).

12 Constable, D. J. C. *et al.* Key green chemistry research areas-a perspective from pharmaceutical manufacturers. *Green Chemistry* **9**, 411-420, (2007).

13 Ludwig, J. R., Zimmerman, P. M., Gianino, J. B. & Schindler, C. S. Iron(III)-catalysed carbonyl–olefin metathesis. *Nature* **533**, 374, (2016).

14 Kumar, A., Jad, Y. E., El-Faham, A., de la Torre, B. G. & Albericio, F. Green solid-phase peptide synthesis 4. γ -Valerolactone and N-formylmorpholine as green solvents for solid phase peptide synthesis. *Tetrahedron Letters* **58**, 2986-2988, (2017).

15 Lyons, D. J. M., Crocker, R. D., Enders, D. & Nguyen, T. V. Tropylium salts as efficient organic Lewis acid catalysts for acetalization and transacetalization reactions in batch and flow. *Green Chemistry* **19**, 3993-3996, (2017).

16 Gu, J. *et al.* A two-step continuous flow synthesis of amides from alcohol using a metal-free catalyst. *RSC Advances* **5**, 95014-95019, (2015).

17 Liu, X. & Jensen, K. F. Multistep synthesis of amides from alcohols and amines in continuous flow microreactor systems using oxygen and urea hydrogen peroxide as oxidants. *Green Chemistry* **15**, 1538-1541, (2013).

18 Martinez-Montero, L., Diaz-Rodriguez, A., Gotor, V., Gotor-Fernandez, V. & Lavandera, I. Broadening the chemical scope of laccases: selective deprotection of N-benzyl groups. *Green Chemistry* **17**, 2794-2798, (2015).

19 Lau, P. L., Allen, R. W. K. & Styring, P. Continuous-flow Heck synthesis of 4-methoxybiphenyl and methyl 4-methoxycinnamate in supercritical carbon dioxide expanded solvent solutions. *Beilstein Journal of Organic Chemistry* **9**, 2886-2897, (2013).

20 Matsuda, T., Watanabe, K., Harada, T. & Nakamura, K. Enzymatic reactions in supercritical CO2: Carboxylation, asymmetric reduction and esterification. *Catalysis Today* **96**, 103-111, (2004).

21 Song, N. *et al.* Green production of pristine graphene using fluid dynamic force in supercritical CO2. *Chemical Engineering Journal* **298**, 198-205, (2016).

22 Kalkhambkar, R. G., Waters, S. N. & Laali, K. K. Highly efficient synthesis of amides via Ritter chemistry with ionic liquids. *Tetrahedron Letters* **52**, 867-871, (2011).

23 Cole, A. C. *et al.* Novel Brønsted Acidic Ionic Liquids and Their Use as Dual Solvent−Catalysts. *Journal of the American Chemical Society* **124**, 5962-5963, (2002).

24 Monopoli, A. *et al.* Selective N-Alkylation of Arylamines with Alkyl Chloride in Ionic Liquids: Scope and Applications. *European Journal of Organic Chemistry* **2012**, 3105-3111, (2012).

25 Yasmin, L., Chen, X., Stubbs, K. A. & Raston, C. L. Optimising a vortex fluidic device for controlling chemical reactivity and selectivity. *Scientific Reports* **3**, 2282, (2013).

26 Falus, P. *et al.* Reductive amination of ketones: novel one-step transfer hydrogenations in batch and continuous-flow mode. *Tetrahedron Letters* **52**, 1310-1312, (2011).

27 Fox, B. R. *et al.* Enhanced oxidative desulfurization in a film-shear reactor. *Fuel* **156**, 142-147, (2015).

28 Koh, M. J., Nguyen, T. T., Zhang, H., Schrock, R. R. & Hoveyda, A. H. Direct synthesis of Z-alkenyl halides through catalytic cross-metathesis. *Nature* **531**, 459, (2016).

29 Saberi, D., Akbari, J., Mahdudi, S. & Heydari, A. Reductive amination of aldehydes and ketones catalyzed by deep eutectic solvent using sodium borohydride as a reducing agent. *Journal of Molecular Liquids* **196**, 208-210, (2014).

30 Bisz, E. & Szostak, M. 2 ‐ Methyltetrahydrofuran: A Green Solvent for Iron ‐ Catalyzed Cross ‐ Coupling Reactions. *ChemSusChem* **11**, 1290-1294, (2018).

31 Fasan, R., Chen Mike , M., Crook Nathan , C. & Arnold Frances , H. Engineered Alkane ‐ Hydroxylating Cytochrome P450BM3 Exhibiting Nativelike Catalytic Properties. *Angewandte Chemie International Edition* **46**, 8414-8418, (2007).

32 Moore, J. C. & Arnold, F. H. Directed evolution of a para-nitrobenzyl esterase for aqueous-organic solvents. *Nature Biotechnology* **14**, 458, (1996).

33 Röthlisberger, D. *et al.* Kemp elimination catalysts by computational enzyme design. *Nature* **453**, 190, (2008).

34 Anastas, P., Warner, J. *Green Chemistry: Theory and Practice*. (Oxford University Press, 1998).

35 Bédard, A.-C. *et al.* Minimizing E-factor in the continuous-flow synthesis of diazepam and atropine. *Bioorganic & Medicinal Chemistry* **25**, 6223-6241, (2017).

36 Snead, D. R. & Jamison, T. F. End-to-end continuous flow synthesis and purification of diphenhydramine hydrochloride featuring atom economy, in-line separation, and flow of molten ammonium salts. *Chemical Science* **4**, 2822-2827, (2013).

37 Wiles, C. & Watts, P. Continuous flow reactors: a perspective. *Green Chemistry* **14**, 38-54, (2012).

38 Kendall, A. J. *et al.* Highly efficient biphasic ozonolysis of alkenes using a high-throughput film-shear flow reactor. *Tetrahedron Letters* **57**, 1342-1345, (2016).

39 Roydhouse, M. D. *et al.* Ozonolysis in flow using capillary reactors. *Organic Process Research and Development* **15**, 989-996, (2011).

40 Irfan, M., Glasnov, T. N. & Kappe, C. O. Continuous flow ozonolysis in a laboratory scale reactor. *Organic Letters* **13**, 984-987, (2011).

41 Pye, S. J., Dalgarno, S. J., Chalker, J. M. & Raston, C. L. Organic oxidations promoted in vortex driven thin films under continuous flow. *Green Chemistry* **20**, 118-124, (2018).

42 White, T. D. *et al.* Development of a Continuous Schotten–Baumann Route to an Acyl Sulfonamide. *Organic Process Research & Development* **16**, 939-957, (2012).

43 Reichart, B. K., O.; Glasnov, T. Phase-Transfer Catalysis: Mixing Effects in Continuous-Flow Liquid/Liquid O- and S-Alkylation Processes. *Synthesis* **24**, 2393-2396, (2013).

44 Bryan, M. C. *et al.* Evaluation of a commercial packed bed flowhydrogenator for reaction screening, optimization, and synthesis. *Beilstein Journal of Organic Chemistry* **7**, 1141-1149, (2011).

45 Losch, P. *et al.* Eco-compatible zeolite-catalysed continuous halogenation of aromatics. *Green Chemistry* **18**, 4714-4724, (2016).

46 Brodmann, T., Koos, P., Metzger, A., Knochel, P. & Ley, S. V. Continuous preparation of arylmagnesium reagents in flow with inline IR monitoring. *Organic Process Research and Development* **16**, 1102-1113, (2012).

47 Sans, V. & Cronin, L. Towards dial-a-molecule by integrating continuous flow, analytics and self-optimisation. *Chemical Society Reviews* **45**, 2032-2043, (2016).

48 Choi, Y.-S. K., Yoon-Jung; Shen, Liu-Lan; Lee, Yong Sup; Jeong, Jin-Hyun. Direct N-Alkylation of Aromatic Amines Using a Microflow Reactor: Enhancement of Selectivity and Reactivity. *Synlett* **26**, 970-974, (2015).

49 Kawaguchi, T., Miyata, H., Ataka, K., Mae, K. & Yoshida, J. i. Room‐Temperature Swern Oxidations by Using a Microscale Flow System. *Angewandte Chemie International Edition* **44**, 2413-2416, (2005).

50 Csajági, C. *et al.* High-Efficiency Aminocarbonylation by Introducing CO to a Pressurized Continuous Flow Reactor. *Organic Letters* **10**, 1589-1592, (2008).

51 Lou, S., Dai, P. & Schaus, S. E. Asymmetric Mannich reaction of dicarbonyl compounds with α-amido sulfones catalyzed by cinchona alkaloids and synthesis of chiral dihydropyrimidones. *Journal of Organic Chemistry* **72**, 9998-10008, (2007).

52 Fox, B. R. *et al.* Enhanced oxidative desulfurization of model fuels using a film-shear reactor. *Fuel* **90**, 898-901, (2011).

53 Bjørsvik, H.-R. & Liguori, L. Continuous Flow Olefin Metathesis Using a Multijet Oscillating Disk Reactor as the Reaction Platform. *Organic Process Research & Development* **18**, 1509-1515, (2014).

54 Liguori, L. & Bjørsvik, H.-R. Multijet Oscillating Disc Millireactor: A Novel Approach for Continuous Flow Organic Synthesis. *Organic Process Research & Development* **15**, 997-1009, (2011).

55 Sleveland, D. & Bjørsvik, H.-R. Synthesis of Phenylboronic Acids in Continuous Flow by Means of a Multijet Oscillating Disc Reactor System Operating at Cryogenic Temperatures. *Organic Process Research & Development* **16**, 1121-1130, (2012).

56 Spaccini, R., Liguori, L., Punta, C. & Bjørsvik, H. R. Organocatalyzed Epoxidation of Alkenes in Continuous Flow using a Multi‐Jet Oscillating Disk Reactor. *ChemSusChem* **5**, 261-265, (2012).

57 Britton, J., Chalker, J. M. & Raston, C. L. Rapid Vortex Fluidics: Continuous Flow Synthesis of Amides and Local Anesthetic Lidocaine. *Chemistry - A European Journal* **21**, 10660-10665, (2015).

58 Britton, J., Stubbs Keith, A., Weiss Gregory, A. & Raston Colin, L. Vortex Fluidic Chemical Transformations. *Chemistry – A European Journal* **23**, 13270-13278, (2017).

59 Nugent, W. A. & McKinney, R. J. Nickel-catalyzed Markovnikov addition of hydrogen cyanide to olefins. Application to nonsteroidal antiinflammatories. *The Journal of Organic Chemistry* **50**, 5370-5372, (1985).

60 Piccolo, O., Spreafico, F., Visentin, G. & Valoti, E. Zinc salt catalyzed rearrangement of acetals of optically active aryl 1-chloroethyl ketones: synthesis of optically active 2-arylpropionic acids and esters. *The Journal of Organic Chemistry* **52**, 10-14, (1987).

61 Cann, M., Connelly, M. E. *Real-World Cases in Green Chemistry*. (ACS, 2000).

62 Kjonaas, R. A., Williams, P. E., Counce, D. A. & Crawley, L. R. Synthesis of Ibuprofen in the Introductory Organic Laboratory. *Journal of Chemical Education* **88**, 825-828, (2011).

63 Tamura, Y., Yakura, T., Shirouchi, Y. & Haruta, J. Oxidative 1, 2-Aryl Migration of Alkyl Aryl Ketones by Using Diacetoxyphenyliodine : Syntheses of Arylacetate, 2-Arylpropanoate, and 2-Arylsuccinate. *Chemical & Pharmaceutical Bulletin* **33**, 1097-1103, (1985).

64 Bogdan, A. R., Poe, S. L., Kubis, D. C., Broadwater, S. J. & McQuade, D. T. The continuous-flow synthesis of ibuprofen. *Angewandte Chemie - International Edition* **48**, 8547-8550, (2009).

65 Snead, D. R. & Jamison, T. F. A three-minute synthesis and purification of ibuprofen: Pushing the limits of continuous-flow processing. *Angewandte Chemie - International Edition* **54**, 983-987, (2015).

66 Sigma-Aldrich. *Iodine monochloride, reagent grade, 98% | ICl | Sigma-Aldrich*, <https://www.sigmaaldrich.com/catalog/product/sigald/208221?lang=en&region=AU>.17/11/2018

67 Sigma-Aldrich. <https://www.sigmaaldrich.com/catalog/product/aldrich/178721?lang=en&region=AU>.17/11/2018

68 Baumann, M. & Baxendale, I. R. Continuous photochemistry: the flow synthesis of ibuprofen via a photo-Favorskii rearrangement. *Reaction Chemistry & Engineering* **1**, 147-150, (2016).

69 Hopkin, M. D., Baxendale, I. R. & Ley, S. V. A flow-based synthesis of Imatinib: The API of Gleevec. *Chemical Communications* **46**, 2450-2452, (2010).

70 Leonetti, F., Capaldi, C. & Carotti, A. Microwave-assisted solid phase synthesis of Imatinib, a blockbuster anticancer drug. *Tetrahedron Letters* **48**, 3455-3458, (2007).

71 Liu, Y.-F. *et al.* A Facile Total Synthesis of Imatinib Base and Its Analogues. *Organic Process Research & Development* **12**, 490-495, (2008).

72 Yang, J. C., Niu, D., Karsten, B. P., Lima, F. & Buchwald, S. L. Use of a “Catalytic” Cosolvent, N,N-Dimethyl Octanamide, Allows the Flow Synthesis of Imatinib with no Solvent Switch. *Angewandte Chemie International Edition* **55**, 2531-2535, (2016).

73 Dai, C., Snead, D. R., Zhang, P. & Jamison, T. F. Continuous-flow synthesis and purification of atropine with sequential in-line separations of structurally similar impurities. *Journal of Flow Chemistry* **5**, 133-138, (2015).

74 Sugasawa, T., Adachi, M., Toyoda, T. & Sasakura, K. A new simple synthesis of 1,4‐benzodiazepines. *Journal of Heterocyclic Chemistry* **16**, 445-448, (1979).

75 Adamo, A. *et al.* On-demand continuous-flow production of pharmaceuticals in a compact, reconfigurable system. *Science* **352**, 61-67, (2016).

76 Gerardy, R., Winter, M., Vizza, A. & Monbaliu, J.-C. M. Assessing inter- and intramolecular continuous-flow strategies towards methylphenidate (Ritalin) hydrochloride. *Reaction Chemistry & Engineering* **2**, 149-158, (2017).

77 Monbaliu, J.-C. M. *et al.* Compact and Integrated Approach for Advanced End-to-End Production, Purification, and Aqueous Formulation of Lidocaine Hydrochloride. *Organic Process Research & Development* **20**, 1347-1353, (2016).

78 Kockmann, N., Thenee, P., Fleischer-Trebes, C., Laudadio, G. & Noel, T. Safety assessment in development and operation of modular continuous-flow processes. *Reaction Chemistry & Engineering* **2**, 258-280, (2017).

79 Park, N. H., Senter, T. J. & Buchwald, S. L. Rapid Synthesis of Aryl Fluorides in Continuous Flow through the Balz–Schiemann Reaction. *Angewandte Chemie International Edition* **55**, 11907-11911, (2016).

80 Newman, S. G. *et al.* Rapid Wolff-Kishner reductions in a silicon carbide microreactor. *Green Chemistry* **16**, 176-180, (2014).

81 Yu, Z.-q., Lv, Y.-w., Yu, C.-m. & Su, W.-k. Continuous flow reactor for Balz–Schiemann reaction: a new procedure for the preparation of aromatic fluorides. *Tetrahedron Letters* **54**, 1261-1263, (2013).

82 Chen, Y. *et al.* Schmidt Reaction of Ketones in DME Solution in a Continuous-Flow Microreactor. *Organic Process Reseaelecrch & Development* **18**, 1589-1592, (2014).

83 Painter Thomas, O. *et al.* In Situ Generation and Intramolecular Schmidt Reaction of Keto Azides in a Microwave ‐ Assisted Flow Format. *Chemistry ‐ A European Journal* **17**, 9595-9598, (2011).

84 Bashore, C. G., Samardjiev, I. J., Bordner, J. & Coe, J. W. Twisted Amide Reduction under Wolff−Kishner Conditions: Synthesis of a Benzo-1-Aza-Adamantane Derivative. *Journal of the American Chemical Society* **125**, 3268-3272, (2003).

85 Eisenbraun, E. J., Payne, K. W. & Bymaster, J. S. Multiple-Batch, Wolff−Kishner Reduction Based on Azeotropic Distillation Using Diethylene Glycol. *Industrial & Engineering Chemistry Research* **39**, 1119-1123, (2000).

86 Kuethe, J. T. *et al.* A Practical, Kilogram-Scale Implementation of the Wolff−Kishner Reduction. *Organic Process Research & Development* **13**, 576-580, (2009).

87 Steinfeldt, N., Abdallah, R., Dingerdissen, U. & Jähnisch, K. Ozonolysis of Acetic Acid 1-Vinyl-hexyl Ester in a Falling Film Microreactor. *Organic Process Research & Development* **11**, 1025-1031, (2007).

88 O'Brien, M., Baxendale, I. R. & Ley, S. V. Flow ozonolysis using a semipermeable Teflon AF-2400 membrane to effect gas - Liquid contact. *Organic Letters* **12**, 1596-1598, (2010).

89 Allian, A. D., Richter, S. M., Kallemeyn, J. M., Robbins, T. A. & Kishore, V. The Development of Continuous Process for Alkene Ozonolysis Based on Combined in Situ FTIR, Calorimetry, and Computational Chemistry. *Organic Process Research & Development* **15**, 91-97, (2011).

90 Smit, C., Fraaije, M. W. & Minnaard, A. J. Reduction of Carbon−Carbon Double Bonds Using Organocatalytically Generated Diimide. *The Journal of Organic Chemistry* **73**, 9482-9485, (2008).

91 Kleinke, A. S. & Jamison, T. F. Hydrogen-free alkene reduction in continuous flow. *Organic Letters* **15**, 710-713, (2013).

92 Burns, N. Z., Baran, P. S. & Hoffmann, R. W. Redox Economy in Organic Synthesis. *Angewandte Chemie International Edition* **48**, 2854-2867, (2009).

93 Webb, D. & Jamison, T. F. Diisobutylaluminum hydride reductions revitalized: A fast, robust, and selective continuous flow system for aldehyde synthesis. *Organic Letters* **14**, 568-571, (2012).

94 Wu, J. *et al.* Continuous flow synthesis of ketones from carbon dioxide and organolithium or grignard reagents. *Angewandte Chemie - International Edition* **53**, 8416-8420, (2014).

95 Soloski, E. J. & Tamborski, C. Carbonation of ortho-, meta- and para-trifluoromethylphenyllithium compounds. *J Organomet Chem* **157**, 373-377, (1978).

96 Chen, X., Dobson, J. F. & Raston, C. L. Vortex fluidic exfoliation of graphite and boron nitride. *Chemical Communications* **48**, 3703-3705, (2012).

97 Martin, A. D., Boulos, R. A., Hubble, L. J., Hartlieb, K. J. & Raston, C. L. Multifunctional water-soluble molecular capsules based on p-phosphonic acid calix[5]arene. *Chemical Communications* **47**, 7353-7355, (2011).

98 Britton, J. & Raston, C. L. Continuous flow vortex fluidic production of biodiesel. *RSC Advances* **4**, 49850-49854, (2014).

99 Yasin, F. M. *et al.* Microfluidic size selective growth of palladium nano-particles on carbon nano-onions. *Chemical Communications* **48**, 10102-10104, (2012).

100 Goh, Y. A. *et al.* Shear flow assisted decoration of carbon nano-onions with platinum nanoparticles. *Chemical Communications* **49**, 5171-5173, (2013).

101 Chen, X. *et al.* Non-covalently modified graphene supported ultrafine nanoparticles of palladium for hydrogen gas sensing. *RSC Advances* **3**, 3213-3217, (2013).

102 Boulos, R. A. *et al.* Spinning up the polymorphs of calcium carbonate. *Scientific Reports* **4**, 3616, (2014).

103 Peng, W., Chen, X., Zhu, S., Guo, C. & Raston, C. L. Room temperature vortex fluidic synthesis of monodispersed amorphous proto-vaterite. *Chemical Communications* **50**, 11764-11767, (2014).

104 D'Alonzo, N. J., Eggers, P. K., Eroglu, E. & Raston, C. L. Shear Stress Induced Fabrication of Dandelion-Shaped Lanthanide Phosphate Nanoparticles. *Australian Journal of Chemistry* **70**, 823-829, (2017).

105 Kumari, H. *et al.* Manipulating three-dimensional gel network entanglement by thin film shearing. *Chemical Communications* **52**, 4513-4516, (2016).

106 Tong, C. L., Boulos, R. A., Yu, C., Iyer, K. S. & Raston, C. L. Continuous flow tuning of ordered mesoporous silica under ambient conditions. *RSC Advances* **3**, 18767-18770, (2013).

107 Tong, C. L., Stroeher, U. H., Brown, M. H. & Raston, C. L. Continuous flow vortex fluidic synthesis of silica xerogel as a delivery vehicle for curcumin. *RSC Advances* **5**, 7953-7958, (2015).

108 Vimalanathan, K., Chen, X. & Raston, C. L. Shear induced fabrication of intertwined single walled carbon nanotube rings. *Chemical Communications* **50**, 11295-11298, (2014).

109 Vimalanathan, K. *et al.* Fluid dynamic lateral slicing of high tensile strength carbon nanotubes. *Scientific Reports* **6**, 22865, (2016).

110 Vimalanathan, K. *et al.* Surfactant - free Fabrication of Fullerene C60 Nanotubules Under Shear. *Angewandte Chemie International Edition* **56**, 8398-8401, (2016).

111 Wahid, M. H., Eroglu, E., Chen, X., Smith, S. M. & Raston, C. L. Functional multi-layer graphene-algae hybrid material formed using vortex fluidics. *Green Chemistry* **15**, 650-655, (2013).

112 Wahid, M. H. *et al.* Microencapsulation of bacterial strains in graphene oxide nano-sheets using vortex fluidics. *RSC Advances* **5**, 37424-37430, (2015).

113 Wahid, M. H., Eroglu, E., Chen, X., Smith, S. M. & Raston, C. L. Entrapment of Chlorella vulgaris cells within graphene oxide layers. *RSC Advances* **3**, 8180-8183, (2013).

114 Eroglu, E., D'Alonzo, N. J., Smith, S. M. & Raston, C. L. Vortex fluidic entrapment of functional microalgal cells in a magnetic polymer matrix. *Nanoscale* **5**, 2627-2631, (2013).

115 Yuan, T. Z. *et al.* Shear-stress-mediated refolding of proteins from aggregates and inclusion bodies. *ChemBioChem* **16**, 393-396, (2015).

116 Britton, J., Meneghini, L. M., Raston, C. L. & Weiss, G. A. Accelerating Enzymatic Catalysis Using Vortex Fluidics. *Angewandte Chemie - International Edition* **55**, 11387-11391, (2016).

117 Gandy, M. N., Raston, C. L. & Stubbs, K. A. Towards aryl C-N bond formation in dynamic thin films. *Organic and Biomolecular Chemistry* **12**, 4594-4597, (2014).

118 Yasmin, L., Stubbs, K. A. & Raston, C. L. Vortex fluidic promoted Diels-Alder reactions in an aqueous medium. *Tetrahedron Letters* **55**, 2246-2248, (2014).

119 Ho, L. A., Raston, C. L. & Stubbs, K. A. Transition-Metal-Free Cross-Coupling Reactions in Dynamic Thin Films To Access Pyrimidine and Quinoxaline Analogues. *European Journal of Organic Chemistry* **2016**, 5957-5963, (2016).

120 Britton, J., Dalziel, S. B. & Raston, C. L. Continuous flow Fischer esterifications harnessing vibrational-coupled thin film fluidics. *RSC Advances* **5**, 1655-1660, (2015).

121 Britton, J., Dalziel, S. B. & Raston, C. L. The synthesis of di-carboxylate esters using continuous flow vortex fluidics. *Green Chemistry* **18**, 2193-2200, (2016).

122 Yasmin, L., Eggers, P. K., Skelton, B. W., Stubbs, K. A. & Raston, C. L. Thin film microfluidic synthesis of fluorescent highly substituted pyridines. *Green Chemistry* **16**, 3450-3453, (2014).

123 Britton, J. & Raston, C. L. Rapid high conversion of high free fatty acid feedstock into biodiesel using continuous flow vortex fluidics. *RSC Advances* **5**, 2276-2280, (2015).

124 Luo, X., Smith, P., Raston, C. L. & Zhang, W. Vortex fluidic device-intensified aqueous two phase extraction of C-phycocyanin from spirulina maxima. *ACS Sustainable Chemistry and Engineering* **4**, 3905-3911, (2016).

125 Britton, J., Castle, J. W., Weiss, G. A. & Raston, C. L. Harnessing Thin-Film Continuous-Flow Assembly Lines. *Chemistry - A European Journal* **22**, 10773-10776, (2016).

126 Kopach, M. E. *et al.* The continuous flow Barbier reaction: an improved environmental alternative to the Grignard reaction? *Green Chemistry* **14**, 1524-1536, (2012).

127 Wong, S.-W. *et al.* Operation Strategy Development for Grignard Reaction in a Continuous Stirred Tank Reactor. *Organic Process Research & Development* **20**, 540-550, (2016).

128 Yadav, M. B., Kulkarni, S., Joshi, R. A. & Kulkarni, A. A. Continuous Flow Doebner–Miller Reaction and Isolation Using Continuous Stirred Tank Reactors. *Organic Process Research & Development* **20**, 1621-1625, (2016).

129 Hampton, P. D., Whealon, M. D., Roberts, L. M., Yaeger, A. A. & Boydson, R. Continuous Organic Synthesis in a Spinning Tube-in-Tube Reactor: TEMPO-Catalyzed Oxidation of Alcohols by Hypochlorite. *Organic Process Research & Development* **12**, 946-949, (2008).

130 Gonzalez, M. A. & Ciszewski, J. T. High Conversion, Solvent Free, Continuous Synthesis of Imidazolium Ionic Liquids In Spinning Tube-in-Tube Reactors. *Organic Process Research & Development* **13**, 64-66, (2009).

131 Zou, J., Swaminathan Iyer, K., Stewart, S. G. & Raston, C. L. Scalable synthesis of catalysts for the Mizoroki-Heck cross coupling reaction: Palladium nanoparticles assembled in a polymeric nanosphere. *New Journal of Chemistry* **35**, 854-860, (2011).

132 Lee, D. S. *et al.* Continuous Photo-Oxidation in a Vortex Reactor: Efficient Operations Using Air Drawn from the Laboratory. *Organic Process Research & Development* **21**, 1042-1050, (2017).

Chapter 2

Development and analysis of a mathematical model for the Vortex Fluidic Device

Until recently, very little work had been undertaken into investigating the shape and nature of the thin film within the Vortex Fluidic Device (VFD), being limited to determining the average film thickness under various operating conditions for the VFD housing a 10 mm diameter glass tube,[1] and determining the residence time at various flow rates for the 20 mm VFD operating at 6950 rpm.[2] The development of a thorough model was initiated in order to better understand the impact of various operating parameters on different reactions, and to allow the calculation of useful operating conditions in order to better understand and better design specific applications of the microfluidic platform, in moving towards a high level of predictability of the outcome of any processing.

All graphs include a full list of conditions used to generate the data in the figure caption. Graphs indicated as using "standard VFD conditions" use $R = 0.00875$ m, $H = 0.18$ m, $\theta = 45°$, and $g = 9.8$ ms^{-2}, unless stated otherwise.

For a list of symbols used in this chapter see the symbol list at the start of this thesis and for step-wise derivations of equations marked with * see Appendix A.

Parts of chapters 2.1, 2.2, 2.3 and 2.4 were included as part of a paper under review by *Scientific Reports* titled: 'Neutron imaging and modelling inclined vortex driven thin films', co-authored by Filomena Salvemini, Stuart Dalziel and Colin Raston.

Chapter 2.1 – Development of a mathematical model

Chapter 2.1.1 – Force balance

There are a number of forces that operate within the VFD, including gravity, the centripetal force, polarity-based interactions between the liquid and the glass, viscous drag within the liquid, and vibrations induced by imperfect rotation of the glass tube. Here, the net force $\vec{F}$ is considered to consist solely of the gravitational force $\overrightarrow{F_g}$ pulling the liquid down and the centrifugal force $\overrightarrow{F_c}$ pushing the liquid towards the walls of the tube

Equation 2.1

$$\vec{F} = \overrightarrow{F_g} + \overrightarrow{F_c}.$$

The effect of surface tension and viscosity is recognised as being significant in some circumstances (particularly below 100 µm in film thickness), however, their inclusion in the model would add unnecessary complexity, as the purpose of the model is to allow the calculation of useful parameters, rather than to gain a high level rigorous understanding of the fluid behaviour. Additionally, surface tension and viscosity are affected by the chemical composition of the film, a composition which is not uniform due to the conversion of reactants to products. Due to the high concentrations often used within the device (up to 0.3 g/mL),[3] chemical composition is expected to significantly affect viscosity, surface tension and temperature, with temperature in turn affecting viscosity and surface tension. The incorporation of surface tension and viscosity into the model would require quantitatively understanding the behaviour of chemical reactions within the device, an understanding which is currently in its infancy.

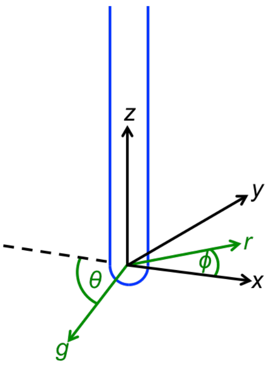

The reference frame used here is (x, y, z), where +x is towards the right, +y is away from the viewer, and +z is upwards. In considering the tilt angle θ, two approaches can be taken; maintaining gravity constantly in the z direction and varying the angle of the tube, or alternatively, keeping the orientation of the tube constant, but varying the angle of gravity; here the latter approach has been taken, where θ is the angle at which gravity acts in relation to the tube. The angular position is defined such that $\theta = 0$ corresponds to gravity acting towards the left $(-g, 0, 0)$ (corresponding to the VFD tube positioned horizontally with the base on the right), and $\theta = \frac{\pi}{2}$ corresponds to gravity acting downwards (0, 0, -*g*) (VFD positioned vertically). The force per unit volume of the liquid due to gravity is therefore

Equation 2.2

$$\overrightarrow{F_g} = -\rho g(\cos\theta, 0, \sin\theta).$$

The centrifugal force per unit volume is

Equation 2.3

$$\overrightarrow{F_c} = \rho r\omega^2(\cos\phi, \sin\phi, 0),$$

where *r* is the radial distance from the rotation (z) axis and *ω* is the rotational speed in radians per second. Here, ϕ is the angular position around the tube in the x-y plane, such that $\phi = 0$ corresponds to the x axis and $\phi = \frac{\pi}{2}$ corresponds to the y axis. The net force per unit volume on the fluid is therefore

Equation 2.4

$$\vec{F} = \rho(r\omega^2\cos\phi - g\cos\theta, r\omega^2\sin\phi, -g\sin\theta).$$

Note that when $0° \leq \theta \leq 90°$, $\phi = 0°$ corresponds to the point closest to the ceiling, whilst $\phi = 180°$ corresponds to the point closest to the floor.

Chapter 2.1.2 – Determining the shape of the thin film

The system, defined as the liquid confined in a tube, is considered only when in equilibrium, and consequently the net force must be exerted in a direction orthogonal to the surface of the liquid. The surface of the film is defined by $z = h(x, y)$, or equivalently $z - h(x, y) = 0$. Here, h is the height of the surface of the liquid for a specified co-ordinate (here, in the x-y plane, later, in terms of distance *r* from the centre of the tube and angular position ϕ). The vector normal to the surface, $\vec{n}$, is therefore

Equation 2.5

$$\vec{n} = \nabla\big(z - h(x, y)\big) = \left(-\frac{\partial h}{\partial x}, -\frac{\partial h}{\partial y}, 1\right).$$

The direction of the net force must be parallel to $\vec{n}$ and so $\vec{F} \times \vec{n} = \vec{0}$. Substituting (2.4) and (2.5) into the vector cross product reveals

Equation 2.6*

$$\frac{\partial h}{\partial y} = \frac{r\omega^2\sin\phi}{g\sin\theta}, \frac{\partial h}{\partial x} = -\frac{\cos\theta}{\sin\theta} + \frac{r\omega^2\cos\phi}{g\sin\theta}.$$

It is useful to use the chain rule to perform a change of variable from $h(x, y)$ to $h(r, \phi)$ noting that

Equation 2.7

$$\frac{\partial h}{\partial r} = \frac{\partial h}{\partial x}\frac{\partial x}{\partial r} + \frac{\partial h}{\partial y}\frac{\partial y}{\partial r},$$

and that $\frac{\partial x}{\partial r}$ and $\frac{\partial y}{\partial r}$ can be easily calculated from $x = r\cos\phi$ and $y = r\sin\phi$, giving $\frac{\partial x}{\partial r} = \cos\phi$ and $\frac{\partial y}{\partial r} = \sin\phi$. This gives

Equation 2.8

$$\frac{\partial h}{\partial r} = \cos\phi\left(-\frac{\cos\theta}{\sin\theta} + \frac{r\omega^2\cos\phi}{g\sin\theta}\right) + \sin\phi\left(\frac{r\omega^2\sin\phi}{g\sin\theta}\right) = \frac{r\omega^2}{g\sin\theta} - \cos\phi\cot\theta,$$

with subsequent integration producing

Equation 2.9

$$h = \frac{r^2\omega^2}{2g\sin\theta} - r\cos\phi\cot\theta + k,$$

giving h as a function of r, ω, g, θ, ϕ and k, where k is the distance from the base of the tube to the height where $r = 0$ (note that $k < 0$).

Chapter 2.1.3 – Determination of *k* from the volume of liquid

In order to calculate k, equation 2.10 is used, where the volume V is calculated by integrating the height around the z-axis from $\phi = 0$ to $\phi = 2\pi$, and from the surface of the film (where $r_i \equiv r$ at $h = 0$) to the glass (R). The constant of integration k can be determined from the volume of fluid in the system. Specifically,

Equation 2.10

$$V = \int_0^{2\pi}\int_{r_i}^{R} hr\,dr\,d\phi,$$

where r_i is the radius at which the film intersects the base of the tube, or zero if the fluid covers the entire base. For a flat-bottomed tube, (2.9) is solved for $h = 0$ and $r = r_i$, giving

Equation 2.11*

$$r_i = A\cos\phi + \sqrt{A^2\cos^2\phi + B},$$

where

Equation 2.12*

$$A = \frac{g\cos\theta}{\omega^2}\; B = -\frac{2g\sin\theta}{\omega^2}k.$$

Computing the inner integral of (2.1) is straight forward, giving

Equation 2.13*

$$V = \int_0^{2\pi}\left(\frac{(R^4 - r_i^4)\omega^2}{8g\sin\theta} - \left(\frac{R^3 - r_i^3}{3}\right)\cos\phi\cot\theta + \frac{1}{2}(R^2 - r_i^2)k\right)d\phi.$$

Substituting for r_i using (2.12) and eliminating terms that contain odd powers of $\cos\phi$ (since these integrate to zero over [0, 2π]) reduces the integral to

Equation 2.14*

$$V = \frac{\pi}{4}\left(\frac{g^3\cos^4\theta}{\omega^6\sin\theta}\right) - \pi\left(\frac{g^2\cos^2\theta}{\omega^4}k\right) + \pi\left(\frac{gk^2\sin\theta}{\omega^2} + \frac{R^4\omega^2}{4g\sin\theta} + R^2k\right).$$

Under confined mode for a finite volume of liquid in the tube, k is solved by specifying the volume, yielding

Equation 2.15*

$$h = \frac{\omega^2}{2g\sin\theta}(r^2 - R^2) - r\cos\phi\cot\theta + \frac{g\cos^2\theta}{\omega^2\sin\theta} + \sqrt{\frac{\omega^2}{g\pi\sin\theta}V - \frac{1}{2}R^2\cot^2\theta}.$$

This is only valid when the maximum height of the film does not exceed the height of the tube H, or specifically, when

$$h(r = R, \phi = \pi) \leq H.$$

There are two other limitations of the model (aside from limitations inherent in discounting viscosity and surface tension). The first is when there is sufficient volume that the bottom of the tube is not dry $(r(h = 0) = 0)$, even if the film does not reach the top of the tube. This occurs at

$$V \geq \frac{\pi R^4\omega^2}{4g\sin\theta} + \frac{\pi g^3\cos^4\theta}{\omega^6\sin\theta} - \frac{\pi R^2\cos^2\theta}{2\omega^2\sin\theta}.$$

The other limitation occurs when there is not sufficient volume to produce a film at all rotational positions $(r(h = 0, \phi = 0) = R)$, occurring when

$$V \leq \frac{3}{2}\frac{\pi g R^2\cos^2\theta}{\omega^2\sin\theta} + \frac{\pi g^3\cos^4\theta}{\omega^6\sin\theta} - \frac{2\pi g^2 R\cos^3\theta}{\omega^4\sin\theta}.$$

For 2000 rpm at $\theta = 45°$, this volume is 56 µL, whilst at 6000 rpm this volume is 6.3 µL.

Chapter 2.2 – Film thickness

One of the major aspects of VFD processing believed to have a significant effect on chemical reactions and material modifications is the small film thickness, which results in a high surface area to volume ratio.[4] As a consequence, it is important to understand the effect that various conditions have on the film thickness. In order to investigate this, equation 2.15 was rearranged as

Equation 2.16*

$$f_t = R - \frac{g}{\omega^2}\cos\phi\cos\theta - \sqrt{R^2 - \frac{g^2}{\omega^4}\cos^2\theta\,(\sin^2\phi) + 2gh\frac{\sin\theta}{\omega^2} - \sqrt{\frac{4gV\sin\theta}{\pi\omega^2} - \frac{2g^2R^2}{\omega^4}\cos^2\theta}}$$

to give the film thickness f_t. From equation 2.16 it is clear the film thickness is a function of two positional variables (the angular position around the tube ϕ and the height of interest h), three operating conditions (rotational speed ω, tilt angle θ, and volume V), one VFD design variable (tube radius R) and one constant but uncontrolled 'variable' (gravity g).

For a particular set of operating conditions of the VFD, the film thickness decreases almost linearly as a function of increasing height (Fig. 2.2.1) and varies almost sinusoidally as a function of angular position around the tube (Fig. 2.2.2). Although f_t is not linearly dependent on h, this near linear dependence arises because the effect of h on the slope $\frac{df_t}{dh}$ is small for typical operating conditions. The slope of the film is given by

$$\frac{df_t}{dh} = -\frac{2g\sin\theta}{\omega^2\sqrt{R^2 - \frac{g^2}{\omega^4}\cos^2\theta(\sin^2\phi) + 2gh\frac{\sin\theta}{\omega^2} - \sqrt{\frac{4gV\sin\theta}{\pi\omega^2} - \frac{2g^2R^2}{\omega^4}\cos^2\theta}}},$$

where the sum of the blue terms is at least ten times greater than the green term. Consequently, for typical operating conditions, the effect of height on the slope is minimal, giving a linear shape. The sinusoidal effect of ϕ arises because the $\cos\phi$ term is significantly more influential than the $\sin^2\phi$ term. For typical operating conditions, the magnitude of the $\cos\phi$ term ranges from 10 µm to 70 µm, whilst the effect of the $\sin^2\phi$ ranges from 0.003 µm to 0.3 µm. Clearly, the $\cos\phi$ term is much more impactful, leading to a near-sinusoidal dependence of f_t on ϕ.

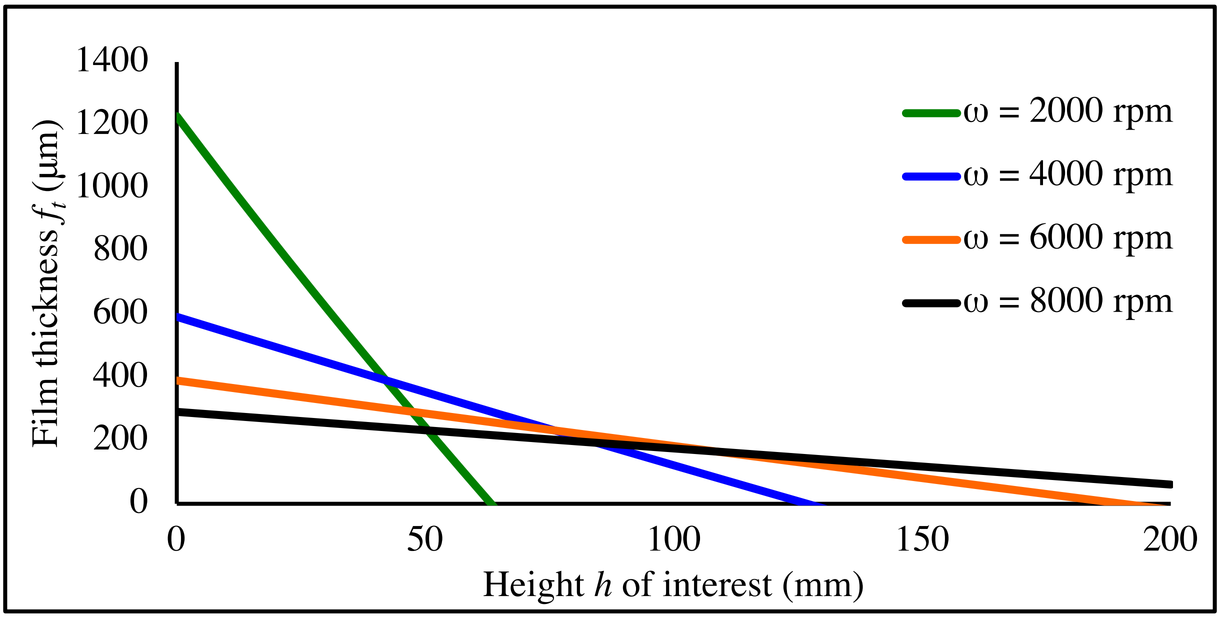

Fig. 2.2.1: The effect of height h on film thickness f_t for various rotational speeds ω. Standard VFD conditions, $\phi = 90°$, $V = 2$ mL.

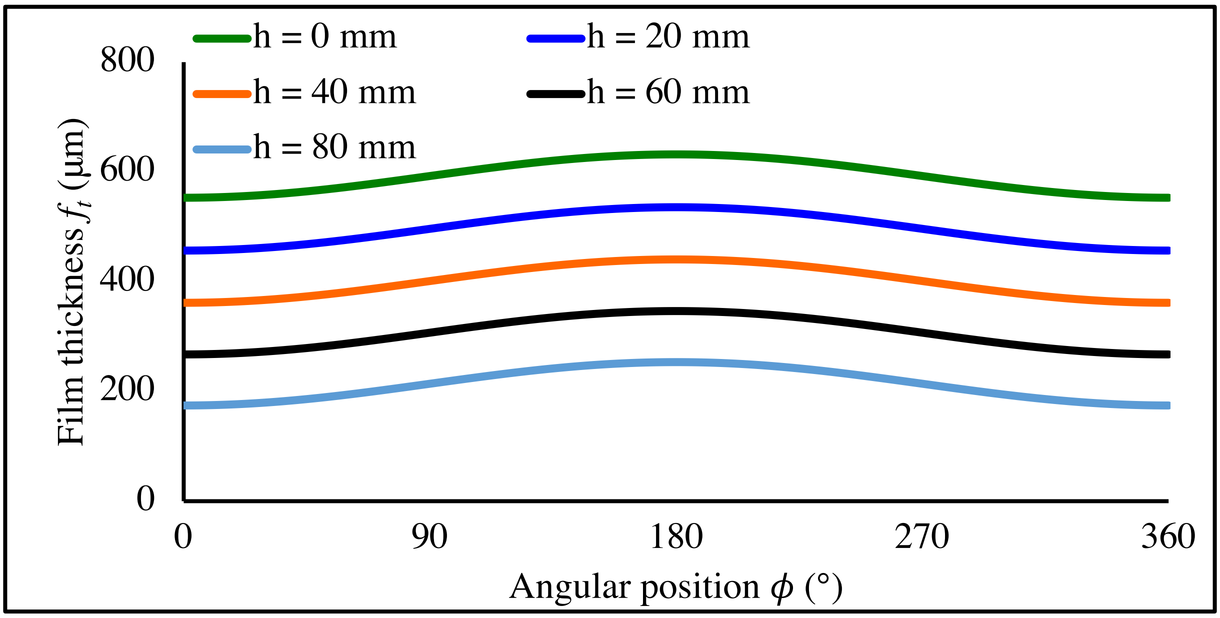

Fig. 2.2.2: The effect of angular position ϕ on film thickness f_t for various heights h. Standard VFD conditions, $V = 2$ mL, and $\omega = 4000$ rpm.

Figures 2.2.3 and 2.2.4 show that as the rotational speed is increased, the film thickness initially exhibits a sharp increase, followed by a gradual decrease as the rotational speed is further increased. The cause of this phenomenon is that initially for a height of h, the rotational speed is too low for the liquid to reach h. As the rotational speed is increased the film thickness increases rapidly from zero once the film reaches h, and continues to increase because a thicker portion of the film reaches height h. However, acting against this increase in film thickness is the overall decrease in the average film thickness. Eventually, this decrease in film thickness sufficiently counters the increase, resulting in a gradual decrease.

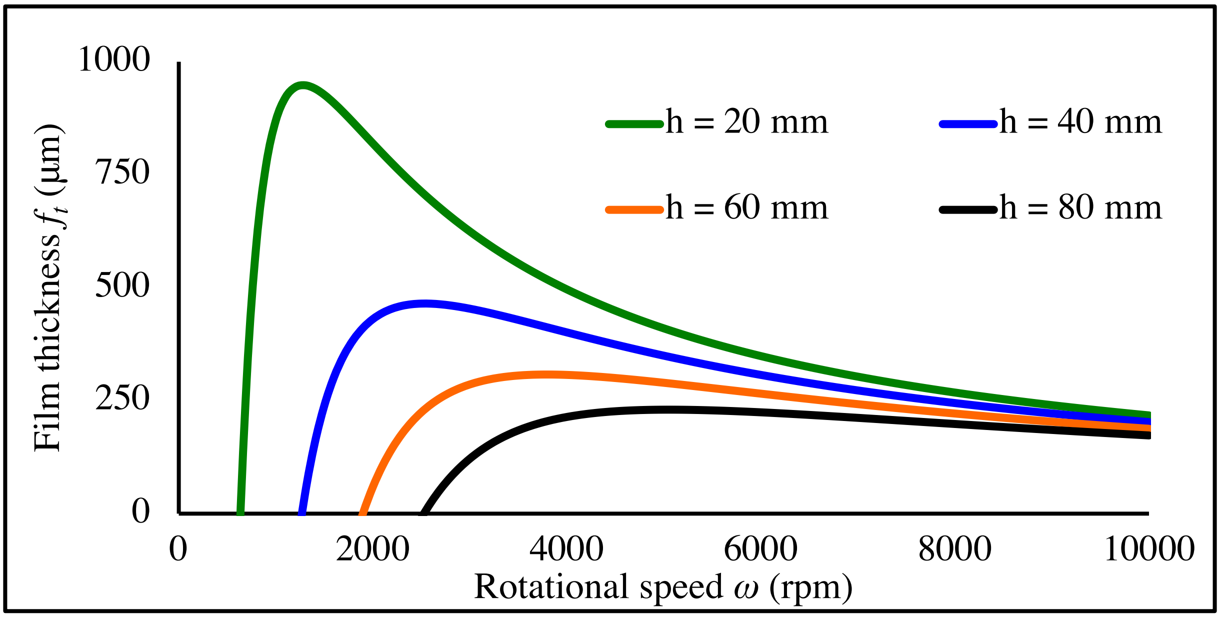

Fig. 2.2.3: The effect of rotational speed ω on film thickness f_t for various low heights. Standard VFD conditions, $\phi = 90°$, $V = 2$ mL.

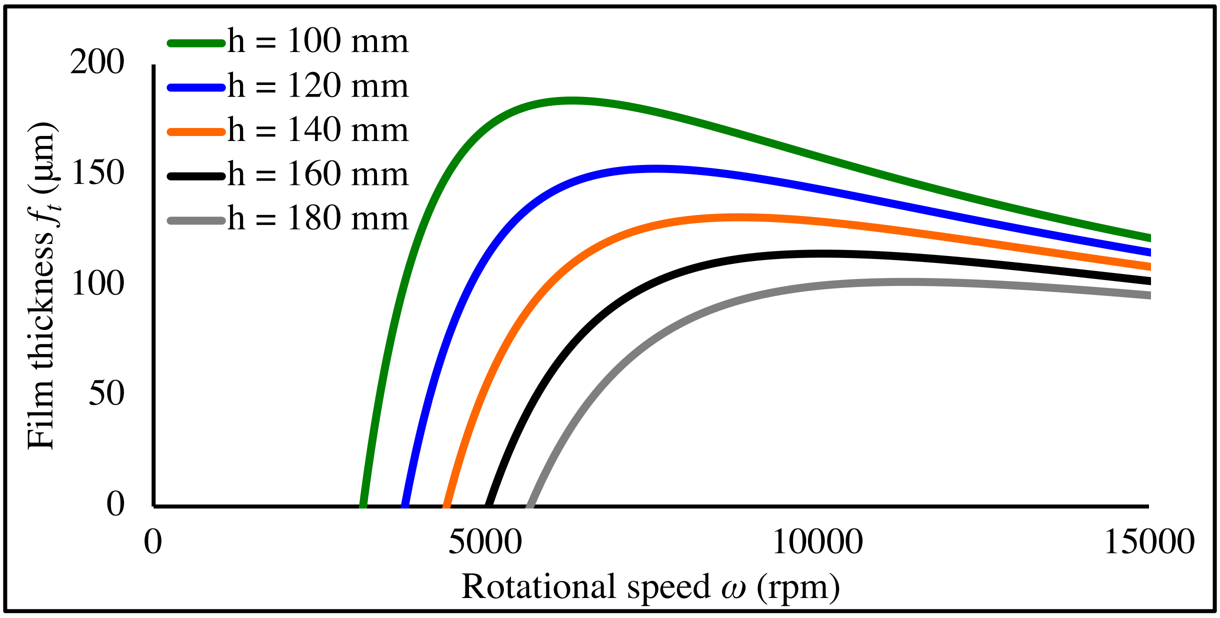

Fig. 2.2.4: The effect of rotational speed on film thickness for various high heights. Standard VFD conditions, $\phi = 90°$, $V = 2$ mL.

Determining the rotational speed which gives the greatest film thickness is useful for applications where certain conditions are applied at specific points on the tube, such as the use of a laser for the slicing of carbon nanotubes,[5] the placement of enzymes for chemical reactions,[6] or when performing *in situ* analytical techniques. In order to calculate the rotational speed ω_m at which the greatest film thickness occurs, equation 2.16 is simplified by neglecting the radial component of gravity, giving

Equation 2.17

$$f_t = R - \sqrt{R^2 + \frac{2g\sin\theta}{\omega^2}h - \frac{2}{\omega}\sqrt{\frac{gV\sin\theta}{\pi}}}.$$

The point giving the maximum film thickness is then calculated as the point where $\frac{df_t}{d\omega} = 0$, or where

$$\frac{d}{d\omega}\left(\frac{2g\sin\theta}{\omega_m^2}h - \frac{2}{\omega_m}\sqrt{\frac{gV\sin\theta}{\pi}}\right) = 0.$$

Solving for ω_m, this gives

$$-\frac{4gh\sin\theta}{\omega_m^3} + \frac{2}{\omega_m^2}\sqrt{\frac{gV\sin\theta}{\pi}} = 0,$$

Equation 2.18

$$\omega_m = 2h\sqrt{\frac{g\pi\sin\theta}{V}}.$$

It is interesting to note that the optimised rotational speed used previously to slice carbon nanotubes (7500 rpm), is approximately the rotational speed calculated to give the greatest film thickness (8000 rpm) for the conditions used (laser height h = 9 cm, θ = 45°, V = 1 mL).[5] This is a consistency that would be interesting to be investigated further. The calculated rotational speed is only applicable to confined mode of operation of the VFD for a fixed volume of liquid in the rotating tube, and is not valid under continuous flow operation, where an increase in rotational speed reduces the volume the tube can hold, consequently decreasing the film thickness at all points along the length of the tube. For the common confined mode operating conditions of V = 1 mL and θ = 45°, heights above 12 cm produce a ω_m value above the maximum operating speed of the device, and hence the film thickness increases with rotational speed. Investigating the effect that radial position has on ω_m (Fig. 2.2.5) reveals significant variation between different radial positions. This variation does not affect the utility of the calculation because equation 2.18 is only useful for systems which are radially uniform (such as for enzymatic reactions), and for systems where a beam is passed through the $\phi = \frac{\pi}{2}$ radial position, for which this calculation remains valid. Further investigation reveals an approximately sinusoidal relationship between ω_m and ϕ (Fig. 2.2.6). It is interesting to note in Fig. 2.2.6 the amplitude of the sinusoidal wave approximately equals double R/h, suggesting a relationship of the form

$$\omega_m \approx 2h\sqrt{\frac{g\pi\sin\theta}{V}}\left(1+\frac{R}{h}\cos\phi\right).$$

One problem with this formula is that it results in a ϕ dependence of ω_m even for $\theta = 90°$, suggesting that a more appropriate relationship is of the form

$$\omega_m \approx 2h\sqrt{\frac{g\pi\sin\theta}{V}}\left(1+\frac{R}{h}\cos\phi\cdot\left(\sqrt{2}\cdot\sin\theta\right)^n\right).$$

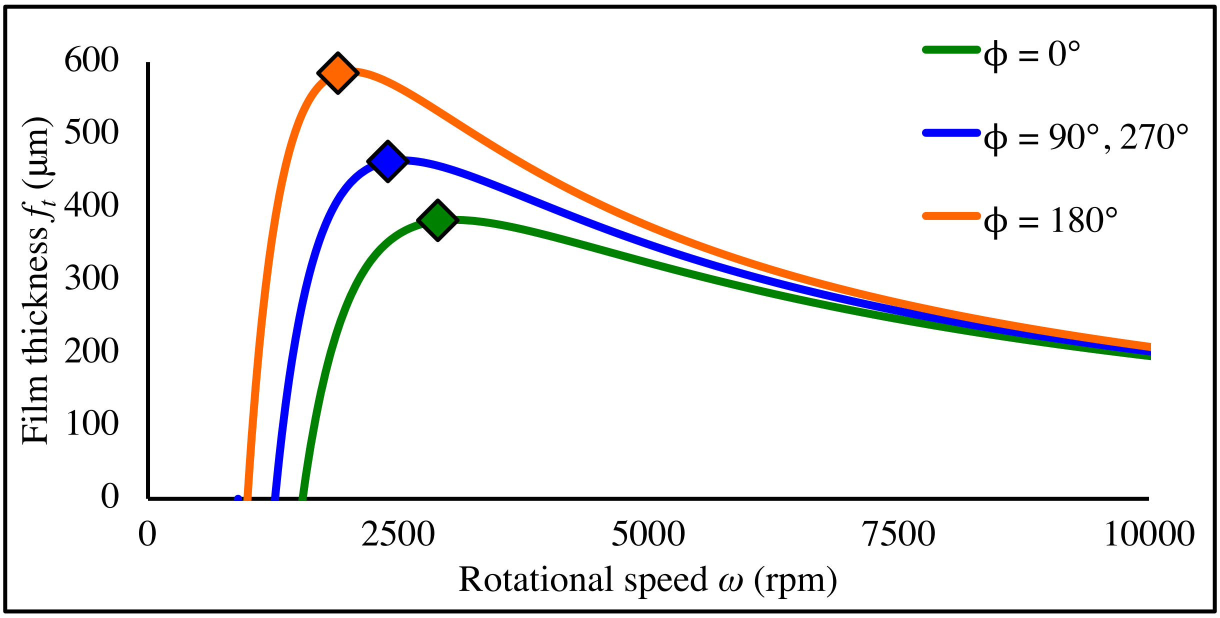

Fig. 2.2.5: The effect of angular position ϕ on the film thickness f_t and rotational speed ω_m giving the maximum film thickness. Standard VFD conditions, $h = 40$ mm, $V = 2$ mL.

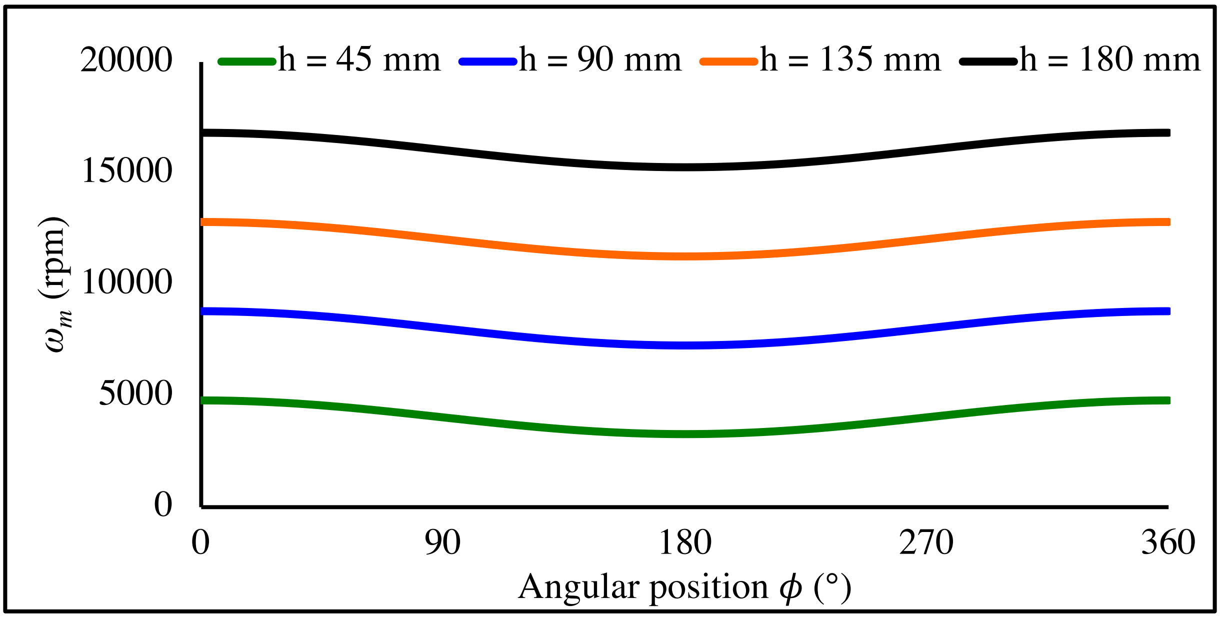

Fig. 2.2.6: The effect of angular position ϕ on ω_m. Standard VFD conditions, $V = 1$ mL.

Changing the tilt angle produces a similar effect to changing rotational speed, with Figures 2.2.7, 2.2.8, 2.2.9 and 2.2.10 showing the same sharp increase followed by a gradual decrease. The tilt angle θ_m giving the greatest film thickness can likewise by calculated through a similar method, producing

$$\frac{d}{d\theta}\left(\frac{2g\sin\theta}{\omega^2}h\right)=\frac{d}{d\theta}\left(\frac{2}{\omega}\sqrt{\frac{gV\sin\theta}{\pi}}\right),$$

$$\frac{2g\cos\theta_m}{\omega^2}h=\frac{\cos\theta_m}{\omega}\sqrt{\frac{gV}{\pi\sin\theta_m}},$$

Equation 2.19

$$\sin\theta_m=\frac{V\omega^2}{4gh^2\pi}.$$

It is observed both from equation 2.19 and Figures 2.2.4 and 2.2.5 that for low speeds and high heights h, this angle is very close to 0°, unsurprisingly as only tilt angles close to 0° will produce a film at these heights for low speeds. It is, however, noted that this approximation is only valid for $\phi=\frac{\pi}{2}$, as highlighted for the rotational speed calculation. One difference between the behaviour of θ_m and ω_m is that it is possible for θ_m to give a negative film thickness under certain conditions. This arises because unlike the rotational speed, which has no (theoretical) limit, the tilt angle of the tube has a limit. Consequently, θ_m will give a negative film thickness for certain ϕ values at low rotational speeds and large h values. The conditions under which this occurs are not of practical interest, and hence are not determined.

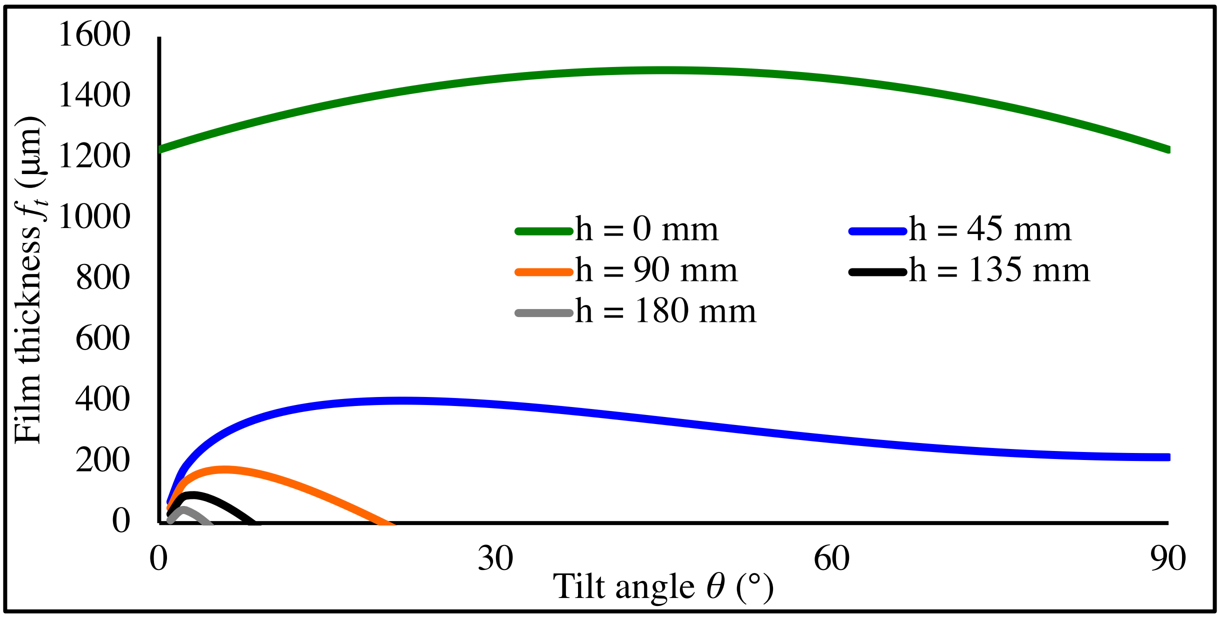

Fig. 2.2.7: The effect of tilt angle θ on film thickness f_t. Standard VFD conditions, ω = 2000 rpm, V = 2 mL, ϕ = 90°.

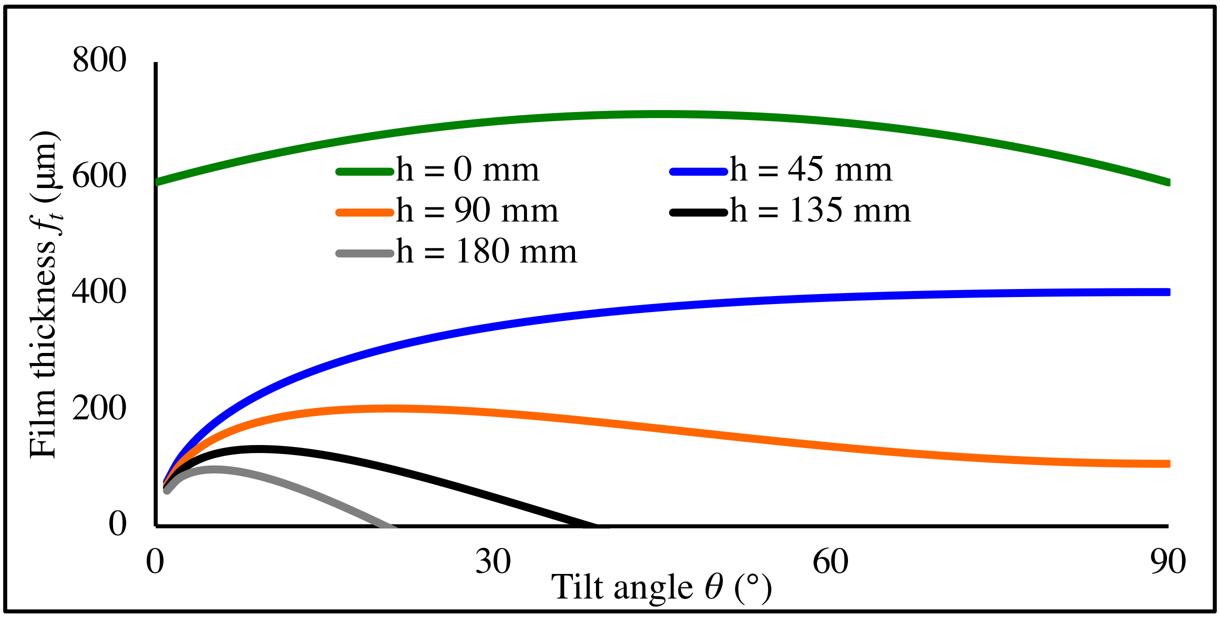

Fig. 2.2.8: The effect of tilt angle θ on film thickness f_t. Standard VFD conditions, ω = 4000 rpm, V = 2 mL, ϕ = 90°.

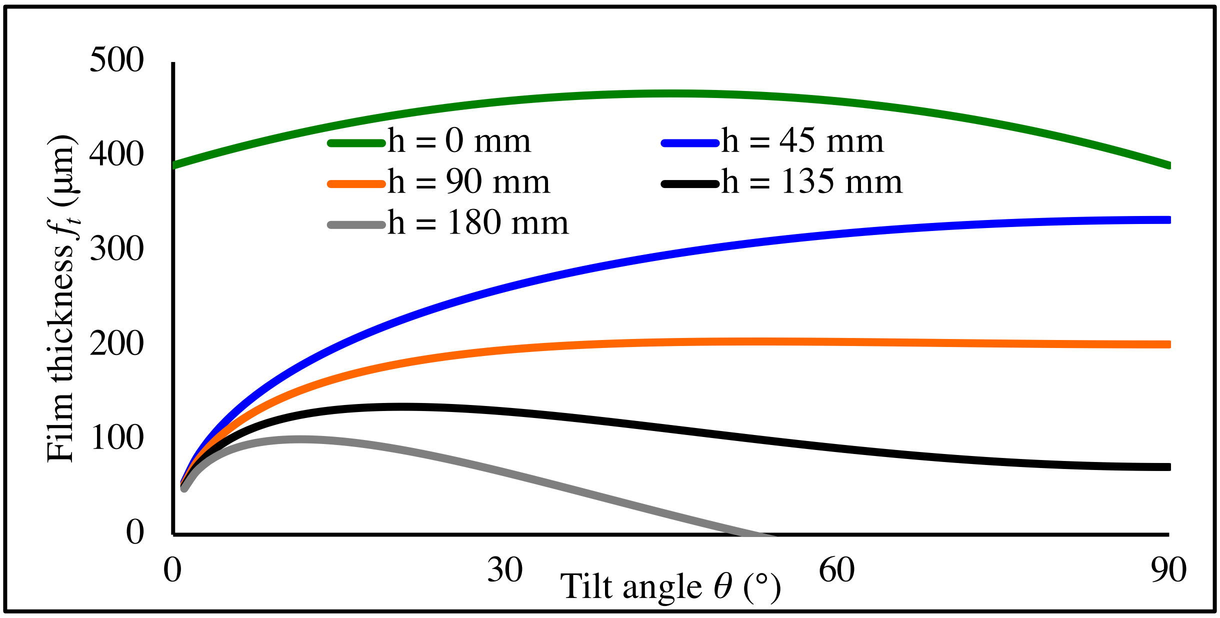

Fig. 2.2.9: The effect of tilt angle θ on film thickness f_t. Standard VFD conditions, ω = 6000 rpm, V = 2 mL, ϕ = 90°.

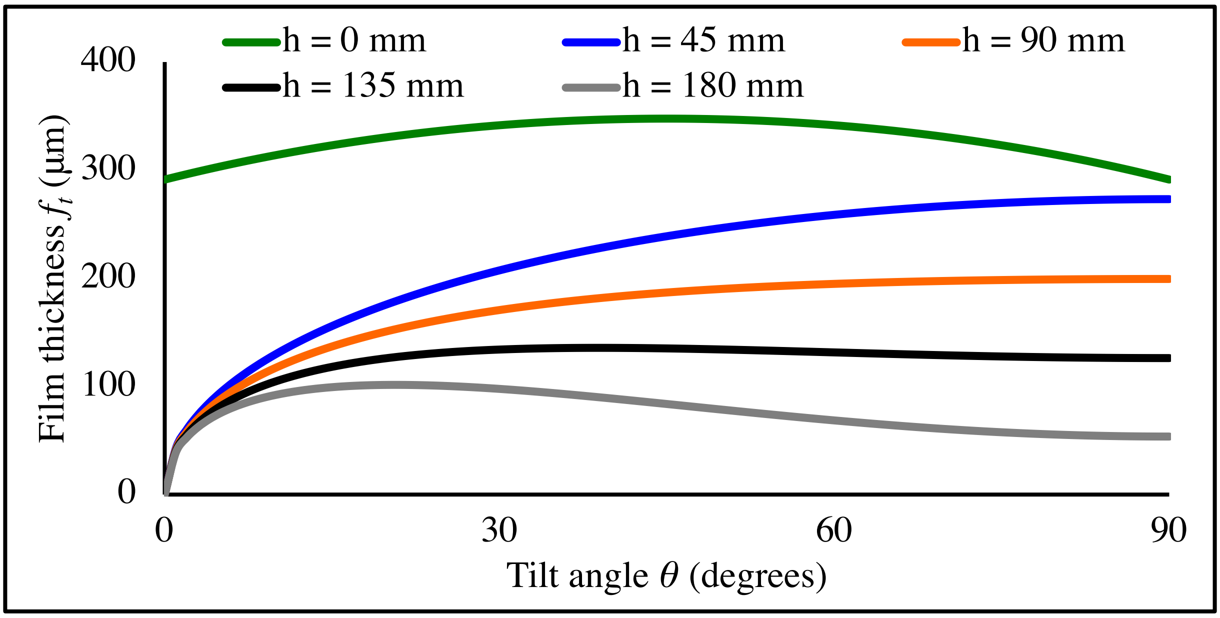

Fig. 2.2.10: The effect of tilt angle θ on film thickness f_t. Standard VFD conditions, ω = 8000 rpm, V = 2 mL, ϕ = 90°.

Two other factors that can be controlled are the volume, which unsurprisingly increases the film thickness (Fig 2.2.11), and the radius of the tube, which also results in a decreased film thickness (Fig 2.2.12). This second observation, although intuitive, occurs from a mathematical standpoint because as R is increased, $\sqrt{R^2 + a}$ approaches R, and hence $f_t = R - \sqrt{R^2 + a}$ approaches 0. It is noted that for 4000 rpm to 8000 rpm, an increased rotational speed produces a small film thickness for all radii, however this trend extends to 2000 rpm only for higher radii of the tube. The last parameter to be considered is gravitational acceleration, which varies from 9.764 m·s^{-2} at the summit of the Huascaràn mountain in Peru, to 9.834 m·s^{-2} at a point in the Arctic Sea.[7] The effect that this variation has on the film thickness is on the order of 1 μm, and hence local variation in gravitational accelerations can be ignored. It is observed, however, that were g to vary significantly, the effect would be similar to that observed for varying the tilt angle, however, without the potential for g_m to give a negative film thickness.

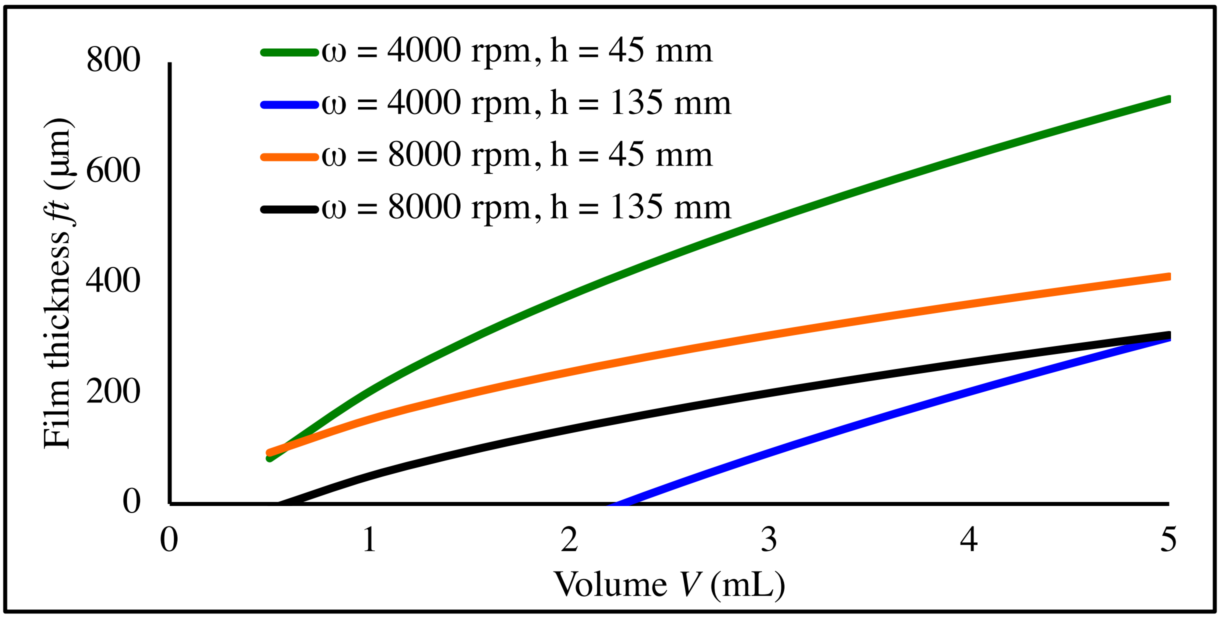

Fig. 2.2.11: The effect of volume V on film thickness f_t. Standard VFD conditions, ϕ = 90°.

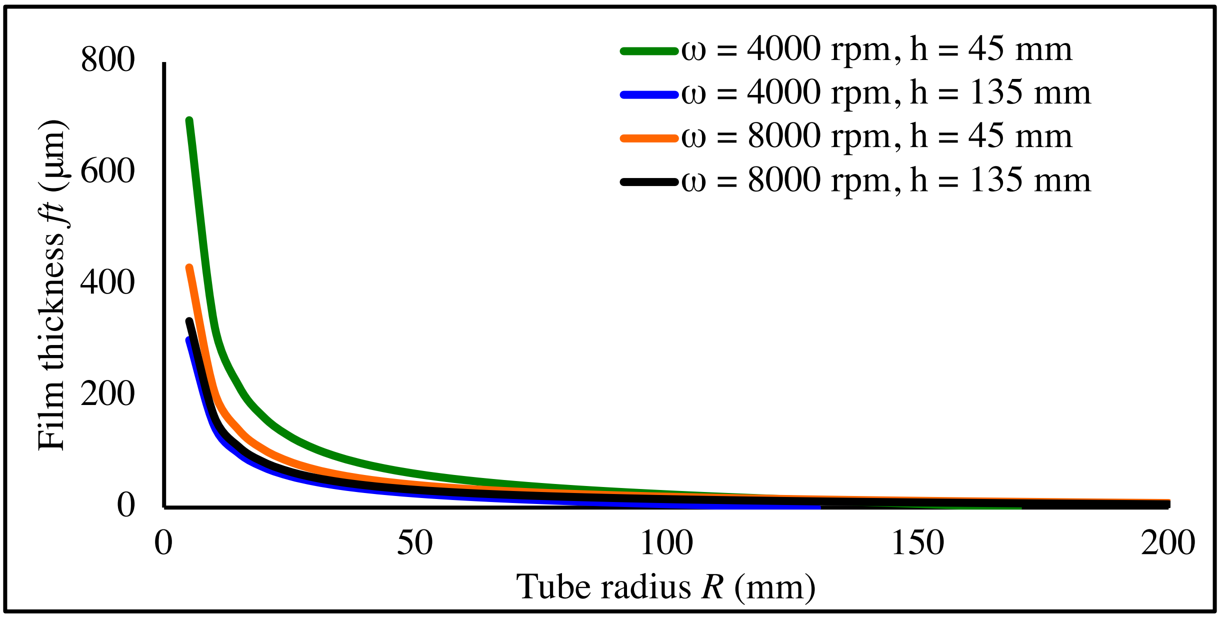

Fig. 2.2.12: The effect of tube radius on film thickness. g = 9.8 m·s^{-2}, ϕ = 90°, V = 2 mL.

Chapter 2.3 – Maximum film height, volume, and residence time

Film thickness is not the only useful quantity that can be obtained from the model. Other information that can be obtained includes the maximum film height, the volume of liquid under continuous flow, and the residence time in various sections of the tube. In addition to these calculable values, the mathematical model also allows the conversion between operating conditions whilst maintaining certain variables constant in order to investigate the effect of specific operating parameters of the VFD.

The height of the top of the film h_m is also of interest, as this is for the maximum volume that the tube can hold without the liquid interacting with the cap or exiting the tube. The maximum height is obtained by using equation 2.15, and setting $h = h_m$ and $r = R$;

$$h_m = \frac{\omega^2}{2g \sin\theta}(R^2 - R^2) - R\cos\phi \cot\theta + \frac{g\cos^2\theta}{\omega^2 \sin\theta} + \sqrt{\frac{\omega^2}{g\pi \sin\theta}V - \frac{1}{2}R^2 \cot^2\theta}.$$

Equation 2.20

$$h_m = \frac{g\cos^2\theta}{\omega^2 \sin\theta} - R\cos\phi \cot\theta + \sqrt{\frac{\omega^2 V}{g\pi \sin\theta} - \frac{1}{2}R^2 \cot^2\theta}.$$

It is interesting to note that the magnitude of the effect of angular position is relatively small at typical operating conditions, with $\omega \geq 4000$ rpm and $V \geq 1$ mL, $\frac{h_m(\phi=180°) - h_m(\phi=0°)}{h_m(\phi=90°)} \leq 0.14$. Given the relatively small effect of angular position on h_m, a useful approximation is neglecting this dependence, giving

Equation 2.21

$$h_m = \omega\sqrt{\frac{V}{g\pi \sin\theta}}.$$

The maximum volume the tube can hold without interference from the cap (or before the liquid begins to exit the tube under continuous flow) is given by setting h_m as the length of the tube H, and rearranging to give

Equation 2.22

$$V = \frac{H^2}{\omega^2} g\pi \sin\theta.$$

Both equations 2.21 and 2.22 are fairly straight forward to use, although it is observed that these equations do not feature the radius, and hence the maximum film height and volume are independent of the radius. It is also noted that decreasing the rotational speed can dramatically increase the volume within the tube, which also increases the residence time for the VFD operating under continuous flow. Calculating the residence time from the volume is simple, using $\tau = VQ^{-1}$, allowing the consideration of the question “Given that rotational speed changes both the residence time and shear forces, how does one maintain constant residence time whilst changing the rotational speed in order to investigate the effect of shear forces?”. The answer to this question is to calculate the flow rate Q using $Q = \frac{H^2}{\omega^2 \tau} g\pi \sin\theta$. This can be rearranged into the form of transitioning from ω_1 and Q_1 to ω_2 and Q_2:

$$Q_2 = \frac{\omega_1^2}{\omega_2^2}\, Q_1.$$

The disadvantage of changing the flow rate according to this formula is that changing as such affects the ability of backflow to occur within the device, potentially affecting reactions where selectivity is a concern. The other option is to change the tube length according to $H = \omega\sqrt{\frac{Q\tau}{g\pi \sin\theta}}$, which significantly limits the rotational speeds that can be tested based on the availability of VFDs housing tubes of different lengths, however, this would be a way to investigate the effect of shear forces on the selectivity of reactions under continuous flow. It is recognised that without a thorough understanding of the shear regimes within the VFD, which would be a major research project in its own right, this may be an undertaking of limited value.

A less straightforward calculation is that of residence time for liquid within a specific portion of the tube. This calculation is important for setting up multi-stage processing within and along a single tube. In order to do this, the cross-sectional area for a particular height is calculated, followed by integration from h_1 to h_2.

$$\tau = \frac{1}{Q}\int_{h_1}^{h_2} \pi R^2 - \pi r^2 \, dh$$

$$\tau = \frac{\pi}{Q}\int_{h_1}^{h_2} \left(-2gh\frac{\sin\theta}{\omega^2} + \sqrt{\frac{4gV\sin\theta}{\pi\omega^2}} \right) dh$$

$$\tau = \frac{\pi}{Q}\left(-g(h_2^2 - h_1^2)\frac{\sin\theta}{\omega^2} + (h_2 - h_1)\sqrt{\frac{4gV\sin\theta}{\pi\omega^2}} \right)$$

When considered under continuous flow operation of the VFD, this produces

Equation 2.23

$$\tau = \frac{g\pi \sin\theta}{Q\omega^2}\left(h_1^2 - h_2^2 + 2H(h_2 - h_1)\right).$$

The application of equation 2.23 to two commonly used operations of the VFD is considered: multi-step reactions, and the use of a laser to slice carbon nanotubes. For a two-stage reaction, the first reaction occurs from $h = h_1 = 0$ to $h = h_2$, whilst the second occurs from $h = h_2$ to $h = h_3 = H$. Increasing the height of the start of the second reaction h_2 only marginally increases the residence time for step 1, producing diminishing returns as h_2 is moved further up the tube, as shown in Fig. 2.3.1. On the other hand, increasing the height of h_2 reduces the residence time for the second step dramatically. For constant flow rate and two sections with the same residence time, the second step should start at $h_2 = \left(1 - \sqrt{0.5}\right)H \approx 0.29H$. This can be generalised as $h_2 = H\left(1 - \sqrt{1 - K}\right)$ where K is the fraction of the residence time in the bottom section of the tube, or as

$$h_2 = H\left(1 - \sqrt{1 - \frac{KQ_1}{KQ_1 - KQ_2 + Q_2}}\right)$$

when $Q_1 \neq Q_2$.

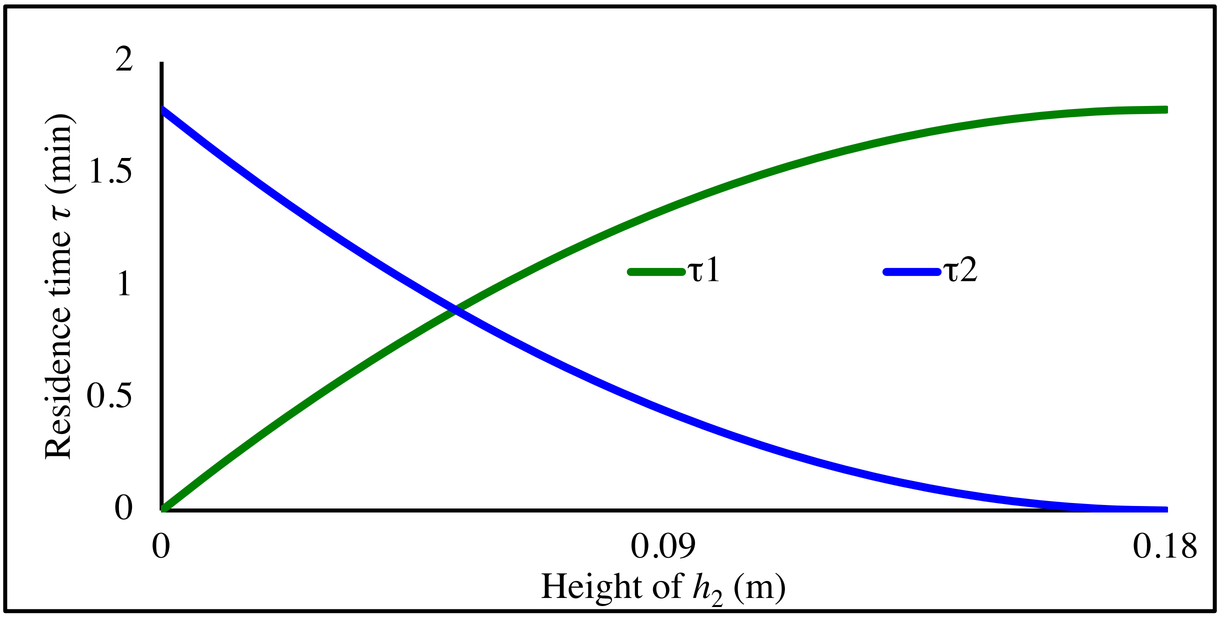

Fig. 2.3.1: The effect of height of h_2 on the residence times τ_1 and τ_2 for two sequential reactions. Standard VFD operating conditions, ω = 6000 rpm, Q = 1 mL/min.

It is noteworthy that there is a minimum h_2 that is practical to ensure there is sufficient separation to circumvent potentially interfering backmixing. The minimum fraction of residence time K_m in the lower portion of the tube for a given height, occurs when $Q_2 = Q_1$

$$K_m = \frac{h_2}{H}\left(2 - \frac{h_2}{H}\right).$$

Application of this model to the two previous multi-stage reactions in a single tube affords interesting insights. The first is the three-step process of the synthesis of Lidocaine, involving the amidation of dimethylaniline with chloroacetyl chloride in chloroform, followed by a solvent exchange to replace chloroform with DMF, and the second amination with diethylamine to produce Lidocaine. Interestingly, when both reaction steps were performed in separate sequential VFDs, a yield of 85% was obtained, whilst performing all three steps in a single tube resulted in a rather low yield of only 15%.[8]

Performing these reactions in a single tube used a total flow rate at the base of the tube (h_1 = 0 cm) of Q_1 = 0.024 mL/min, the addition of DMF at h_2 = 5 cm at $\Delta Q_{1\rightarrow 2}$ = 0.05 mL/min to give Q_2 = 0.074 mL/min, and the addition of diethylamine at h_3 = 9.5 cm at $\Delta Q_{2\rightarrow 3}$ = 0.1 mL/min to give Q_3 = 0.174 mL/min, with H = 0.18 cm and ω = 6950 rpm.[8] Inputting these values into equation 2.23 reveals the following residence times: τ_1 = 26.5 minutes, τ_2 = 5.3 minutes, and τ_3 = 1.7 minutes. This gives a total residence time of 33.5 minutes, significantly more than the 13 minutes originally reported using the total flow rate. It is informative to note that for the slower amination reaction step, only a small amount of time was allowed, whereas for the faster amide formation reaction, an extended period of time was allowed. This possibly explains the low reported yield for the lidocaine synthesis in a single tube. That said, there was also a challenge in this reported work, in maintaining a high temperature in a heated portion of the tube without heating the rest of the tube, for the amination step. It is also noted that the amide formation step is more efficient at lower temperatures and heat leaking towards this part of the tube likely to reduce the percent conversion for the reaction. It is not currently possible to adequately maintain separate controlled temperatures at different points on the VFD. However, once equipment is developed capable of doing that, there is still a limitation on the residence time for the second step. If the procedure is simplified by assuming the ability to perform the solvent exchange simultaneously with the amination[a], and a minimum h_2 of h_2 = 3 cm is

---

[a] The justification for the solvent exchange is the inefficiency of the amination in chloroform, rather than solubility issues, meaning simultaneous solvent exchange and reaction should be possible.

assumed (this is probably an underestimation of the minimum h_2 that can be used without backflow), and concentrations are adjusted such that $Q_1 \approx Q_2$. This gives:

$$\tau = \frac{g\pi \sin\theta}{Q\omega^2}\left(h_1^2 - h_2^2 + 2H(h_2 - h_1)\right)$$

$$\frac{\tau_2}{\tau_1} = \frac{\left(h_2^2 - H^2 + 2H(H - h_2)\right)}{\left(0 - h_2^2 + 2H(h_2 - 0)\right)} = \frac{(h_2^2 + H^2 - 2Hh_2)}{2Hh_2 - h_2^2} = \frac{(H - h_2)^2}{h_2(2H - h_2)} = 2.27$$

Evidently, even under optimal design conditions, the residence time for the slower step can only be a little over double that for the faster step, unless a longer VFD tube is used and a suitable multi-stage heating unit is developed.

The second multi-stage reaction performed in a single VFD tube is the synthesis of an α-aminophosphonate from aniline, benzaldehyde and diethylphosphite. This involved the addition of aniline and benzaldehyde in methanol at h_1 = 0 cm for a total Q_1 = 0.2 mL/min, followed by a solvent exchange to replace methanol with DMF at h_2 = 4.5 cm and $\Delta Q_{1\to 2}$ = 0.1 mL/min to give Q_2 = 0.3 mL/min, followed by the addition of diethylphosphite at h_3 = 8 cm and $\Delta Q_{2\to 3}$ = 0.1 mL/min to give Q_3 = 0.4 mL/min, finally with the addition of I_2 in at h_4 = 10.5 cm with $\Delta Q_{3\to 4}$ = 0.1 mL/min to give Q_4 = 0.5 mL/min. Applying mathematics reveals: τ_1 = 2.9 minutes, τ_2 = 1.1 minute, τ_3 = 1.3 minutes and τ_4 = 0.46 minutes, giving a total residence time of 5.8 minutes, shorter than the 7.4 minutes originally reported. This procedure achieved 80% yield, close to the multi-VFD yield of 87%, indicating that although the mathematical model provides additional information about the reaction, there is limited scope for it to provide insights into tracking towards higher yields.[3]

The other processing capability of the VFD considered is applying effects at different positions along the tube, for example laser irradiation, a magnetic field, or a neutron beam.[5] In this instance, a laser beam of fixed width z can be placed at different heights up the tube. The effect of changing this height for a fixed width is considered, with Fig. 2.3.2 revealing a linear decrease in residence time for liquid passing through the beam as the height is increased, as predicted by equation 2.23.

Equation 2.23

$$\tau = \frac{2zg\pi \sin\theta}{Q\omega^2}(H - h).$$

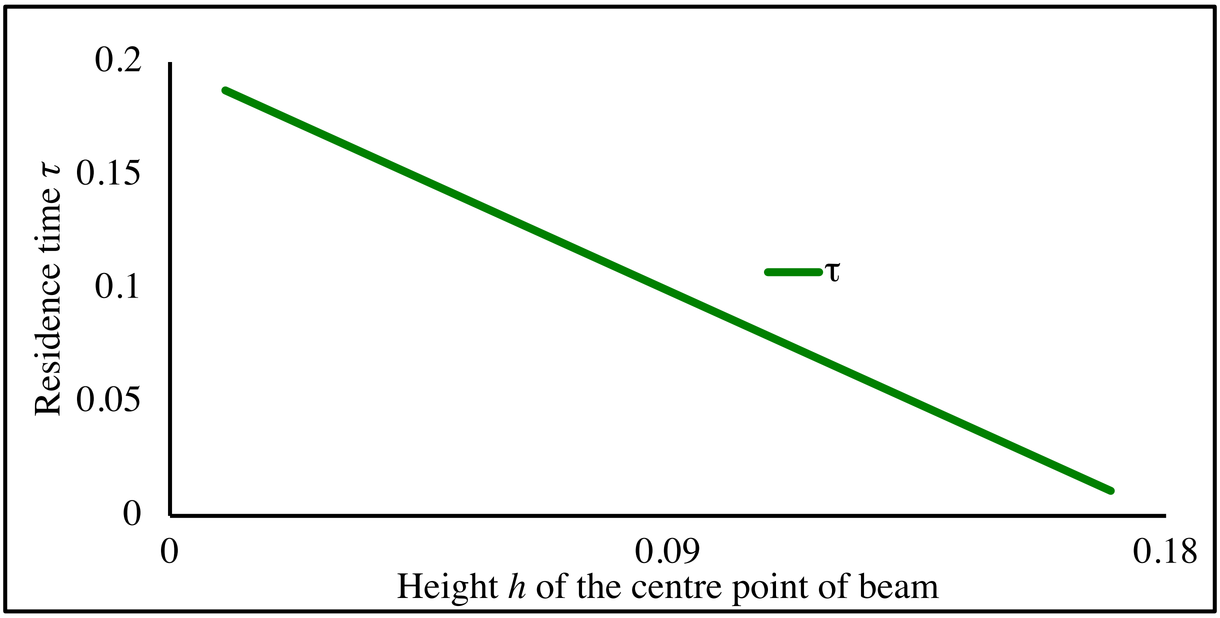

Fig. 2.3.2: Residence time within a zone of fixed width and variable position. Standard VFD, $\omega = 6000$ rpm, $Q = 1$ mL/min, $z = 1$ cm.

In addition to these applications and calculations, the mathematics that have been developed allows several simple formulas for converting between conditions which are equivalent in a particular manner (for example, having the same residence time or the same film thickness at a particular height). When optimising conditions for reactions in plug-flow reactors, each parameter is varied separately, safe in the knowledge that each controllable parameter only influences a single behaviour of the fluid system. However, in the VFD, this is not the case. In confined mode of operation of the device, there are four controllable variables: tilt angle, rotational speed, volume, and height of laser (if used). Factors that can be important are the shear forces within the device, the maximum film height as it affects the surface area to volume ratio, and film thickness at the height of the laser (if used). Additionally, the choice of volume of liquid in the tube is important, especially for cases where there is a minimum volume that must be used (this can be due to maximum solubility of substrate and the minimum quantity of substrate required for analysis). Under confined mode of operation of the VFD, varying the tilt angle will affect the maximum volume, the film thickness, and the maximum film height, and may alter the shear forces. Varying the rotational speed varies all of these four factors. In addition to varying rotational speed whilst keeping residence time constant, there are other useful conversions, outlined below.

Maintaining constant film thickness under confined mode at a specified height whilst changing the rotational speed requires changing the volume per:

$$V_2 = V_1 \frac{\omega_2^2}{\omega_1^2}\left(1 + h\left(\frac{\omega_1}{\omega_2^2} - \frac{1}{\omega_1}\right)\sqrt{\frac{\pi g \sin\theta}{V_1}}\right)^2.$$

This would be useful when investigating the effect that rotational speed has on the slicing of carbon nanotubes independent of film thickness.

Given the recent intra-research group interest in developing larger vortex fluidic devices for high throughput applications, a consideration in designing such platforms is needing to ensure that a thin film is maintained under continuous flow without increasing the rotational speed to speeds which are difficult or expensive to achieve. In order to calculate the rotational speed required to produce a thin film of maximum thickness f_t, equation 2.16 is set to continuous flow conditions, the height is set to 0, and the formula is rearranged to give the rotational speed required to achieve a set film thickness at the base of the tube under continuous flow conditions:

$$f_t = R - \sqrt{R^2 - \frac{2H}{\omega^2} g \sin\theta},$$

$$R^2 - \frac{2gH\sin\theta}{\omega^2} = R^2 + f_t^2 - 2Rf_t,$$

$$\omega = \sqrt{\frac{2gH\sin\theta}{2Rf_t - f_t^2}} \approx \sqrt{\frac{gH\sin\theta}{Rf_t}}.$$

This allows the determination of the speed required for a specific radius and length VFD tube to achieve a film of desired thinness. It is an interesting observation that this speed is higher for longer VFDs, but shorter for wider VFDs. Rearranging this equation to one which allows the calculation of the length required to achieve both a desired film thickness and a desired volume, for a VFD of certain radius yields

$$V = \frac{H^2}{\omega^2} g\pi \sin\theta,$$

$$H \approx \frac{V}{\pi R f_t}.$$

Chapter 2.4 – Comparison of the mathematical model with experimental results

Some early work on the VFD involved measuring the average film thickness within a 10 mm VFD, which was performed by measuring the film height for various rotational speeds and calculating the average film thickness from there.[1] The resultant equation is

$$f_t = R - \sqrt{R^2 - \frac{\sqrt{gV\sin\theta}}{\omega\sqrt{\pi}}}$$

Comparing the prediction to previous experimental results[1] indicates that the predicted values are within experimental error for 3000 rpm and above, and almost within experimental error for 2000 rpm (Fig. 2.4.1). However, the predicted average film thickness for 1000 rpm is significantly higher than measured. This deviation is not surprising given that the mathematical model is less reliable at lower speeds where viscosity becomes more important.

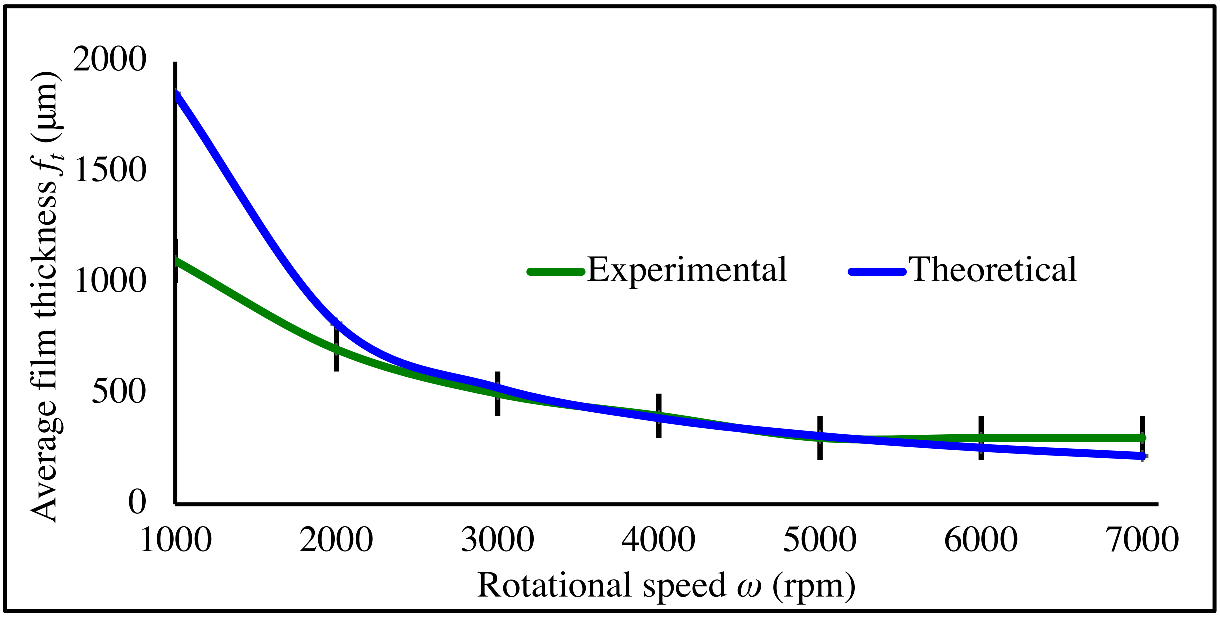

Fig. 2.4.1: Average film thickness as measured in a R = 0.00475 m VFD, compared to average film thickness predicted by the model.

The second set of experiments performed previously involved measuring the residence time as a function of flow rate for the 20 mm VFD at a rotational speed of 6950 rpm.[2] These experiments found a relationship between the flow rate and residence time of $\tau = 152.37Q^{-0.934}$, corresponding to an R^2 value of 0.9831. Reanalysis of the original data revealed that a relationship of $\tau = 158.57Q^{-1}$ results in a greater R^2 value of 0.9894, and a precisely inverse relationship between residence time and flow rate, which is consistent with the theoretical model. One difference between the experimental and predicted mathematical model is that the experimental measurements included time spent for the liquid entering and exiting the Teflon housing unit at the top of the tube, whilst these are not accounted for in the model. Consequently, the residence time can be predicted from the model as

$$\tau = \left(V_E + \frac{gH^2\pi \sin\theta}{\omega^2}\right)Q^{-1},$$

where V_E is the volume of liquid within the system that is external to the tube (including in the Teflon housing unit, which is only partially filled). Equating this to the equation determined from experimental data results in a calculated V_E of 1.16 mL, which is a reasonable amount to be in the Teflon housing unit and plastic pipette. This consistency of the model with experimental data lends further credibility to the model developed in this chapter.

Although very little work has previously been done on the film within the VFD, other literature provides five relevant similar systems. The first system is that of liquid mirror telescopes, which are used as relatively cheap astronomical telescopes. Liquid mirror telescopes involve rotating a large dish of mercury at low rotational speeds to form a paraboloidal reflective film on the surface of the dish, the perfect shape for a telescope because all reflected light will pass through a specific point.[9,10] In the case of a liquid mirror telescope where $\theta = 90°$ and $h = 0$ is defined as the base of the parabola, equation 2.15 reduces to:

$$h = \frac{r^2\omega^2}{2g},$$

which is consistent with the equation derived for liquid mirror telescopes.[9]

The second system is a set of experiments published in 1981, which investigated the variation in film thickness in a horizontally aligned rotating tube.[11] In the system investigated, a horizontally aligned glass tube containing various liquids was rotated, whilst a laser was directed down the centre of the tube. The laser was reflected off a mirror placed within the tube and directed through the film towards a photodiode attached to the outside of the tube (Fig. 2.4.2). The photodiode signal was amplified and recorded as the system rotated. The typical output depicted in the paper is shown in Fig. 2.4.3, indicating a sinusoidal influence of angular position on film thickness, as determined by the mathematical model developed here.

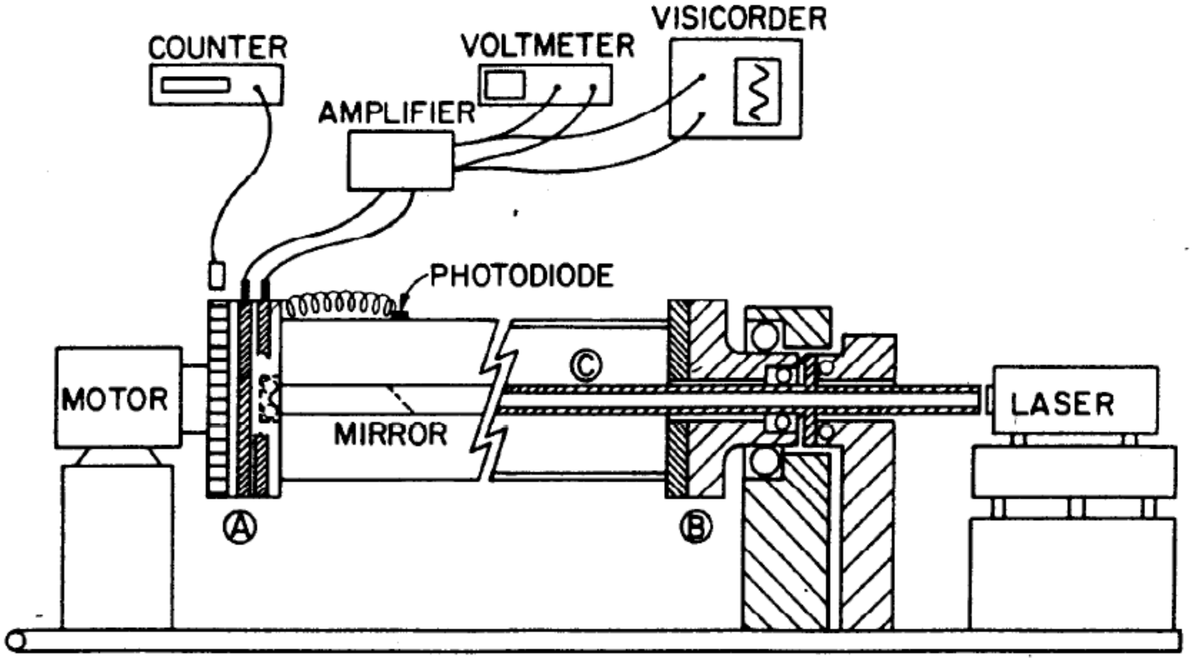

Fig. 2.4.2: The setup of a horizontal spinning tube, with a laser pointed down the centre of the tube, reflected from a mirror, detected by a photodiode, and its intensity recorded.[11]

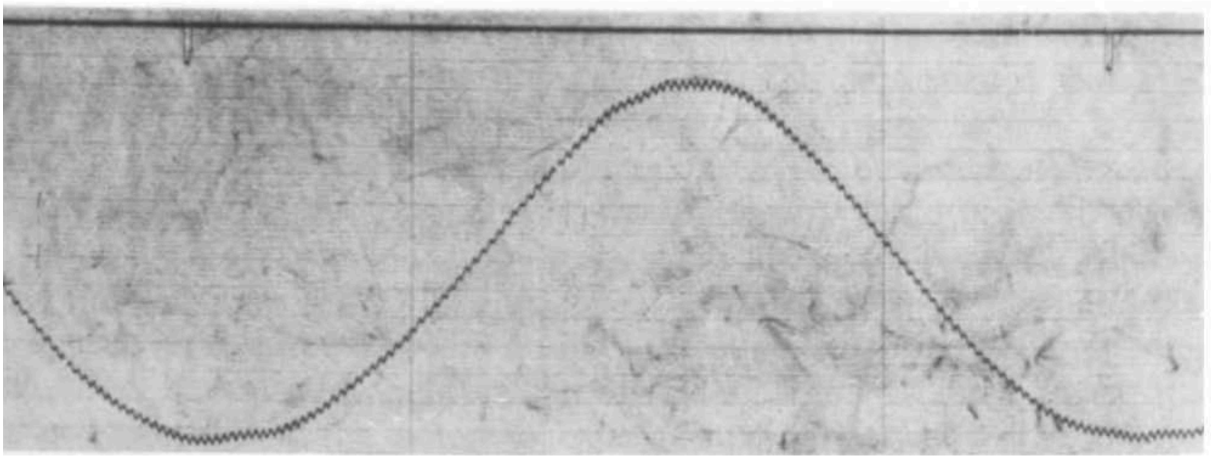

Fig. 2.4.3: The output of the visicorder as depicted in Fig. 2.4.2.[11]

The third relevant system of interest is presented in a paper from 1972, which discussed the behaviour of thin films inside rotating tubes and focused on the volume within horizontally aligned rotating tubes. The authors assume that the film thickness is not dependent on ϕ, and derive a generalised formula for film thickness of the form $h = af_t + b\Bigg(\frac{1}{2}\ln\left(\frac{\left(1+\frac{f_t}{c}\right)^2}{1-\frac{f_t}{c}+\frac{f_t^2}{c^2}}\right) +$

$\sqrt{3}\arctan\left(\frac{\frac{2ft}{c}-1}{\sqrt{3}}\right)+\frac{\pi}{2\sqrt{3}}\Bigg)$, which is not neatly solvable for the film thickness. The inability to readily solve this equation for the film thickness did not interfere with their focus on the behaviour of the fluid in a horizontally aligned tube, however, it does mean that their generalised formula cannot be compared to the formulas derived in this chapter.[12]

The fourth relevant system is an investigation by Lubarda in 2013, who theoretically modelled liquid behaviour in a rotating vertically aligned tube with a focus on surface tension, considering only the conditions where the base of the tube is not dry. A part of this involved noting the produced formula in the absence of surface tension, giving (rewritten using our notation)

$$h=\frac{R^2\omega^2}{4g}\left(\frac{2r^2}{R^2}-1\right)+h_r,$$

where h_r is the height of the liquid relative to the rest height of the liquid such that $h_r=\frac{V}{\pi R^2}$, giving $h=\frac{\omega^2}{2g}\left(r^2-\frac{1}{2}R^2\right)+\frac{V}{\pi R^2}$, which is different to that produced by our equation here, $h=\frac{\omega^2}{2g}(r^2-R^2)+\sqrt{\frac{\omega^2}{g\pi}V}$. The reason for this difference is that their equation is only valid for $h(r=0)\geq 0$, whilst ours is only valid for $h(r=0)\leq 0$. Under the specific condition of $h(r=0)=0$, corresponding to the base of the parabola meeting precisely the base of the tube, both equations are valid. Under this condition, they both converge to the same result.

For theirs:

$$0=-\frac{R^2\omega^2}{4g}+\frac{V}{\pi R^2},$$

$$V=\pi R^2\left(\frac{R^2\omega^2}{4g}\right)=\frac{\pi R^4\omega^2}{4g}.$$

For ours:

$$0=-\frac{R^2\omega^2}{2g}+\sqrt{\frac{\omega^2 V}{g\pi}},$$

$$V=\left(\frac{R^2\omega^2}{2g}\right)^2\frac{g\pi}{\omega^2}=\frac{\pi R^4\omega^2}{4g}.$$

Consequently, their result is consistent with ours.[13]

The final relevant system involves investigating the behaviour of liquid in partially filled rotating inclined pipes, reported by Chatterjee, *et al.*, looking at when the fluid transitions from a pool to a film. This work could provide some insights into the intrafluid behaviour within the

VFD, although it is noted that the systems investigated involved larger tubes (R = 27 mm, 22 mm and 17 mm), and only investigated speeds up to 1200 rpm, and flow rates up to 1000 mL/min. Their focus was on operating parameters outside of what we are interested in, and did not involve theoretical modelling, but could nonetheless provide useful insight into some of the intrafluid behaviour.[14]

Overall, the literature provides support for the mathematical model in cases where investigated systems have some overlap with ours, and importantly, none of the literature contradicts the results obtained involving the mathematical model here.

Chapter 2.5 – References

1 Yasmin, L., Chen, X., Stubbs, K. A. & Raston, C. L. Optimising a vortex fluidic device for controlling chemical reactivity and selectivity. *Scientific Reports* **3**, 2282, (2013).

2 Britton, J. & Raston, C. L. Rapid high conversion of high free fatty acid feedstock into biodiesel using continuous flow vortex fluidics. *RSC Advances* **5**, 2276-2280, (2015).

3 Britton, J., Castle, J. W., Weiss, G. A. & Raston, C. L. Harnessing Thin-Film Continuous-Flow Assembly Lines. *Chemistry - A European Journal* **22**, 10773-10776, (2016).

4 Yasin, F. M. *et al.* Microfluidic size selective growth of palladium nano-particles on carbon nano-onions. *Chemical Communications* **48**, 10102-10104, (2012).

5 Vimalanathan, K. *et al.* Fluid dynamic lateral slicing of high tensile strength carbon nanotubes. *Scientific Reports* **6**, 22865, (2016).

6 Britton, J., Dyer, R. P., Majumdar, S., Raston, C. L. & Weiss, G. A. Ten-Minute Protein Purification and Surface Tethering for Continuous-Flow Biocatalysis. *Angewandte Chemie - International Edition* **56**, 2296-2301, (2017).

7 Hirt, C. *et al.* New ultrahigh-resolution picture of Earth's gravity field. *Geophysical Research Letters* **40**, 4279-4283, (2013).

8 Britton, J., Chalker, J. M. & Raston, C. L. Rapid Vortex Fluidics: Continuous Flow Synthesis of Amides and Local Anesthetic Lidocaine. *Chemistry - A European Journal* **21**, 10660-10665, (2015).

9 Gibson, B. K. *An Experimental 2.7 Meter Liquid Mirror Telescope* Master of Science thesis, The University of British Columbia, (1990).

10 Olsson-Steel, D. A Note on the History of the Liquid Mirror Telescope. *Journal of the Royal Astronomical Society of Canada* **80**, 128, (1986).

11 Sanders, J., Joseph, D. D. & Beavers, G. S. Rimming flow of a viscoelastic liquid inside a rotating horizontal cylinder. *Journal of Non-Newtonian Fluid Mechanics* **9**, 269-300, (1981).

12 Barnea, E., Kovalivker, E., Mizrahi, J. & Yacoub, N. The flow of thin films inside rotating cylindrical tubes. *The Canadian Journal of Chemical Engineering* **50**, 685-689, (1972).

13 Lubarda, V. A. The shape of a liquid surface in a uniformly rotating cylinder in the presence of surface tension. *Acta Mechanica* **224**, 1365-1382, (2013).

14 Chatterjee, S., Sugilal, G. & Prabhu, S. V. Flow transitions in a partially filled rotating inclined pipe with continuous flow. *Experimental Thermal and Fluid Science* **83**, 47-56, (2017).

Chapter 3

Film Thickness and Neutron Imaging

The utility of a mathematical model describing the film shape and related information is enhanced if there are experimental results supporting the accuracy of the model. Attempts to use spectroscopic measurements and the Beer-Lambert Law were unsuccessful because the non-parallel alignment of the liquid with the surface caused refraction, as discussed below in Chapter 3.1. Attempts to use Neutron Imaging to measure the film thickness were successful, however experiments were reliant on the availability of the DINGO Neutron Tomography Station at ANSTO, limiting the quantity of experiments that could be performed.

Parts of chapters 3.3 and 3.4 were included as part of a paper under review by *Scientific Reports* titled ‘Neutron imaging and modelling inclined vortex driven thin films’, co-authored by Filomena Salvemini, Stuart Dalziel and Colin Raston.

Chapter 3.1 – Attempted spectroscopic measurements

Attempts to use spectroscopic techniques to determine the film thickness according to the Beer-Lambert Law resulted in implausibly high film thicknesses. This occurs because the film surface is not parallel to the surface of the tube, resulting in refraction. This refraction causes a significant portion of the emitted light to miss the detector, an effect which from the perspective of the detector, is indistinguishable from absorption. To demonstrate that this effect is large enough to be impactful, the distance travelled by light along the axis of the tube (Δh) is calculated. The path of the light is depicted in Fig. 3.1.1 as the red line, with Δh being the sum of the black lines (being, from left to right, d_1, d_2 and d_3). When setting up spectroscopic measurements in the VFD, the light source and detector are positioned at $\phi = 0°$ and $\phi = 180°$ respectively. Consequently, the film shape can be treated as axisymmetric because the asymmetry has an effect on the order of < 1 μm for the two positions considered here. To simplify the calculations further, the film is treated as linear instead of parabolic, a reasonable approximation as demonstrated in Chapter 2, and the hemispherical shape of the base is discounted, as usual. Note also that Fig. 3.1.1 is not drawn to scale.

The light beam (red) enters the glass tube perpendicularly to the surface of the glass at a height of h_0, and then enters the liquid at the same height, travelling a distance of f_1 through the film, meeting the liquid-air interface an angle of θ_1. This angle is determined using

$$\tan(\theta_1) = \frac{h_m - h_0}{f_1} = \frac{h_m}{f_0},$$

where h_m is the maximum height of the film and f_0 is the film thickness at the base of the tube. The light exits the film at an angle of θ_2, calculated using Snell's Law as

$$\sin\left(\frac{\pi}{2} - \theta_2\right) = \frac{n_1}{n_2}\sin\left(\frac{\pi}{2} - \theta_1\right),$$

where n_1 is the refractive index of the liquid, n_2 is the refractive index of air, and n_3 is the refractive index of the glass. In order to calculate d_1, the intersection between the path of the light and the second film is determined. The path now taken by the light is described by $(f_1 + k\cos(\theta_1 - \theta_2), h_0 - L\sin(\theta_1 - \theta_2))$, where L is the distance travelled by the light since exiting the first film (noting that $d_1 = L\sin(\theta_1 - \theta_2)$). The path of the second film (approximated as linear) is $\left(\frac{f_0}{h_m}h + R - f_0, h\right)$, where h is the height of the liquid. The intersection of the light with the second film occurs when these two lines intersect:

$$h = h_0 - L\sin(\theta_1 - \theta_2),$$

$$f_1 + L\cos(\theta_1 - \theta_2) = \frac{f_0}{h_m}(h_0 - L\sin(\theta_1 - \theta_2)) + R - f_0 = d_1$$

$$L\left(\cos(\theta_1 - \theta_2) + \frac{f_0}{h_m}\sin(\theta_1 - \theta_2)\right) = \frac{f_0 h_0}{h_m} + R - f_0 - f_1,$$

$$d_1 = \frac{\sin(\theta_1 - \theta_2)}{\cos(\theta_1 - \theta_2) + \frac{f_0}{h_m}(\sin(\theta_1 - \theta_2))}\left(\frac{f_0 h_0}{h_m} + R - f_0 - f_1\right)$$

The angle at which the light meets the second film θ_3 is calculated as follows

$$\theta_3 = 2\pi - \theta_2 - 2 \cdot \left(\pi - \tan^{-1}\frac{h_0}{f_0}\right) = 2\tan^{-1}\left(\frac{h_0}{f_0}\right) - \theta_2.$$

The angle θ_4 at which the light enters the second film is calculated from Snell's Law,

$$\sin\left(\theta_4 - \frac{\pi}{2}\right) = \frac{n_2}{n_1}\sin\left(\frac{\pi}{2} - \theta_3\right),$$

$$d_2 = f_0 \tan\left(\theta_4 - \tan^{-1}\left(\frac{h_0}{f_0}\right)\right).$$

The angle θ_5 that the light strikes the glass is calculated from

$$\theta_5 = \frac{\pi}{2} - \tan^{-1}\left(\frac{d_2}{f_2}\right),$$

where f_2 is the film thickness at $h = h_0 - d_2$. The angle θ_6 at which the light enters the glass is calculated from

$$\sin\left(\frac{\pi}{2} - \theta_6\right) = \frac{n_3}{n_2}\sin\left(\frac{\pi}{2} - \theta_5\right),$$

$$d_3 = L_G \tan\left(\frac{\pi}{2} - \theta_6\right),$$

where L_G is the thickness of the glass tube.

Fig. 3.1.2 and Fig. 3.1.3 show the distance along the tube axis travelled by a beam of light for various heights, as a function of rotational speed ω for the standard VFD with 1 mL of liquid at 45° tilt angle. The wall thickness L_G is 1.25 mm, the beam of light is positioned at a height of 4.5 cm, and the refractive indexes for air, water, and glass are 1, 1.33 and 1.5 respectively. At lower rotational speeds the movement is up to 89 μm at the upper end of the film, whilst even at higher speeds it can reach above 20 μm. This is sufficient movement to cause significant misalignment of the light and detector.

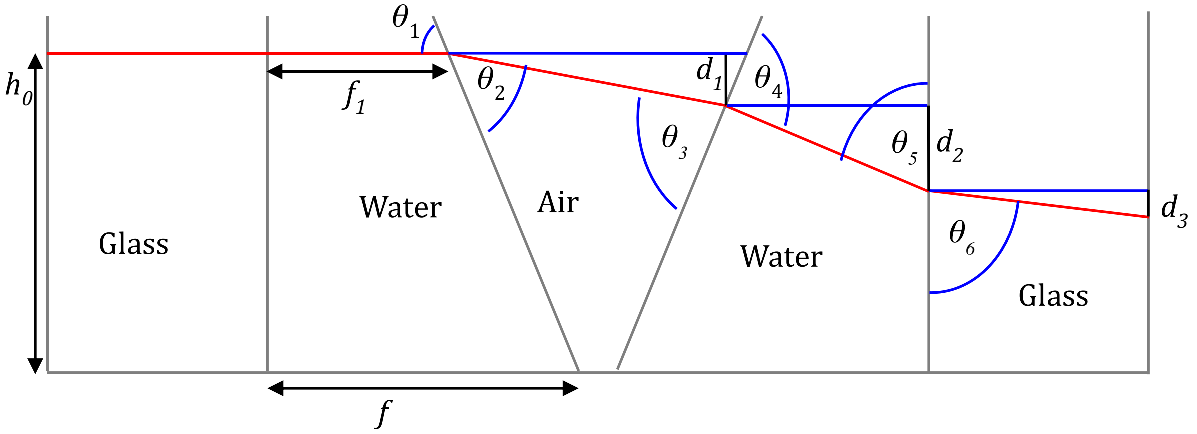

Fig. 3.1.1: Diagram of refraction of a ray of light through a VFD tube with a thin film.

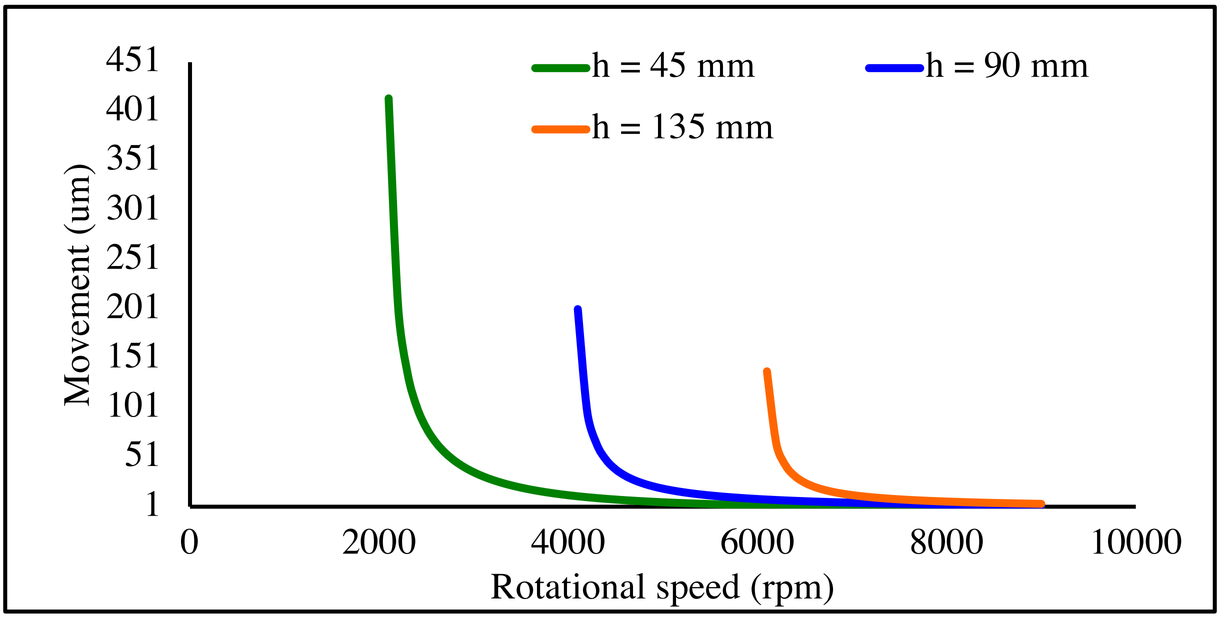

Fig. 3.1.2: The movement along the axis of the tube by a beam of light, for various heights of interest. Standard VFD conditions, $\phi = 90°$, $V = 1$ mL.

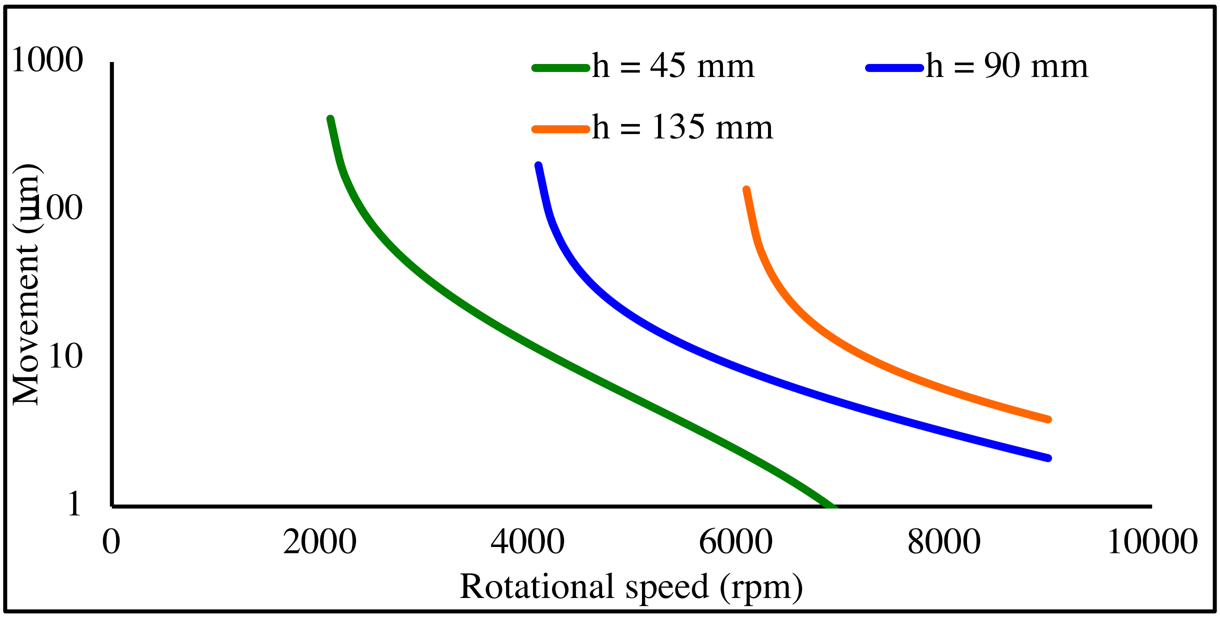

Fig. 3.1.3: Fig. 3.1.2 presented on a logarithmic-logarithmic scale for clarity purposes. The movement along the axis of the tube by a beam of light, for various heights of interest. Standard VFD conditions, $\phi = 90°$, $V = 1$ mL.

Chapter 3.2 – Neutron Imaging Theory

Neutrons are uncharged particles with a mass of $1.6749 \cdot 10^{-27}$ kg and interact primarily and (usually) non-destructively with atomic nuclei. One type of neutron-nuclei interaction is absorption of the neutron, the extent to which is described in terms of the absorption cross-section. The absorption cross section varies widely between adjacent elements on the periodic table, and even varies widely between different isotopes of the same element. Consequently, neutron imaging provides a useful contrast to x-ray imaging, which can easily distinguish between sample regions of different densities but struggles to distinguish between regions of similar density. One particular pair of cross sections that is useful is that for ^{1}H (0.3326 b), and that for ^{2}H (0.000519 b). The ability for ^{1}H to absorb neutrons much more readily than deuterium allows for the differentiation between deuterated compounds and non-deuterated compounds. The cross sections of ^{12}C and ^{18}O are 0.00353 b and 0.00016 b respectively, and consequently are sufficiently small enough that they do not interfere with the ability to distinguish between samples containing ^{1}H and ^{2}H.[1,2]

Neutron detection methods involve the absorption of neutrons by nuclei and subsequent emission of a more easily detected (and usually charged) particle. These charged particles then interact with a scintillator, which emits light. This light is then reflected using a mirror at a 45° angle to a detection camera. The use of a mirror ensures the detection camera is not in the neutron beam path. The most common nuclei used as neutron imaging are lithium-6, boron-10, and gadolinium.[3] Lithium-6 has a relatively large cross section (940 barns) and does not produce any gamma radiation ($^{1}_{0}n + ^{6}_{3}Li \rightarrow ^{3}_{1}H + ^{4}_{2}He$), reducing the noise produced by the detector. The two most common forms of ^{6}Li used for neutron detection are ^{6}Li glass and $^{6}LiF/ZnS$, both of which combine the neutron absorber and the scintillator into a single material. ^{6}Li glass is not often used for neutron imaging for several reasons: the thickness required for good efficiency is more than 1 mm and limits the spatial resolution, it is more sensitive to ambient gamma radiation than desirable, and the number of photons produced per neutron (approximately 8000) is considered low for neutron imaging. $^{6}LiF/ZnS$, however, has photon/neutron ratios on the order of 160,000, and high spatial resolution can be achieved using $^{6}LiF/ZnS$ films with thickness below 50 μm, although films of this thickness sacrifice high absorption efficiency in order to obtain high resolution.

Like ^{6}Li, Boron-10 has a high neutron capture cross section (3835 barns), however, unlike ^{6}Li, gamma radiation is produced as a by-product of its degradation ($^1_0\mathrm{n} + ^{10}_5\mathrm{B} \rightarrow ^4_2\mathrm{He} + ^7_3\mathrm{Li} + ^0_0\gamma$), increasing the level of background noise. The other challenge when using Boron-10 is that the products are more difficult to detect because their low velocity results in a shorter range. Gadolinium is of interest because of the very large absorption cross section of non-isotopically pure gadolinium (49700 b), however, unlike the other nuclei discussed, it does not release a charged particle, instead releasing only high-energy gamma radiation. Gadolinium oxide detectors are of particular interest because of the high resolution they can afford, as recently demonstrated at the Paul Scherrer Institut in Switzerland.[4]

The neutron imaging facility in Australia is DINGO,[a] and is situated on the HB2 thermal neutron port of the Open-Pool Australian Lightwater (OPAL) Reactor at the Australian Nuclear Science and Technology Organisation (ANSTO) site at Lucas Heights, near Sydney. Construction of DINGO (Fig. 3.2.1) was completed in June 2013, becoming operational in 2014, and is capable of operating in either high flux or high resolution configuration.[5-7] DINGO contains two neutron beams, a high flux beam with flux of 5.33×10^7 neutrons/cm^2/s, and a low flux beam for high resolution with flux of 1.1×10^7 neutrons/cm^2/s. Six different scintillation screens are generally available for neutron imaging, consisting of ^{6}LiF/ZnS coated on aluminium with ^{6}LiF/ZnS thicknesses from 50 μm to 200 μm for areas of either 200x200 mm^2 or 100x100 mm^2. Two cameras are available for use, an Andor IKON-L CCD camera for standard operation, and an Andor NEO 5.5 sCMOS camera for fast data acquisition. [5]

---

[a] The convention used widely at ANSTO is for instrument names to be written in capitals.

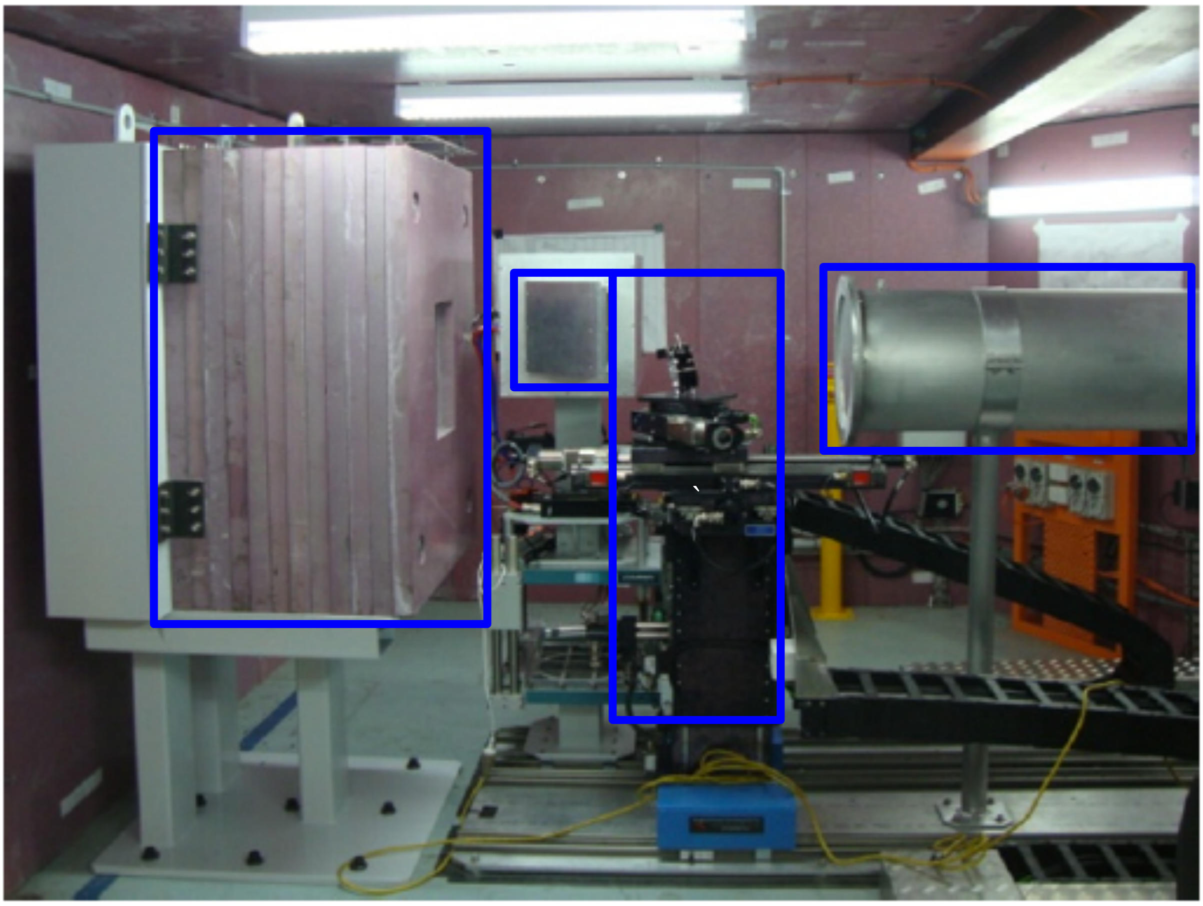

Fig. 3.2.1: The DINGO Neutron Tomography Station at Lucas Heights. The parts of the image outlined in blue are, from right to left: a pipe through which the neutron beam passes through from the reactor; a movable and rotatable sample stage; a box containing the neutron detector; and lead shielding.[7]

Chapter 3.3 – Dynamic Camera Methodology

Neutron imaging experiments were performed at the DINGO imaging station at ANSTO, using the high flux beam. The scintillation screen used was the 100 µm thick ^{6}LiF/ZnS screen, and the camera used was the Andor NEO 5.5 sCMOS camera. The acquisition time used was 1 s, which was determined to provide a sufficient balance between image quality and temporal resolution. An additional 0.02 s was required to transmit the data from the camera to the computer, resulting in 1120 acquisitions over 1140 s, a frame rate of 0.982 Hz. Five no-beam acquisitions were collected as a background.

The Vortex Fluidic Device was positioned on the sample stage and 5 empty-tube acquisitions with the VFD rotating but without liquid were recorded. This step was necessary before each experiment because any slight movement of the device during tube changeover would result in slight misalignment interfering with the ability to subtract the background images from the experimental images. The VFD was set to run at a sequence of 60 rotational speeds in 50 rpm increments for 10 seconds each, with 10 seconds stationary between each speed. The limitation of a sequence of 60 speeds was due to the programming of the device at the time. Additionally, because the VFD was controlled from within the instrument enclosure, there was a delay of approximately 55 seconds between the start-up of the device and when safety measures allowed acquisition of the first image. Consequently, only 57 speeds could be recorded in a single experiment (a range of 2800 rpm). One consequence of the acquisition process was that the first image would be acquired partly whilst the VFD was stationary, and partly whilst the VFD was rotating.

Experiments for speeds above 4800 rpm resulted in a film thickness on the order of less than 6 pixels and yielded no reliable data. The images used to measure the film thickness were processed in the following manner using the program ImageJ: the sets of background images and the empty-tube images were each averaged to produce a single background image, along with an empty-tube image for each experiment. The despeckle function of ImageJ was then applied to each image to reduce the noise, and the background image was then subtracted from the experimental and empty-tube experiments. The experimental images were then divided by the appropriate empty-tube image. The brightness and contrast were then auto-adjusted to produce easily interpretable images.

Chapter 3.4 – Dynamic Camera Experiments

Water (1 mL) was inserted into the VFD tube and the VFD was operated as described in Chapter 3.3. The VFD is depicted stationary in Fig. 3.4.1 a), whilst in b) the VFD is shown during spin-up to 4000 rpm across t = 0 s to 1 s, and in c) the VFD is shown post spin-up to 4000 rpm across t = 1 s to 2 s, at which point the film appears stable. The time taken to reach a stable state can be determined by subtracting from each image the previous image to show the difference, as seen in Fig. 3.4.2, a) shows a very large difference between stationary and during spin-up, as expected, b) shows a significant difference because the fluid is still very much moving towards equilibrium, c) shows only a slight difference distinguishable from noise, indicating that the film is nearly stable, whilst d) shows no difference that can be differentiated from noise. Consequently, it can be concluded that the film reaches stability within 2 s. To determine if the short time required to achieve stability is maintained at higher speed, the same process was used to analyse data acquired for 7000 rpm, with the subtractions presented in Fig. 3.4.3. As can be seen in e), the film is stable (within detectable noise limits) after 3 s. Blue ovals indicate the regions where differences exist but may be difficult to identify visually.

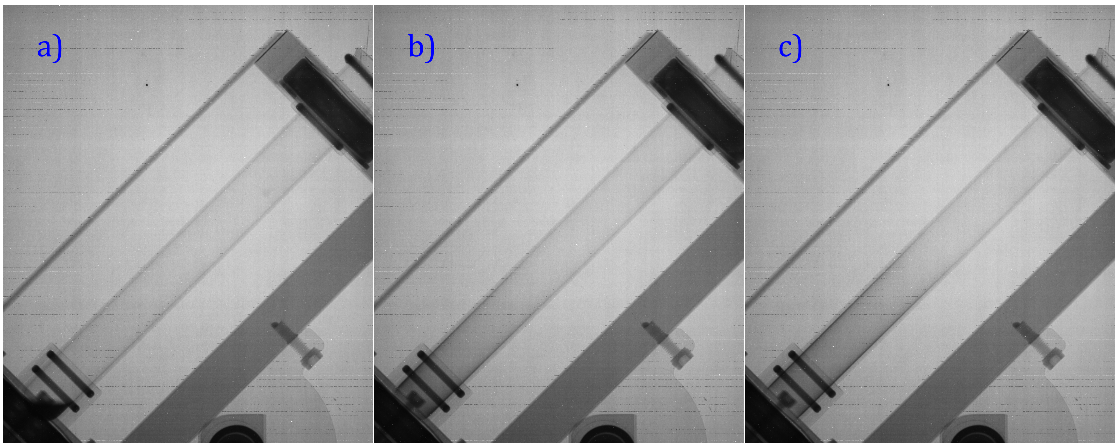

Fig. 3.4.1: 1 mL of water in the VFD during spin-up at ω = 4000 rpm: a) before spin-up; b) during spin-up (t = 0 s to 1 s); c) after spin-up (2s).

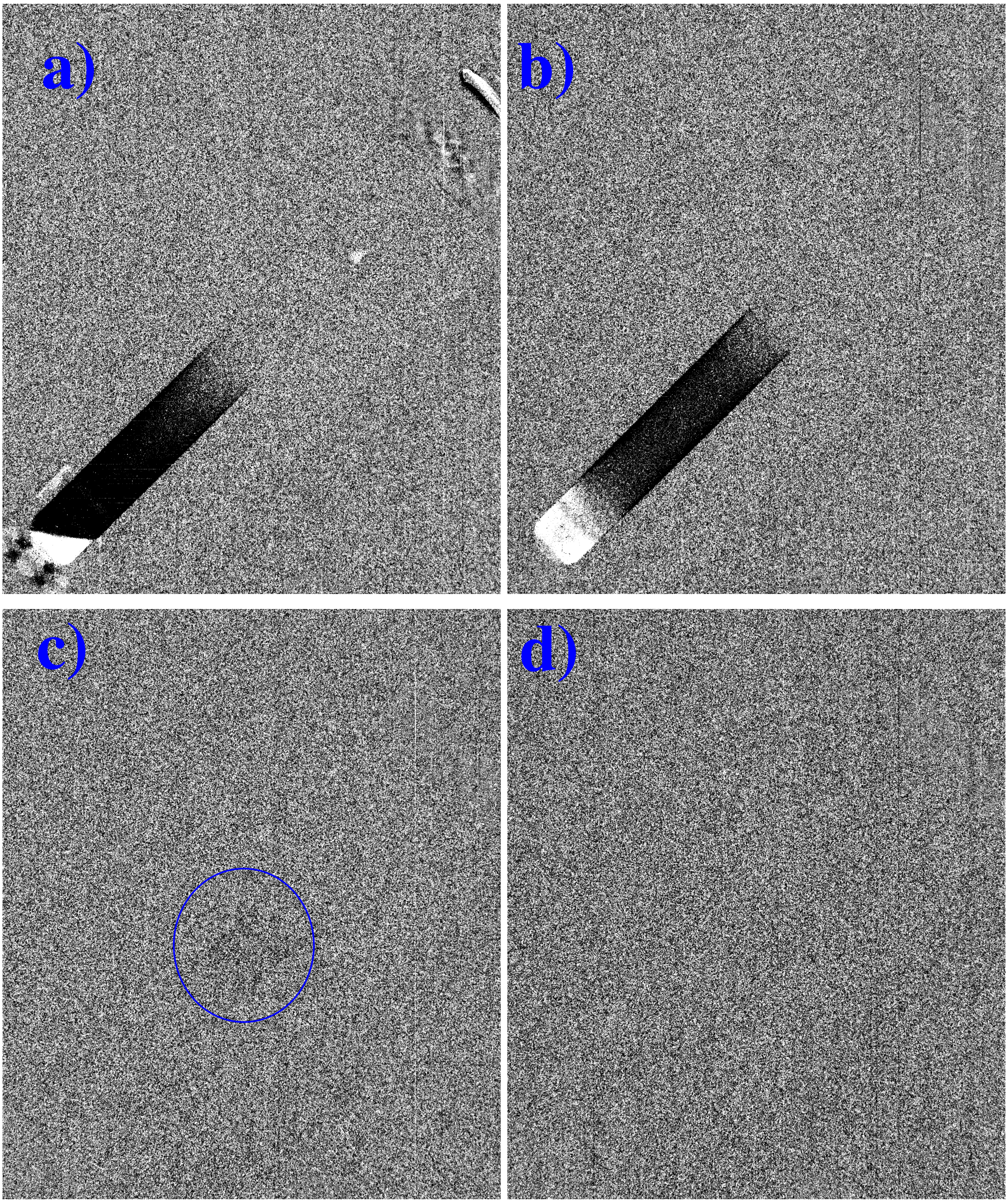

Fig. 3.4.2: Subtractions of the VFD operating at $\omega = 4000$ rpm (H_2O, $V = 1$ mL) at various time points: a) During spin-up minus stationary; b) $t \approx 0$ s minus during spin-up; c) $t \approx 1$ s minus $t \approx 0$ s; d) $t \approx 2$ s minus $t \approx 1$ s.

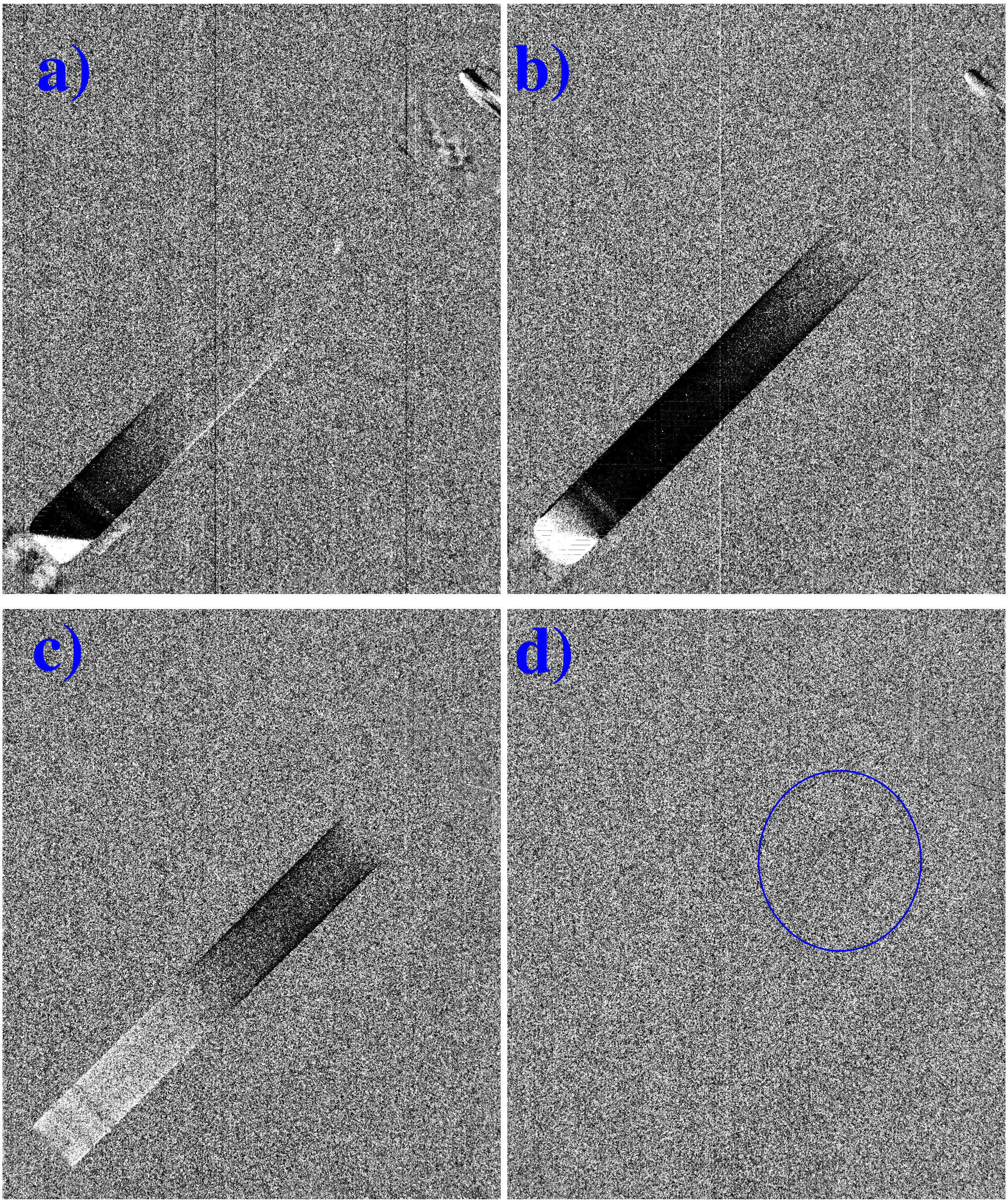

Fig. 3.4.3: Subtractions of the VFD operating at $\omega = 7000$ rpm (H_2O, $V = 1$ mL) at various time points: a) During spin-up minus stationary; b) $t \approx 0$ s minus during spin-up; c) $t \approx 1$ s minus $t \approx 0$ s; d) $t \approx 2$ s minus $t \approx 1$ s.

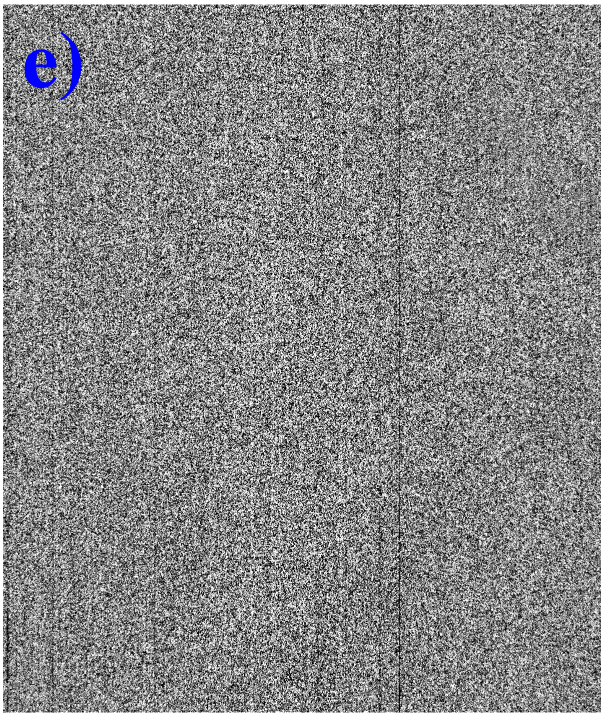

Fig. 3.4.3: Subtractions of the VFD operating at $\omega = 7000$ rpm (H_2O, $V = 1$ mL) at various time points: e) $t \approx 3$ s minus $t \approx 2$ s.

The time required for a biphasic system of water and toluene to stabilise was also investigated by using D_2O and toluene to investigate the toluene stability, and H_2O and d_8-toluene to investigate the water stability. Fig. 3.4.4 shows the subtraction series for the VFD operating at 2500 rpm with 0.5 mL of D_2O and 0.5 mL of toluene. It can be clearly seen that the film has reached stability within 2 s, whilst Fig. 3.4.5 shows that the same system set at 7000 rpm reaches stability within 3 s. In contrast, Fig. 3.4.6 shows the subtraction series for 0.5 mL H_2O and 0.5 mL d_8-toluene at 2500 rpm, showing that it does not reach equilibrium within 8 s. However, at 7000 rpm the system reaches stability within 2 s (Fig. 3.4.7). Investigation of the individual speeds shows that from 2050 rpm to 2600 rpm, the VFD does not reach stability within 8 s, whilst it takes about 5 to 7 s to reach stability for 2650 rpm to 2950 rpm and reaches stability within 2 or 3 s for 3000 rpm and above. Consequently, it is concluded that the time required for a single phase to reach an equilibrium state is generally less than 3 seconds, however, it can take longer for biphasic systems to reach equilibrium, particularly at lower rotational speeds.

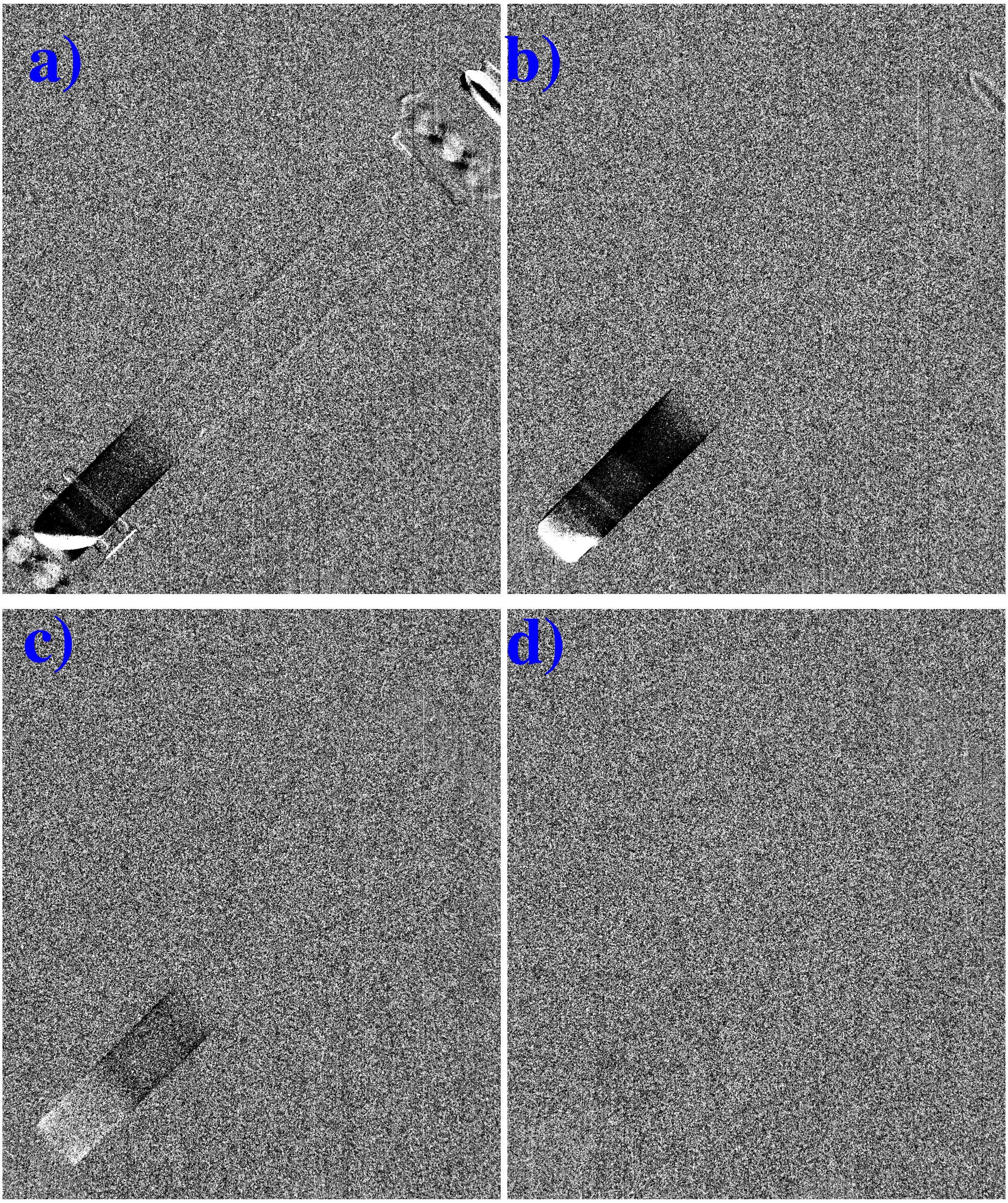

Fig. 3.4.4: Subtractions of the VFD operating at ω = 2500 rpm (D_2O, V = 0.5 mL + toluene, V = 0.5 mL) at various time points: a) during spin-up minus stationary; b) $t \approx 0$ s minus during spin-up; c) $t \approx 1$ s minus t ≈ 0 s; d) $t \approx 2$ s minus t ≈ 1 s.

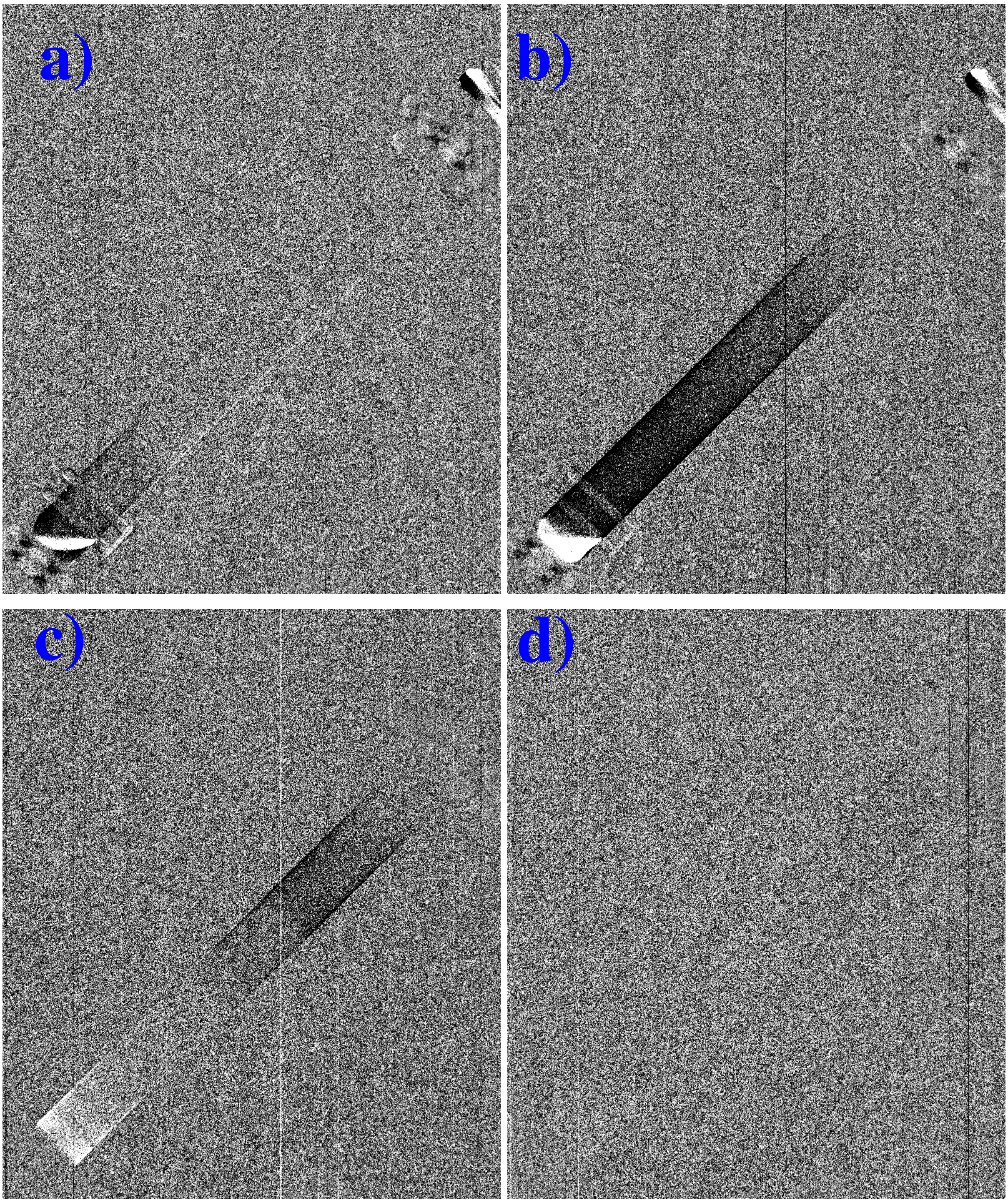

Fig. 3.4.5: Subtractions of the VFD operating at ω = 7000 rpm (D_2O, V = 0.5 mL + toluene, V = 0.5 mL) at various time points: a) during spin-up minus stationary; b) $t \approx 0$ s minus during spin-up; c) $t \approx 1$ s minus t ≈ 0 s; d) $t \approx 2$ s minus $t \approx 1$ s.

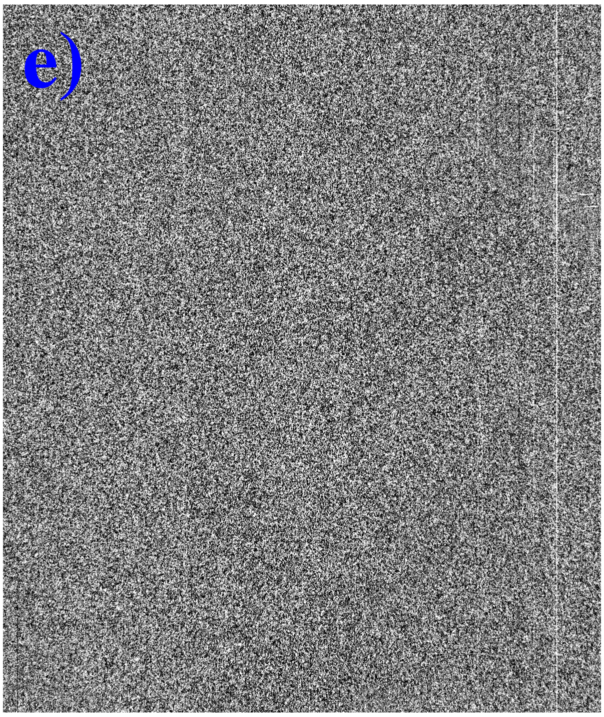

Fig. 3.4.5: Subtractions of the VFD operating at ω = 7000 rpm (D_2O, V = 0.5 mL + toluene, V = 0.5 mL) at various time points: e) $t \approx 3$ s minus $t \approx 2$ s.

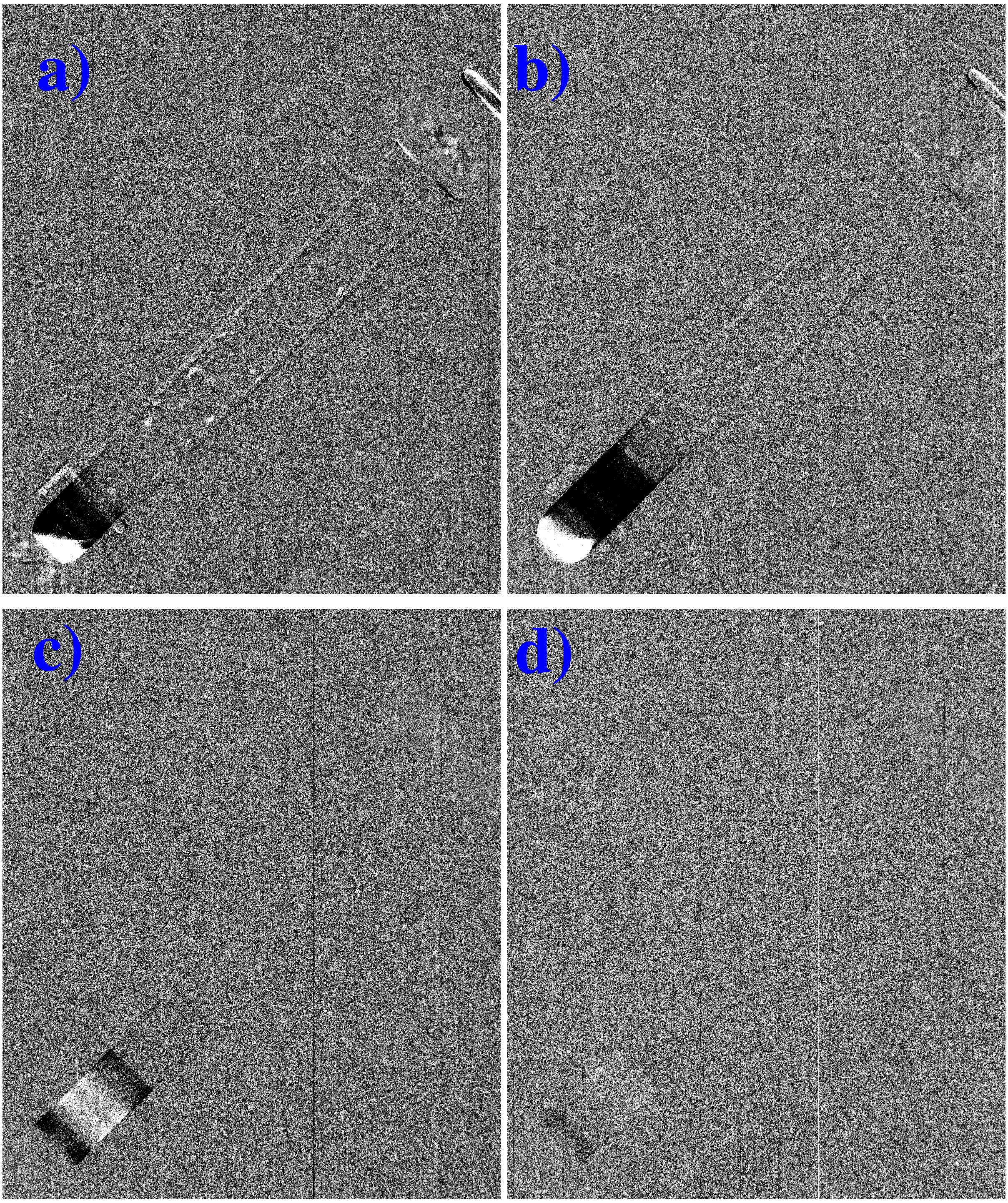

Fig. 3.4.6: Subtractions of the VFD operating at ω = 2500 rpm (H_2O, V = 0.5 mL + d_8-toluene, V = 0.5 mL) at various time points: a) during spin-up minus stationary; b) $t \approx 0$ s minus during spin-up; c) $t \approx 1$ s minus $t \approx 0$ s; d) $t \approx 2$ s minus $t \approx 1$ s.

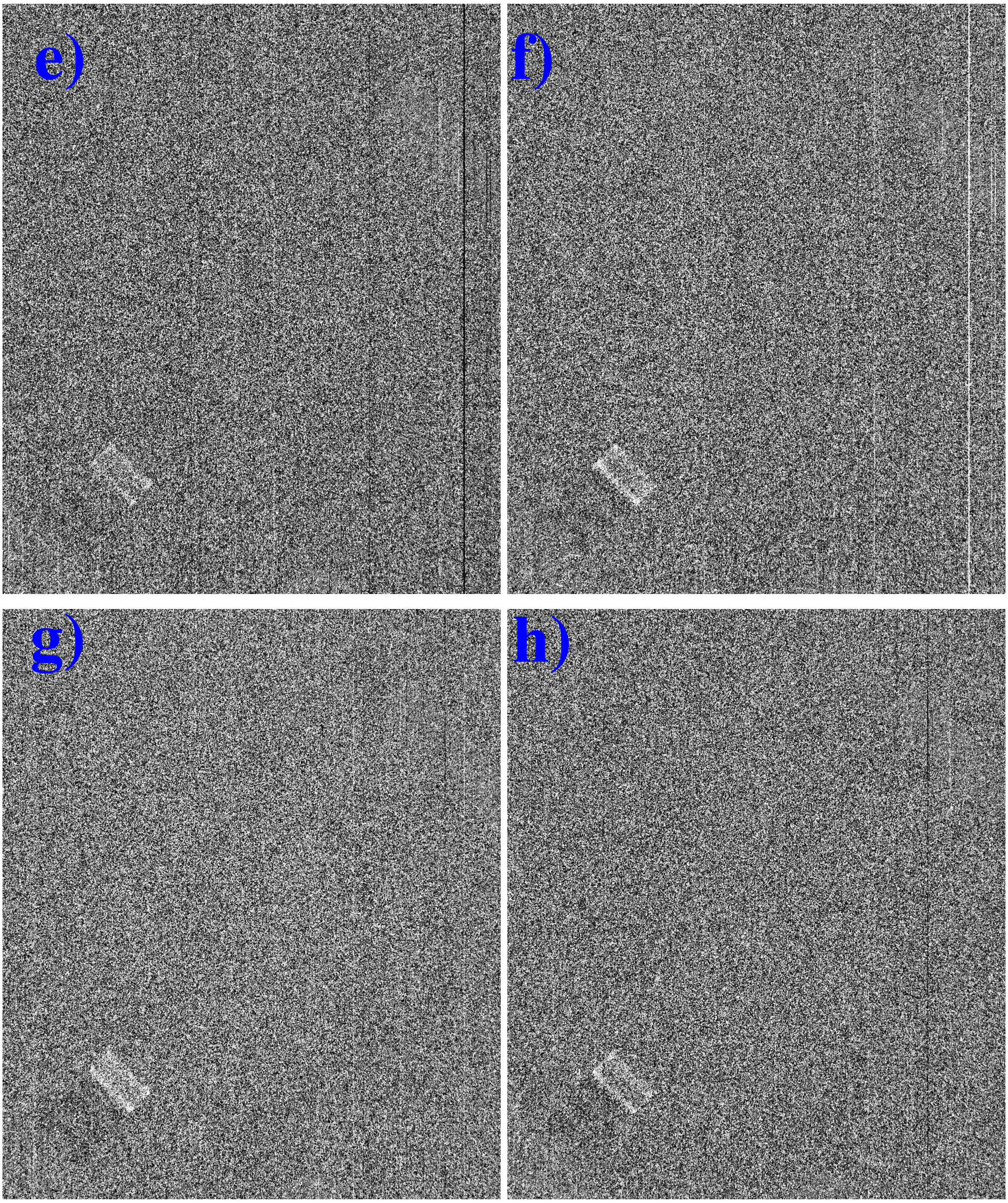

Fig. 3.4.6: Subtractions of the VFD operating at ω = 2500 rpm (H_2O, V = 0.5 mL + d_8-toluene, V = 0.5 mL) at various time points: e) $t \approx 3$ s minus $t \approx 2$ s; f) $t \approx 4$ s minus $t \approx 3$ s; g) $t \approx 5$ s minus $t \approx 4$ s; h) $t \approx 6$ s minus $t \approx 5$ s.

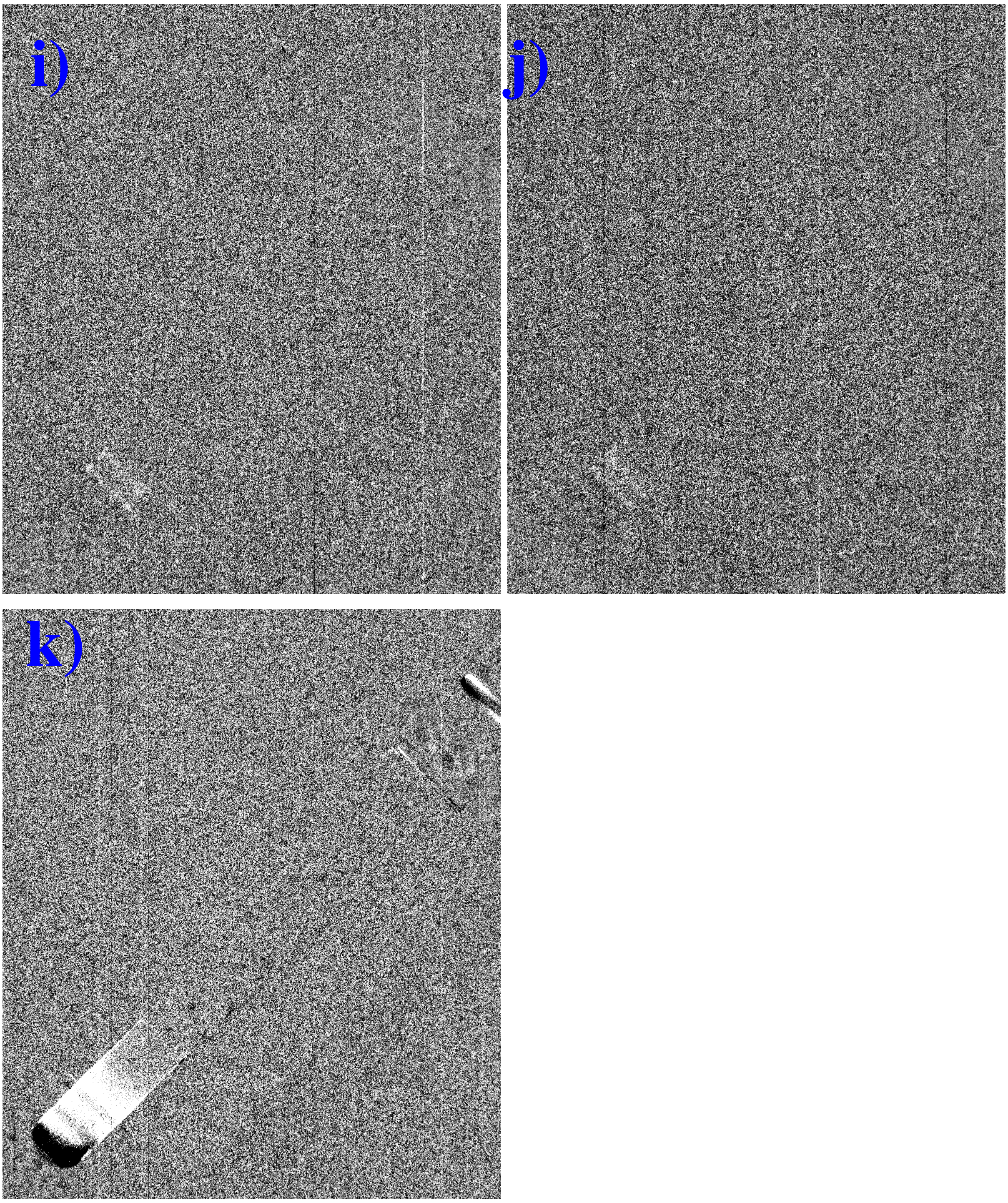

Fig. 3.4.6: Subtractions of the VFD operating at $\omega = 2500$ rpm (H_2O, $V = 0.5$ mL + d_8-toluene, $V = 0.5$ mL) at various time points: i) $t \approx 7$ s minus $t \approx 6$ s; j) $t \approx 8$ s minus $t \approx 7$ s; k) during spin-down minus $t \approx 8$ s.

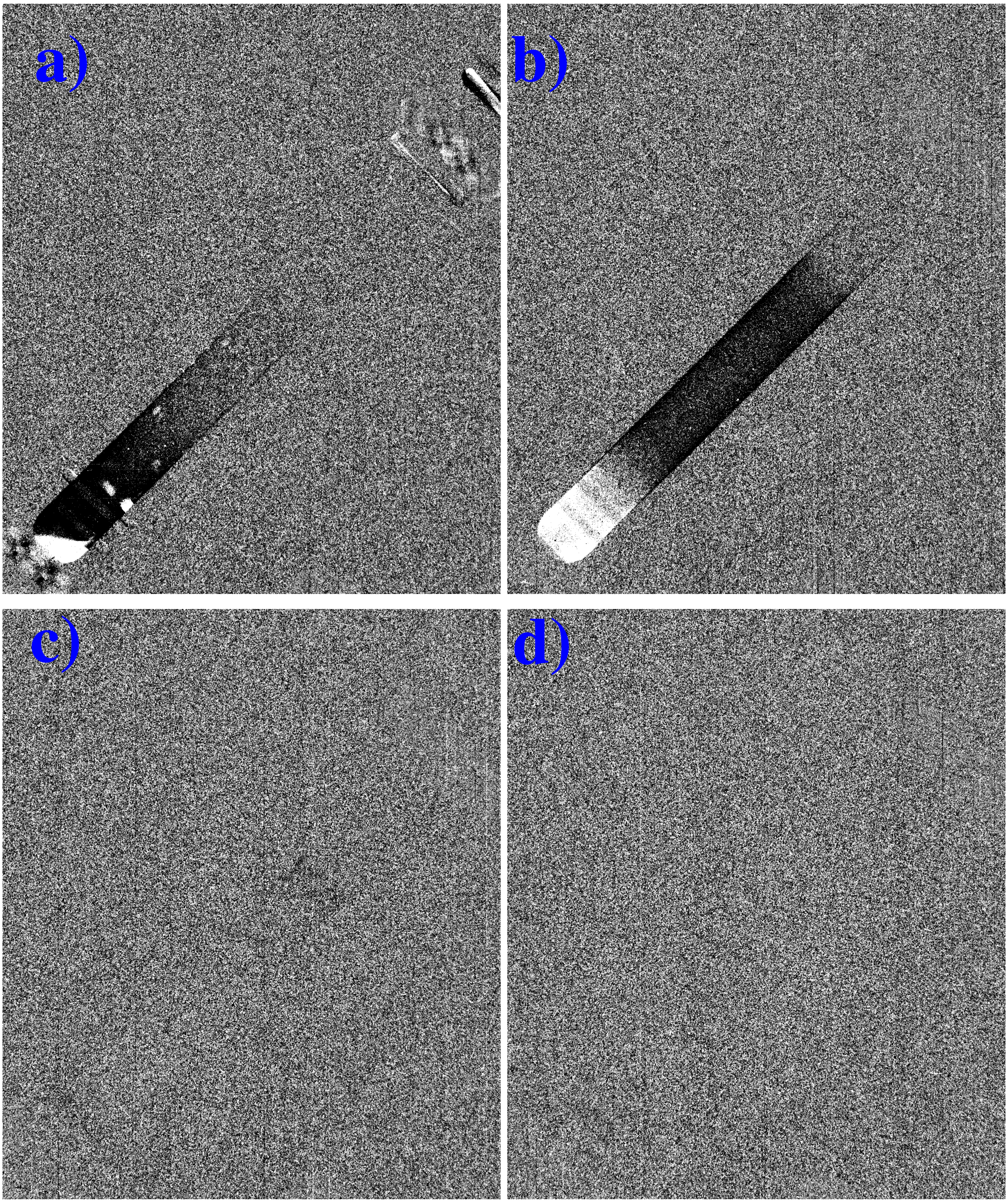

Fig. 3.4.7: Subtractions of the VFD operating at $\omega = 7000$ rpm (H_2O, $V = 1$ mL + d_8-toluene, $V = 1$ mL) at various time points: a) during spin-up minus stationary; b) $t \approx 0$ s minus during spin-up; c) $t \approx 1$ s minus $t \approx 0$ s; d) $t \approx 2$ s minus $t \approx 1$ s.

To determine if the film thickness observed through neutron imaging was consistent with the film thickness predicted by the mathematical model along the length of the tube, the film thickness was measured using the processed images, as seen in Fig. 3.4.8a. The start and end of the film was determined visually and the distance between the start and end of the film was measured using ImageJ. The external width of the tube was used for internal calibration, giving a pixel size of 66 µm. Due to the low resolution and the relatively high amount of noise, the film thickness was measured at four points (Fig. 3.4.8b), with each point measured twice. The average of these 8 measurements was then compared to the average film thickness of the four points as predicted by the mathematical model. Fig. 3.4.9 shows reasonable correlation given the significant noise, resulting in an R^2 correlation coefficient of 0.686. The height reached by the film was also measured, with the average of the two sides compared to the average predicted by the model (Fig. 3.4.10). The height reached by the thin film shows good correlation with that predicted by the mathematical model, giving an R^2 coefficient of 0.959.

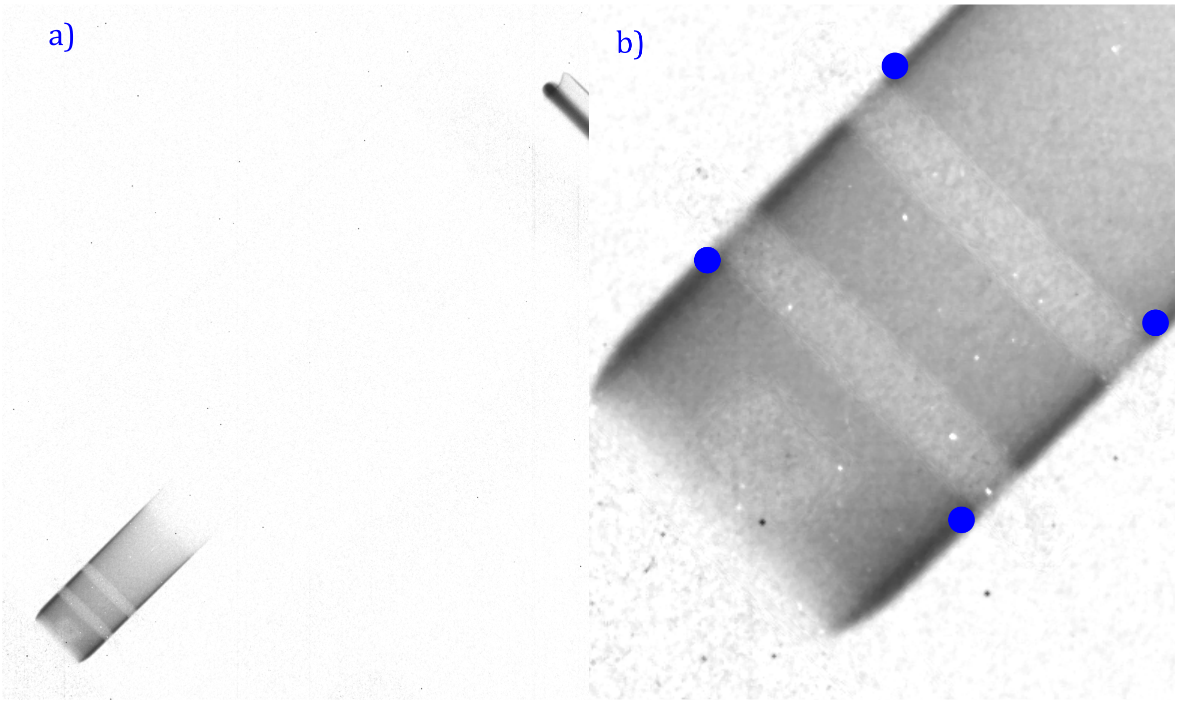

Fig. 3.4.8: a) Processed image of the thin film in a Vortex Fluidic Device (H_2O, $V = 1$ mL, $\omega = 2000$ rpm), taken using neutron imaging; b) points on image a) used to measure the film thickness.

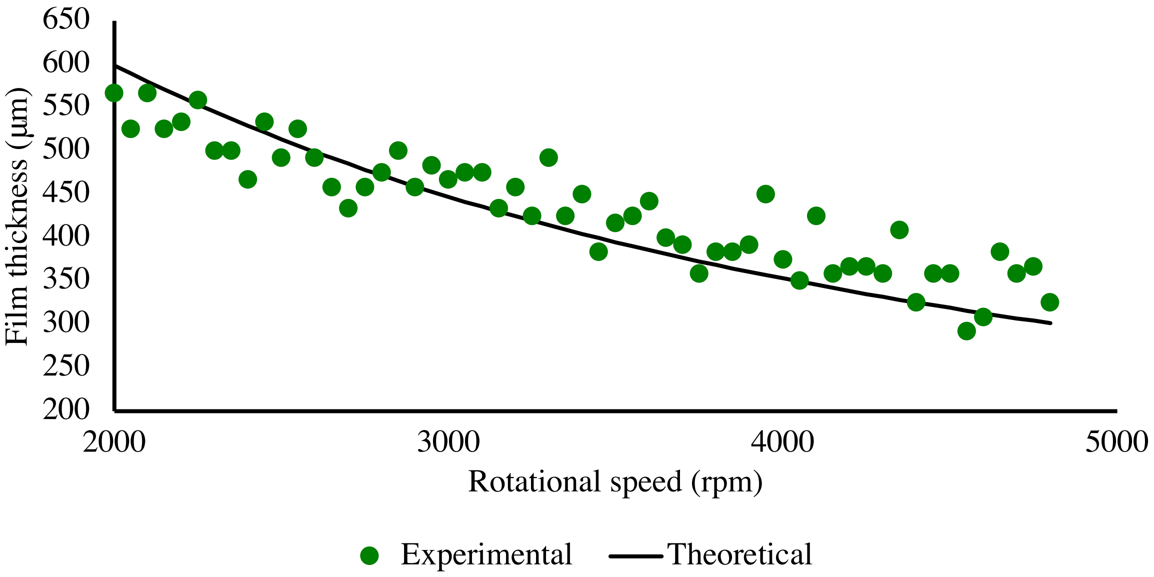

Fig. 3.4.9: The film thickness measured by the dynamic camera compared to theoretical.

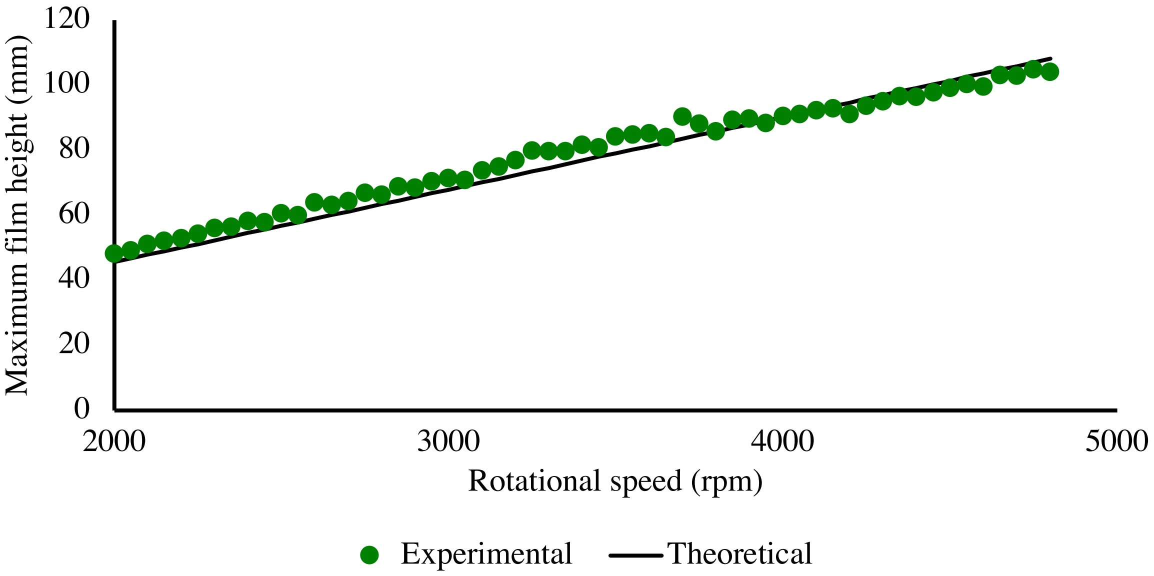

Fig. 3.4.10: Measured maximum film height compared to theoretical.

Chapter 3.5 – High Resolution Camera Methodology

Neutron imaging experiments were performed at the DINGO imaging station at ANSTO, using the low flux beam**.** The scintillation screen used was a 10 μm thick gadolinium oxide screen, and the camera used was the Andor IKON-L CCD camera. The acquisition time used was 90 s, which was determined to provide sufficient image quality. Five no-beam acquisitions were collected as a background. For these experiments, the field of view within the camera is approximately 1 cm x 1 cm. Consequently, it was necessary to record multiple images at different positions in order to acquire a full image of the VFD. A program was written using the DINGO operating language in order to allow the automated collection of the required images. This program is summarised as performing the following steps:

1) Start timer (at this point, the VFD was also started).
2) Collection a 90 s acquisition.
3) Move the sample stage to the next higher VFD position.
4) Repeat steps 2 and 3 until 11 images have been acquired, and not moving the sample stage after the 11th image.
5) Wait until the timer reaches t = 1374 s (at this point, the VFD switches speeds).
6) Repeat steps 2 through 5 but moving the sample stage downwards.
7) Repeat steps 1 through 6 until complete images have been acquired for all desired speeds.

The procedure for performing the experiments was to set the DINGO sample stage to the start position, and to run the above program for an empty tube spinning at approximately 1000 rpm. The desired sample was then inserted into the VFD (whilst not spinning), the tube was capped, and the program was run for the desired set of speeds. The 1374 s timer was required because the high precision of motor position required for neutron imaging may result in the motor restarting its movement several times in order to reach a sufficiently precise position. A consequence of this is that the exact time required for the sequence of acquisitions was slightly variable, and the total time required for each speed was slightly variable.

The images were processed in the following manner using the program ImageJ: the five no-beam background measurements were averaged to produce a single image. The despeckle function of ImageJ was then applied to each image to reduce the noise, the remove outliers function was applied, and the background image was then subtracted from the experimental and empty-tube experiments, followed by despeckle a second time. The experimental images were then divided by the appropriate empty-tube image. Each set of images for a single sample and speed were then merged into a single image using the program Avizo, producing images of the type depicted in Fig. 3.5.1.

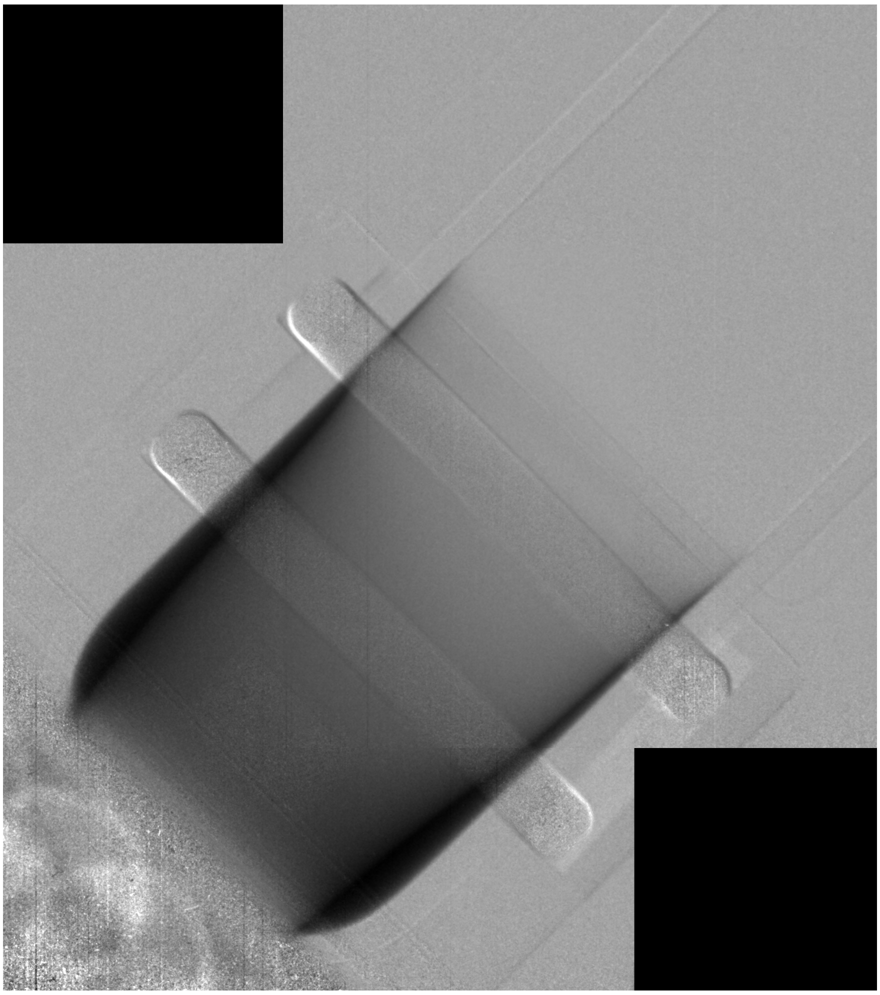

Fig. 3.5.1: Processed image of the Vortex Fluidic Device, V = 1 mL (toluene), ω = 1000 rpm, taken using a high resolution neutron imaging configuration.

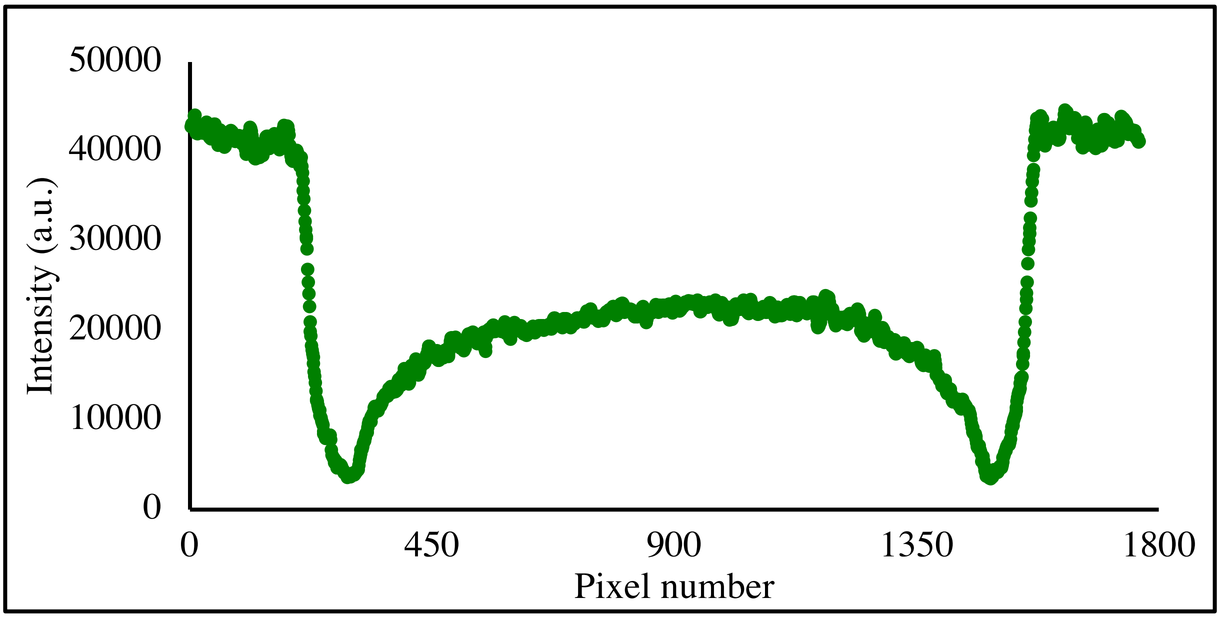

Fig. 3.5.2: The neutron intensity across the thin film as a function of position for $V = 1$ mL (toluene), $\omega = 1000$ rpm, $h = 7.5$ mm.

The film thickness for each image was determined by taking a 1D cross-section at a given height on the VFD tube ($h = 7.5$ mm and $h = 15.8$ mm, using the two o-rings as guides) and plotting the intensity as a function of position, producing graphs of the type depicted in Figure 3.5.2. From left to right, the intensity starts high before the film is present, then drops sharply as the neutrons are passingly tangentially through the film, until the thickest part of the film is reached at the air-liquid interface. The intensity then increases where the neutrons are passing through the film perpendicularly. This shape is then mirrored on the other side. The film thickness is the width of the decrease in intensity. Due to the uncertainty of the locations of the start and end of each side of the film, a range for the film thickness was determined. Achieving a reduction in noise may be possible through an increase in acquisition time.

The hydrophobic coating on a quartz tube used for these experiments was prepared in the following manner. The quartz tube was washed extensively (water) and dried extensively (150 °C). The quartz tube was then soaked in piranha solution (3:1 conc. H_2SO_4:H_2O_2) for 1 hour, then rinsed extensively (water) and dried at 120 °C for 1 hour. The tube was then submerged in a toluene-filled measuring cylinder, to which several drops of trichlorooctadecylsilane were then added. The measuring cylinder was then sealed, and the tube was allowed to sit overnight. The tube was then rinsed extensively with toluene, resulting in a hydrophobic coating as determined through visual inspection.

Chapter 3.6 – Effect of viscosity

Viscosity is an important property of liquids when describing their behaviour, however, due to the complexity of including it in the above mathematical model, the effect of viscosity was ignored when developing this model. Nonetheless, it is a reasonable expectation that within a certain viscosity range, the effect of viscosity is negligible. In order to determine this range, the film shape of four liquids was recorded, with kinematic viscosities ranging over three orders of magnitude at 25 °C. These four liquids were toluene ($\nu = 6\cdot10^{-7}$ m^{2}s^{-1}),[8] 1:1 H_2O:glycerol ($\nu = 4\cdot10^{-6}$ m^{2}s^{-1}),[9] propylene glycol ($\nu = 4\cdot10^{-5}$ m^{2}s^{-1})[10] and glycerol ($\nu = 7\cdot10^{-4}$ m^{2}s^{-1}).[9] In selecting a solvent for the lowest viscosity, water was considered, however having already confirmed the appropriateness of the model for water (albeit to the precision of the dynamic camera), it was determined that using an alternative solvent would allow the confirmation of the reliability of the model for a second solvent.[b] Experiments that are excluded from the analysis because a stitched image could not be successfully produced are glycerol at ω = 3000 rpm, propylene glycol at ω = 9000 rpm, and 1:1 water:glycerol at ω = 9000 rpm.

Comparing the measured range of the film thickness for $\phi = 0°$ and $\phi = 180°$ for toluene, it is observed that for h = 0.75 cm, the measured film thickness ranges for both ϕ positions overlap for all speeds. Even across all 64 measurements for the four liquids, there was overlap in all but 2 instances (propylene glycol, h = 7.5 mm, ω = 7000 rpm; toluene h = 15.8 mm, ω = 1000 rpm). This is in contrast to the predictions of the mathematical model, which predicts that the difference in film thickness should be greater than 100 μm up to 3600 rpm, a clearly detectable difference, particularly at 1000 rpm where the difference should be 1263 μm. This deviation between the model and reality is unsurprising, given that viscosity and surface tension would both pull the liquid around the tube, resulting in a more uniform film thickness than would be predicted by ignoring both effects. Fig. 3.6.1 compares the predicted film thickness (averaged between $\phi = 0°$ and $\phi = 180°$) with the measured film thickness (averaged between $\phi = 0°$ and $\phi = 180°$). It is observed that for most measurement points the predicted thickness is below the measured range. Looking more closely at the images, it is observed that the film is significantly blurry at both interfaces. This is likely the result of an imperfect axis of rotation. Measurements

---

[b] Although water was tested in chapter 3.7 using the high resolution configuration, it was part of a different allocation of beam time and comparison of Neutron Imaging experiments between different beam time uses is avoided where possible.

of the radial movement of the tube during rotation reveal a fluctuation in position of approximately 100 µm. This fluctuation would result in a slight blurring of the film, increasing the apparent film thickness by 100 µm. Adjusting the measured film thickness by this amount results in a significantly closer agreement between the measured and predicted values (Fig. 3.6.2). This process also produces measurements usually in good agreement with predicted values for 1:1 water:glycerol (Fig. 3.6.3) and propylene glycol (Fig. 3.6.4), as well as for glycerol at speeds above 2000 rpm (Fig. 3.6.5). For h = 1.58 cm, the correlation is not as good, but still reasonable (Fig. 3.6.6).

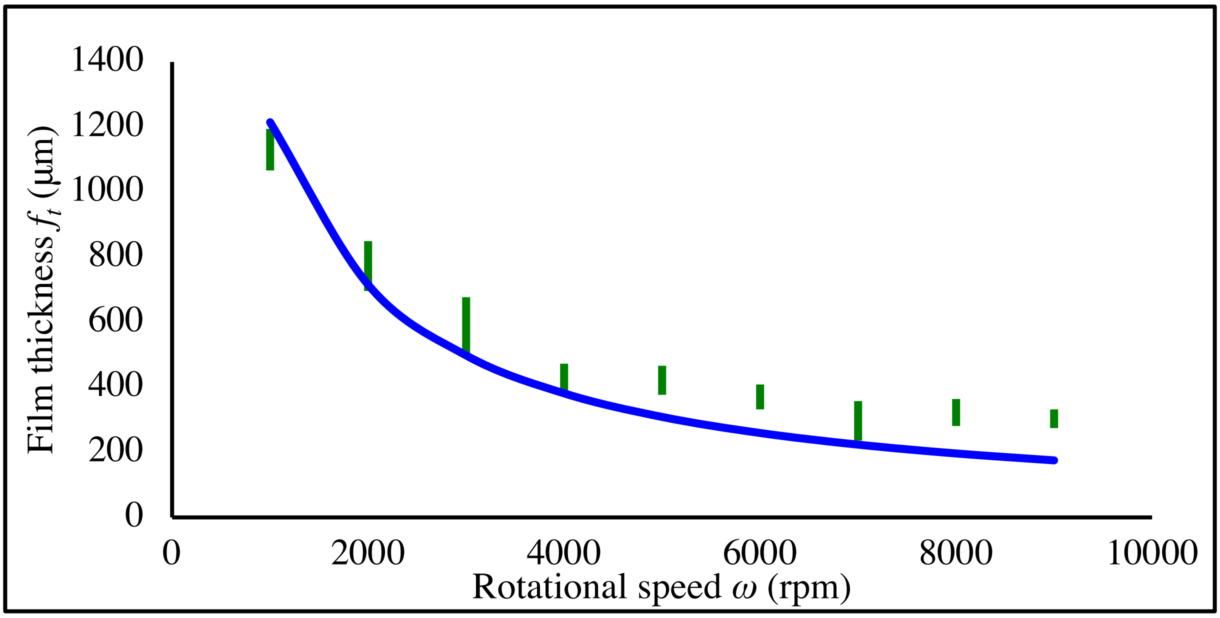

Fig. 3.6.1: Measured film thickness compared to theoretically predicted. Standard VFD, V = 1 mL (toluene), θ = 45°, h = 7.5 mm.

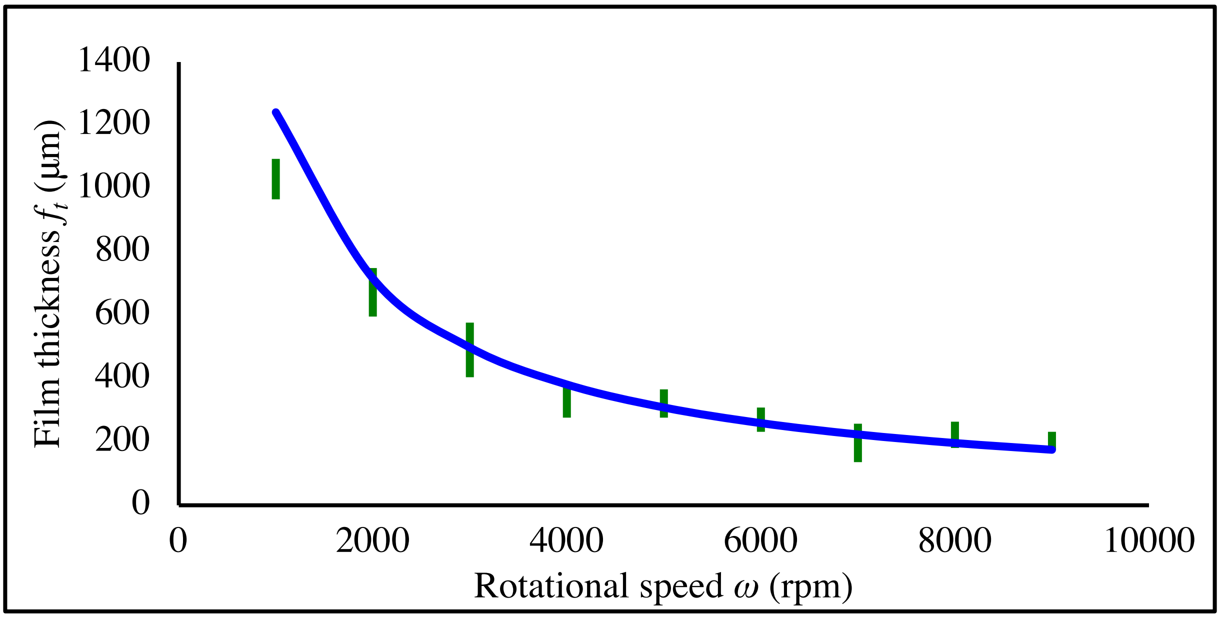

Fig. 3.6.2: Measured film thickness adjusted for imperfect rotation compared to theoretically predicted. Standard VFD, $V = 1$ mL (toluene), $\theta = 45°$, $h = 7.5$ mm.

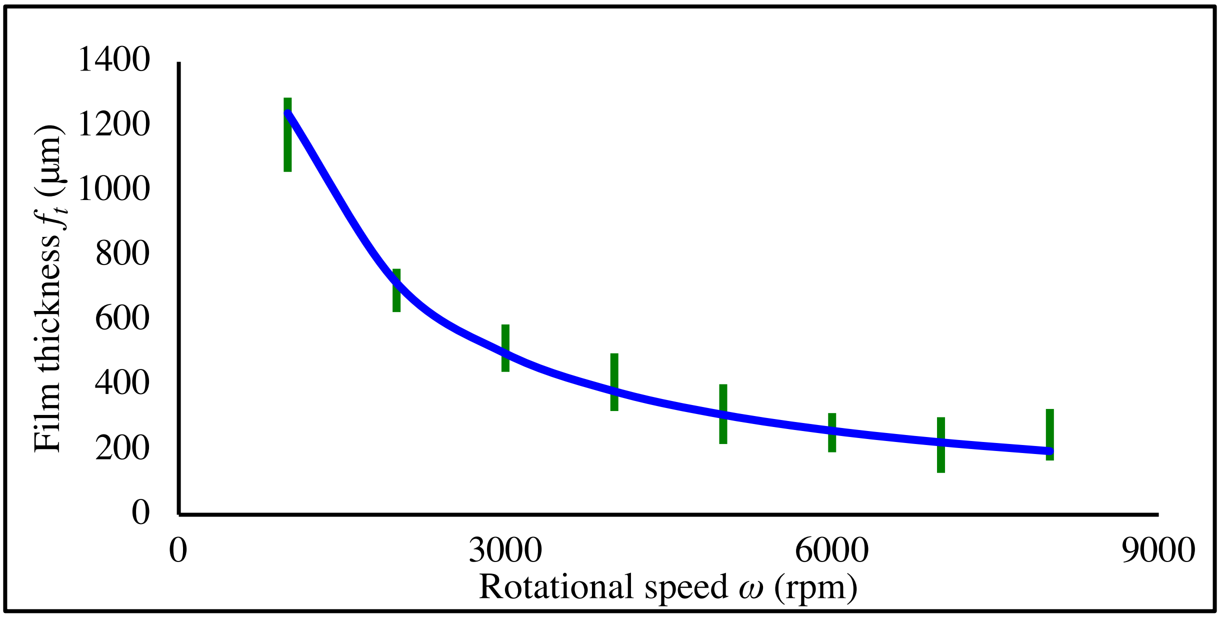

Fig. 3.6.3: Measured film thickness adjusted for imperfect rotation compared to theoretically predicted. Standard VFD, $V = 1$ mL (1:1 water:glycerol), $\theta = 45°$, $h = 7.5$ mm.

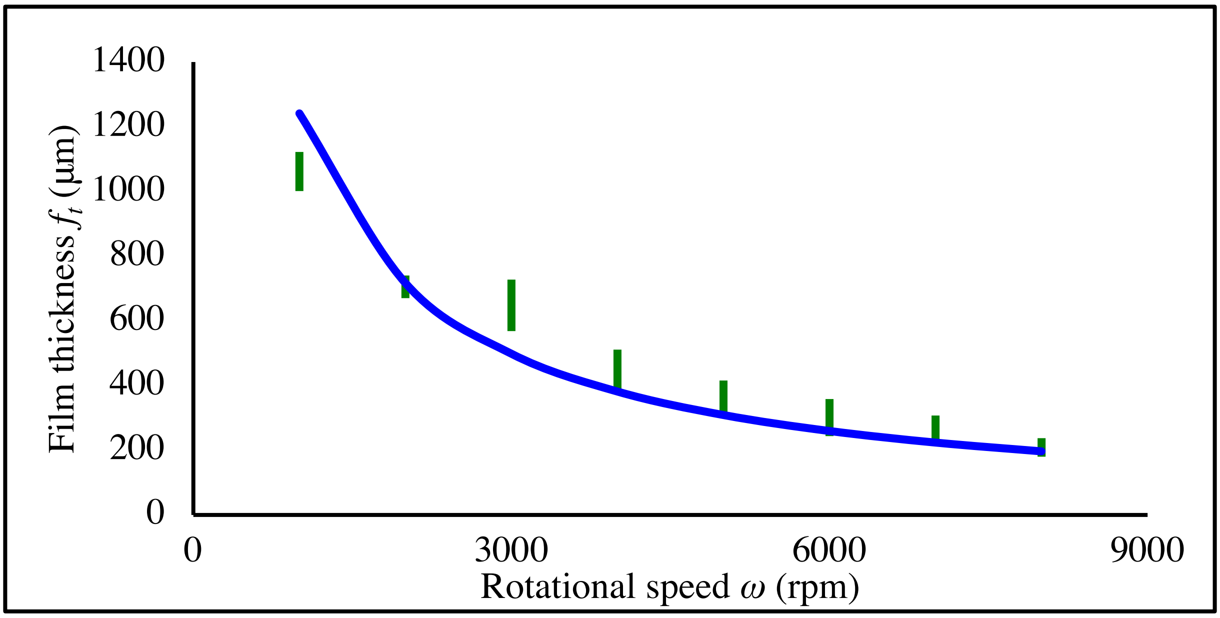

Fig. 3.6.4: Measured film thickness adjusted for imperfect rotation compared to theoretically predicted. Standard VFD, $V = 1$ mL (propylene glycol), $\theta = 45°$, $h = 7.5$ mm.

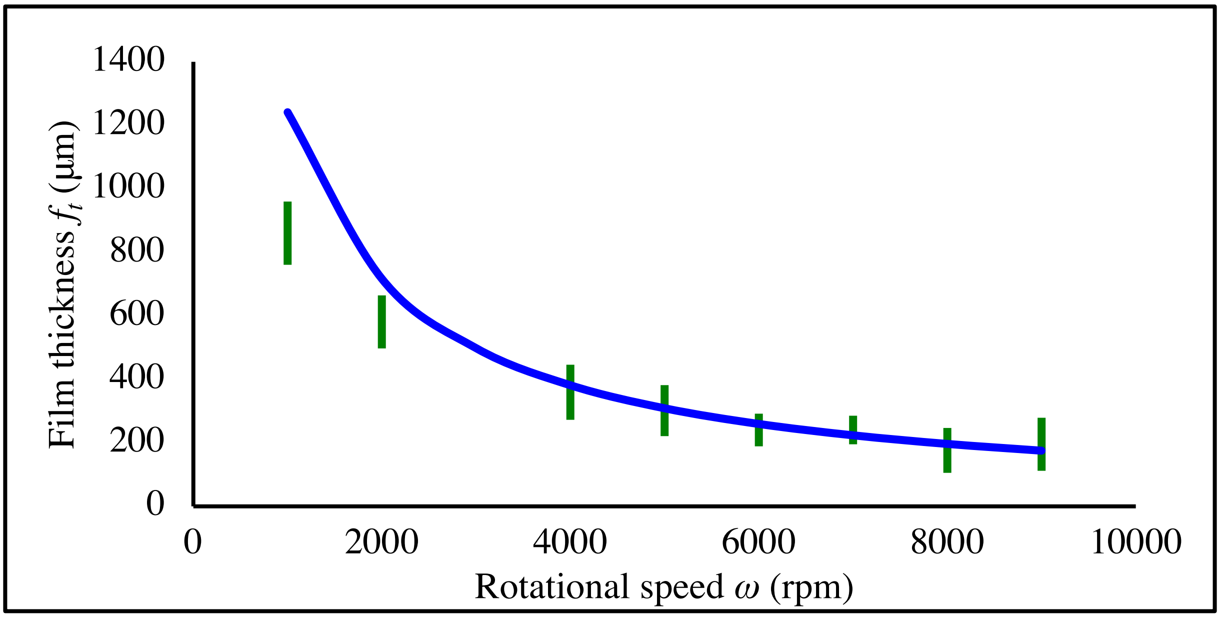

Fig. 3.6.5: Measured film thickness adjusted for imperfect rotation compared to theoretically predicted. Standard VFD, $V = 1$ mL (glycerol), $\theta = 45°$, $h = 7.5$ mm.

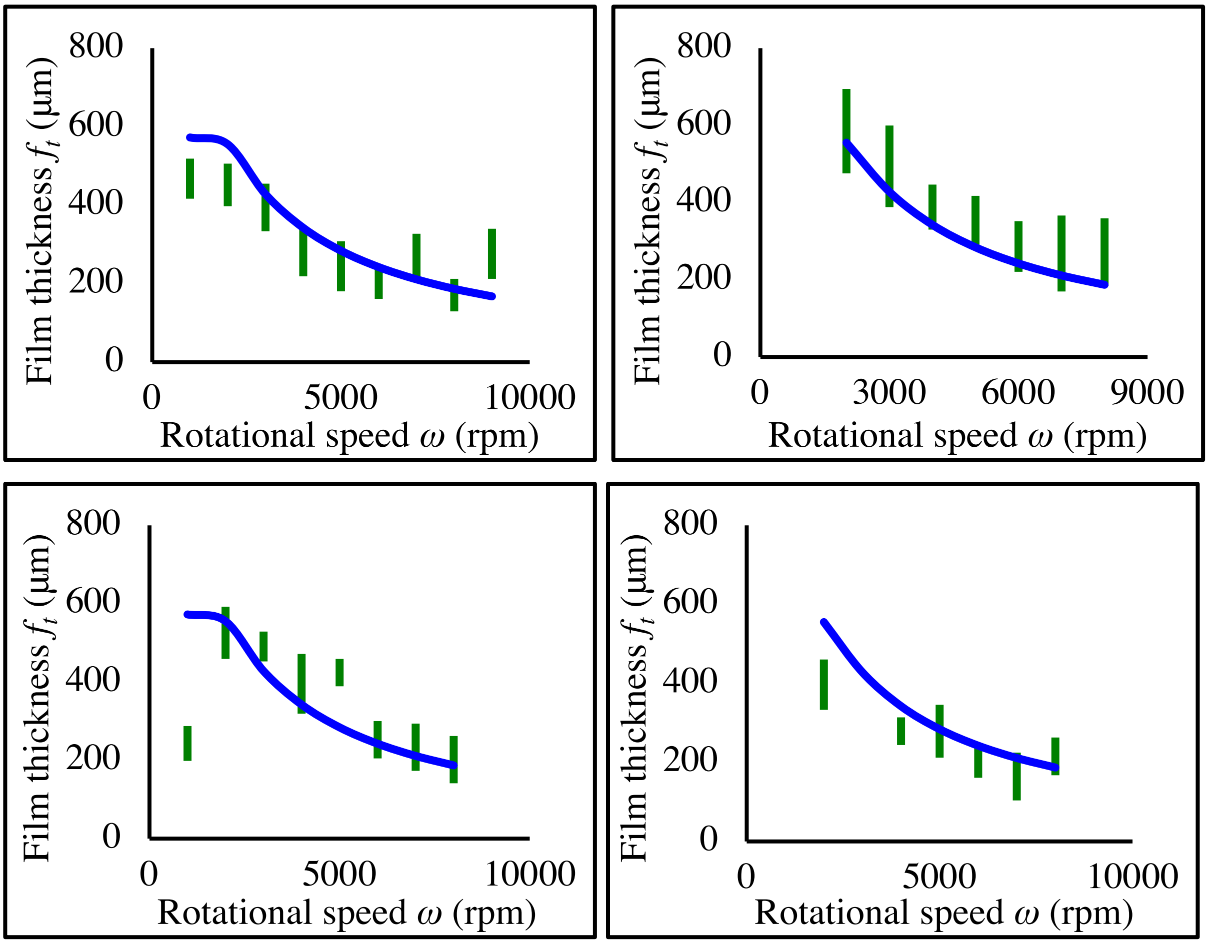

Fig. 3.6.6: Measured film thickness adjusted for imperfect rotation compared to theoretically predicted. Standard VFD, $\theta = 45°$, $h = 15.8$ mm: a) $V = 1$ mL (toluene); b) $V = 1$ mL (1:1 water:glycerol); c) $V = 1$ mL (propylene glycol); d) $V = 1$ mL (glycerol).

Consequently, it can be concluded that for the standard VFD, the average film thickness across all radial positions predicted by the model is in good agreement with the measured film thickness at the radial positions $\phi = 90°$ and $\phi = 270°$, for solvents up to a viscosity of $\nu = 4{\cdot}10^{-5}$ m^{2}s^{-1} at $\omega \geq 1000$ rpm, and for solvents up to a viscosity of $\nu = 7{\cdot}10^{-4}$ m^{2}s^{-1} at $\omega \geq 2000$ rpm. This indicates that the radial dependence of the film thickness is not as strong as predicted by the model, presumably because of the effect of viscosity, which would impede the ability of the film to produce a non-radially-uniform shape.

Measurement of the maximum film height shows predicted results being within 1 cm of the measured results for toluene, whilst for glycerol:water, propylene glycol, and glycerol, the mathematical model over predicts the film height by on average of 0.9 cm, 1.2 cm, and 1.9 cm respectively (Fig. 3.6.7). One method to take into account viscosity is to treat viscosity as affecting the effective rotational speed. The effective rotational speed ω_e can be calculated by determining the rotational speed required to achieve a certain maximum film height:

$$\omega_e = h_m\sqrt{\frac{\pi g \sin\theta}{V}}.$$

This can be used to produce a relationship between rotational speed and effective rotational speed for each solvent measured. A linear relationship shows good correlation for toluene ($\omega_e = 1.034\omega + 0.3$, $R^2 = 0.996$), glycerol:water ($\omega_e = 1.032\omega - 486$, $R^2 = 0.98$) and glycerol ($\omega_e = 0.7926\omega + 149$, $R^2 = 0.989$), but a much poorer correlation for propylene glycol ($R^2 = 0.90$). Attempts to fit the propylene glycol data using other common functions gives reasonable correlation for exponential fit ($\omega_e = 1.45.6e^{0.0002\omega} – 650$, $R^2 = 0.96$), power fit ($\omega_e = 0.017{\cdot}\omega^{1.44} + 700$, $R^2 = 0.95$), and quadratic fit ($\omega_e = 0.0002\omega^2 - 0.27\omega + 1370$, $R^2 = 0.97$), whilst for a logarithmic fit it gives a poor correlation ($\omega_e = 2354{\cdot}\ln(\omega) - 15854$, $R^2 = 0.75$).

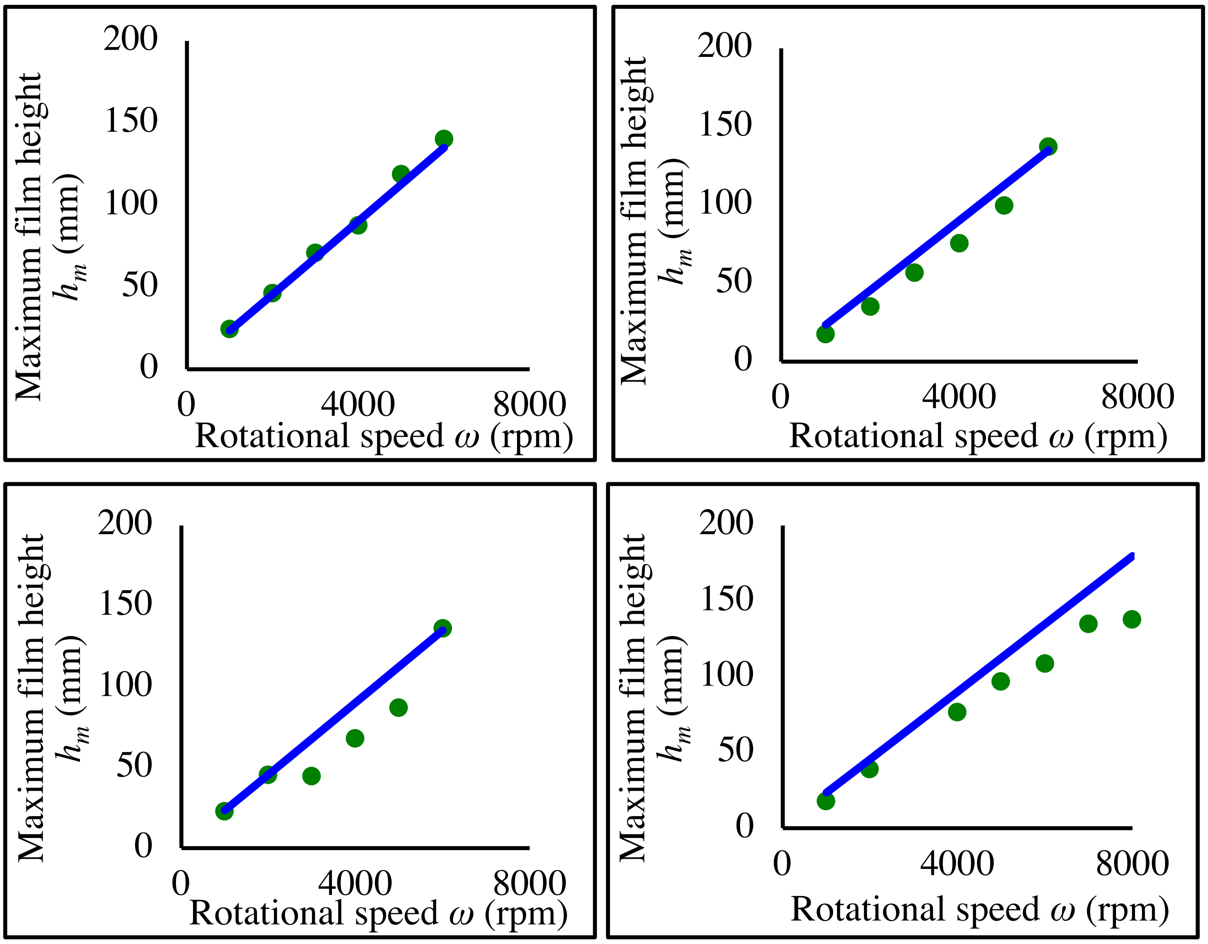

Fig. 3.6.7: Measured maximum film height compared (dots) to theoretically predicted maximum film height (lines). Standard VFD, $\theta = 45°$, h = 15.8 mm. a) $V = 1$ mL (toluene); b) $V = 1$ mL (1:1 water:glycerol); c) $V = 1$ mL (propylene glycol); d) $V = 1$ mL (glycerol).

This results in an adjusted film thickness equation of:

$$f_t = R - \sqrt{R^2 + \frac{2gh\sin\theta}{(a\omega+b)^2} - \frac{2}{(a\omega+b)}\sqrt{\frac{gV\sin\theta}{\pi}}},$$

Where a and b are experimentally determined coefficients for each solvent. Utilisation of this model for further comparison with the film thickness data results in slightly better agreement between experimental and theoretical film thicknesses for toluene and propylene glycol, but slightly worse agreement for glycerol for $\omega \geq 4000$ rpm. Consequently, it is concluded that viscosity can be taken into consideration through the experimental determination of an effective rotational speed linearly related to the actual rotational speed.

Chapter 3.7 – Effect of hydrophobic surface

Several projects involving the VFD have shown an effect caused by switching from an uncoated tube with a hydrophilic surface, to a tube coated with a hydrophobic surface. Consequently, it is of interest to compare the behaviour of water in a hydrophobic tube to in a hydrophilic tube to determine the effect of surface tension on the film shape. In order to investigate this, images were recorded for 1 mL of water in an uncoated tube and a tube coated with trichlorooctadecylsilane, at speeds from 1000 rpm to 9000 rpm in 1000 rpm increments. Additionally, images were recorded for 4 mL of water in the same tubes for 1000 rpm to 5000 rpm in 1000 rpm increments. As with the investigation into the effect of viscosity, the film thickness was measured for h = 7.5 mm and h = 15.8 mm, and $\phi = 0°$ and $\phi = 180°$. In some recorded images the film thickness was unable to be measured, for a variety of reasons. These reasons were: the film did not reach the height at which the film thickness was being measured (uncoated tube, V = 1 mL, h = 15.8 mm, ω = 1000 rpm), a timing error resulted in part of the image being acquired whilst the tube was stationary (hydrophobic tube, V = 1 mL, h = 7.5 mm and 15.8 mm, ω = 1000 rpm), and the conditions failed to produce a dry hemisphere, falling outside the scope of the mathematical model (uncoated and hydrophobic tubes, V = 4 mL, h = 7.5 mm and 15.8 mm, ω = 1000 rpm). This resulted in 98 usable film thickness measurements, with no difference in film thickness being observed between $\phi = 0°$ in comparison to $\phi = 180°$, for any of the images analysed.

Measurements of these film thicknesses determined using the method described previously show good agreement with the mathematical model for the uncoated tube for both 1 mL (Fig. 3.7.1 and 3.7.2) and 4 mL (Fig. 3.7.5 and 3.7.6), as well as good agreement for the hydrophobic tube with 4 mL (Fig. 3.7.7 and 3.7.8). However, it does not show agreement for the hydrophobic tube with 1 mL (Fig. 3.7.3 and 3.7.4), with the theoretical model consistently under predicting the film thickness. This is unsurprising because the increased contact angle between water and a hydrophobic surface would decrease the height that the liquid is able to reach, feeding liquid back down to increase the film thickness. It is interesting that this phenomenon is only detected for the lower volume, but not the greater volume. A possible explanation for this is that the feeding of liquid back down towards the base of the tube is more significant near the top of the film than near the base, and by increasing the volume, this effect is diminished for the measured points because of their proximity to the base of the tube.

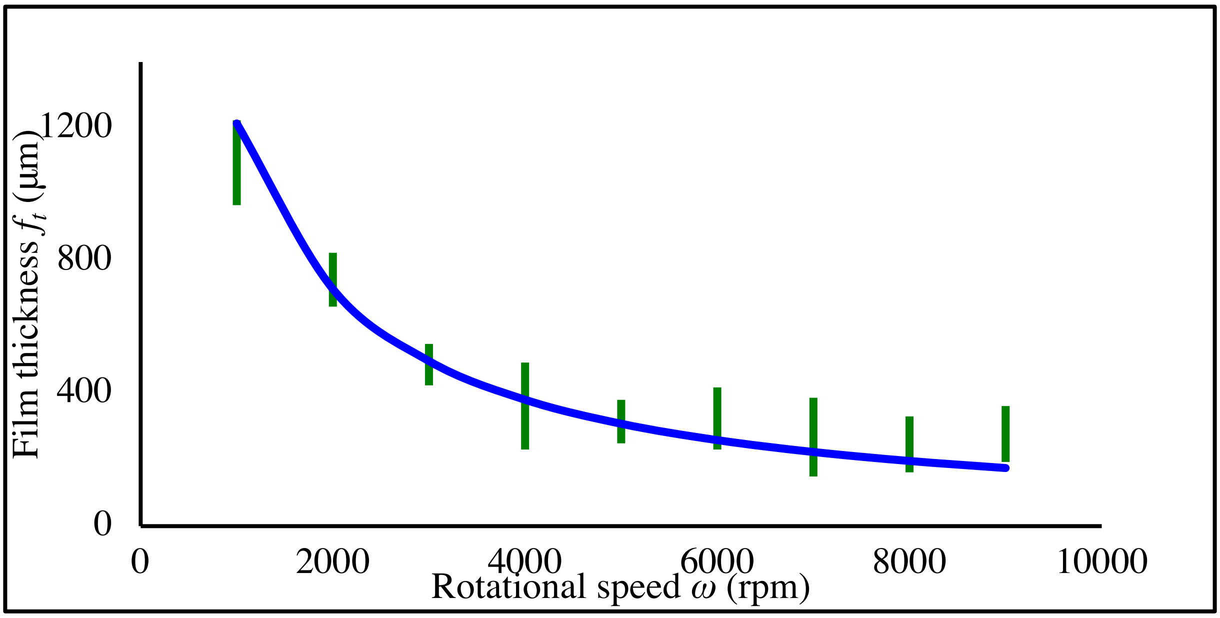

Fig. 3.7.1: Measured film thickness at $h = 7.5$ mm in an uncoated tube, adjusted for imperfect rotation compared to theoretically predicted and averaged between $\phi = 0°$ and $\phi = 180°$. Standard VFD, $V = 1$ mL (water), $\theta = 45°$.

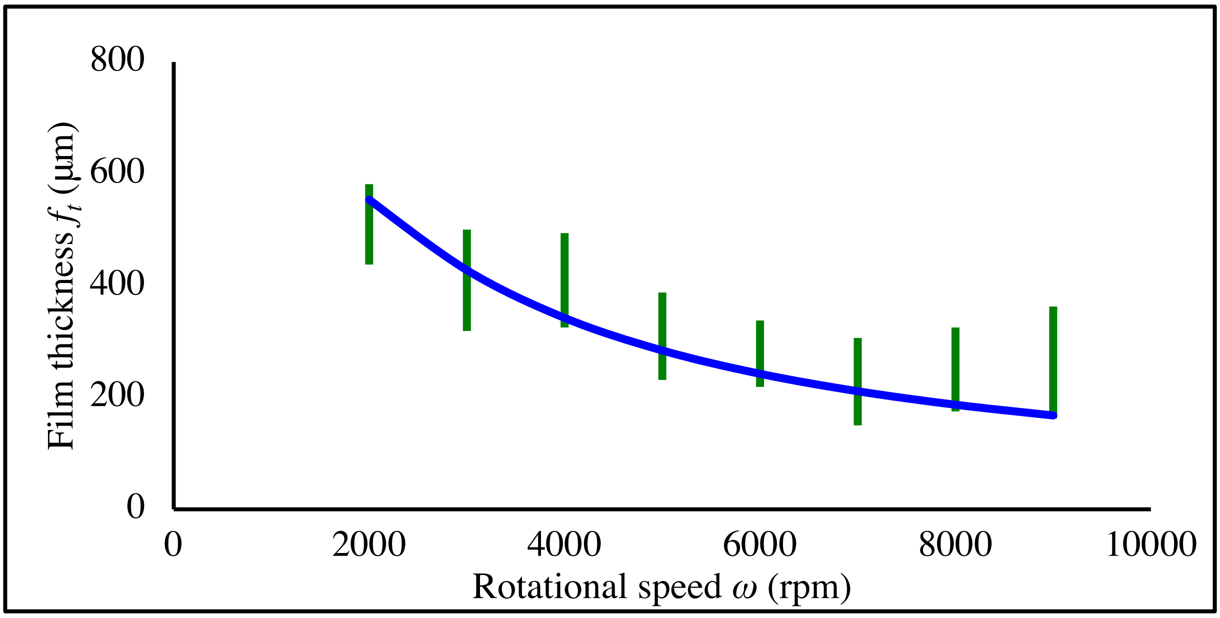

Fig. 3.7.2: Measured film thickness at $h = 15.8$ mm in an uncoated tube, adjusted for imperfect rotation compared to theoretically predicted and averaged between $\phi = 0°$ and $\phi = 180°$. Standard VFD, $V = 1$ mL (water), $\theta = 45°$.

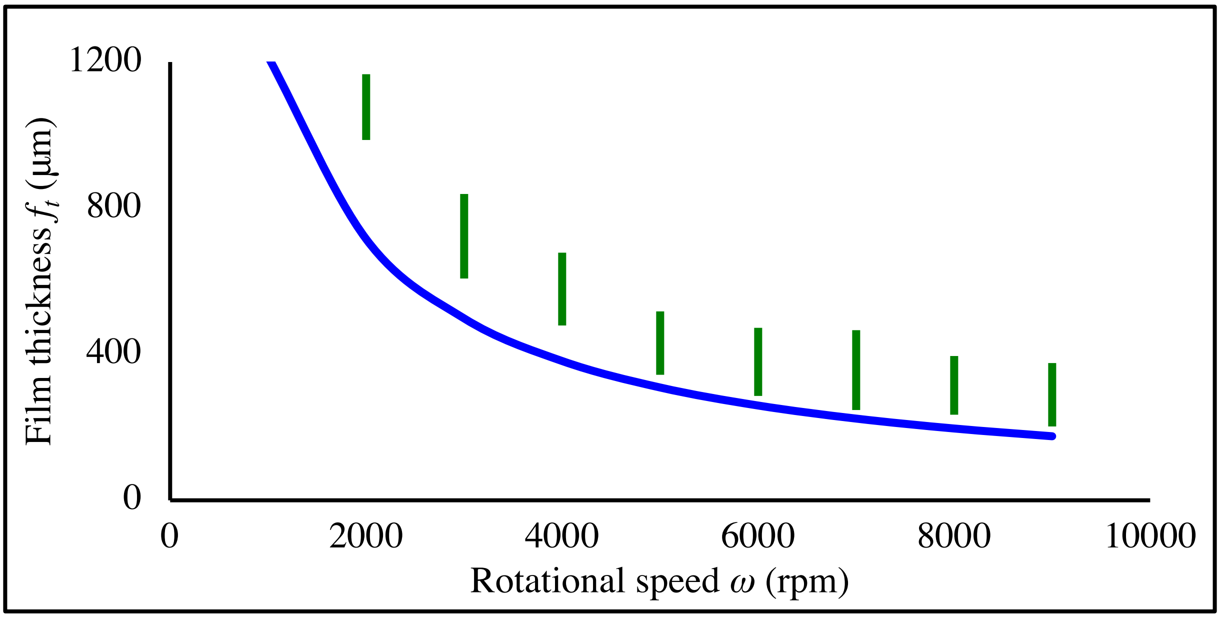

Fig. 3.7.3: Measured film thickness at $h = 7.5$ mm in a hydrophobic tube, adjusted for imperfect rotation compared to theoretically predicted and averaged between $\phi = 0°$ and $\phi = 180°$. Standard VFD, $V = 1$ mL (water), $\theta = 45°$.

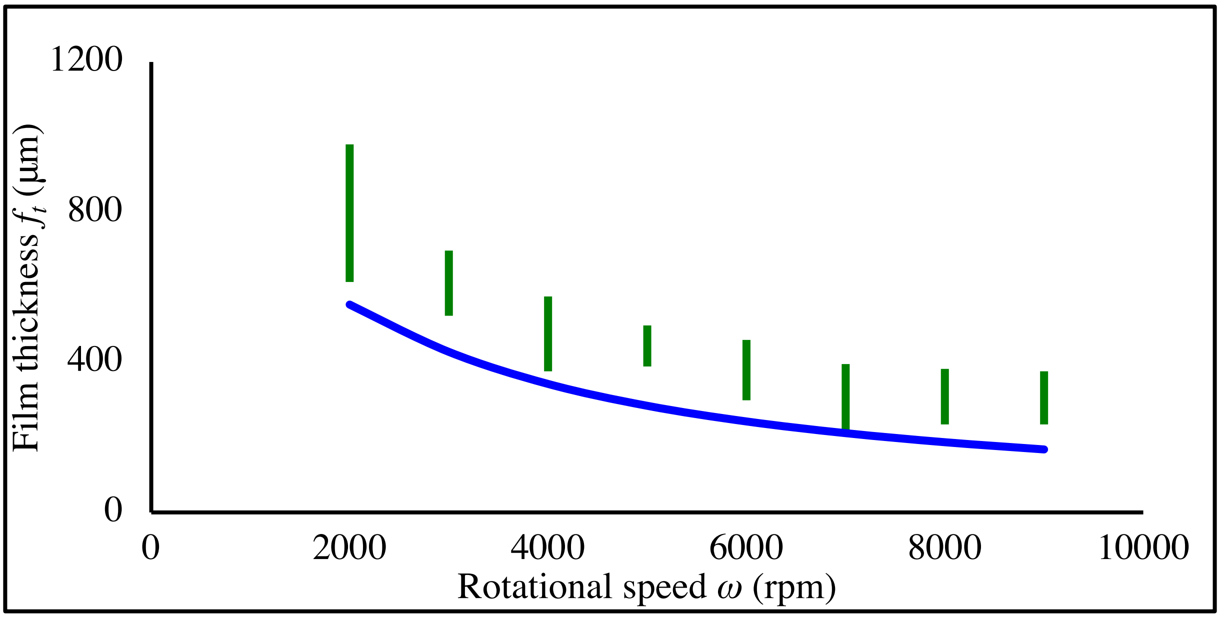

Fig. 3.7.4: Measured film thickness at $h = 15.8$ mm in a hydrophobic tube, adjusted for imperfect rotation compared to theoretically predicted and averaged between $\phi = 0°$ and $\phi = 180°$. Standard VFD, $V = 1$ mL (water), $\theta = 45°$.

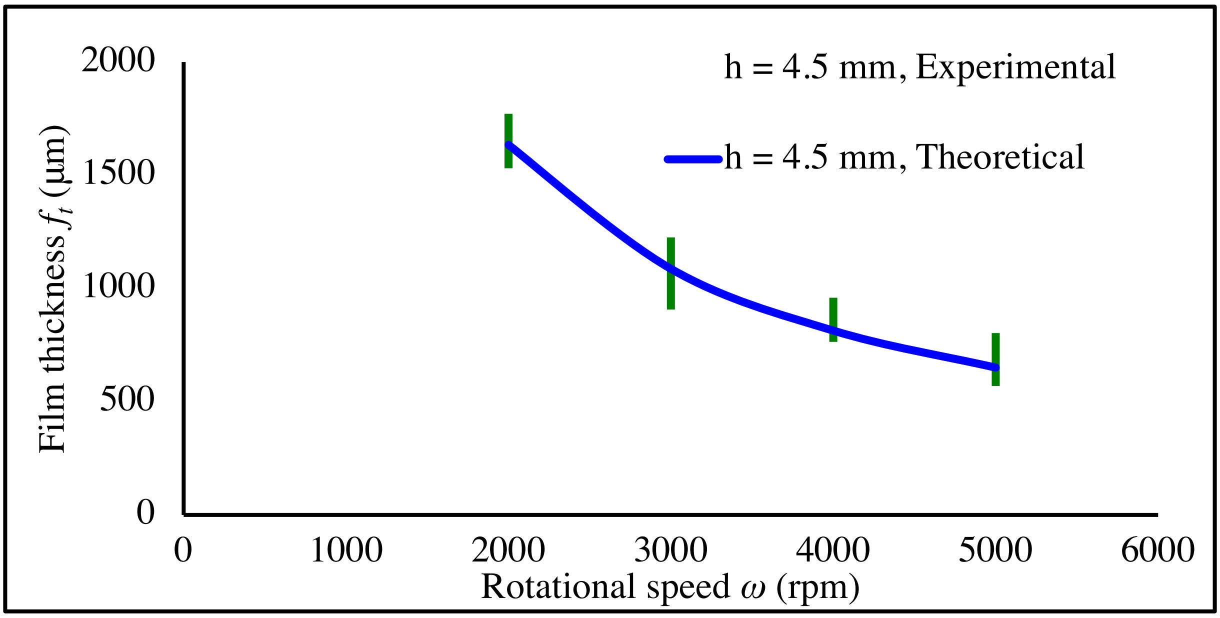

Fig. 3.7.5: Measured film thickness at h = 7.5 mm in an uncoated tube, adjusted for imperfect rotation compared to theoretically predicted and averaged between $\phi = 0°$ and $\phi = 180°$. Standard VFD, V = 4 mL (water), $\theta = 45°$.

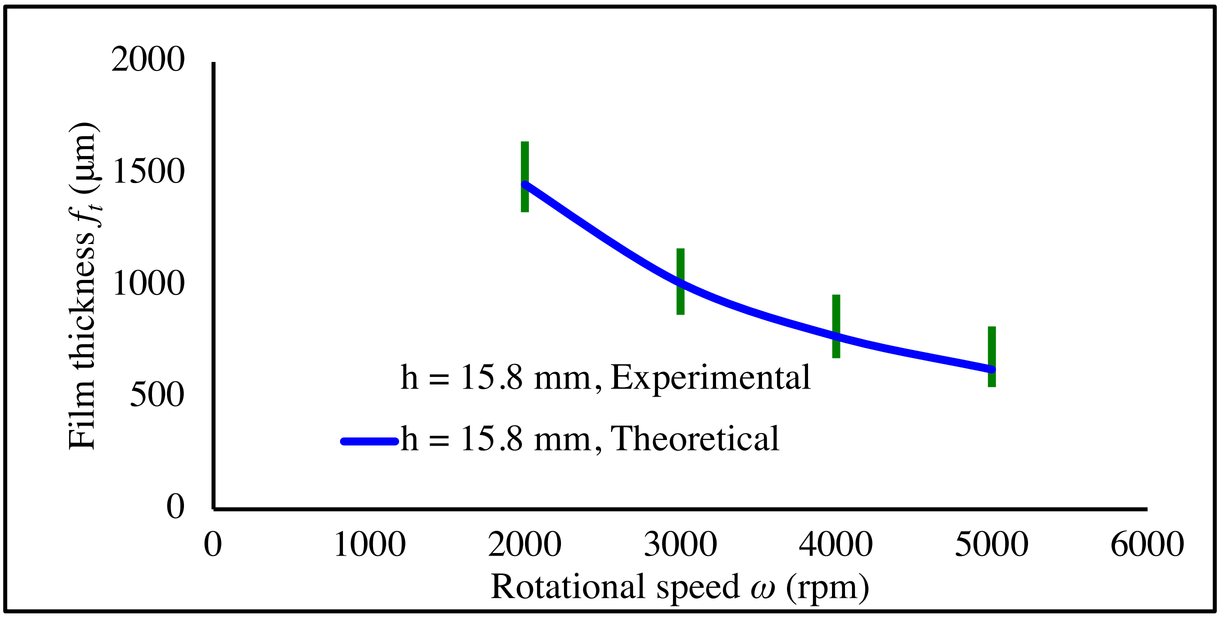

Fig. 3.7.6: Measured film thickness at h = 15.8 mm in an uncoated tube, adjusted for imperfect rotation compared to theoretically predicted and averaged between $\phi = 0°$ and $\phi = 180°$. Standard VFD, V = 4 mL (water), $\theta = 45°$.

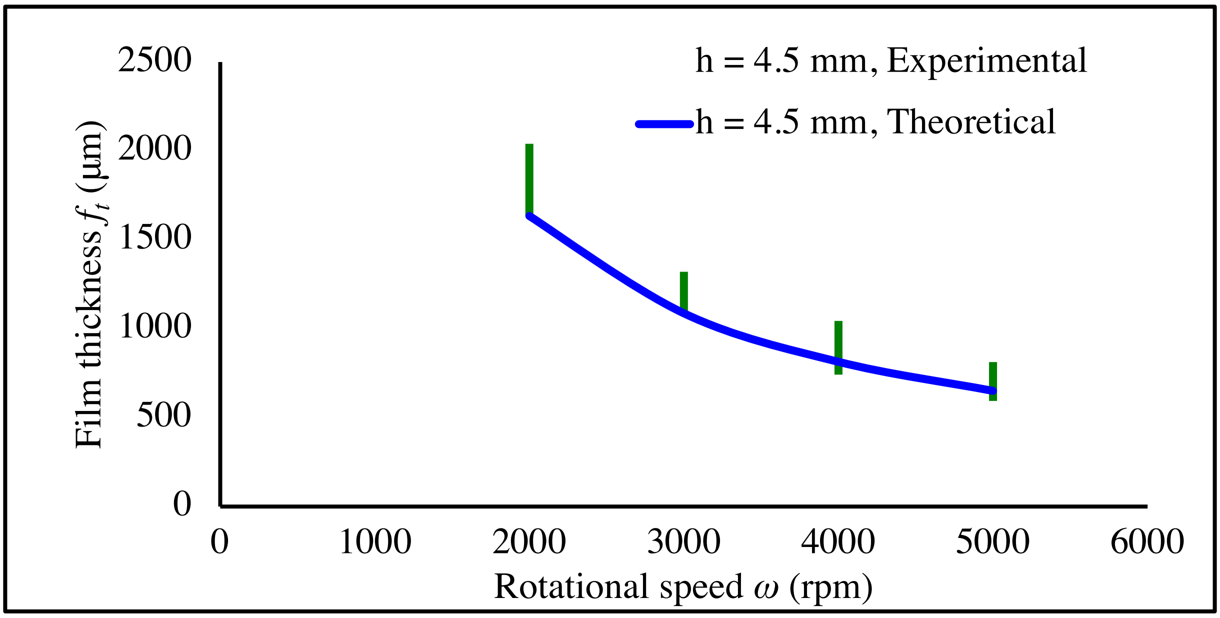

Fig. 3.7.7: Measured film thickness at $h = 7.5$ mm in a hydrophobic tube, adjusted for imperfect rotation compared to theoretically predicted and averaged between $\phi = 0°$ and $\phi = 180°$. Standard VFD, $V = 4$ mL (water), $\theta = 45°$.

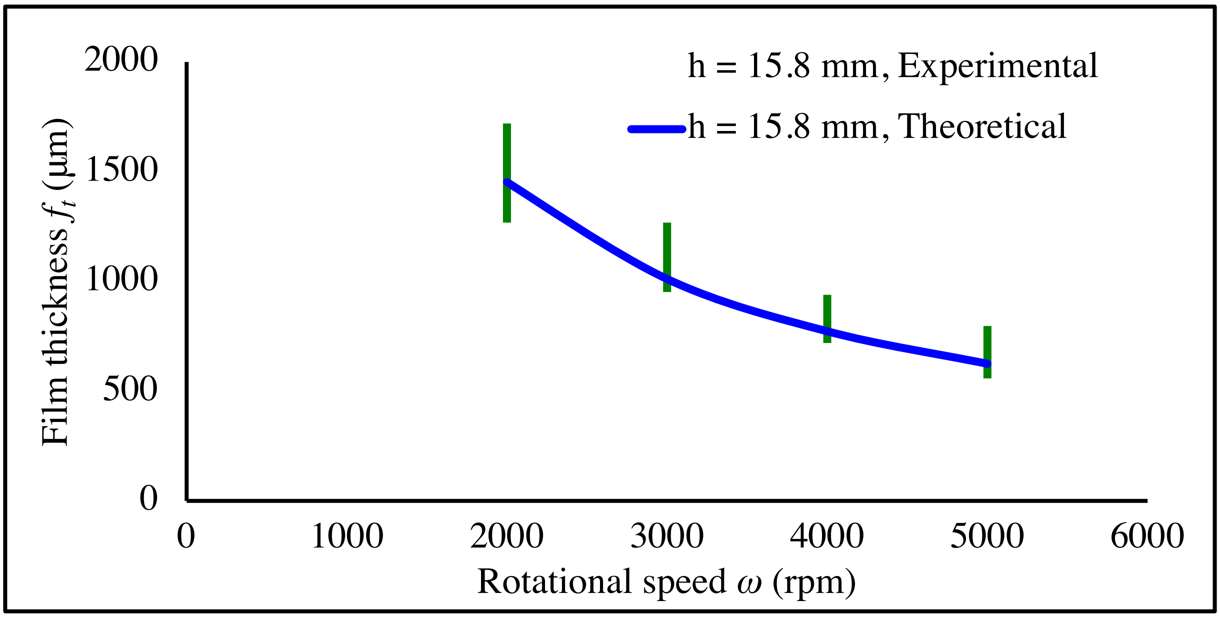

Fig. 3.7.8: Measured film thickness at $h = 15.8$ mm in a hydrophobic tube, adjusted for imperfect rotation compared to theoretically predicted and averaged between $\phi = 0°$ and $\phi = 180°$. Standard VFD, $V = 4$ mL (water), $\theta = 45°$.

Comparison of the maximum theoretical height with the measured heights reveals that for 1 mL in an uncoated tube, the results agree well with the model for low rotational speeds. However, the model tends to under predict the height for higher speeds (Fig. 3.7.9) and this is explained by the favourable surface-water interactions spreading water up the tube in order to decrease the contact angle. This effect is observed only at higher rotational speeds because the magnitude of the effect is greater there. For 4 mL in an uncoated tube, the model fits the experimental data for 2000 rpm and 3000 rpm, but over predicts it for 4000 rpm (Fig. 3.7.2b). This is unexpected and deserves further investigation. For a hydrophobic coated tube, the film does not reach as high as predicted by the model, unsurprisingly for reasons stated above (Fig. 3.7.2c and d). For 1 mL of water, the film reaches about 55% to 60% of the predicted height, whilst for 4 mL of water it reaches about 70% of the predicted height. Using the previous method to generate linear relationships between ω and ω_e gives the relationships of $\omega_e = 1.1063\omega - 92.6$ for an uncoated surface ($V = 1$ mL, $R^2 = 0.99$), $\omega_e = 0.5961\omega - 48.7$ for a hydrophobic surface ($V = 1$ mL, $R^2 = 0.998$), $\omega_e = 0.7632\,\omega + 550.3$ for an uncoated surface ($V = 4$ mL, $R^2 = 0.97$) and $\omega_e = 0.6566\omega + 124.4$ for a hydrophobic surface ($V = 4$ mL, $R^2 = 0.999$). Aside from the useful numbers this produces, it is noteworthy that the constants a and b are volume-dependent. Comparison of the newly predicted numbers gives equally good agreement for an uncoated surface for $V = 1$ mL and significantly better agreement for a hydrophobic surface for $V = 1$ mL, but significantly worse agreement for a hydrophobic tube for $V = 4$ mL. This is an interesting result because it indicates that the effect of a hydrophobic tube cannot be modelled simply by an alteration to the effective rotational speed. The finding is unsurprising given viscosity is affects the whole liquid, whilst surface tension only directly influences liquid at the surfaces. One method that may allow the adjustment of the film thickness formula to account for different surface tensions involves setting $f_t(h = h_m) \neq 0$, which would require adjustment of equation 2.10 to $V = \int_0^{2\pi}\int_{r_i}^{R} hr\,dr\,d\phi - \int_0^{2\pi}\int_{R-f_m}^{R}\big(h - h(r = R - f_m)\big)r\,dr\,d\phi$, where f_m is the minimum film thickness as a function of ϕ. The adaptation of this is left for future work.

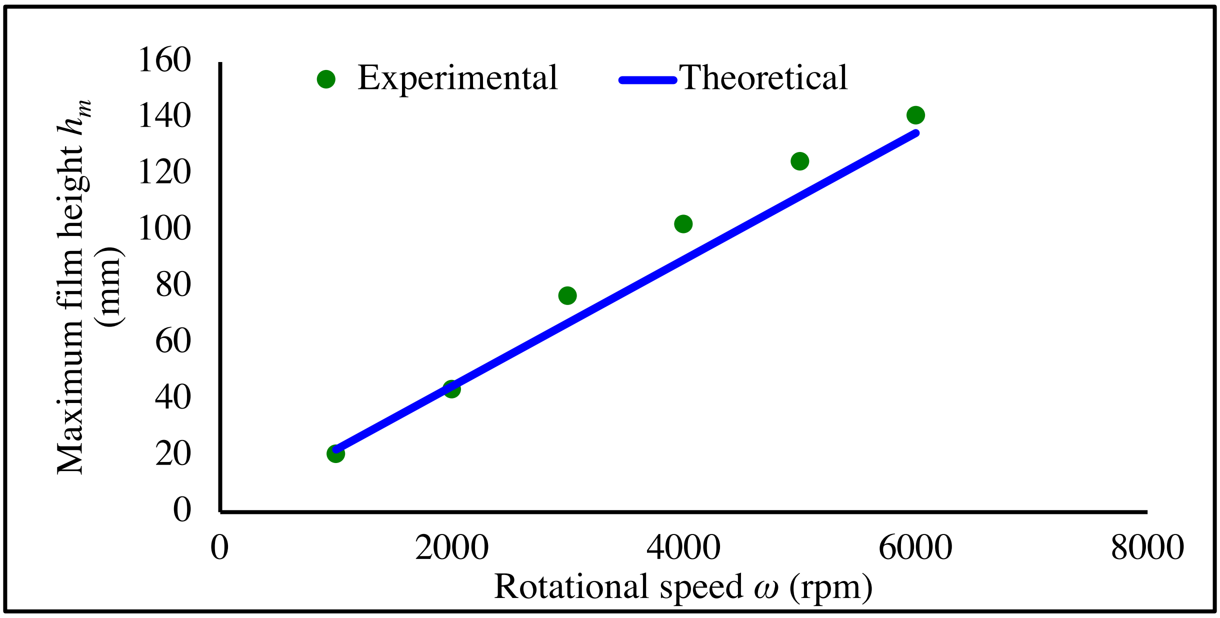

Fig. 3.7.9: Measured maximum film height h_m in an uncoated tube averaged over $\phi = 0°$ and $\phi = 180°$, compared to theoretically predicted. Standard VFD, $V = 1$ mL (water), $\theta = 45°$.

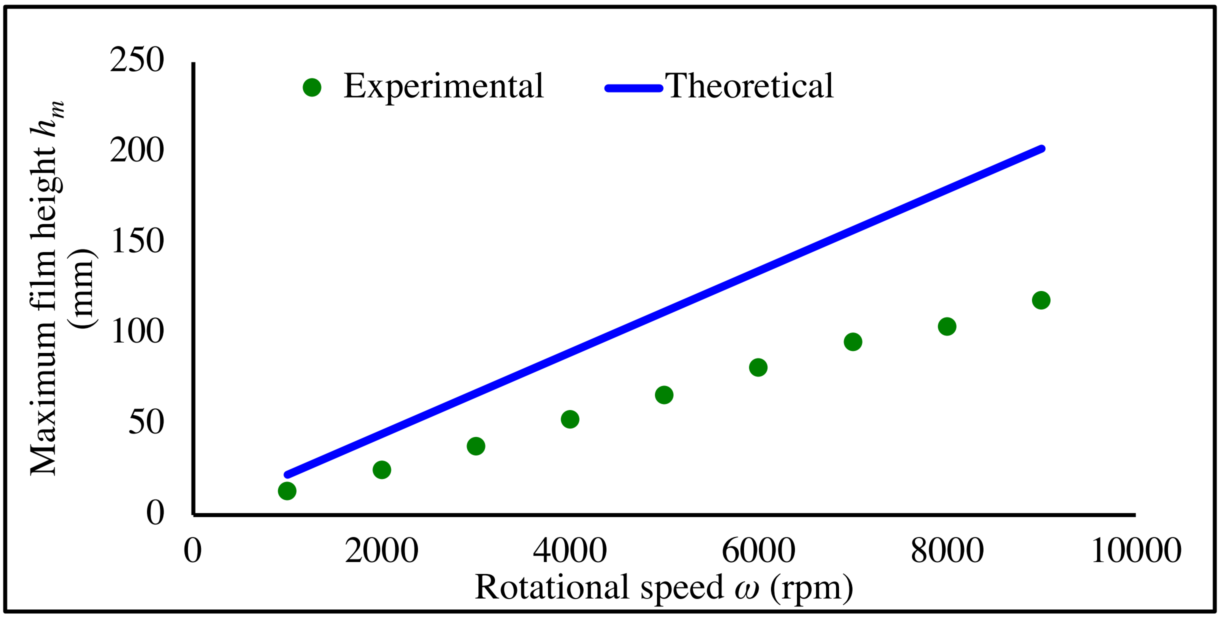

Fig. 3.7.10: Measured maximum film height h_m in a hydrophobic tube averaged over $\phi = 0°$ and $\phi = 180°$, compared to theoretically predicted. Standard VFD, $V = 1$ mL (water), $\theta = 45°$.

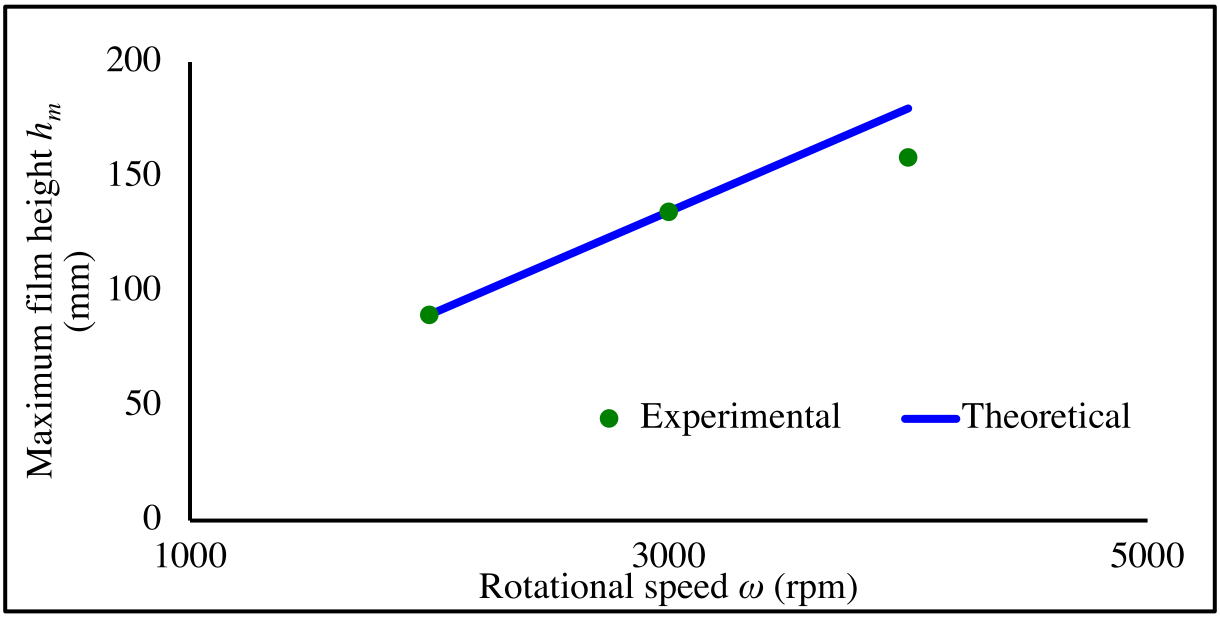

Fig. 3.7.11: Measured maximum film height h_m in an uncoated tube averaged over $\phi = 0°$ and $\phi = 180°$, compared to theoretically predicted. Standard VFD, $V = 4$ mL (water), $\theta = 45°$.

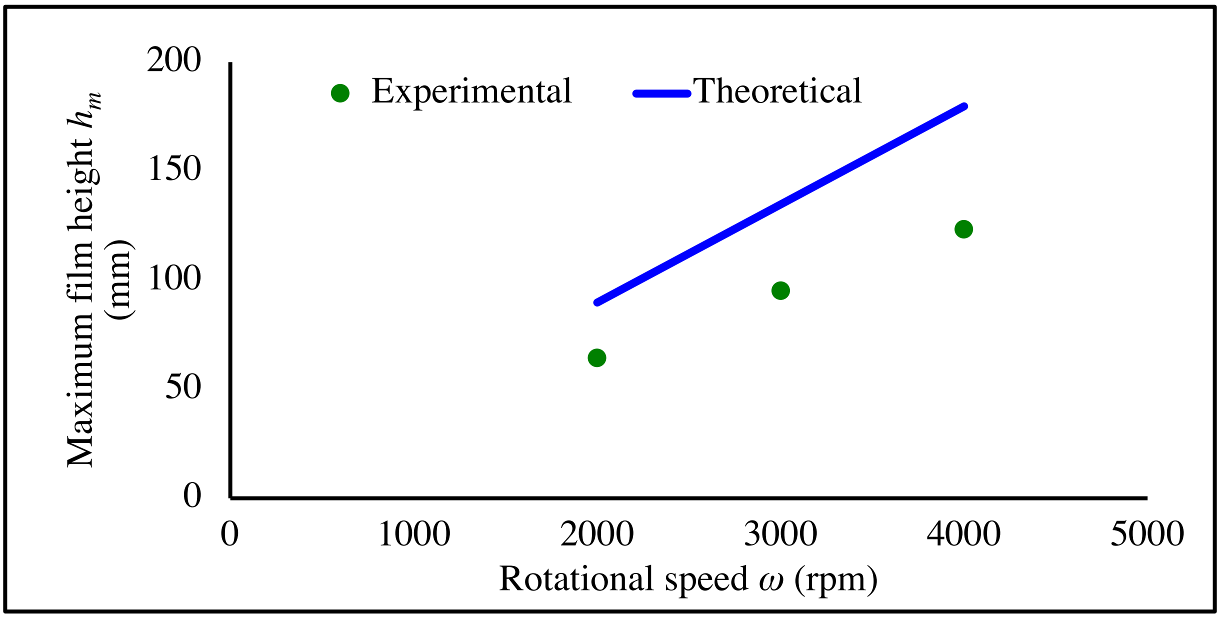

Fig. 3.7.12: Measured maximum film height h_m in a hydrophobic tube averaged over $\phi = 0°$ and $\phi = 180°$, compared to theoretically predicted. Standard VFD, $V = 4$ mL (water), $\theta = 45°$.

Further experiments that would be of interest include investigating the behaviour of other solvents in uncoated and hydrophobic coated tubes, including toluene and short-chain alcohols like methanol and ethanol. It would be particularly interesting to investigate how a hydrophobic tube used under continuous flow (with water) affects the film thickness. For this design, the flow rate would need to be low enough that the dropping of liquid droplets and their incorporation into the film occurs rarely enough to not show under the 90 s acquisition time of the camera. Performing this under high resolution may be challenging due to the necessity of setting up syringe pumps on a mobile stage. Unfortunately, it is not possible to include a real-time camera of the setup (other than the neutron camera), because light in the instrument enclosure is limited during operation to reduce noise caused by stray photons.

Chapter 3.8 – Biphasic systems

The growing interest in using the VFD for biphasic reactions makes the investigation into the arrangement of biphasic systems within the VFD important. One of the easiest biphasic systems to observe is water and toluene. Attempts to use H_2O/d_8-toluene resulted in images with no apparent separation between the two phases because the darkest liquid, H_2O, is present at all parts of the film viewable. In contrast, the D_2O/toluene system resulted in clear images (Fig. 3.8.1), however, attempts to measure the film thickness of each solvent using the previous method resulted in graphs where the interface was not easily discernible. The likely cause of this is the slight imperfections in the tube, resulting in a slightly off-axis rotation and a blurred interface. Although quantitative results cannot be obtained from the biphasic system, useful qualitative information can nonetheless be obtained. As can be seen in Fig. 3.8.1, the water lies only in the lower section of the tube, whilst the toluene forms a film on top of the water, both closer to the axis of rotation and further up the tube. It is likely that the space occupied by the 0.5 mL of water is the same space it would occupy if it were the only solvent in the tube, however, the images here are not clear enough to support or disprove this. Comparing the behaviour of the biphasic system in an uncoated tube (Fig. 3.8.1) with a hydrophobic tube (Fig. 3.8.2) indicates that the water does not reach as high in a hydrophobic tube, a result of the unfavourable water-surface interactions working to reduce their contact area. Additionally, it appears that the amount of toluene lying on the surface of the water is minimal. Another interesting observation is that the contact angle at the base in the hydrophobic tube is noticeable.

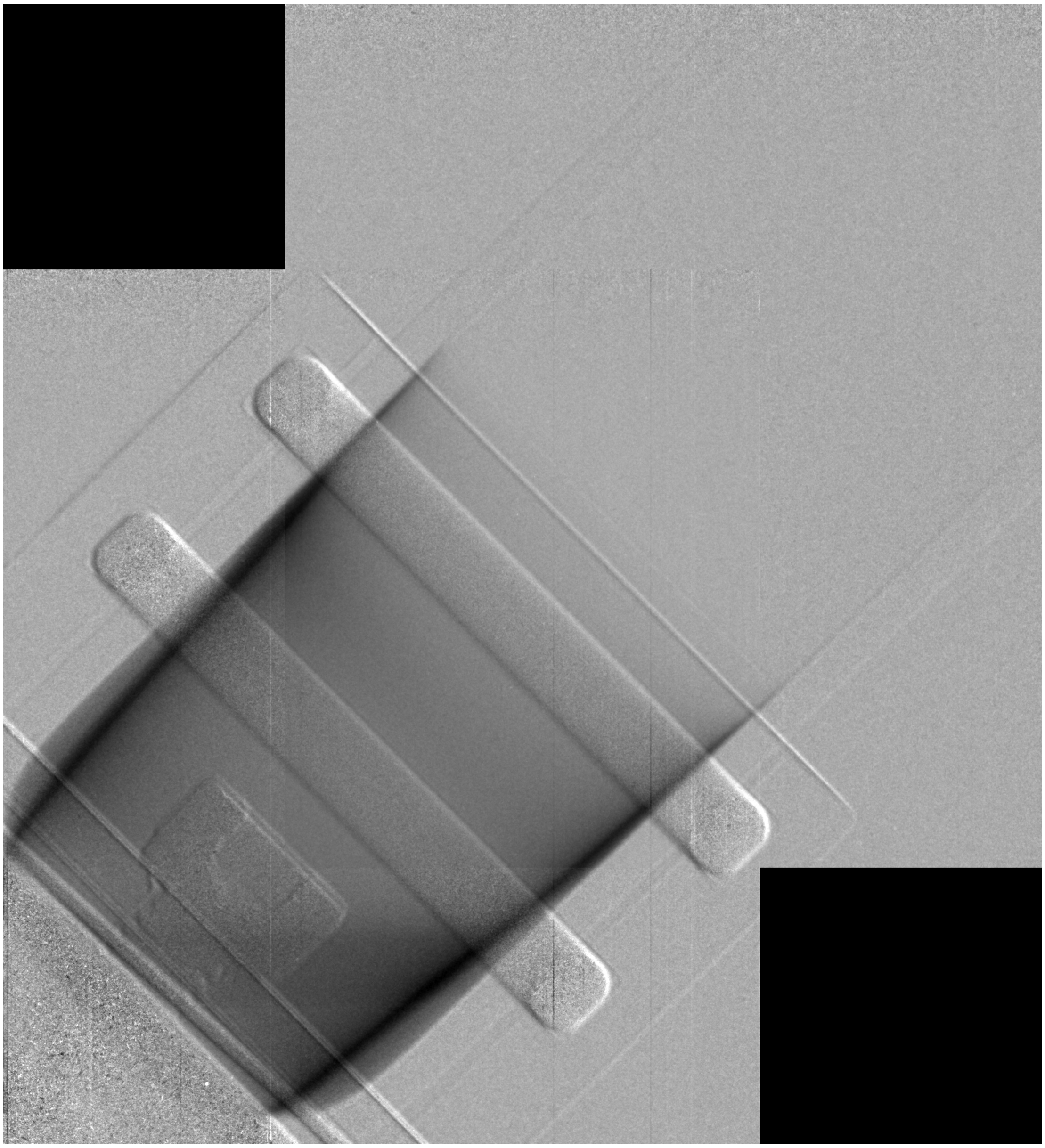

Fig. 3.8.1: Standard VFD. $V = 1$ mL (0.5 mL toluene + 0.5 mL D_2O), $\omega = 1000$ rpm, uncoated tube.

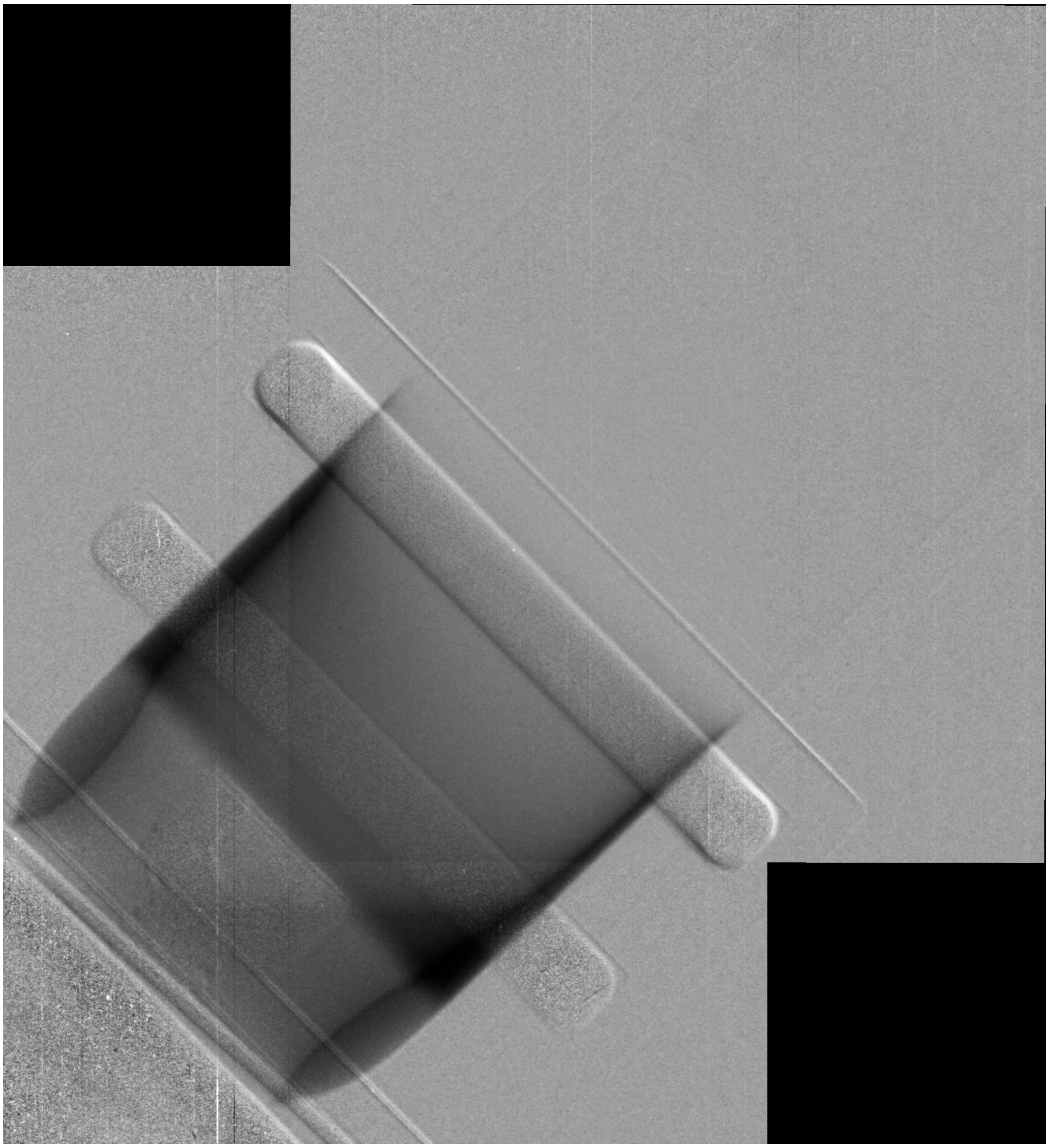

Fig. 3.8.2: Standard VFD. $V = 1$ mL (0.5 mL toluene + 0.5 mL D_2O), $\omega = 1000$ rpm, hydrophobic tube.

It may be possible to obtain more useful information from biphasic systems under neutron imaging by extending the acquisition time. Additionally, in order to obtain usable images, the densest liquid must have the lowest neutron absorption cross-section. For liquids consisting solely of hydrogen, oxygen-16, and carbon, this is easily arranged by using the deuterated form of the densest liquid. However, the absorption cross-sections of nitrogen-14 and chlorine-35 are significantly higher than hydrogen-1, causing complications attempting to view systems where the denser liquid contains one of these isotopes. The use of solvents with nitrogen-15 or chlorine-37 would enable the viewing of these difficult biphasic systems, however isotopically enriched solvents are expensive, particularly so in this instance because the isotopically enriched solvent would also need to be deuterated. An alternative would be to use an additive to the less dense solvent, however the addition of a compound with a high absorption cross section may be technically challenging, and may result in a highly radioactive sample, resulting in long periods of time between experiments in order to safely handle the activated sample. If the use of biphasic processing conditions in the VFD is continued, which it should be given it is one of the major advantages of the VFD, the ability to obtain useful information through neutron imaging should be investigated further.

For future experiments, it would be of interest to alter the VFD to reduce imperfections in the surface of the tube and to increase the precision of the axis of rotation. Until this is done, there is minimal benefit to increasing the resolution of the images. Additionally, few neutron imaging stations around the world are capable of comparable resolution, with only six beamlines providing resolution < 50 μm: ICON (Villigen, Switzerland), NEUTRA (Villigen, Switzerland), ANTARES (Munich, Germany), CONRAD (Berlin, Germany), NIF (NIST, USA), and DINGO (Sydney, Australia). Out of these instruments, the only instruments to have achieved a pixel size <10 μm are ICON and NEUTRA at the Paul Scherrer Institut, which is not accepting new proposals until early 2020 after the completion of an upgrade program.[11] The other option is ODIN, the new imaging facility at the European Spallation Source that is expected to become operational in 2019.

Chapter 3.9 – References

1 Bilheux, H., McGreevey, R., Anderson, I. *Neutron Imaging and Applications*. (Springer, 2009).

2 Squires, G. L. *Introduction to the Theory of Thermal Neutron Scattering*. 3 edn, (Cambridge University Press, 2012).

3 Lehmann, E. H., Vontobel, P., Frei, G. & Brönnimann, C. Neutron imaging—detector options and practical results. *Nuclear Instruments and Methods in Physics Research Section A: Accelerators, Spectrometers, Detectors and Associated Equipment* **531**, 228-237, (2004).

4 Morgano, M. *et al.* Unlocking high spatial resolution in neutron imaging through an add-on fibre optics taper. *Opt. Express* **26**, 1809-1816, (2018).

5 Garbe, U. *et al.* Industrial Application Experiments on the Neutron Imaging Instrument DINGO. *Physics Procedia* **88**, 13-18, (2017).

6 Garbe, U. *et al.* A New Neutron Radiography / Tomography / Imaging Station DINGO at OPAL. *Physics Procedia* **69**, 27-32, (2015).

7 Klose, F., Constantine, P., J Kennedy, S. & A Robinson, R. *The Neutron Beam Expansion Program at the Bragg Institute*. Vol. 528 012026 (2014).

8 Gonçalves, F. A., Hamano, K., Sengers, J. V. & Kestin, J. Viscosity of liquid toluene in the temperature range 25–75°C. *International Journal of Thermophysics* **8**, 641-647, (1987).

9 Shankar, P. N. K., Manoj;. Experimental determination of the kinematic viscosity of glycerol-water mixtures. *Proceedings of the Royal Society of London. Series A: Mathematical and Physical Sciences* **444**, 573, (1994).

10 Bajić, D. M. *et al.* Densities, viscosities, and refractive indices of the binary systems (PEG200+1,2-propanediol, +1,3-propanediol) and (PEG400+1,2-propanediol, +1,3-propanediol) at (288.15 to 333.15)K and atmospheric pressure: Measurements and modeling. *The Journal of Chemical Thermodynamics* **57**, 510-529, (2013).

11 Institut, P. S. *Call for Proposals | Paul Scherrer Institut (PSI)*, <https://www.psi.ch/sinq/call-for-proposals>.4/11/2018

Chapter 4

Small Angle Neutron Scattering (SANS)

In situ analysis of systems within the Vortex Fluidic Device (VFD) is wrought with challenges because the most useful and widely available analytical techniques are incompatible with *in situ* analysis. The only techniques adapted for *in situ* analysis within the VFD thus far are UV-Vis spectroscopy, fluorescence spectroscopy, and neutron imaging. The first two provide information about the molecular composition of the film, whilst the third can only give information down to the 100 μm scale and is unable to investigate the internal behaviour of the liquid. The possibility of inserting various probes down the centre of the VFD tube has oft been suggested, however, there is large uncertainty about the impact this would have on the air flow within the VFD, and whether this in turn would interfere with the fluid behaviour. If the insertion of probes within the VFD significantly affects the fluid behaviour, then any data obtained from inserted probes would have limited usefulness until those effects are better understood. In order to partially fill this gap in analytical scale, Small Angle Neutron Scattering (SANS) has been used here to investigate the *in situ* effect of the VFD on macromolecular structures on the scale of 10-100 nm. The aim here was to determine if structures within the thin film can be successfully detected using SANS, using Pluronic P-123 micelles as a model.

Chapter 4.1 – Small Angle Neutron Scattering (SANS) theory

A consequence of quantum mechanics is that matter typically treated classically as particles (such as protons, neutrons, and electrons), can also be described as waves and can exhibit behaviour typical of waves. One of these behaviours is diffraction, which results in scattering at small angles. The diffraction of neutrons by atomic nuclei occurs when a neutron with momentum **k** travelling towards a nucleus interacts with the nucleus, and experiences a change in momentum **q**, scattering at an angle 2θ (Fig. 4.1.1). This change in momentum **q** can be calculated from **k** and θ (and hence from the neutron wavelength λ and θ) through

$$q = |\boldsymbol{q}| = 2|\boldsymbol{k}|\sin\theta = \frac{4\pi}{\lambda}\sin\theta,$$

where q is the magnitude of the change in momentum.[a] The extent to which a specific nucleus scatters neutrons away from itself is called its scattering length, and is given in units of angstroms. It is usually more convenient to talk about scattering length per volume, termed scattering length density (SLD) ρ, given in units of Å^{-2}.

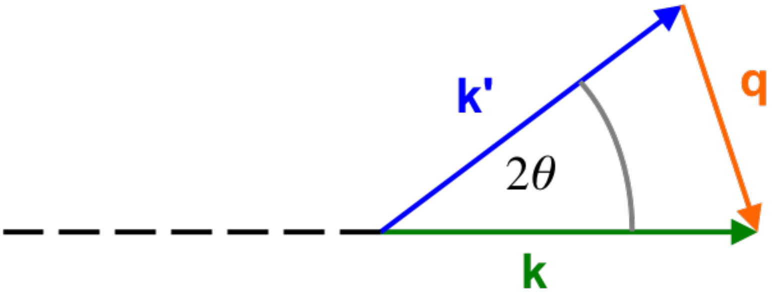

Fig. 4.1.1: Small Angle Neutron Scattering occurs when an incident neutron beam (black) interacts with a sample scatters with a vector **k'** (blue) compared to its original vector **k** (green), with a scattering vector of **q** (orange). **q** is related to the scattering angle *2θ* through the equation $q = 2k\sin\theta = \frac{4\pi}{\lambda}\sin\theta$, where λ is the wavelength of the incident neutron beam.

This scattering has two components, coherent scattering, and incoherent scattering. Coherent scattering is the result of interference between scattering waves from different nuclei, whilst incoherent scattering is the result of scattering waves that do not interfere with waves from other nuclei. Coherent scattering is strongly q dependent, and provides structural information about the system, whilst incoherent scattering is neither q dependent nor provides structural

---

[a] It is common to see Q used in place of q in the literature. Some articles also present scattering patterns in terms of k instead of q.

information about the system. The coherent scattering intensity I(q) for a monodisperse system of particles is described by

$$I(q) = (\Delta\rho)^2 \cdot P(q) \cdot S(q),^{b}$$

where m is the number of scatterers, $\Delta\rho$ is the difference in scattering length density of the solvent and the particles, $P(q)$ is the particle form factor describing the shape of the particles, and $S(q)$ is the structure factor describing the interactions between the particles. P(q) tends to 1 at low q, whilst S(q) tends to 1 at high q or at low concentration.[1]

The ability of neutrons to easily penetrate the electron cloud and the significant differences in attenuation ability between elements and isotopes with similar atomic masses makes neutrons a useful and unique probe for investigating a variety of systems.[2-4] Structures with a size range of 1 nm to 100 nm can be investigated using small angle neutron scattering (SANS), whilst structures with a size range of 100 nm to 1000 nm can be investigated using ultra-small angle neutron scattering (USANS). Analysis of SANS data typically involves the development of a model which fits the observed scattering pattern. SANS data is commonly plotted either on a standard linear-linear scale,[1,5] or on a logarithmic-logarithmic scale.[6,7] For ease of comparison with literature, both types of plots are presented here.

---

[b] This equation is often written as $I(q) = N \cdot (\Delta\rho)^2 \cdot P(q) \cdot S(q)$ when the data is presented after the intensity is normalised to a standard.

Chapter 4.2 – SANS Methodology and background experiments

The SANS experiments presented here were performed on the QUOKKA beamline (Fig. 4.2.1) at the Open-Pool Australian Lightwater (OPAL) Reactor at the Australian Nuclear Science and Technology Organisation (ANSTO) in Lucas Heights, New South Wales, Australia.[8] The VFD was attached to the sample stage using clamps and was aligned with the neutron beam such that there was a 5 mm space between the top of the VFD tube holder and the bottom of the neutron beam. This positioning corresponds to a neutron beam height of 35 mm from the base of the VFD tube. The usual borosilicate glass tubes were replaced with quartz tubes due to the high absorption of neutrons by boron, and the usual polycarbonate safety shield was replaced with an aluminium shield in order to reduce the background noise caused by incoherent scattering.[9] The neutron wavelength used was 5 Å with a resolution of 0.1 Å. Experiments were performed with a detector distance of 20 m and q range of 0.000158 Å to 0.042928 Å in increments of 0.000317 Å. Transmission experiments were performed to produce scattering patterns independent of the flux of the neutron beam. Ordinarily the data would also be divided by the film thickness to give data independent of the path length, however, this requires knowledge of the film thickness to a precision of 1%. Although the film thickness can be predicted to a precision of 1% using the mathematical model described in Chapter 2, the reliability of the model to a precision of 1% has not been demonstrated.

Scattering patterns of the beam without a sample (Fig. 4.2.2), the aluminium shield (Fig. 4.2.3), quartz VFD tube (Fig. 4.2.4), and aluminium shield with quartz tube (Fig. 4.2.5) were recorded at low q. The very low intensity at very low q is caused by the beam stop blocking the beam from reaching the detectors, preventing the collection of data at very small angles. This is followed by an increase at the start of the actual scattering, followed by a gradual decrease at higher q. As can be seen in the scattering patterns, neither the quartz tube nor the aluminium shield significantly affect the scattering pattern. Consequently, it should be possible to successfully perform *in situ* SANS in the VFD.

Fig. 4.2.1: The small angle neutron scattering instruments QUOKKA (grey) and BILBY (red).[10]

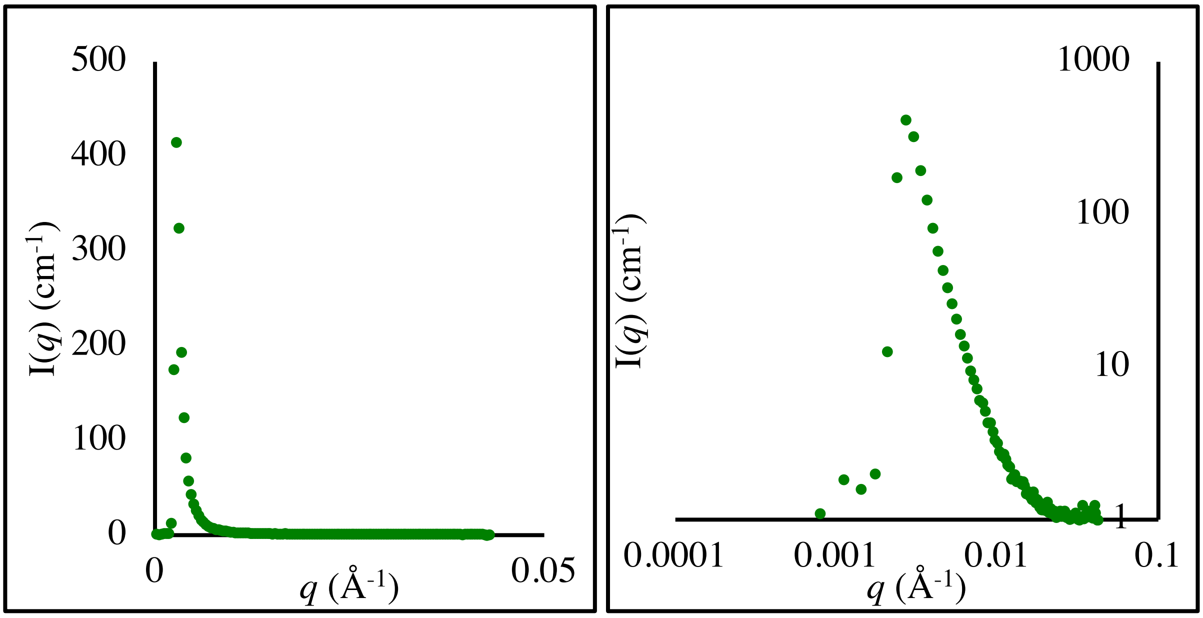

Fig. 4.2.2: Small Angle Neutron Scattering: Background of QUOKKA (neutron beam with no tube or VFD shield) shown as a linear-linear plot (left) and a logarithmic-logarithmic plot (right).

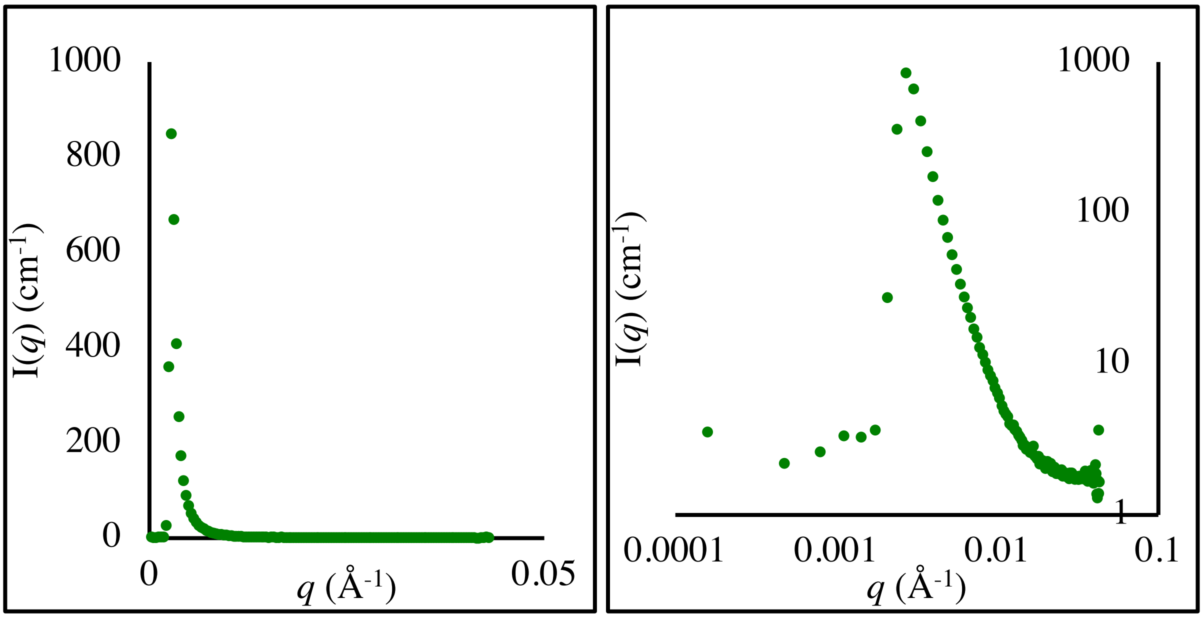

Fig. 4.2.3: Small Angle Neutron Scattering: Vortex Fluidic Device aluminium shield shown as a linear-linear plot (left) and a logarithmic-logarithmic plot (right).

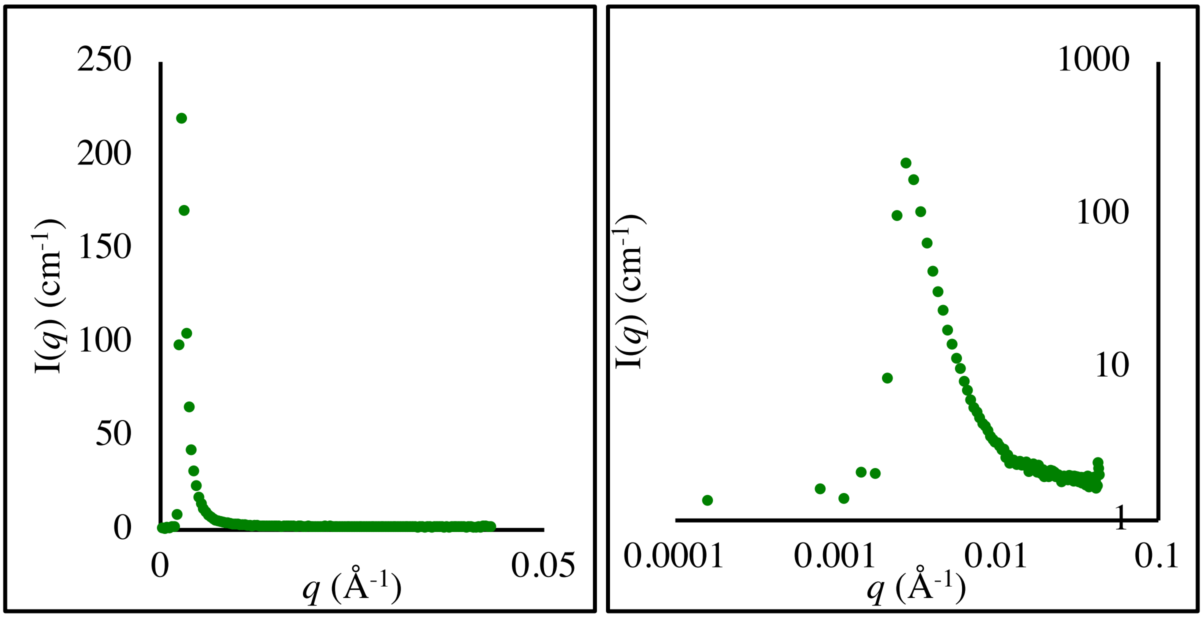

Fig. 4.2.4: Small Angle Neutron Scattering: Vortex Fluidic Device quartz tube (shown as a linear-linear plot (left) and a logarithmic-logarithmic plot (right).

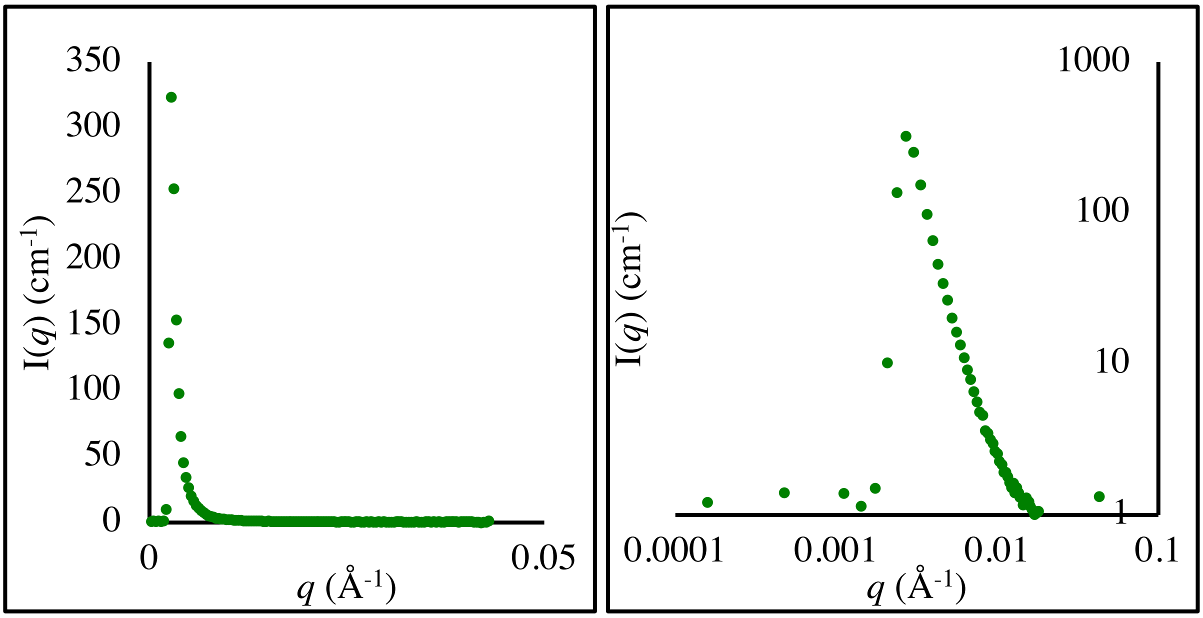

Fig. 4.2.5: Small Angle Neutron Scattering: Vortex Fluidic Device aluminium shield with quartz tube, spinning at $\omega = 2000$ rpm (shown as a linear-linear plot (left) and a logarithmic-logarithmic plot (right).

Chapter 4.3 – SANS of Pluronic P-123 Micelles

The establishment that neither the quartz tube nor the aluminium shield produced a significant scattering pattern allowed the investigation of the scattering pattern produced by samples. Block copolymers of poly(ethylene oxide) (PEO) and poly(propylene oxide) (PPO) form micelles when the concentration and temperature are above the critical micelle concentration and critical micelle temperature.[1,5-7,9] These micelles usually take the form of a spherical hydrophobic core containing PPO surrounded by a hydrophilic shell containing PEO, and scattering patterns are simple, easily modelled, and well understood. Although the assumption of complete segregation of the PPO and PEO chains is not precisely accurate, the presence of some PPO chains in the shell and some PEO chains in the core does not generally affect the scattering pattern due to the similar scattering length densities and mass densities of the two chains.[1,5]

A 5% w/w solution of Pluronic P123 ($PEO_{20}PPO_{70}PEO_{20}$) was prepared in D_2O, and scattering patterns were obtained for 1 mL of liquid in the VFD at a tilt angle of 45° and operating at 3000 rpm, 5000 rpm and 7000 rpm. Fig. 4.3.1 shows the scattering pattern for Pluronic P123 at 3000 rpm, 5000 rpm, and 7000 rpm, with the empty tube + shield measurement subtracted from the presented data. Data points for $q < 0.005$ are not considered in the analysis because of interference from the beam stop ($q < 0.0025$) and the high background at low q ($0.0025 < q < 0.005$), whilst, data points for $q > 0.0417$ are not considered because the error bars for the measurements are relatively high (> 3%). Given that the datasets for 3000 rpm, 5000 rpm and 7000 rpm are almost identical, only the analysis for $\omega = 3000$ rpm is presented here, whilst the analyses for $\omega = 5000$ rpm and $\omega = 7000$ rpm are presented in Appendix C.

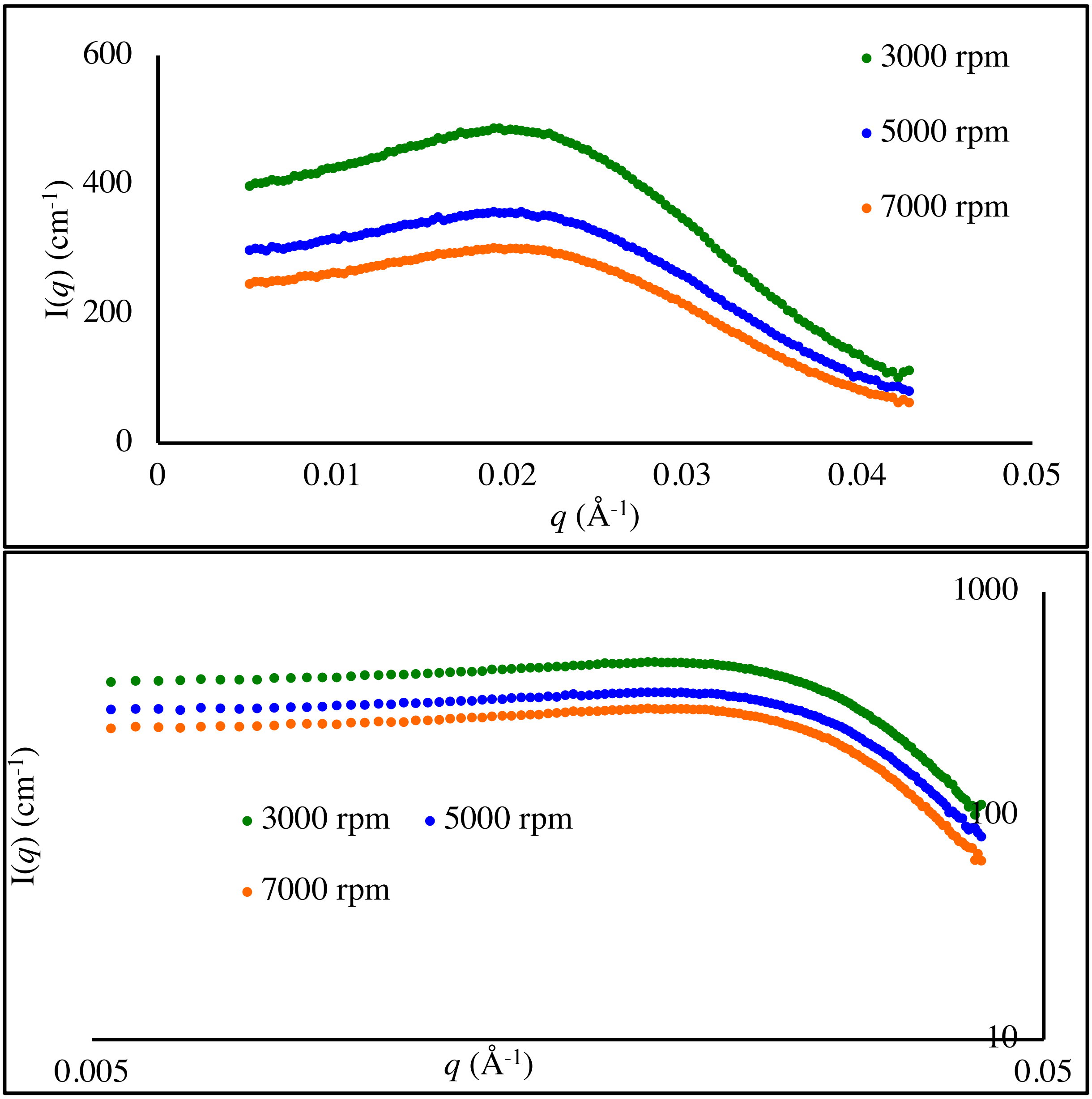

Fig. 4.3.1: SANS of 5% w/w Pluronic P123 in D_2O in the VFD at rotational speeds of 3000 rpm, 5000 rpm and 7000 rpm, with SANS data of Empty tube and VFD aluminium shield subtracted, presented as a linear-linear plot (top) and a logarithmic-logarithmic plot (bottom).

The broad curve observed over the q-range is caused by scattering from the micelles. The form factor $P(q)$ and structure factor $S(q)$ equations for a spherical micellar system are

$$P(q) \cdot (\Delta\rho)^2 = \left[\frac{4\pi}{3} R_c^3 (\rho_c - \rho_s) \frac{3(\sin(qR_c) - qR_c \cos(qR_c))}{(qR_c)^3} + \frac{4\pi}{3} R_S^3 (\rho_s - \rho_{solv}) \frac{3(\sin(qR_S) - qR_S \cos(qR_S))}{(qR_S)^3}\right]^2,$$

and

$$S(q) = \frac{1}{1 + \frac{12\phi G}{qR_S}},$$

where ϕ and G are

$$\phi = \frac{(c - c_{CMC}) 4\pi R_s^3}{3N},$$

and

$$G = \frac{1}{4}\frac{(1+2\phi)^2}{(1-\phi)^4}(\sin(2qR_s) - 2qR_s\cos(2qR_s))(qR_s)^{-2} - \frac{3}{4}\frac{\phi\left(1+\frac{\phi}{2}\right)^2}{(1-\phi)^4}(4qR_s\sin(2qR_s) + (2 - 4q^2R_s^2)\cos(2qR_s) - 2)(qR_s)^{-3} + \frac{1}{64}\frac{\phi(1+2\phi)^2}{(1-\phi)^4}\left(-16q^4R_s^4\cos(2qR_s) + 4\left((12q^2R_s^2 - 6)\cos(2qR_s) + (8q^3R_s^3 - 12qR_s)\sin(2qR_s) + 6\right)\right)(qR_s)^{-5}.$$

Here, ρ_c is the SLD for the hydrophobic core, ρ_s is the SLD for the hydrophilic shell, ρ_{solv} is the SLD for the solvent, R_c is the radius of the core, R_s is the radius of the shell, c is the concentration in units of number of molecules per Å^3, c_{CMC} is the critical micelle concentration, and N is the aggregation number, or the number of molecules within each micelle. A procedure for analysing pluronic micelles under SANS is described by Goldmints *et al.*, where four models based on different distributions of D_2O within the micelle are investigated to determine which models produce a scattering pattern which fits the observed data.[1] Model 1 forbids the presence of D_2O in both the micelle core and shell. Model 2 allows for the presence of D_2O in both the core and shell but requires the volume fraction of polymer in each to be equal. Model 3 allows D_2O in the shell but not in the core, and Model 4 allows for different amounts of D_2O in the core and in the shell. All four models make the assumptions that the micelles are spherical, that polydispersity is minimal, and that the hydrophobic parts of the micelle are located solely in the core, whilst the hydrophilic parts are located solely in the shell. The assumptions made for the various models result in Model 1 having only 1 independent variable, Models 2 and 3 having 2 independent variables, and Model 4 having 3 independent variables (all in addition to a scale multiplier m and a background level B).

The variables of ρ_c and ρ_s can be calculated from R_c, R_s, and N (as well as known constants) using the following equations:

$$\rho_c = a_1\rho_{PPO} + (1 - a_1)\rho_{solv},$$

$$\rho_s = a_2\rho_{PEO} + (1 - a_2)\rho_{solv},$$

$$a_1 = \frac{3NV_{PPO}}{4\pi R_c^3},$$

$$a_2 = \frac{3NV_{PEO}}{4\pi(R_s^3 - R_c^3)}.$$

Here, ρ_c and ρ_s are calculated as the volume average of the SLD of the contents of the core and shell respectively, where a_1 is the volume fraction of PPO in the core, a_2 is the volume fraction of PEO in the shell, ρ_{PPO} is the SLD of PPO, and ρ_{PEO} is the SLD of PEO. The volume fractions themselves can be calculated as the fraction of the volume occupied by polymer in their respective sections. The assumptions made by the first three models result in the following simplifications:

Model 1

$$\rho_c = \rho_{PPO},$$

$$\rho_s = \rho_{PEO},$$

$$N = \frac{4\pi R_c^3}{3V_{PPO}},$$

$$R_s = R_c\sqrt[3]{\left(1 + \frac{V_{PEO}}{V_{PPO}}\right)},$$

$$R_c = \frac{R_m}{1+\sqrt[3]{\left(1+\frac{V_{PEO}}{V_{PPO}}\right)}};$$

Model 2

$$R_s = R_c\sqrt[3]{\left(1 + \frac{V_{PEO}}{V_{PPO}}\right)};$$

Model 3

$$\rho_c = \rho_{PPO},$$

$$R_c = \sqrt[3]{\frac{3NV_{PPO}}{4\pi}}.$$

In order to determine the fit of Model 1, the R^2 values were determined for $1 \leq R_m \leq 200$ Å in increments of 1 Å. A scale factor m and background factor B were included in the equation and allowed to vary freely in order to allow for background noise and an uncertain film thickness. The m and B combinations producing the best fit for $R_m \leq 84$ Å involve $m < 0$, which would require a film thickness less than 0, and hence are unrealistic. The micelle radius above 84 Å giving the best fit, as determined by calculation of the R^2 values is 116 Å (Fig. 4.3.2). The model for $R_m = 116$ Å is plotted in Fig. 4.3.3, which clearly does not fit the data well and gives an $R^2 = 0.86$. Consequently, Model 1 is insufficient to describe the shape of micelles in the solution. Hence it is concluded that there is some D_2O in the micelle core and/or the micelle shell.

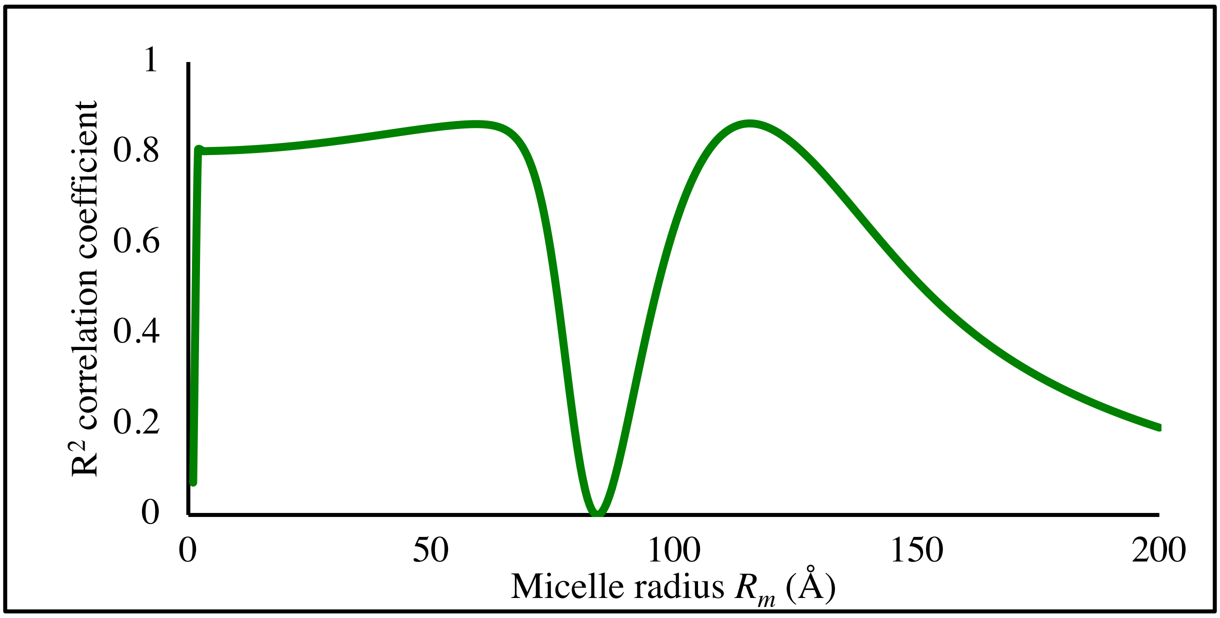

Fig. 4.3.2: R^2 values of Model 1 fitted to SANS data of 5% w/w Pluronic P123 in D_2O in the VFD at ω = 3000 rpm.

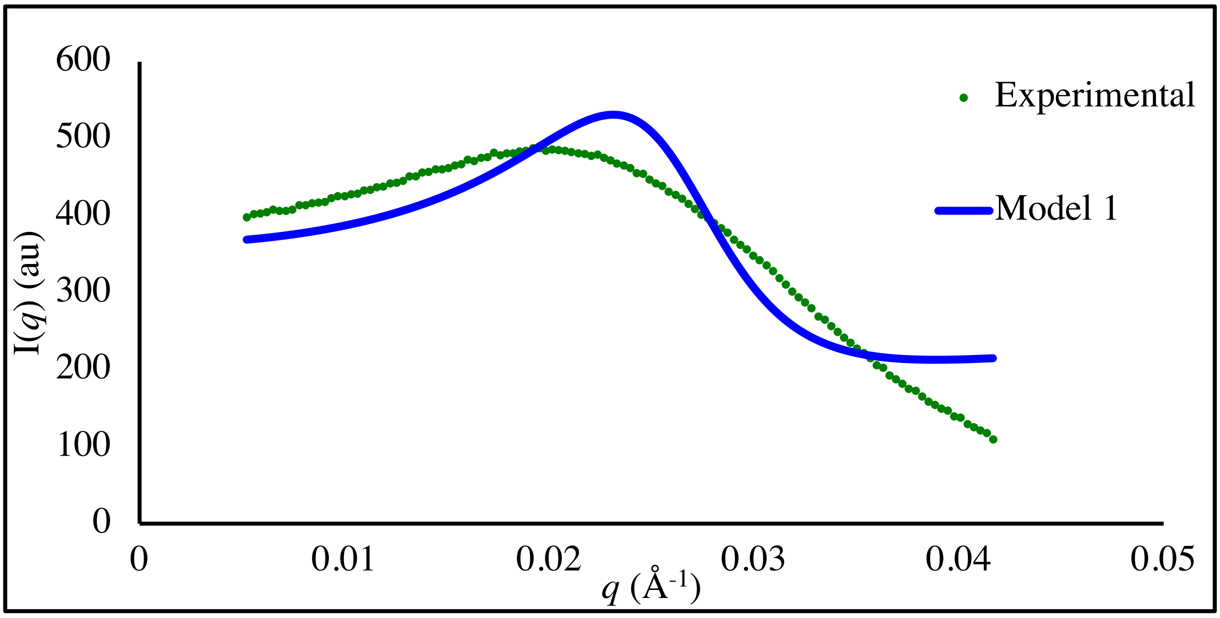

Fig. 4.3.3: Best fit of Model 1 (R_m = 116 Å) for 5% w/w Pluronic P123 in D_2O in the VFD at ω = 3000 rpm, compared to experimental data.

Model 2 allows for the presence of water in the micelle, however, it includes the limitation of requiring the volume fractions of polymer in the core and in the shell to be equal. The R^2 values were determined for all combinations of R_m and N in the range 1 Å $\leq R_m \leq$ 200 Å and $1 \leq N \leq$ 200 in increments of 1 Å and 1 respectively. The scale factor m and background B were allowed to vary freely, as for Model 1. Although the greatest R^2 value is above 0.99, plotting the corresponding best-fit against the experimental data shows that although the fit is significantly better than for Model 1 (Fig. 4.3.4). Despite this, the differences between the modelled data and experimental data are greater than is expected for SANS data, indicating that the model is insufficient to accurately describe the shape of the micelles. Consequently, it is concluded that not only is there D_2O in either the core, the shell, or both, but additionally that the volume fraction in the core is different to the volume fraction in the shell.

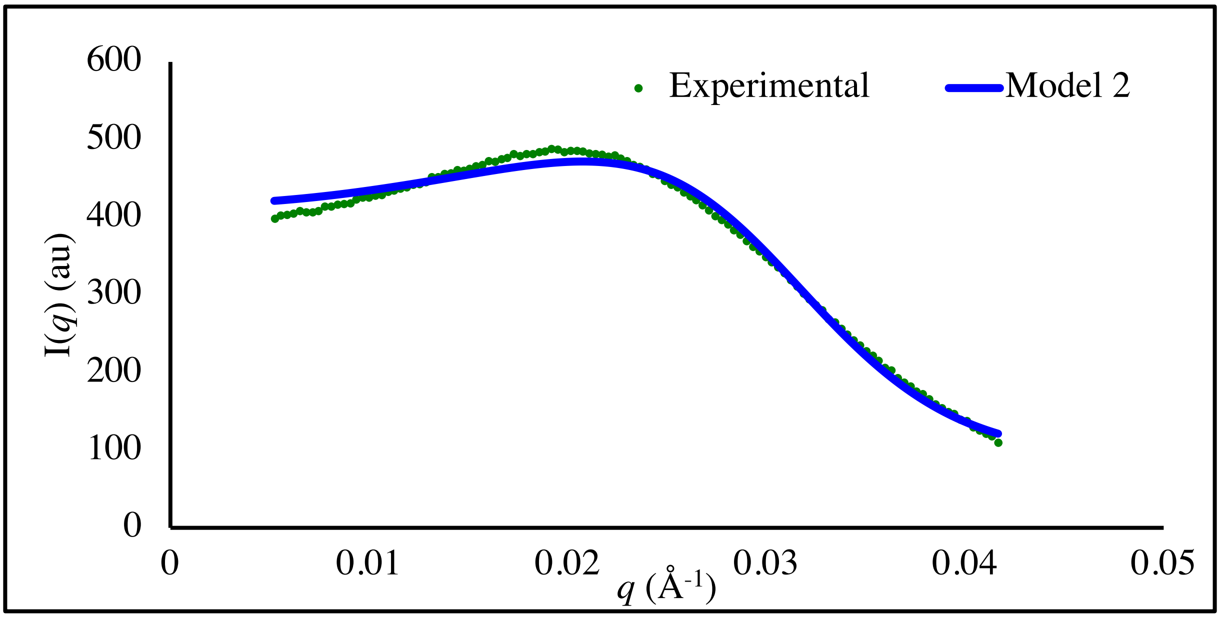

Fig. 4.3.4: Best fit of Model 2 (R_m = 91 Å, N = 103) for 5% w/w Pluronic P123 in D_2O in the VFD at ω = 3000 rpm, compared to experimental data.

Model 3 allows for the presence of water in the micelle shell but not in the micelle core. For Model 3, the R^2 values were determined for all combinations of R_m and N in the range 1 Å $\leq R_m \leq$ 200 Å and $1 \leq N \leq 200$ in increments of 1 Å and 1 respectively. The scale factor m and background B were allowed to vary freely, as for Model 1. Similar to Model 2, the R_m and N combination giving the greatest R^2 correlation gives a correlation of $R^2 > 0.99$, however, unlike for Model 2, this combination of R_m and N (R_m = 97 Å, N = 171) produces a scattering pattern which fits the experimental data (Fig. 4.3.5). A list of all R_c and N combinations giving $R^2 >$ 0.998 (Table 4.3.1) reveals 43 combinations, all in the range of R_m = 97 ± 3 Å and $N = 2.5 \cdot R_m - 72 \pm 5$. Manually checking these 43 combinations to identify the combinations which align the theoretical and experimental peak (an alignment which does not significantly affect the R^2) reveals only 9 which could be reasonably described to fit well (highlighted in Table 4.3.1), all with $R^2 > 0.9986$. Together, this gives the result of R_m = 97 ± 1 Å and N = 171 ± 5.

Consequently, the volume fraction a_2 of polymer in the shell is 0.208 ± 0.006, the radius of the micelle core R_c is 58.5 ± 0.5 Å and the shell thickness t_s is 38 ± 1 Å.

Table 4.3.1: Table of Model 3 parameter combinations which give $R^2 > 0.998$. Parameter combinations which give a reasonable fit are highlighted.

R_m (Å)	N	R^2	R_m (Å)	N	R^2
97	171	0.99901	96	170	0.99851
97	170	0.99900	95	166	0.99846
98	174	0.99897	95	163	0.99838
98	173	0.99896	99	179	0.99838
97	172	0.99889	96	165	0.99837
96	168	0.99888	99	174	0.99832
96	167	0.99886	100	180	0.99832
98	175	0.99885	100	179	0.99832
97	169	0.99884	97	174	0.99828
98	172	0.99881	98	177	0.99824
96	169	0.99876	95	167	0.99821
99	177	0.99874	100	181	0.99820
99	176	0.99873	100	178	0.99819
96	166	0.99870	96	171	0.99813
97	173	0.99864	94	162	0.99812
99	178	0.99862	94	161	0.99809
98	176	0.99860	98	170	0.99808
99	175	0.99860	97	167	0.99808
95	165	0.99858	95	162	0.99804
95	164	0.99856	99	180	0.99803
97	168	0.99854	94	163	0.99800
98	171	0.99852			

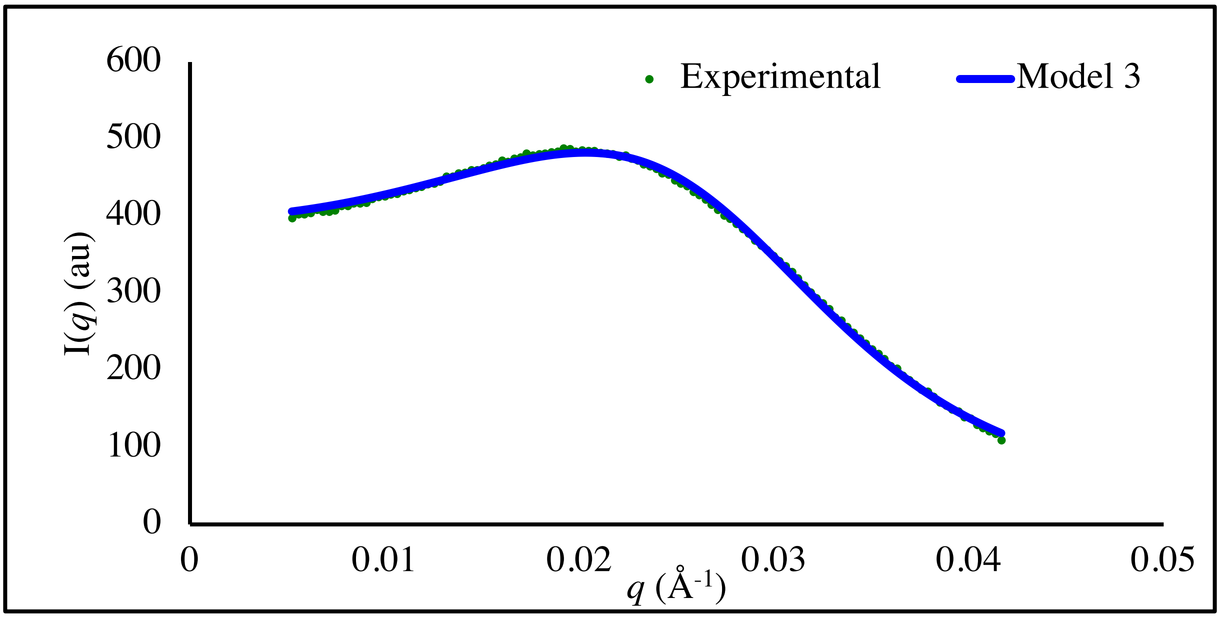

Fig. 4.3.5: Best fit of Model 3 (R_m = 97 Å, N = 171) for 5% w/w Pluronic P123 in D_2O, in the VFD at ω = 3000 rpm, compared to experimental data.

Model 4 allows the additional freedom of separating R_c from R_m, resulting in 3 variables, R_m, R_c and N. Calculation of all R^2 values in the realm of 1 Å $\leq R_c \leq 100$ Å, 1 Å $\leq R_m \leq 100$ Å and $1 \leq N \leq 200$, with increments of 1 Å, 1 Å and 1 respectively, resulted in 42 values with $R^2 > 0.9986$, 29 of which are considered to fit the data well (Table 4.3.2). These modelled fits result in the following determination for the parameters, all of which are similar to those obtained for Model 3; $R_m = 97.5 \pm 2$ Å, $R_c = 60 \pm 1$ Å, $N = 167 \pm 9$, $t_s = 36.5 \pm 1.5$ Å, $a_1 = 0.92 \pm 0.08$, $a_2 = 0.208 \pm 0.006$. Combining the parameter ranges for Models 3 and 4 gives the following final values: $R_m = 97.5 \pm 2$ Å, $R_c = 59.5 \pm 1.5$ Å, $N = 167 \pm 9$, $t_s = 36.5 \pm 2.5$ Å, $a_1 = 0.92 \pm 0.08$, $a_2 = 0.208 \pm 0.006$.

Table 4.3.2: Table of Model 4 parameter combinations which give $R^2 > 0.9986$. Parameter combinations which give a reasonable fit are highlighted.

R_m (Å)	R_c (Å)	N	R^2	R_m (Å)	R_c (Å)	N	R^2
97	59	170	0.99900	97	61	165	0.99872
97	59	171	0.99898	96	60	162	0.99872
97	59	169	0.99896	96	60	164	0.99872
97	60	167	0.99890	98	60	169	0.99871
97	59	172	0.99888	96	59	168	0.99871
98	60	171	0.99887	98	61	167	0.99870
97	60	166	0.99886	96	59	164	0.99868
96	59	166	0.99885	98	61	169	0.99868
98	60	172	0.99884	99	60	175	0.99867
97	59	168	0.99883	96	61	160	0.99866
98	60	170	0.99883	99	60	176	0.99864
98	59	172	0.99882	97	62	161	0.99864
96	59	167	0.99882	99	60	174	0.99863
96	59	165	0.99881	97	61	162	0.99863
97	61	164	0.99877	97	59	167	0.99863
96	60	163	0.99876	96	61	159	0.99862
97	60	169	0.99874	98	59	171	0.99862
97	61	163	0.99874	97	62	160	0.99861
97	60	165	0.99874	96	61	161	0.99860
98	60	173	0.99873	96	60	161	0.99860
98	61	168	0.99873				

Table 4.3.3: Literature values for Pluronic P123 dimensions, in comparison to those reported here.

T (°C)	C (w/w%)	R_c (Å)	R_s (Å)	R_m (Å)	N	a_c	a_s	Ref.
20		61	30	91	81	0.43	0.13	[11]
30	15	49	26	75	80	0.81	0.23	[12]
30	10	45	45	90	58	0.76	0.08	[13]
45	10	47.5	52.5	99	67	0.75	0.06	[14]
≈ 20	5	59.5	36.5	97.5	167	0.92	0.21	Here.

There are four literature sources that give details on the measured micelle information using SANS, summarised in Table 4.3.3, with the polymer content in the core and shell calculated using $a_1 = \frac{3NV_{PPO}}{4\pi R_c^3}$ and $a_2 = \frac{3NV_{PEO}}{4\pi(R_s^3 - R_c^3)}$. As can be seen in Table 4.3.3, the micelle dimensions determined are consistent with the varying literature values, although the aggregation number and core polymer content are significantly higher than in the literature. This suggests that the VFD is inhibiting water-hydrophobic interactions. Unfortunately, time constraints prevented the performance of conventional SANS experiments of the same samples, so it cannot be confirmed that the differences observed here are due to the VFD rather than the concentration used, and further experiments are vital in order to confirm this observation. Despite this uncertainty, it is encouraging that this conclusion is consistent with other work performed in the VFD, where the ability of the VFD to influence solvent-substrate interactions has been a hypothesis consistently produced.[15,16]

It would be worthwhile to reproduce these experiments with conventional SANS for the same samples in order to confirm the tentative conclusions made here, but the time scale for this in securing beam time and subsequent experiments is beyond the scope of the PhD research program. Additionally, it would be interesting to conduct experiments at different temperatures and concentrations. Unfortunately, temperature controlled VFD-SANS is not currently possible because it would require a heating unit with a very thin piece of aluminium positioned at the desired height instead of a heating element. One VFD attachment currently in the conceptual phase is a segmented heating and cooling unit with interchangeable blocks to allow for heating and cooling different parts of the tube to different temperatures. It should be possible to include a segment for SANS in this interchangeable unit.

Chapter 4.4 – References

1 Goldmints, I., von Gottberg, F. K., Smith, K. A. & Hatton, T. A. Small-Angle Neutron Scattering Study of PEO−PPO−PEO Micelle Structure in the Unimer-to-Micelle Transition Region. *Langmuir* **13**, 3659-3664, (1997).

2 Bilheux, H., McGreevey, R., Anderson, I. *Neutron Imaging and Applications*. (Springer, 2009).

3 Squires, G. L. *Introduction to the Theory of Thermal Neutron Scattering*. 3 edn, (Cambridge University Press, 2012).

4 Fritzsche, H. H., Jacques; Fruchart, Daniel. *Neutron Scattering and Other Nuclear Techniques for Hydrogen in Materials* (Springer, 2016).

5 Liu, Y., Chen, S.-H. & Huang, J. S. Small-Angle Neutron Scattering Analysis of the Structure and Interaction of Triblock Copolymer Micelles in Aqueous Solution. *Macromolecules* **31**, 2236-2244, (1998).

6 Sharma, P. K. & Bhatia, S. R. Effect of anti-inflammatories on Pluronic® F127: micellar assembly, gelation and partitioning. *International Journal of Pharmaceutics* **278**, 361-377, (2004).

7 Lettow, J. S., Lancaster, T. M., Glinka, C. J. & Ying, J. Y. Small-Angle Neutron Scattering and Theoretical Investigation of Poly(ethylene oxide)−Poly(propylene oxide)−Poly(ethylene oxide) Stabilized Oil-in-Water Microemulsions. *Langmuir* **21**, 5738-5746, (2005).

8 Gilbert, E. P., Schulz, J. C. & Noakes, T. J. 'Quokka'—the small-angle neutron scattering instrument at OPAL. *Physica B: Condensed Matter* **385-386**, 1180-1182, (2006).

9 Hammouda, B. (Available online at https://www.ncnr.nist.gov/staff/hammouda/the_SANS_toolbox.pdf, accessed 12/1/2018, 2016).

10 Klose, F., Constantine, P., J Kennedy, S. & A Robinson, R. *The Neutron Beam Expansion Program at the Bragg Institute*. Vol. 528 012026 (2014).

11 Manet, S. *et al.* Structure of Micelles of a Nonionic Block Copolymer Determined by SANS and SAXS. *The Journal of Physical Chemistry B* **115**, 11318-11329, (2011).

12 Vekariya, R. L. Reduction of micellar size of PEO−PPO−PEO triblock copolymer in presence of ionic liquid in aqueous solutions: A SANS study. *Journal of Dispersion Science and Technology* **39**, 517-521, (2018).

13 Ganguly, R. & Aswal, V. K. Improved Micellar Hydration and Gelation Characteristics of PEO−PPO−PEO Triblock Copolymer Solutions in the Presence of LiCl. *The Journal of Physical Chemistry B* **112**, 7726-7731, (2008).

14 Ganguly, R., Kumbhakar, M. & Aswal, V. K. Time Dependent Growth of the Block Copolymer P123 Micelles near Cloud Point: Employing Heat Cycling as a Tool to form Kinetically Stable Wormlike Micelles. *The Journal of Physical Chemistry B* **113**, 9441-9446, (2009).

15 Chen, X., Dobson, J. F. & Raston, C. L. Vortex fluidic exfoliation of graphite and boron nitride. *Chemical Communications* **48**, 3703-3705, (2012).

16 Vimalanathan, K. & Raston Colin, L. Dynamic Thin Films in Controlling the Fabrication of Nanocarbon and Its Composites. *Advanced Materials Technologies* **2**, 1600298, (2017).

Chapter 5

Controlling and Scaling-Up Organic Reactions in the VFD

A variety of organic reactions have been previously performed in the VFD. However, these reactions have not been investigated for larger-scale synthesis, nor has there been significant investigation into any control over selectivity that the VFD may afford, a capability that has been demonstrated by some other continuous flow systems. Here, a mathematical model has been developed to design a scaled-up process for the synthesis of several compounds previously prepared within the Raston group, and an investigation into the ability of the VFD to control the synthesis of *N*-substituted piperazines over *N*,*N*-disubstituted piperazines was performed.

The VFD used for the synthesis of *N*-substituted piperazines is designed for a 20 mm external diameter tube with length of 20 cm. The device has four pins to allow the precise placement of a heating unit with a gap of several millimetres between the heating unit and the tube. The tubes used are made from borosilicate glass with an internal diameter of 17.5 mm. All chemicals used in this project were purchased from either Sigma-Aldrich or ChemSupply.

All ^{1}H NMR spectra were recorded using a 600 MHz Bruker NMR spectrometer with a relaxation time of 1 s and 128 scans. All ^{13}C NMR spectra were recorded using the same spectrometer with a relaxation time of 2 s and 2048 scans.

Parts of chapters 5.1 and 5.4 were included as part of a paper under review by *Scientific Reports* titled ‘Neutron imaging and modelling inclined vortex driven thin films’, co-authored by Filomena Salvemini, Stuart Dalziel and Colin Raston.

Chapter 5.1 – Scaled up synthesis

The ability to scale reactions in flow systems up to greater production rates is of interest to industry. Scaling up continuous flow reactions in the VFD is possible through 3 methods: the utilisation of multiple units, re-optimisation of conditions for higher flow rates, and translation of the reaction into a larger VFD. The first method is not ideal because it increases the number of other units required, such as syringe pumps, whilst the second is not ideal because re-optimisation requires a significant amount of additional work. Here, a new VFD with an extended tube (H = 380 mm) was used to scale-up two previous reactions: the formation of imines and amides. The scaled-up conditions were determined using the mathematical model to identify the conditions allowing the greatest volume, conditions which in turn allowed the greatest flow rate. Equations 2.17 and 2.22 demonstrate that lower rotational speeds allow a greater volume in the tube, and that for a VFD with R = 8.75 mm and H = 380 mm, a thin film will be produced for rotational speeds above 2504 rpm. The actual speed used was 2970 rpm because a slightly higher speed was desired to ensure that surface tension and other effects did not act to prevent the formation of a thin film at the utilised speed. Using these conditions, the flow rate required to achieve the same residence time is calculated using

$$Q_2 = \frac{H_2^2 g\pi \sin\theta}{\tau_1 \omega_2^2} = Q_1 \left(\frac{H_2 \omega_1}{H_{1\omega_2}}\right)^2.$$

For the synthesis of imines (Scheme 5.1.1) where the original conditions were ω = 6950 rpm, θ = 45°, H = 180 mm, and Q = 0.45 mL/min, with a calculated residence time of 3.0 min, the scaled-up conditions suggest a new flow rate of 11 mL/min (reduced slightly to 10 mL/min). For the synthesis of amides (Scheme 5.1.2) where the original conditions were ω = 6950 rpm, θ = 45°, H = 180 mm, Q = 2 mL/min and T = 60 °C, with a calculated residence time of was 40 s (in contrast to the reported 80 s), the scaled-up conditions suggest a new flow rate of 49 mL/min. Unfortunately, the long VFD operating at 3000 rpm is unable to incorporate liquid into its film at a rate of 50 mL/min, resulting in pooling of liquid in the tube, eventually completely filling the tube. To resolve this problem, the rotational speed was increased to 4500 rpm, requiring an altered flow rate of 20 mL/min. Utilising these conditions, three previously reported imines and three previously reported amides were synthesised (Table 5.1.1).

Table 5.5.1: Up-scaled synthesis of imines and amides.

Compound	Isolated yield (Conversion)		Production rate (g/hr)	
	Original	New	Original	New
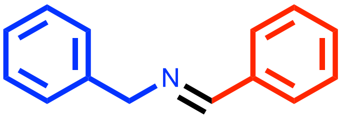	84%	82% (82%)	4.3	92
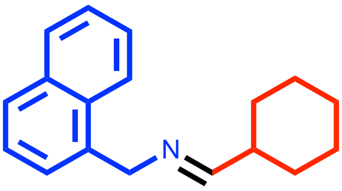	81%	45% (87%)[a]	5.0	62
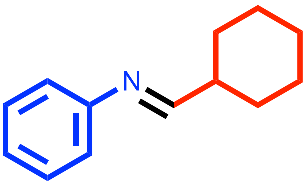	95%	83% (92%)	4.5	86
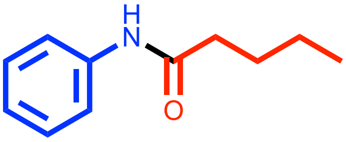	95%	48%	8.0	38
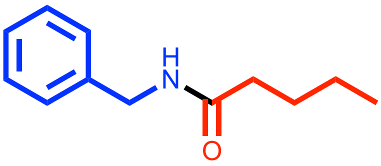	95%	26%	8.7	22
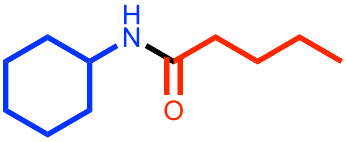	94%	28%	8.2	22

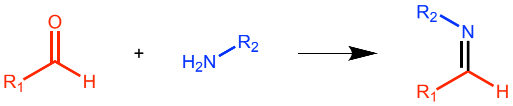

Scheme 5.1.1: The synthesis of imines from amines and aldehydes.

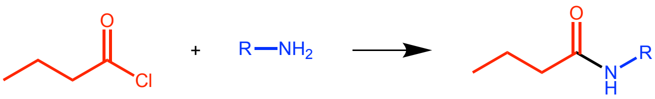

Scheme 5.1.2: The synthesis of amides from butyric chloride and amines.

---

[a] The originally reported compound contained the imine at the 2- position instead of the 1- position reported herein. The originally reported NMR and internal records strongly suggest that the originally synthesized imine was misreported as at the 2- position, and that the synthesized molecule was the imine substituted at the 1- position.

The conversions achieved for the imines here were determined using ^{1}H NMR of the crude sample and are comparable to those originally reported.[1] The production rates are significantly higher than in the original synthesis, due to the new designed conditions. This demonstrates the successful ability to scale up reactions in the VFD, using the developed mathematical model and a larger VFD. In contrast, the yields obtained for the amides are significantly lower.[2] The likely explanation for this is that the improved yields obtained in the VFD compared to batch are caused by heat dissipation allowed by the thin film. The conditions here were designed to maximise the volume within the tube, requiring the maximisation of the thickness of the thin film, even to the extent where it cannot be reasonably described as a 'thin' film anymore. The thickness of the film is likely to have interfered with the ability of the film to dissipate heat, effectively resulting in batch conditions. Nonetheless, in 2 of 3 cases, the obtained yield was greater than the reported batch yield and was achieved using only half the residence time. From this, it is clear that the mathematics can be used to design scaled-up conditions of previously optimised reactions, however, simply maximising the volume is not sufficient for reactions where the utilisation of a thin film is beneficial.

Chapter 5.2 – Literature procedures for the preparation of N-substituted piperazines

Piperazine moieties are present in 81 pharmaceuticals approved by the US Food and Drug Administration, including ranolazine,[3] buclizine[4] and imatinib (Fig. 5.2.1).[5-7] These 81 pharmaceuticals include 60 which are asymmetrically substituted at one or both nitrogen atoms, and do not contain any substituents on any of the piperazine carbon atoms. Due to the symmetrical nature of piperazine, the synthesis of mono-substituted piperazines as intermediates for unsymmetric piperazines is challenging because both sides of piperazine can react, producing the disubstituted product. Traditional batch processes avoid this by either using protecting groups[8] or several excesses of piperazine,[9-13] often in conjunction with long reaction times,[8,12-14] low temperatures,[8,13] or additional reagents.[15]

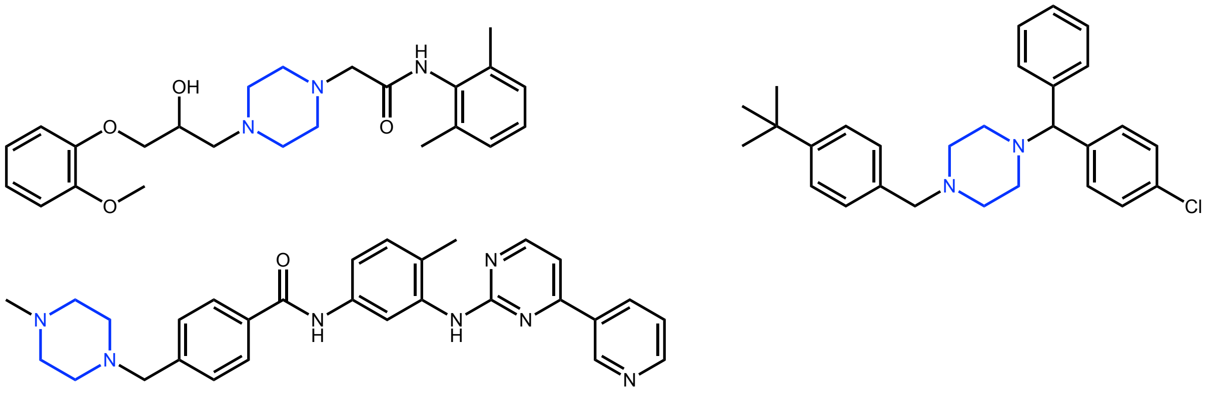

Fig. 5.2.1: Three pharmaceuticals containing a piperazine moiety; ranolazine (top left), buclizine (top right) and imatinib (bottom left).

The use of piperazines in continuous flow processes has previously been minimal, and mostly restricted to either using methylpiperazine (such as for the synthesis of imatinib[5-7] and olanzapine[16]) where disubstitution is not a concern, or have involved protecting groups.[17,18] There are, however, three examples where piperazine itself has been used under continuous flow, being for the synthesis of 1-(diphenylmethyl)piperazine based pharmaceuticals,[4] the synthesis of a casein kinase I inhibitor,[19] and for the synthesis of a benzylpiperazine (although reductive amination was performed instead of *N*-substitution).[20] The use of piperazine for the synthesis of a casein kinase I inhibitor involved the arylation of piperazine (Scheme 5.2.1), using 20 equivalents of piperazine, 177 °C, 100 minutes, and a flow rate of 0.02 mL/min, in order to reach full conversion.[19] The continuous flow reductive amination of a benzaldehyde

(Scheme 5.2.2) was motivated by a need to prepare the compound on a large scale as part of a drug discovery program. When performing large-scale synthesis involving piperazine, the use of 1-boc-piperazine is impractical due to its prohibitive cost of $2788 AUD/100g. The optimised conditions involved using 4 equivalents of piperazine and 70 °C, but a reasonable flow rate of 6 mL/min.[20]

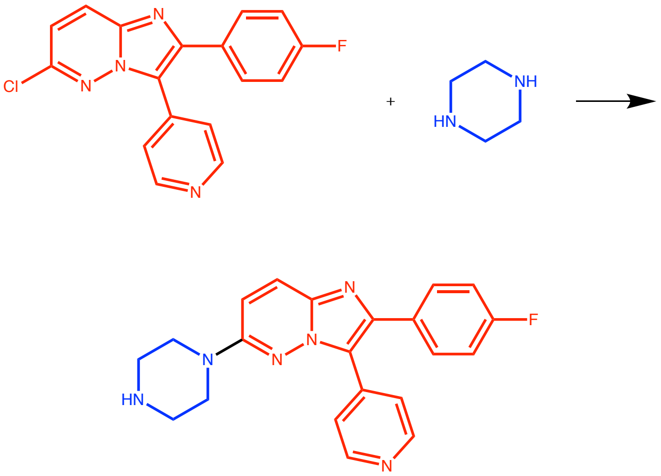

Scheme 5.2.1: The continuous flow synthesis of a casein kinase I inhibitor using piperazine.

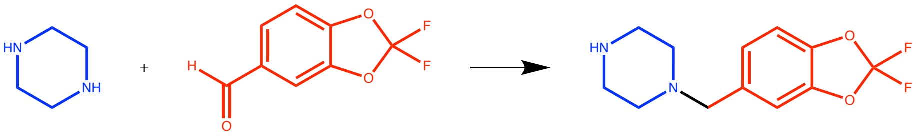

Scheme 5.2.2: Reductive amination using piperazine.

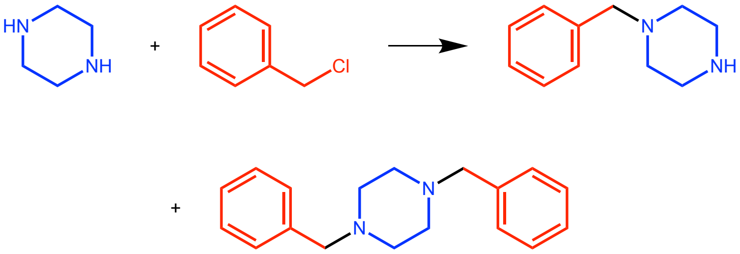

Scheme 5.2.3: Substitution of benzyl chloride with piperazine.

The third case in the literature involving piperazine under continuous flow was for the synthesis of the pharmaceuticals cinnarizine and cyclizine from alcohols under continuous flow (Scheme 5.2.3).[4] Here, hydrochloric acid was used to chlorinate alcohols, thereby achieving high yields (with 9 of 13 examples achieving 85% yield or above). The system was then connected to a cyclic amine dissolved in methyl carbitol for the amination reaction, achieving 96% and 97% yields for morpholine and *N*-methylpiperazine respectively, whilst a yield of only 63% was achieved for piperazine. This process was used to synthesise cyclizine (using *N*-methylpiperazine), and coupled with a second chlorination system for cinnarizine, and a buclizine and meclizine derivative. In all three cases, yields above 80% were achieved using 1.5 equivalents of piperazine. Because of the excess of piperazine used, 2 equivalents of the second chloride were required to ensure full conversion to the desired product. This example highlights one of the disadvantages of using excess piperazine: it increases the require quantity of subsequent reagents.[4]

Chapter 5.3 – Piperazine alkylation using benzyl chloride

Inspired by the demonstrated ability of continuous flow systems to provide a measure of control over chemical reactions,[21] use of the VFD was applied to the challenge of synthesising mono-substituted piperazines under continuous flow. The purpose of this investigation was twofold; 1) to determine if the VFD is capable of the same fine control that other flow systems are capable of, and 2) to selectively generate mono-substituted piperazines using a minimal excess of piperazine, which could be immediately coupled with a second separate substitution reaction to form disubstituted asymmetric piperazines. Coupling flow reactors with flow purification is a standard procedure for many synthetic flow laboratories, with software available to aid in the design of flow purification, however it is not yet a capability of this laboratory. Because industrial utilisation of this procedure (if successful) would involve flow purification, it was determined that the steady-state conversion would provide a more useful comparison than the yield obtained after batch purification. The steady-state conversion was assumed to have been reached after an input of 15 mL, corresponding to the collection of liquid that entered the VFD at $V = 12.3$ mL.

The selection of a model reaction (Scheme 5.3.1) involved selecting a halide expected to show significant reactivity and selectivity. Benzyl halides are more reactive than their alkyl counterparts, suggesting the use of either benzyl chloride or benzyl bromide. Benzyl chloride was selected in favour of benzyl bromide due to its enhanced selectivity.[22] Protic solvents are known to be effective solvents for these types of substitution reactions, leading to the selection of methanol and ethanol as solvents for the initial testing.[20] Moderate values of rotational speed, flow rate and temperature were selected as the initial operating conditions ($\omega = 6000$ rpm, $Q = 0.5$ mL/min, $\theta = 45°$, and $T = 60$ °C). Solutions of benzyl chloride (1.72 M) and piperazine (1.93 M, 1.1 equivalents) were prepared and were injected into the VFD at equal flow rates. The steady-state conversion was determined through analysis of the ^{1}H NMR spectra of the first three drops collected after 15 mL had been input into the VFD, with the ^{1}H NMR spectra recorded immediately after sample collection. The ratios of benzyl chloride, *N*-benzylpiperazine (BZP) and *N*,*N*-dibenzylpiperazine (DBP) were determined through the peaks at 4.56 ppm (2H, BnCl), 3.47 ppm (4H, DBP) and 3.45 ppm (2H, BZP) (Fig. 5.3.1, Fig. 5.3.2). To confirm the correct assignment of the 3.46 ppm and 3.44 ppm peaks to the correct products, their integration was compared to that the integration of the triplet at 2.83 ppm, a peak confidently assignable to benzylpiperazine.

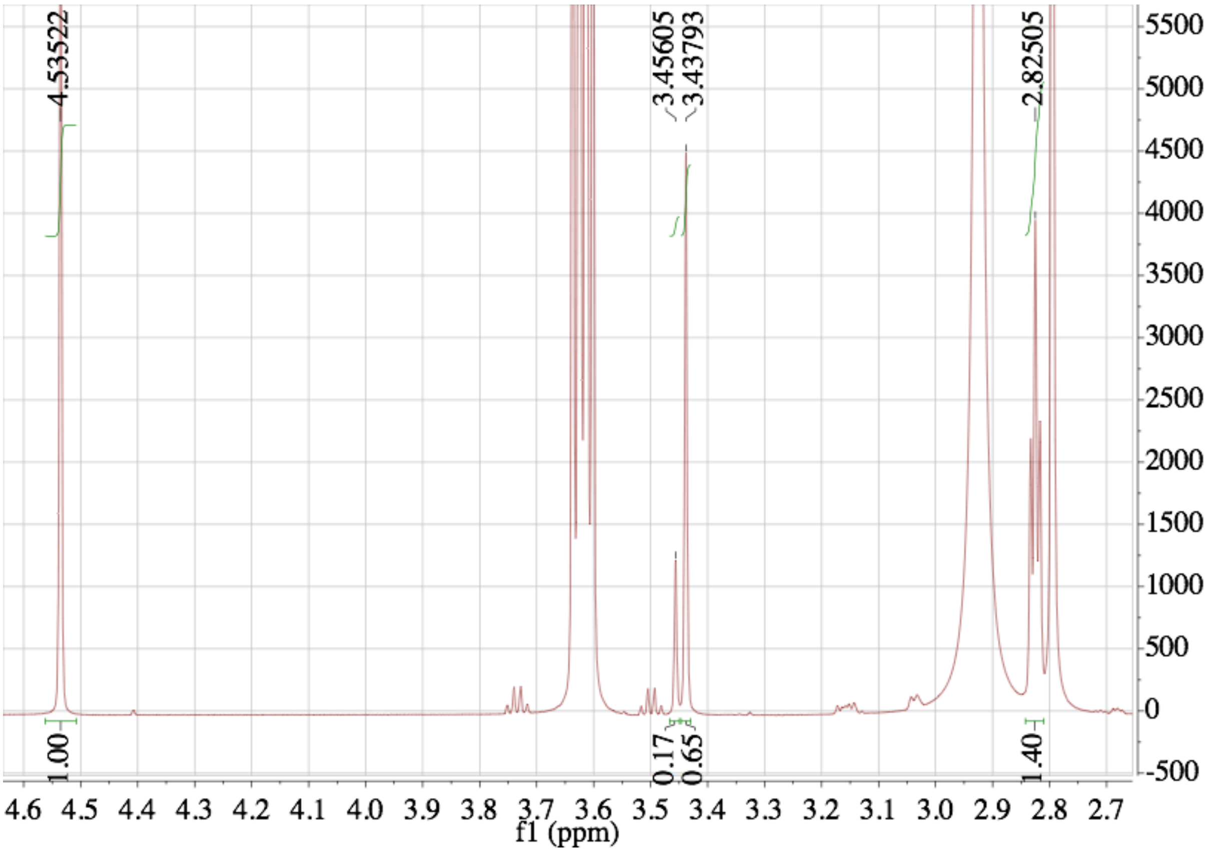

Fig. 5.3.1: ^{1}H NMR of a crude reaction mixture containing ethanol, tripropylamine, benzyl chloride, piperazine, monobenzylpiperazine and dibenzylpiperazine. The selected peaks are: benzyl chloride (4.54 ppm, 2H), dibenzylpiperazine (3.46 ppm, 4H), monobenzylpiperazine (3.44 ppm, 2H) and monobenzylpiperazine (2.83 ppm, 4H).

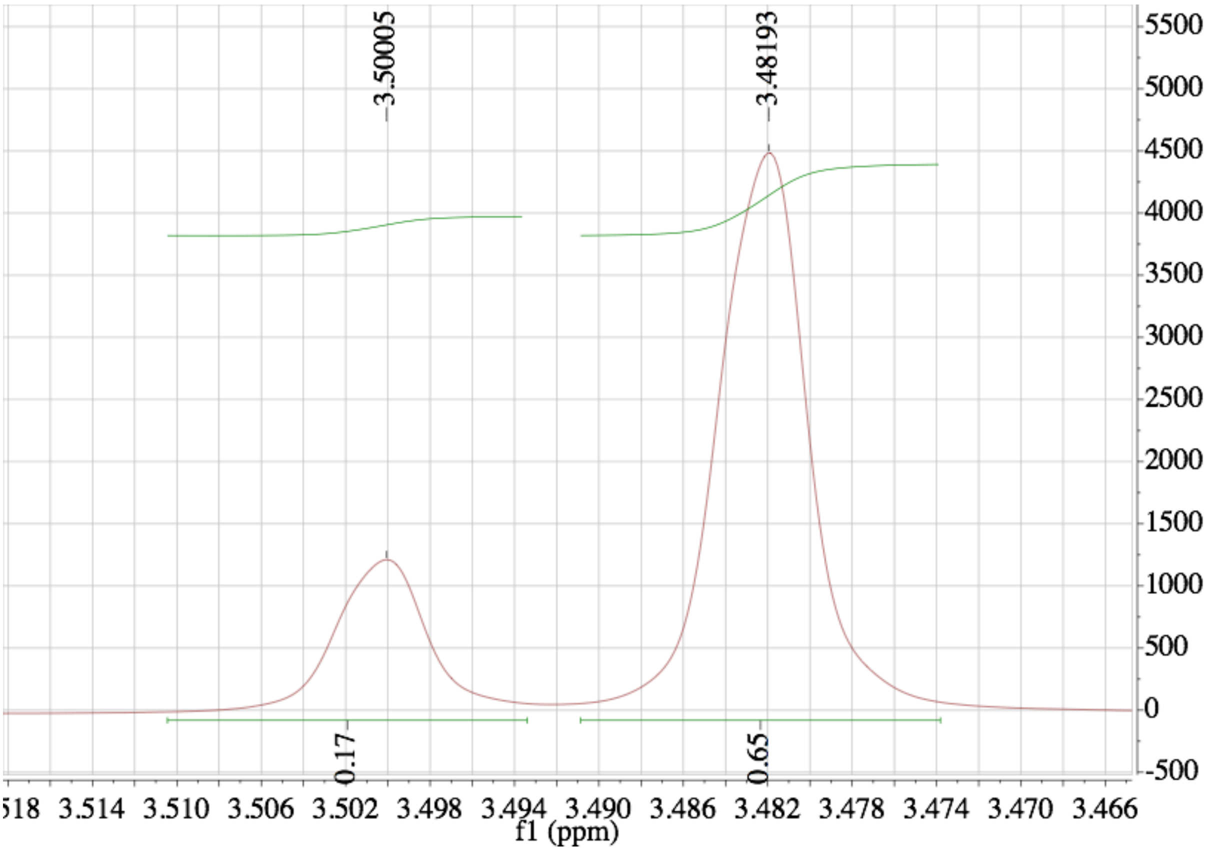

Fig. 5.3.2: ^{1}H NMR of a crude reaction mixture containing ethanol, tripropylamine, benzyl chloride, piperazine, monobenzylpiperazine and dibenzylpiperazine. The shown peaks are: dibenzylpiperazine (3.46 ppm, 4H) and monobenzylpiperazine (3.44 ppm, 2H).

Initial experiments showed that using only methanol or ethanol significantly favoured formation of the dibenzylated product, with only ethanol showing any of the monobenzylated product (and only in 1 of 3 replicates) (Fig. 5.3.3). Previous work by Kommi *et al.*[3] has shown that the addition of surfactants has been beneficial at enhancing selectivity for a similar system, particularly tetrabutylammonium bromide (TBAB). Hence, TBAB was tested as an additional reagent, despite the goal of avoiding additional reagents. The results showed the formation of benzylpiperazine for both ethanol and methanol, with ethanol producing greater conversion (47%) and selectivity (70%) than methanol (27% yield, 49% selectivity). Despite this improvement, the selectivity was still considered insufficient, and hence the use of a base was investigated. Sodium hydroxide and other ionic bases were avoided so to avoid the possibility of hydrolysis of benzyl chloride. As an alternative, triethylamine was tested as a common organic base, whilst tripropylamine was also tested as a higher boiling point alternative to triethylamine (155-158 °C compared to 89 °C). Triethylamine and tripropylamine were both tested in conjunction with ethanol (in a 1:1 v/v ratio), and both significantly increased the selectivity towards the monobenzylated product (Fig. 5.3.3). Having developed two satisfactory solvent systems, temperature and flow rate were investigated in an attempt to increase the conversion and selectivity towards the monobenzylated product. Tripropylamine was selected in favour of triethylamine for further investigation because its higher boiling point allowed the testing of a wider range of temperatures.

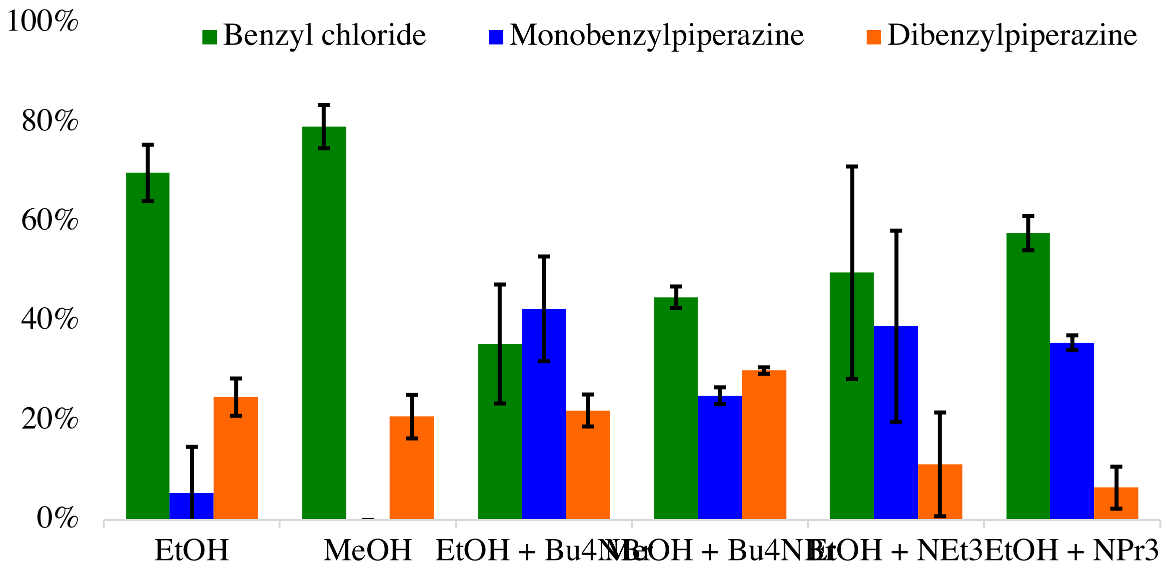

Fig. 5.3.3: The conversion of benzyl chloride to monobenzylpiperazine and dibenzylpiperazine in a range of solvents, using the VFD.

The conversion and selectivity obtained for the tested temperature and flow rate combinations are shown in Table 5.4.1. As seen in the table, conditions that produced conversion > 30% and selectivity > 80% were $Q = 0.1$ mL/min and T = ambient (yield = 33% and selectivity = 89%) and $Q = 0.5$ mL/min and $T = 60$ °C (yield = 34% and selectivity = 85%). The overall trends observed here of increased selectivity at lower temperatures and higher flow rates are unsurprising, as are the trends of greater total conversion for higher temperatures and lower flow rates.

Although further optimisation to increase the yield is left for future work, a brief investigation into future directions was performed, as well as a comparison between the optimised VFD conditions and a batch equivalent (Table 5.3.2). Firstly, the rotational speed was lowered from 6000 rpm to 4000 rpm for both optimised conditions ($Q = 0.1$ mL/min, T = ambient; and $Q = 0.5$ mL/min, $T = 60$ °C), approximately doubling the residence time. For the conditions of $Q =$

0.1 mL/min and T = ambient, both the conversion and selectivity were slightly lower for ω = 4000 rpm than for ω = 6000 rpm, whilst for Q = 0.5 mL/min and T = 60 °C, the conversion was marginally higher (statistically insignificant), whilst the selectivity dropped from 85% to 72%. The other direction investigated was use of the H = 38 cm VFD used previously in Chapter 5.1. A heating unit for this longer tube VFD is not yet available, so only the condition of Q = 0.1 mL/min, T = ambient, could be tested. This resulted in a slightly lower conversion than for H = 18 cm, and a much lower selectivity of 64%. Several conclusions can be made from this information. Firstly, decreasing the rotational speed or increasing the VFD length results in decreased selectivity, presumably because of an increase in back mixing. This could either be the result of the increased residence time, or it could be caused by the increased film thickness allowing additional back mixing. In order to isolate the effect for a changed rotational speed, the rotational speed and flow rate could be varied simultaneously to maintain a constant residence time whilst changing the film thickness. Similarly, isolating this effect for changing VFD length could be achieved by altering either the rotational speed or flow rate to achieve the same residence time. As a comparison to the optimised conditions of T = 60 °C and Q = 0.5 mL/min (τ = 4 min), a batch comparison was performed at the same temperature for the same residence time, giving 79% selectivity and 48% conversion. The similar selectivity demonstrates that the flow process is not significantly increasing the selectivity of the reaction. The increased conversion for the batch process is likely due to the differences between the ability of the heating element to heat the two systems. For the batch reaction, the heating mantle surrounds and is in contact with the flask used. In contrast, for the VFD process, an air gap of about 2 mm exists between the heating unit and the tube. This air gap, in combination with the heating unit only heating half the radial positions, results in a tube heated to a lower temperature than the heating mantle. This lower temperature for the VFD system is likely to be the cause of the lower conversion.

Table 5.3.2: The conversion and selectivity obtained for the synthesis of monobenzylpiperazine from benzyl chloride and piperazine at various conditions.

VFD	Rpm	Q (mL/min)	T (°C)	Conversion	Selectivity
Standard	4000	0.1	Ambient	29%	84%
Standard	4000	0.5	60	35%	72%
Long VFD	6000	0.1	Ambient	31%	64%
Batch	N/A	N/A	60	48%	79%

With a single exception, all literature methods found including a procedure for the synthesis of 4-benzylpiperazine from piperazine and benzyl chloride utilised either piperazine dihydrochloride as an additive or used excess of piperazine (ranging from 2 equivalents to 10 equivalents). The procedures using an excess are not comparable because using an excess of piperazine obviously increases selectivity and was deliberately avoided here. The use of piperazine dihydrochloride was avoided because it is only significantly soluble in water, whilst the solubility of piperazine in water and alcohols allowed a broader investigation.[23] Consequently, the only method reasonably comparable is the flow synthesis published by Borukhova. In this case, a yield of 63% was achieved, and the selectivity is not reported. Although the selectivity is not reported, it can be reasonably assumed that the reaction went to near-completion because similar reactions involving methylpiperazine and morpholine instead of piperazine achieved yields of 97% and 96% respectively. If it is assumed that the combined conversion to BZP and DBP was 95%, this gives a selectivity of only 66%, significantly lower than that achieved here for the VFD.

Chapter 5.4 – Synthetic methods and characterisation

5.4.1 – Synthesis of imines

Solutions of amine and aldehyde (55 mL) were prepared in methanol with a concentration of 1.94 M. The 38 cm long VFD was operated at 2970 rpm (due to technical issues of maintaining 3000 rpm for this modified VFD) and each solution was injected into the VFD at 5 mL/min for 10 minutes. The VFD was subsequently operated for an additional 3 minutes to allow all injected reagents to experience 3 minutes within the device. Output from the VFD was quenched in 500 mL of gently stirring water. *N*-benzylbenzylimine and *N*-(1-naphthyl)cyclohexylimine formed an oil, and the water was split into 250 mL fractions, each washed with ethyl acetate (200 mL x3), recombined, dried ($MgSO_4$), and the solvent removed under reduced pressure and *in vacuo* to give *N*-benzylbenzylimine as a yellow oil (15.9 g, with 3% residual aldehyde, giving a yield of 15.5 g, 83%) and *N*-(1-naphthyl)cyclohexylimine as a solid. *N*-(1-naphthyl)cyclohexylimine was subsequently vacuum filtered to give an impure yellow solid (21.1 g, 87%) which was recrystallised from ethyl acetate affording an off white solid (10.3 g, 45%). *N*-phenylcyclohexylimine formed a solid, which was filtered, dissolved in ethyl acetate, dried ($MgSO_4$), and the solvent removed under reduced pressure. Cooling gave an impure yellow solid (17.9 g, 92%) which was recrystallised form ethanol affording pale yellow crystals (14.6 g, 83%).

5.4.2 – Amide synthesis

Solutions of amine (55 mL, 0.43 M) in chloroform with 7% v/v triethylamine were prepared, along with solutions of acyl chloride (55 mL, 0.755 M) in chloroform. The VFD housing a 38 cm long glass tube was operated at 4500 rpm and each solution was injected into the VFD at 10 mL/min for 5 minutes. The VFD was subsequently operated for an additional 40 seconds to allow all injected reagents to experience 40 seconds within the device. Output from the VFD was quenched in 500 mL of gently stirring 2 M HCl. The organic layer was separated from the aqueous layer, dried ($MgSO_4$), and the solvent was removed under reduced pressure, giving *N*-phenylbutanamide as a solid and *N*-benzylbutanamide and *N*-cyclohexylbutanamide as liquids. *N*-phenylbutanamide was vacuum filtered and recrystallised from ethanol affording a white solid (3.1 g, 48%). *N*-benzylbutanamide and *N*-cyclohexylbutanamide were dried *in vacuo* and recrystallised from ethanol affording *N*-benzylbutanamide as a white solid (1.8 g, 26%), and *N*-cyclohexylbutanamide as a transparent solid (1.8 g, 28%).

5.4.3 – *N*-benzylpiperazine synthesis

The optimisation experiments for the substitution of piperazine with benzyl chloride were performed in the following manner: 12 mL solutions of benzyl chloride (1.72 M) and piperazine (1.93 M, 1.1 equivalents) were prepared in the selected solvent. The VFD (H = 18 cm) was heated to the appropriate temperature, and the solutions were injected into the VFD at equal flow rates for the selected total flow rate. For the optimisation experiments, the rotational speed used was 6000 rpm. Once 15 mL had been injected into the VFD, the output at that time point was collected and immediately analysed through ^{1}H NMR to determine the conversion.

To conclusively demonstrate the synthesis of monobenzylpiperazine, a procedure to prepare and purify monobenzylpiperazine was performed as follows: 12 mL solutions of halide (1.72 M) and piperazine (1.93 M, 1.1 equivalents) were prepared in 1:1 tripropylamine:ethanol. The VFD (H = 18 cm) was heated to 60 °C, and the solutions were injected into the VFD at 0.25 mL/min each for a total flow rate of 0.5 mL/min. The rotational speed used was 4000 rpm. Once 15 mL had been injected into the VFD, the output at that time point was collected and analysed through ^{1}H NMR immediately to determine the conversion. Once 20 mL had been injected into the VFD, the syringe pumps were halted, and after an additional 4 minutes the VFD was stopped in order to allow the last liquid injected to experience the same residence time as the rest. The tube was rinsed with 0.1 M HCl (40 mL) and ethyl acetate (40 mL) and added to the collected fraction. The two portions were separated, and the aqueous layer was rinsed twice more with ethyl acetate (50 mL). The aqueous layer was then basified with NaOH (2 g) and washed with ethyl acetate (50 mL x3). The organic layer was dried ($MgSO_4$), vacuum filtered, and the solvent was removed *in vacuo* to yield a white powder. The identity of the powder was then confirmed using ^{1}H NMR and ^{13}C NMR to conclusively demonstrate that the desired product had been synthesised.

The batch procedure used as a comparison to the substrate scope involved the preparation of a 20 mL solution of piperazine (0.95 M, 1.1 equivalents) in 1:1 tripropylamine:ethanol, which was then heated to 60 °C on a hot plate for 30 minutes. Benzyl chloride (1.9 mL, 16.5 mmol) was then added to the flask and allowed to react for 4 minutes. A fraction was then collected and analysed through ^{1}H NMR. The flask was emptied and rinsed with 0.1 M HCl (40 mL) and ethyl acetate (40 mL) and added to the collected fraction. The two portions were separated, and the aqueous layer was rinsed twice more with ethyl acetate (50 mL). The aqueous layer was then basified with NaOH (2 g) and washed with ethyl acetate (50 mL x3). The organic layer was dried ($MgSO_4$), vacuum filtered, and the solvent was removed *in vacuo* to yield a white powder. The identity of the powder was then confirmed using ^{1}H NMR and ^{13}C NMR to conclusively demonstrate that the desired product had been synthesised.

5.4.4 – Characterisation

***N*-benzylbenzylimine** ^{1}H NMR (600 MHz, $CDCl_3$): δ 8.42 (s, 1H), 7.82 (m, 2H), 7.45-7.44 (m, 3H), 7.37 (d ^3J(H,H) = 4.4 Hz, 4H), 7.31-7.28 (hex, ^3J(H,H) = 4.2 Hz, 1H), 4.86 (s, 2H). ^{13}C NMR (600 MHz, $CDCl_3$): δ 162.1, 139.3, 136.2, 130.8, 128.7, 128.5, 128.3, 128.0, 127.0, 65.1. This is consistent with literature.[14]

***N*-(1-naphthyl)cyclohexylimine** ^{1}H NMR (600 MHz, $CDCl_3$): δ 8.99 (s, 1H), 8.86 (d, ^3J(H,H) = 9 Hz, 1H), 7.89-7.88 (m, 3H), 7.59-7.56 (m, 1H), 7.51-7.49 (m, 2H), 3.31 (tt, ^3J(H,H) = 10.4 Hz, 4.1 Hz, 1H), 1.87 (m, 4H), 1.71 (m, 3H), 1.44 (qt, ^3J(H,H) = 12.4, 3.3, 2H), 1.33 (qt, ^3J(H,H) = 12.3, 3.5, 1H). ^{13}C NMR (600 MHz, $CDCl_3$): δ 157.9, 133.8, 132.2, 131.4, 130.6, 128.6, 128.2, 126.9, 125.9, 125.3, 124.3, 70.9, 34.6, 25.8, 24.8. This is consistent with literature.[14]

***N*-phenylcyclohexylimine** ^{1}H NMR (600 MHz, $CDCl_3$): δ 8.47 (s, 1H), 7.92-7.90 (m, 2H), 7.49-7.47 (m, 3H), 7.40 (t, ^3J(H,H) = 7.8 Hz, 2H), 7.25-7.21 (m, 3H). ^{13}C NMR (600 MHz, $CDCl_3$): δ 160.4, 152.1, 136.2, 131.4, 129.2, 128.83, 128.79, 126.0, 120.9. This is consistent with literature.[14]

***N*-phenylbutanamide** ^{1}H NMR (600 MHz, $CDCl_3$): δ 7.51 (d, ^3J(H,H) = 7.9 Hz, 2H), 7.31 (t, ^3J(H,H) = 7.4 Hz, 2H), 7.17 (bs, 1H), 7.10 (t, ^3J(H,H) = 7.4 Hz, 1H), 2.34 (t, ^3J(H,H) = 7.5 Hz, 2H), 1.77 (hextet, ^3J(H,H) = 7.4, 2H), 1.01 (t, ^3J(H,H) = 7.4 Hz, 3H). ^{13}C NMR (600 MHz, $CDCl_3$): δ 171.2, 138.0, 129.0, 124.2, 119.8, 39.8, 19.1, 13.8. This is consistent with literature.[19]

***N*-benzylbutanamide** ^{1}H NMR (600 MHz, $CDCl_3$): δ 7.34 (t, ^3J(H,H) = 7.4 Hz, 2H), 7.28-7.27 (m, 3H), 5.67 (bs, 1H), 4.45 (d, ^3J(H,H) = 5.7 Hz, 2H), 2.20 (t, ^3J(H,H) = 7.5 Hz, 2H), 1.70, (hextet, ^3J(H,H) = 7.4 Hz, 2H), 0.96 (t, ^3J(H,H) = 7.4 Hz, 3H). ^{13}C NMR (600 MHz, $CDCl_3$): δ 172.8, 138.4, 128.7, 127.9, 127.5, 43.6, 38.8, 19.2, 13.8. This is consistent with literature.[17]

***N*-cyclohexylbutanamide** ^{1}H NMR (600 MHz, $CDCl_3$): δ 5.26 (bs, 1H), 3.77 (m, 1H), 2.11 (t, ^3J(H,H) = 7.5 Hz, 2H), 1.92-1.90 (m, 2H), 1.72-1.68 (m, 2H), 1.65 (q, ^3J(H,H) = 7.5 Hz, 2H), 1.63-1.59 (m, 1H + water), 1.36 (qt, ${}^3J$(H,H) = 12.5, 3.4 Hz, 2H), 1.18-1.07 (m, 3H), 0.94 (t, ${}^3J$(H,H) = 7.4 Hz, 3H). ^{13}C NMR (600 MHz, $CDCl_3$): δ 172.0, 48.0, 39.1, 33.3, 25.6, 24.9, 19.3, 13.7. This is consistent with literature.[20]

***N*-benzylpiperazine** ^{1}H NMR (600 MHz, $CDCl_3$): δ 7.33-7.26 (m, 5H), 3.52 (s, 2H), 2.97 (t, ${}^3J$(H,H) = 4.9 Hz, 4H), 2.5 (bs, 4H). ^{13}C NMR (600 MHz, $CDCl_3$): δ 137.6, 129.2, 128.3, 127.2, 63.3, 52.8, 44.9. This is consistent with literature.[9]

Chapter 5.5 – References

1 Britton, J., Castle, J. W., Weiss, G. A. & Raston, C. L. Harnessing Thin-Film Continuous-Flow Assembly Lines. *Chemistry - A European Journal* **22**, 10773-10776, (2016).

2 Britton, J., Chalker, J. M. & Raston, C. L. Rapid Vortex Fluidics: Continuous Flow Synthesis of Amides and Local Anesthetic Lidocaine. *Chemistry - A European Journal* **21**, 10660-10665, (2015).

3 Kommi, D. N., Kumar, D. & Chakraborti, A. K. "All water chemistry" for a concise total synthesis of the novel class anti-anginal drug (RS), (R), and (S)-ranolazine. *Green Chemistry* **15**, 756-767, (2013).

4 Borukhova, S., Noël, T. & Hessel, V. Continuous-Flow Multistep Synthesis of Cinnarizine, Cyclizine, and a Buclizine Derivative from Bulk Alcohols. *ChemSusChem* **9**, 67-74, (2016).

5 Hopkin, M. D., Baxendale, I. R. & Ley, S. V. A flow-based synthesis of Imatinib: The API of Gleevec. *Chemical Communications* **46**, 2450-2452, (2010).

6 Yang, J. C., Niu, D., Karsten, B. P., Lima, F. & Buchwald, S. L. Use of a “Catalytic” Cosolvent, N,N-Dimethyl Octanamide, Allows the Flow Synthesis of Imatinib with no Solvent Switch. *Angewandte Chemie International Edition* **55**, 2531-2535, (2016).

7 Hopkin, M. D., Baxendale, I. R. & Ley, S. V. An expeditious synthesis of imatinib and analogues utilising flow chemistry methods. *Organic & Biomolecular Chemistry* **11**, 1822-1839, (2013).

8 Chandrika, N. T., Shrestha, S. K., Ngo, H. X. & Garneau-Tsodikova, S. Synthesis and investigation of novel benzimidazole derivatives as antifungal agents. *Bioorganic & Medicinal Chemistry* **24**, 3680-3686, (2016).

9 Myochin, T. *et al.* Rational Design of Ratiometric Near-Infrared Fluorescent pH Probes with Various pKa Values, Based on Aminocyanine. *Journal of the American Chemical Society* **133**, 3401-3409, (2011).

10 Boukli, L. *et al.* Design of new potent and selective secretory phospholipase A2 inhibitors. Part 5: Synthesis and biological activity of 1-alkyl-4-[4,5-dihydro-1,2,4-[4H]-oxadiazol-5-one-3-ylmethylbenz-4′-yl(oyl)] piperazines. *Bioorganic & Medicinal Chemistry* **16**, 1242-1253, (2008).

11 Meddad-Belhabich, N. *et al.* Design of new potent and selective secretory phospholipase A2 inhibitors. 6-Synthesis, structure–activity relationships and molecular modelling of 1-substituted-4-[4,5-dihydro-1,2,4-(4H)-oxadiazol-5-one-3-yl(methyl)]-functionalized aryl piperazin/one/dione derivatives. *Bioorganic & Medicinal Chemistry* **18**, 3588-3600, (2010).

12 Valyaev, D. A. *et al.* Grafting a homogeneous transition metal catalyst onto a silicon AFM probe: a promising strategy for chemically constructive nanolithography. *Chemical Science* **4**, 2815-2821, (2013).

13 Onajole, O. K. *et al.* Pentacyclo-undecane derived cyclic tetra-amines: Synthesis and evaluation as potent anti-tuberculosis agents. *European Journal of Medicinal Chemistry* **44**, 4297-4305, (2009).

14 Nikbin, N. & Watts, P. Solid-Supported Continuous Flow Synthesis in Microreactors Using Electroosmotic Flow. *Organic Process Research & Development* **8**, 942-944, (2004).

15 Wang, J., Li, S., Hu, X. & Yang, J. A Convenient Synthesis of N-Benzylpiperazine, 1-Aralkyl-4-benzylpiperazines and an Isostere of Idebenone. *Organic Preparations and Procedures International* **46**, 469-474, (2014).

16 Hartwig, J., Ceylan, S., Kupracz, L., Coutable, L. & Kirschning, A. Heating under High-Frequency Inductive Conditions: Application to the Continuous Synthesis of the Neurolepticum Olanzapine (Zyprexa). *Angewandte Chemie International Edition* **52**, 9813-9817, (2013).

17 Petersen, T. P., Ritzén, A. & Ulven, T. A Multistep Continuous-Flow System for Rapid On-Demand Synthesis of Receptor Ligands. *Organic Letters* **11**, 5134-5137, (2009).

18 Petersen, T. P. *et al.* Multistep Continuous-Flow Synthesis in Medicinal Chemistry: Discovery and Preliminary Structure–Activity Relationships of CCR8 Ligands. *Chemistry – A European Journal* **19**, 9343-9350, (2013).

19 Venturoni, F., Nikbin, N., Ley, S. V. & Baxendale, I. R. The application of flow microreactors to the preparation of a family of casein kinase I inhibitors. *Organic & Biomolecular Chemistry* **8**, 1798-1806, (2010).

20 Liu, J., Fitzgerald, A. E. & Mani, N. S. Reductive amination by continuous-flow hydrogenation: Direct and scalable synthesis of a benzylpiperazine. *Synthesis (Germany)* **44**, 2469-2473, (2012).

21 Webb, D. & Jamison, T. F. Diisobutylaluminum hydride reductions revitalized: A fast, robust, and selective continuous flow system for aldehyde synthesis. *Organic Letters* **14**, 568-571, (2012).

22 Choi, Y.-S. K., Yoon-Jung; Shen, Liu-Lan; Lee, Yong Sup; Jeong, Jin-Hyun. Direct N-Alkylation of Aromatic Amines Using a Microflow Reactor: Enhancement of Selectivity and Reactivity. *Synlett* **26**, 970-974, (2015).

23 *CRC Handbook of Chemistry and Physics*. (CRC Press, Inc., 1983-1984).

Chapter 6 – Conclusions and Future Work

A mathematical model describing the shape of the thin liquid film in the Vortex Fluidic Device was developed, which describes the film thickness as

$$f_t = R - \frac{g}{\omega^2}\cos\phi\cos\theta - \sqrt{R^2 - \frac{g^2}{\omega^4}\cos^2\theta\,(\sin^2\phi) + 2gh\frac{\sin\theta}{\omega^2} - \sqrt{\frac{4gV\sin\theta}{\pi\omega^2} - \frac{2g^2R^2}{\omega^4}\cos^2\theta}}.$$

This equation is consistent with previous literature models for similar and related systems. This model allows the determination of useful information, including the residence time under continuous flow and film thickness at specific points, as well as aiding in the design of experiments where the residence time is kept constant and other parameters are varied. Further work involving the mathematical model could include advancing the model to take into account imperfections in the surface of the tube, an option that would require solving equation 2.10 for a ϕ-dependent R. Further advancement could also include taking into consideration surface-liquid interactions and/or viscosity, however, this would require introducing additional forces into Equation 2.1, meaning that $\vec{F} = \overrightarrow{F_g} + \overrightarrow{F_c}$ would no longer be valid. The understanding gained by this model will also allow future investigations into the internal behaviour of fluid within the film, including investigating the extent of backflow within the VFD tube. This will reveal useful insights into how to reduce the variation in amount of time materials spend in a laser beam, and how far apart reaction zones must be when performing sequential synthetic procedures within the VFD.

The accuracy of the model was confirmed using neutron imaging, with both high-speed and high-resolution methodologies employed. From these experiments, it was shown that for most systems, the film reaches stability within several seconds, and that for low viscosity systems, the model accurately predicts the shape of the film, although no ϕ-dependence was observed, even when predicted by the model. The absence of an observed ϕ-dependence is likely due to viscosity and surface tension, both of which would inhibit radial variation and are not accounted for in the model. For high viscosity systems, an adjustment to the model where $\omega_e = a \cdot \omega + b$ is used in place of ω, where a and b are experimentally determined values, was shown to be effective. The model was determined to not accurately describe the behaviour of water in a hydrophobic coated tube, and an adjustment of $\omega_e = a \cdot \omega + b$ was unsuccessful in adapting the model, although a possible method for adapting the model was proposed through the adjustment of equation 2.10 from $V = \int_0^{2\pi}\int_{r_i}^{R} hr\,dr\,d\phi$ to $V = \int_0^{2\pi}\int_{r_i}^{R} hr\,dr\,d\phi - \int_0^{2\pi}\int_{R-f_m}^{R}\big(h - h(r = R - f_m)\big)r\,dr\,d\phi$. These insights allow the calculation of residence time for highly viscous solutions, a capability that can be used when investigating processes involving microalgae, as well as the potential to use glycerol or propylene glycol as a green solvent for performing organic reactions within the VFD.

Further work involving neutron imaging includes investigating a wider range of solvents and determining the range of solvents where $\omega_e = a \cdot \omega + b$ successfully alters the mathematical model. This would allow for the easier investigation of solvent behaviour because when $\omega_e = a \cdot \omega + b$ is assumed to be a valid adjustment for the conditions, a and b can be determined through experiments in a standard laboratory without the need for neutron imaging. Further neutron imaging work also includes investigating the behaviour of non-aqueous systems in a hydrophobic tube, with non-polar solvents being of particular interest. Investigations extending the use of the model to a wider range of systems will enable the utilisation of the mathematical model as a general tool for designing synthetic procedures and separating the effects that shear rate, film thickness and residence time have on the processing of materials.

Experiments involving biphasic systems demonstrated that qualitative information can be obtained when the denser liquid has a lower neutron absorption cross-section, but that under the current methodology, quantitative information cannot be obtained. The most effective method for increasing the effective resolution of the images would be an increased precision in the tube design and in the position of its axis of rotation. This would especially benefit the investigation of biphasic systems because it would significantly reduce the overlap in the image of the two solvents. Other methods that may increase the resolution are increasing the acquisition time, utilising a thinner gadolinium oxide film, or utilising a neutron imaging station capable of higher resolution. Unfortunately, as mentioned above, only two instruments in the world are capable of higher resolution, both situated in Switzerland and are currently offline, whilst a third is set to come online in Sweden in 2019 or 2020. Another approach to increasing resolution could be increasing the absorption cross-section of the solvent through the addition of chlorinated compounds such as sodium chloride.

Small Angle Neutron Scattering experiments have confirmed the viability of SANS as an *in situ* technique for analysis within the VFD, which has successfully lead to subsequent work by colleagues investigating the shape of red blood cells within the VFD under SANS. The Pluronic P-123 micelles investigated here showed similar dimensions under shear compared to literature values, however, they showed higher polymer content in the hydrophobic core compared to literature (0.92 volume fraction in the VFD compared to 0.81 and below in literature). Future work involving this should include repeating the experiments with comparable conventional SANS, as well as variation of concentration and temperature. Future work also extends beyond SANS of Pluronic P123 micelles to investigating the behaviour of other macromolecular structures, including red blood cells, liposomes, and carbon nanomaterials. Investigating the *in situ* behaviour of these structures is likely to reveal important insights into the nature of the environment within the thin film.

Two main conclusions were achieved from the organic synthesis experiments: firstly, the mathematics can be used to easily scale up reactions under flow where heat dissipation is not a concern, as demonstrated by the highly successful scale-up of imine synthesis, and the moderately successful scale-up of amide synthesis to higher production rates. Secondly, there appears to be too significant back mixing for control over selectivity to be achieved through strict control of the residence time. Further experiments of interest would be to further develop the selective synthesis of mono-substituted piperazines to be high yielding. Additionally, the further scale up of previous reactions to larger VFDs would also be of interest, particularly for investigating if biphasic reactions are still successful at larger scales.

In general, these results provide useful information for designing synthetic procedures within the VFD. The mathematical model allows the calculation of residence time, allowing reliable comparisons between different continuous flow conditions, as well as batch processing. The overall understanding of the film thickness within the VFD also points the way towards investigations into any backmixing within the VFD, allowing the identification of conditions required to maintain separation between sequential reactions that may interfere with each if performed simultaneously. The demonstration that the model can also be used for highly viscous liquids allows the calculation of residence time for high viscosity green solvents such as glycerol and propylene glycol, and indeed ionic liquids as so-called designer solvents. The demonstration that although the VFD can selectively prepare *N*-benzylpiperazine in favour of *N*,*N*-dibenzylpiperazine, that this selectivity is comparable to that achieved in batch processing, suggests that the VFD may have limitations in controlling selectivity of this kind. The demonstration that simple reactions can be easily scaled-up using the mathematics is a significant advance, in leading the way to designing continuous flow conditions for reactions over extended periods.

These results are also useful for understanding materials processing within the VFD, and for probing the structure of macromolecular systems. Understanding how the rotational speed affects the film thickness and residence time is informative when explaining the optimised conditions for producing various materials. Further investigations using neutron imaging into the behaviour of biphasic systems will be informative for the numerous biphasic procedures developed for producing a variety of materials using the VFD. The ability to probe the *in situ* behaviour of macromolecular structures using SANS will provide insights into how those structures are formed. This in turn will lead to a better understanding of the environment within the VFD, providing insights into the generation of materials and macromolecular structures which cannot be investigated using SANS.

Overall, the development of a mathematical model and the demonstration of its accuracy through neutron imaging has resulted in the successful scale-up of organic reactions. This has resulted in further insights into previous work, demonstrating the utility of the model as a tool for guiding experimental design. The model and demonstrated neutron techniques can also be used for further insights into how a variety of structures are prepared using VFD mediated processing. This understanding contributes to the ability to successfully utilise the VFD as a continuous flow processing platform to prepare a variety of compounds and materials using environmentally friendly processing, in turn contributing to the broader global goal of developing sustainable alternatives to current wasteful and energy-intensive processes.

Appendix A – Derivation of mathematical equations

The derivation of Equation 2.6 starts with Equations 2.4 and 2.5:

Equation 2.4

$$\vec{F} = \rho(r\omega^2 \cos\phi - g\cos\theta\, , r\omega^2 \sin\phi\, , -g\sin\theta)$$

Equation 2.5

$$\vec{n} = \nabla\big(z - h(x,y)\big) = \left(-\frac{\partial h}{\partial x}, -\frac{\partial h}{\partial y}, 1\right)$$

Equating $\vec{F} \times \vec{n} = \vec{0}$ gives the following three results:

$$\rho(r\omega^2 \cos\phi - g\cos\theta) \cdot \left(-\frac{\partial h}{\partial y}\right) - \rho r\omega^2 \sin\phi \cdot \left(-\frac{\partial h}{\partial x}\right) = 0$$

$$\rho r\omega^2 \sin\phi \cdot 1 - \left(-\frac{\partial h}{\partial y}\right) \cdot (-\rho g \sin\theta) = 0$$

$$-\rho g \sin\theta \cdot \left(-\frac{\partial h}{\partial x}\right) - \rho(r\omega^2 \cos\phi - g\cos\theta) \cdot 1 = 0$$

Because the purpose is to find $\frac{\partial h}{\partial x}$ and $\frac{\partial h}{\partial y}$ separately, the first result is ignored as it contains both $\frac{\partial h}{\partial x}$ and $\frac{\partial h}{\partial y}$, whilst the other two are simplified and rearranged to find $\frac{\partial h}{\partial y}$ as follows,

$$\rho r\omega^2 \sin\phi \cdot 1 - \left(-\frac{\partial h}{\partial y}\right) \cdot (-\rho g \sin\theta) = 0$$

$$r\omega^2 \sin\phi - \left(\frac{\partial h}{\partial y}\right) \cdot (g\sin\theta) = 0$$

$$\frac{\partial h}{\partial y} = \frac{r\omega^2 \sin\phi}{g\sin\theta}$$

and $\frac{\partial h}{\partial x}$ as follows,

$$-\rho g \sin\theta \cdot \left(-\frac{\partial h}{\partial x}\right) - \rho(r\omega^2 \cos\phi - g\cos\theta) \cdot 1 = 0$$

$$g\sin\theta \cdot \left(\frac{\partial h}{\partial x}\right) + (g\cos\theta - r\omega^2 \cos\phi) = 0$$

$$\frac{\partial h}{\partial x} = -\frac{\cos\theta}{\sin\theta} + \frac{r\omega^2 \cos\phi}{g\sin\theta}$$

The derivations of Equations 2.11 and 2.12 begin with Equation 2.9:

Equation 2.9

$$h = \frac{r^2\omega^2}{2g\sin\theta} - r\cos\phi\cot\theta + k$$

Inserted into Equation 2.9 is the conditions of $h = 0$ and $r = r_i$, giving:

$$\frac{r_i^2\omega^2}{2g\sin\theta} - r_i\cos\phi\cot\theta + k = 0$$

Which is then solved using the quadratic formula:

$$r_i = -\frac{(-\cos\phi\cot\theta) \pm \sqrt{(-\cos\phi\cot\theta)^2 - 4\cdot\frac{\omega^2}{2g\sin\theta}\cdot k}}{2\cdot\frac{\omega^2}{2g\sin\theta}}$$

$$r_i = \frac{g\cos\phi\cos\theta \pm g\sin\theta\sqrt{\cos^2\phi\cot^2\theta - \frac{2\omega^2}{g\sin\theta}\cdot k}}{\omega^2}$$

$$r_i = \frac{g\cos\phi\cos\theta}{\omega^2} \pm \sqrt{\frac{g^2}{\omega^4}\cos^2\phi\cos^2\theta - \frac{2gk\sin\theta}{\omega^2}}$$

This gives two solutions for r_i, one of which is always negative because $k < 0$ causes $\frac{g\cos\phi\cos\theta}{\omega^2} < \sqrt{\frac{g^2}{\omega^4}\cos^2\phi\cos^2\theta - \frac{2gk\sin\theta}{\omega^2}}$, and hence is not a solution of interest. The other solution is of interest, and can be written more neatly by defining

Equation 2.12

$A \equiv \frac{g\cos\theta}{\omega^2}, B \equiv -\frac{2g\sin\theta}{\omega^2}k,$

giving Equation 2.11:

Equation 2.11

$$r_i = A\cos\phi + \sqrt{A^2\cos^2\phi + B}$$

The derivation of Equation 2.13 begins substituting Equation 2.9

Equation 2.9

$$h = \frac{r^2\omega^2}{2g\sin\theta} - r\cos\phi\cot\theta + k$$

Into equation 2.10

Equation 2.10

$$V = \int_0^{2\pi}\int_{r_i}^{R} hr\,dr\,d\phi$$

to give

$$V = \int_0^{2\pi} \int_{r_i}^{R} \left(\frac{r^2 \omega^2}{2g \sin \theta} - r \cos \phi \cot \theta + k \right) r \, dr \, d\phi$$

$$V = \int_0^{2\pi} \int_{r_i}^{R} \frac{r^3 \omega^2}{2g \sin \theta} - r^2 \cos \phi \cot \theta + kr \, dr \, d\phi$$

The inner integral is then computed to give Equation 2.13

$$V = \int_0^{2\pi} \left[\frac{r^4 \omega^2}{8g \sin \theta} - \frac{1}{3} r^3 \cos \phi \cot \theta + \frac{1}{2} k r^2 \right]_{r_i}^{R} d\phi$$

Equation 2.13

$$V = \int_0^{2\pi} \frac{(R^4 - r_i^4)\omega^2}{8g \sin \theta} - \left(\frac{R^3 - r_i^3}{3} \right) \cos \phi \cot \theta + \frac{1}{2}(R^2 - r_i^2) k \, d\phi$$

The derivation of Equation 2.14 beings with substituting in Equation 2.11 into Equation 2.13:

$$V = \int_0^{2\pi} \frac{\left(R^4 - \left(A \cos \phi + \sqrt{A^2 \cos^2 \phi + B} \right)^4 \right) \omega^2}{8g \sin \theta}$$
$$- \left(\frac{R^3 - \left(A \cos \phi + \sqrt{A^2 \cos^2 \phi + B} \right)^3}{3} \right) \cos \phi \cot \theta$$
$$+ \frac{1}{2} \left(R^2 - \left(A \cos \phi + \sqrt{A^2 \cos^2 \phi + B} \right)^2 \right) k \, d\phi$$

This is followed by expanding the bracketed sections

$$V = \int_0^{2\pi} \left(\frac{R^4 \omega^2}{8g \sin \theta} - \frac{A^4 \omega^2 \cos^4 \phi}{8g \sin \theta} - \frac{A^3 \omega^2 \cos^3 \phi \sqrt{A^2 \cos^2 \phi + B}}{2g \sin \theta} - \frac{3A^4 \omega^2 \cos^4 \phi}{4g \sin \theta} \right.$$
$$- \frac{3A^2 B \omega^2 \cos^2 \phi}{4g \sin \theta} - \frac{A^3 \omega^2 \cos^3 \phi \sqrt{A^2 \cos^2 \phi + B}}{2g \sin \theta}$$
$$- \frac{AB \omega^2 \cos \phi \sqrt{A^2 \cos^2 \phi + B}}{2g \sin \theta} - \frac{A^4 \omega^2 \cos^4 \phi}{8g \sin \theta} - \frac{A^2 B \omega^2 \cos^2 \phi}{4g \sin \theta} - \frac{B^2 \omega^2}{8g \sin \theta}$$
$$- \frac{R^3 \cos \phi \cot \theta}{3} + \frac{A^3 \cos^4 \phi \cot \theta}{3} + A^2 \cos^3 \phi \cot \theta \sqrt{A^2 \cos^2 \phi + B}$$
$$+ A^3 \cos^4 \phi \cot \theta + AB \cos^2 \phi \cot \theta + \frac{A^2 \cos^3 \phi \cot \theta \sqrt{A^2 \cos^2 \phi + B}}{3}$$
$$+ \frac{B \cos \phi \cot \theta \sqrt{A^2 \cos^2 \phi + B}}{3} + \frac{R^2 k}{2} - \frac{A^2 k \cos^2 \phi}{2}$$
$$\left. - Ak \cos \phi \sqrt{A^2 \cos^2 \phi + B} - \frac{A^2 k \cos^2 \phi}{2} - \frac{Bk}{2} \right) d\phi$$

In order to simplify this, it is observed that when integrating any function from x_1 to x_2, functions satisfying $f(x) = -f\left(x + \frac{1}{2}(x_2 - x_1)\right)$ for $x = x_1$ to $x = x_2$ integrate to zero because

$$\int_{x_1}^{x_2} f(x)\,dx = \int_{x_1}^{\frac{1}{2}(x_1+x_2)} f(x)\,dx + \int_{\frac{1}{2}(x_1+x_2)}^{x_2} f(x)\,dx$$
$$= \int_{x_1}^{\frac{1}{2}(x_1+x_2)} f(x)\,dx - \int_{x_1}^{\frac{1}{2}(x_1+x_2)} f(x)\,dx = 0$$

For $x_1 = 0$ and $x_2 = 2\pi$, this condition is satisfied for the following relevant functions $\cos\,\phi, \cos^3\phi, \cos\phi\sqrt{A^2\cos^2\phi + B}$ and $\cos^3\phi\sqrt{A^2\cos^2\phi + B}$,
simplifying the above to:

$$V = \int_0^{2\pi}\left(\frac{R^4\omega^2}{8g\sin\theta} - \frac{A^4\omega^2\cos^4\phi}{g\sin\theta} - \frac{A^2B\omega^2\cos^2\phi}{g\sin\theta} - \frac{B^2\omega^2}{8g\sin\theta} + \frac{4A^3\cos^4\phi\cot\theta}{3}\right.$$
$$\left. + AB\cos^2\phi\cot\theta + \frac{R^2k}{2} - A^2k\cos^2\phi - \frac{Bk}{2}\right)d\phi$$

$$V = \left(\frac{R^4\omega^2}{4g\sin\theta}\pi - \frac{A^4\omega^2 3\pi}{4g\sin\theta} - \frac{A^2B\omega^2\pi}{g\sin\theta} - \frac{B^2\omega^2}{4g\sin\theta}\pi + A^3\pi\cot\theta + AB\pi\cot\theta + R^2k\pi\right.$$
$$\left. - A^2k\pi - Bk\pi\right)$$

The definitions for A and B from Equation 2.12 are used to give Equation 2.14

Equation 2.14

$$V = \pi\left(\frac{R^4\omega^2}{4g\sin\theta} + \frac{g^3\cos^4\theta}{4\omega^6\sin\theta} - \frac{g^2k\cos^2\theta}{\omega^4} + R^2k + \frac{gk^2\sin\theta}{\omega^2}\right)$$

The derivation of Equation 2.15 begins with rearranging Equation 2.14:

$$k^2\left(\frac{g\sin\theta}{\omega^2}\right) + k\left(R^2 - \frac{g^2\cos^2\theta}{\omega^4}\right) + \frac{R^4\omega^2}{4g\sin\theta} + \frac{g^3\cos^4\theta}{4\omega^6\sin\theta} - \frac{V}{\pi} = 0$$

$$k^2 + k\left(\frac{\omega^2R^2}{g\sin\theta} - \frac{g\cos^2\theta}{\omega^2\sin\theta}\right) + \frac{R^4\omega^4}{4g^2\sin^2\theta} + \frac{g^2\cos^4\theta}{4\omega^4\sin^2\theta} - \frac{\omega^2V}{\pi g\sin\theta} = 0$$

The quadratic equation is then used to find k:

$$k = \frac{g\cos^2\theta}{2\omega^2\sin\theta} - \frac{\omega^2R^2}{2g\sin\theta}$$
$$\pm\frac{1}{2}\sqrt{\left(\frac{\omega^2R^2}{g\sin\theta} - \frac{g\cos^2\theta}{\omega^2\sin\theta}\right)^2 - 4\left(\frac{R^4\omega^4}{4g^2\sin^2\theta} + \frac{g^2\cos^4\theta}{4\omega^4\sin^2\theta} - \frac{\omega^2V}{\pi g\sin\theta}\right)}$$

$$k=\frac{g\cos^2\theta}{2\omega^2\sin\theta}-\frac{\omega^2R^2}{2g\sin\theta}$$

$$\pm\frac{1}{2}\sqrt{\frac{\omega^4R^4}{g^2\sin^2\theta}+\frac{g^2\cos^4\theta}{\omega^4\sin^2\theta}-\frac{2R^2\cos^2\theta}{\sin^2\theta}-\frac{R^4\omega^4}{g^2\sin^2\theta}-\frac{g^2\cos^4\theta}{\omega^4\sin^2\theta}+\frac{4\omega^2V}{\pi g\sin\theta}}$$

$$k=\frac{g\cos^2\theta}{2\omega^2\sin\theta}-\frac{\omega^2R^2}{2g\sin\theta}\pm\frac{1}{2}\sqrt{-\frac{2R^2\cos^2\theta}{\sin^2\theta}+\frac{4\omega^2V}{\pi g\sin\theta}}$$

$$k=\frac{g\cos^2\theta}{2\omega^2\sin\theta}-\frac{\omega^2R^2}{2g\sin\theta}\pm\sqrt{\frac{\omega^2V}{\pi g\sin\theta}-\frac{R^2\cos^2\theta}{2\sin^2\theta}}$$

The case of the ± being negative would result in h almost always being negative, a solution that is not of interest here, and hence the ± is positive. This gives

Equation 2.15

$$h=\frac{\omega^2}{2g\sin\theta}(r^2-R^2)-r\cos\phi\cot\theta+\frac{g\cos^2\theta}{2\omega^2\sin\theta}+\sqrt{\frac{\omega^2}{g\pi\sin\theta}V-\frac{1}{2}R^2\cot^2\theta}$$

The derivation of Equation 2.16 begins with rearranging Equation 2.15 to find r

$$r^2\left(\frac{\omega^2}{2g\sin\theta}\right)-r(\cos\phi\cot\theta)-\frac{R^2\omega^2}{2g\sin\theta}-h+\frac{g\cos^2\theta}{2\omega^2\sin\theta}+\sqrt{\frac{\omega^2}{g\pi\sin\theta}V-\frac{1}{2}R^2\cot^2\theta}$$
$$=0$$

$$r^2-r\left(\frac{2g}{\omega^2}\cos\phi\cos\theta\right)-R^2-\frac{2gh\sin\theta}{\omega^2}+\frac{g^2\cos^2\theta}{\omega^4}+\sqrt{\frac{4g\sin\theta}{\omega^2\pi}V-\frac{2g^2R^2\cos^2\theta}{\omega^4}}=0$$

This is then solved using the quadratic equation to give:

$$r=-\frac{-\frac{2g\cos\phi\cos\theta}{\omega^2}}{2}$$

$$\pm\frac{1}{2}\sqrt{\left(-\frac{2g}{\omega^2}\cos\phi\cos\theta\right)^2-4\cdot\left(-R^2-\frac{2gh\sin\theta}{\omega^2}+\frac{g^2\cos^2\theta}{\omega^4}+\sqrt{\frac{4g\sin\theta}{\omega^2\pi}V-\frac{2g^2R^2\cos^2\theta}{\omega^4}}\right)}$$

$$r=\frac{g\cos\phi\cos\theta}{\omega^2}$$

$$\pm\frac{1}{2}\sqrt{\frac{4g^2}{\omega^4}\cos^2\phi\cos^2\theta+4\cdot\left(R^2+\frac{2gh\sin\theta}{\omega^2}-\frac{g^2\cos^2\theta}{\omega^4}-\sqrt{\frac{4g\sin\theta}{\omega^2\pi}V-\frac{2g^2R^2\cos^2\theta}{\omega^4}}\right)}$$

$$r = \frac{g\cos\phi\cos\theta}{\omega^2} \pm \sqrt{R^2 + \frac{2gh\sin\theta}{\omega^2} - \frac{g^2\cos^2\theta}{\omega^4}\sin^2\phi - \sqrt{\frac{4gV\sin\theta}{\omega^2\pi} - \frac{2g^2R^2\cos^2\theta}{\omega^4}}}$$

f_t is then calculated using $f_t = R - r$

Equation 2.16

$$\begin{aligned} f_t = R &- \frac{g\cos\phi\cos\theta}{\omega^2} \\ &\mp \sqrt{R^2 + \frac{2gh\sin\theta}{\omega^2} - \frac{g^2\cos^2\theta}{\omega^4}\sin^2\phi - \sqrt{\frac{4g\sin\theta}{\omega^2\pi}V - \frac{2g^2R^2\cos^2\theta}{\omega^4}}} \end{aligned}$$

Appendix B – Neutron imaging data

Table B.1: Experimental (Exp.) and theoretical (Theor.) data measured for the film thickness of H_2O (1 mL) in the VFD (θ = 45°), as measured according to the dynamic methodology described in chapter 3.3. The values listed are in micrometres (μm).

ω (rpm)	Exp.	Theor.	Rpm	Exp.	Theor.	Rpm	Exp.	Theor.
2000	567	589	2950	483	453	3900	392	361
2050	525	589	3000	467	447	3950	450	357
2100	567	580	3050	475	441	4000	375	353
2150	525	571	3100	475	436	4050	350	349
2200	533	562	3150	433	430	4100	425	346
2250	558	554	3200	458	425	4150	358	342
2300	500	545	3250	425	419	4200	367	339
2350	500	537	3300	492	414	4250	367	335
2400	467	529	3350	425	409	4300	358	332
2450	533	521	3400	450	404	4350	408	329
2500	492	514	3450	383	400	4400	325	325
2550	525	506	3500	417	395	4450	358	322
2600	492	499	3550	425	390	4500	358	319
2650	458	492	3600	442	386	4550	292	316
2700	433	485	3650	400	381	4600	308	313
2750	458	478	3700	392	377	4650	383	310
2800	475	472	3750	358	373	4700	358	307
2850	500	465	3800	383	369	4750	367	304
2900	458	459	3850	383	365	4800	325	302

Table B.2: Experimental (Exp.) and theoretical (Theor.) data measured for the maximum film height of H_2O (1 mL) in the VFD ($\theta = 45°$), as measured according to the dynamic methodology described in chapter 3.3. The values listed are in millimetres (mm).

ω (rpm)	Exp.	Theor.	Rpm	Exp.	Theor.	Rpm	Exp.	Theor.
2000	48.21	45.65	2950	70.37	66.75	3900	89.73	87.95
2050	49.06	46.75	3000	71.27	67.85	3950	88.20	89.05
2100	51.16	47.85	3050	70.67	68.95	4000	90.43	90.25
2150	52.00	48.95	3100	73.68	70.15	4050	91.07	91.35
2200	52.92	50.05	3150	74.87	71.25	4100	92.27	92.45
2250	54.23	51.15	3200	76.89	72.35	4150	92.84	93.55
2300	55.99	52.25	3250	79.79	73.45	4200	90.97	94.65
2350	56.40	53.35	3300	79.61	74.55	4250	93.60	95.85
2400	58.10	54.55	3350	79.52	75.65	4300	94.88	96.95
2450	57.77	55.65	3400	81.54	76.85	4350	96.62	98.05
2500	60.57	56.75	3450	80.75	77.95	4400	96.39	99.15
2550	60.00	57.85	3500	84.22	79.05	4450	97.71	100.25
2600	63.81	58.95	3550	84.73	80.15	4500	99.14	101.35
2650	63.17	60.05	3600	85.10	81.25	4550	100.25	102.55
2700	64.22	61.15	3650	83.92	82.35	4600	99.56	103.65
2750	66.89	62.35	3700	90.27	83.55	4650	103.10	104.75
2800	66.23	63.45	3750	88.03	84.65	4700	102.79	105.85
2850	68.77	64.55	3800	85.66	85.75	4750	104.88	106.95
2900	68.42	65.65	3850	89.30	86.85	4800	103.93	108.15

Table B.3: Experimental (Exp.) and theoretical (Theor.) data measured for the film thickness of toluene (1 mL) in the VFD ($\theta = 45°$), as measured according to the high resolution methodology described in chapter 3.5. The values listed are in micrometres (μm).

	h = 7.5 mm			h = 15.8 mm		
ω (rpm)	Exp.	Theor.	Exp. Error	Exp.	Theor.	Exp. Error
1000	1030	1241	64	468	573	51
2000	673	717	77	452	555	54
3000	491	498	86	394	428	61
4000	325	381	48	279	342	61
5000	321	309	45	244	284	64
6000	270	259	38	200	242	38
7000	197	224	61	273	211	54
8000	222	197	42	171	187	41
9000	203	175	29	276	168	64

Table B.4: Experimental (Exp.) and theoretical (Theor.) data measured for the film thickness of 1:1 water:glycerol (1 mL) in the VFD ($\theta = 45°$), as measured according to the high resolution methodology described in chapter 3.5. The values listed are in micrometres (μm).

	h = 7.5 mm			h = 15.8 mm		
ω (rpm)	Exp.	Theor.	Exp. Error	Exp.	Theor.	Exp. Error
1000	1175	1241	115	No data	No data	No data
2000	693	717	67	585	555	109
3000	515	498	73	494	428	106
4000	410	381	89	388	342	58
5000	311	309	92	352	284	66
6000	254	259	61	286	242	66
7000	215	224	86	268	211	98
8000	247	197	80	272	187	87
9000	1175	1241	115	585	555	109

Table B.5: Experimental (Exp.) and theoretical (Theor.) data measured for the film thickness of propylene glycol (1 mL) in the VFD (θ = 45°), as measured according to the high resolution methodology described in chapter 3.5. The values listed are in micrometres (µm).

	h = 7.5 mm			*h* = 15.8 mm		
ω (rpm)	Exp.	Theor.	Exp. Error	Exp.	Theor.	Exp. Error
1000	1062	1241	60	243	573	44
2000	705	717	35	526	555	67
3000	648	498	80	491	428	38
4000	444	381	67	395	342	76
5000	358	309	57	424	284	35
6000	301	259	57	252	242	48
7000	269	224	38	233	211	60
8000	209	197	29	202	187	60
9000	1062	1241	60	243	573	44

Table B.6: Experimental (Exp.) and theoretical (Theor.) data measured for the film thickness of glycerol (1 mL) in the VFD (θ = 45°), as measured according to the high resolution methodology described in chapter 3.5. The values listed are in micrometres (µm).

	h = 7.5 mm			*h* = 15.8 mm		
ω (rpm)	Exp.	Theor.	Exp. Error	Exp.	Theor.	Exp. Error
1000	860	1241	100	No data	No data	No data
2000	581	717	84	397	555	64
3000	No data	498	No data	No data	428	No data
4000	359	381	87	279	342	35
5000	301	309	80	279	284	67
6000	240	259	51	203	242	41
7000	240	224	45	164	211	61
8000	176	197	71	215	187	48
9000	195	175	84	397	555	64

Table B.7: Experimental and theoretical (Theor.) data measured for the maximum film height of various solvents (1 mL) in the VFD (θ = 45°), as measured according to the high resolution methodology described in chapter 3.5. The values listed are in millimetres (mm).

		Experimental data			
ω (rpm)	Theor.	Toluene	1:1 H_2O:glycerol	Propylene glycol	Glycerol
1000	24	24	17	22	18
2000	46	46	35	45	39
3000	68	71	57	44	No data
4000	90	87	75	68	76
5000	113	119	99	87	97
6000	135	140	137	136	108
7000	157	No data	No data	No data	135
8000	180	No data	No data	No data	138
9000	202	No data	No data	No data	No data

Table B.8: Experimental (Exp.) and theoretical (Theor.) data measured for the film thickness of water (1 mL) in the VFD (θ = 45°) in an uncoated tube, as measured according to the high resolution methodology described in chapter 3.5. The values listed are in micrometres (µm).

	h = 7.5 mm			h = 15.8 mm		
ω (rpm)	Exp.	Theor.	Exp. Error	Exp.	Theor.	Exp. Error
1000	1096	1215	128	No data	No data	No data
2000	743	715	81	510	554	72
3000	487	498	62	410	428	91
4000	362	381	131	410	342	84
5000	315	309	66	310	284	78
6000	325	259	94	278	242	59
7000	269	224	119	228	211	78
8000	247	197	84	250	187	75
9000	278	175	84	263	168	100

Table B.9: Experimental (Exp.) and theoretical (Theor.) data measured for the film thickness of water (1 mL) in the VFD (θ = 45°) in a hydrophobically coated tube, as measured according to the high resolution methodology described in chapter 3.5. The values listed are in micrometres (µm).

	h = 7.5 mm			*h* = 15.8 mm		
ω (rpm)	Exp.	Theor.	Exp. Error	Exp.	Theor.	Exp. Error
1000	No data	No data	No data	No data	No data	No data
2000	1077	715	90	797	554	183
3000	723	498	116	611	428	87
4000	578	381	100	476	342	100
5000	430	309	87	443	284	55
6000	379	259	93	379	242	80
7000	356	224	109	302	211	93
8000	315	197	80	308	187	74
9000	289	175	87	305	168	71

Table B.10: Experimental (Exp.) and theoretical (Theor.) data measured for the film thickness of water (4 mL) in the VFD (θ = 45°) in an uncoated tube, as measured according to the high resolution methodology described in chapter 3.5. The values listed are in micrometres (µm).

	h = 7.5 mm			*h* = 15.8 mm		
ω (rpm)	Exp.	Theor.	Exp. Error	Exp.	Theor.	Exp. Error
2000	1651	1634	120	1487	1452	158
3000	1066	1087	159	1018	1011	149
4000	862	814	97	818	773	142
5000	686	651	117	682	625	136

Table B.11: Experimental (Exp.) and theoretical (Theor.) data measured for the film thickness of water (4 mL) in the VFD (θ = 45°) in a hydrophobically coated tube, as measured according to the high resolution methodology described in chapter 3.5. The values listed are in micrometres (μm).

	h = 7.5 mm			h = 15.8 mm		
ω (rpm)	Exp.	Theor.	Exp. Error	Exp.	Theor.	Exp. Error
2000	1838	1634	202	1494	1452	226
3000	1198	1087	122	1110	1011	158
4000	893	814	151	829	773	110
5000	703	651	109	678	625	119

Table B.12: Experimental and theoretical (Theor.) data measured for the maximum film height of water (1 mL, 4 mL) in the VFD (θ = 45°) in an uncoated tube (UCT) and a hydrophobically coated tube (HCT), as measured according to the high resolution methodology described in chapter 3.5. The values listed are in millimetres (mm).

Volume	1 mL	1 mL	1 mL	4 mL	4 mL	4 mL
Tube	N/A	UCT	HCT	N/A	UCT	HCT
ω (rpm)	Theor.	Exp.	Exp.	Theor.	Exp.	Exp.
1000	22.25	20.77	12.91	No data	No data	No data
2000	44.75	43.65	24.69	89.75	89.72	64.12
3000	67.25	76.77	37.67	134.75	134.47	94.81
4000	89.75	102.25	52.61	179.75	158.23	123.06
5000	112.25	124.59	65.88	No data	No data	No data
6000	134.75	140.92	81.11	No data	No data	No data
7000	157.25	No data	95.11	No data	No data	No data
8000	179.75	No data	103.85	No data	No data	No data
9000	202.25	No data	118.38	No data	No data	No data

Appendix C – SANS analysis of 5000 rpm and 7000 rpm

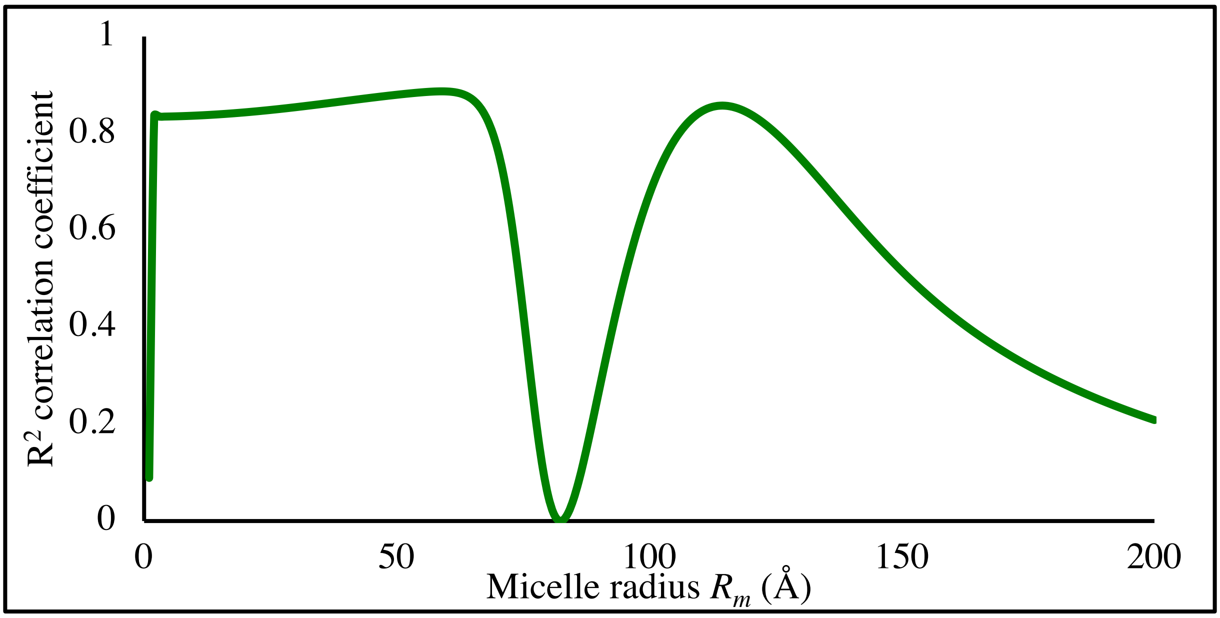

Fig. C.1: R^2 values of Model 1 fitted to SANS data of 5% w/w Pluronic P123 in D_2O in the VFD at ω = 5000 rpm.

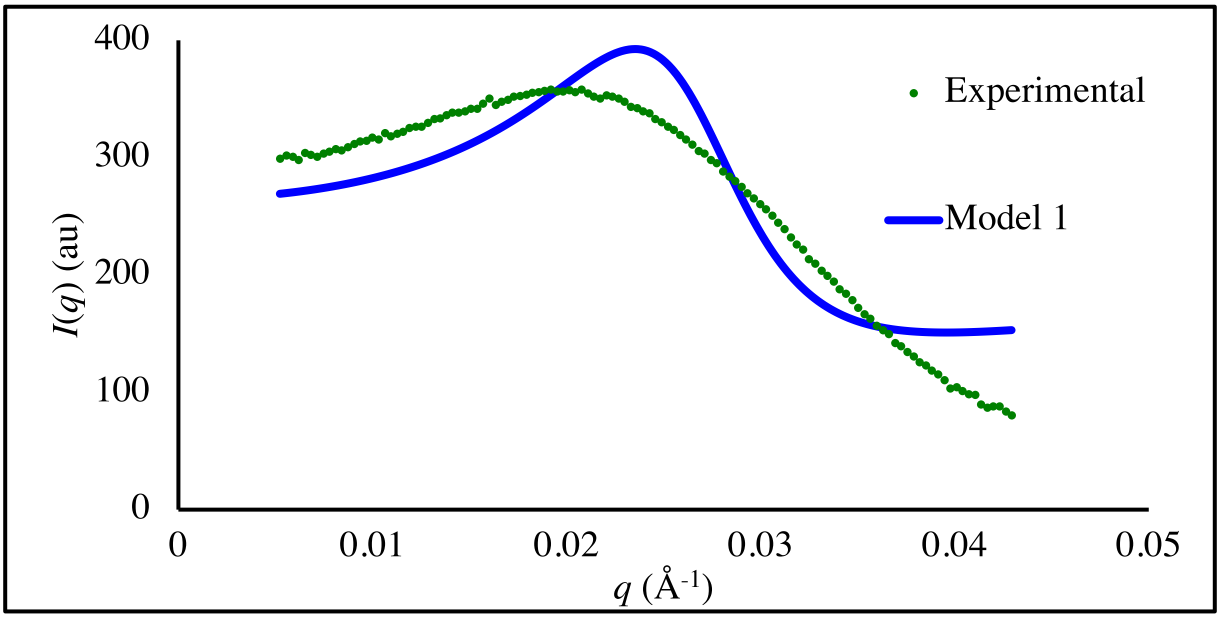

Fig. C.2: Best fit of Model 1 (R_m = 114 Å) for 5% w/w Pluronic P123 in D_2O in the VFD at ω = 5000 rpm, compared to experimental data.

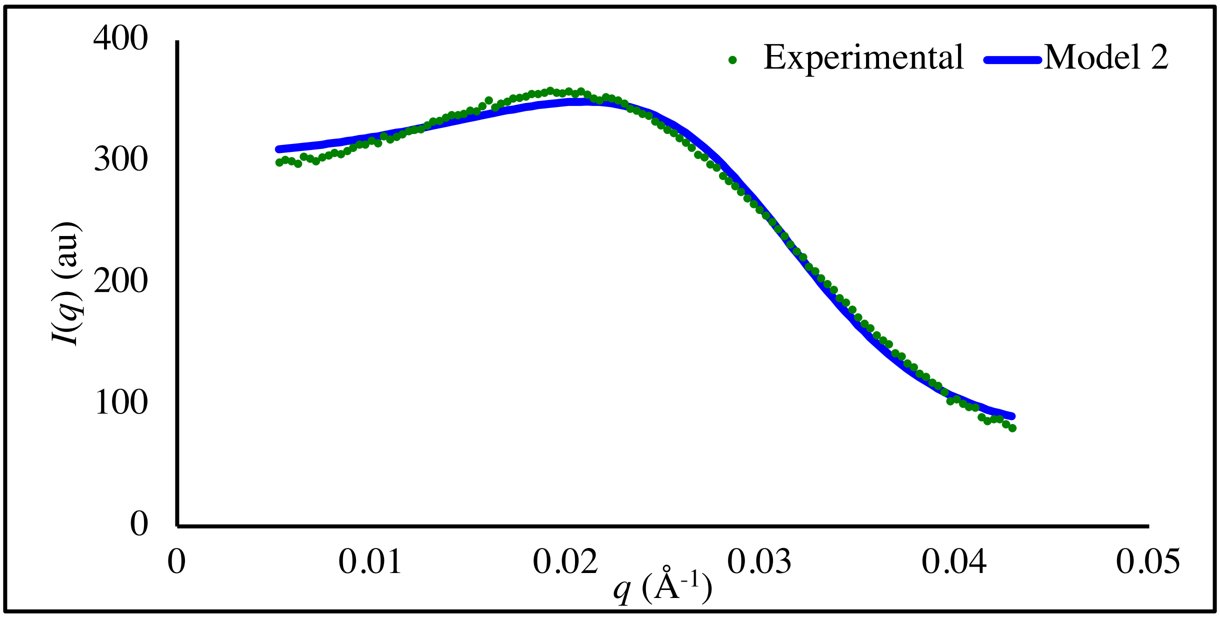

Fig. C.3: Best fit of Model 2 ($R_m = 92$ Å, $N = 104$) for 5% w/w Pluronic P123 in D_2O in the VFD at ω = 5000 rpm, compared to experimental data.

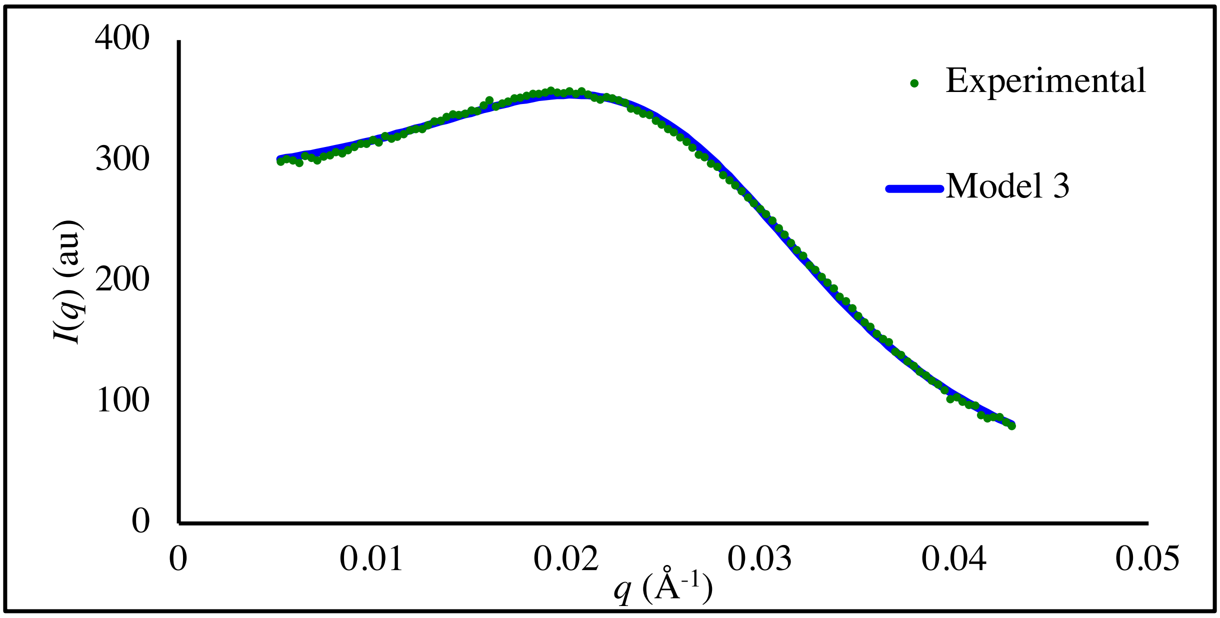

Fig. C.4: Best fit of Model 3 ($R_m = 96$ Å, $N = 168$) for 5% w/w Pluronic P123 in D_2O, in the VFD at ω = 5000 rpm, compared to experimental data.

Table C.1: Table of Model 3 parameter combinations for ω = 5000 rpm which give $R^2 > 0.998$. Parameter combinations which give a reasonable fit are highlighted.

R_m (Å)	N	R^2	R_m (Å)	N	R^2
96	168	0.99914	98	176	0.99857
96	167	0.99908	97	174	0.99853
97	171	0.99908	94	164	0.99850
96	169	0.99907	95	168	0.99849
97	170	0.99904	94	160	0.99842
95	165	0.99902	99	177	0.99841
97	172	0.99901	95	162	0.99840
95	166	0.99896	99	176	0.99838
95	164	0.99895	98	171	0.99838
96	166	0.99890	99	178	0.99832
96	170	0.99889	98	177	0.99828
97	169	0.99887	93	159	0.99827
98	174	0.99884	99	175	0.99825
97	173	0.99882	93	160	0.99823
98	173	0.99881	94	165	0.99822
95	167	0.99878	96	172	0.99820
98	175	0.99876	93	158	0.99817
95	163	0.99875	97	167	0.99814
94	162	0.99872	97	175	0.99814
94	163	0.99868	99	179	0.99813
98	172	0.99865	96	164	0.99812
94	161	0.99864	95	169	0.99809
96	171	0.99860	93	161	0.99806
96	165	0.99858	94	159	0.99805
97	168	0.99857			

Table C.2: Table of Model 4 parameter combinations for ω = 5000 rpm which give $R^2 > 0.9987$. Parameter combinations which give a reasonable fit are highlighted.

R_m (Å)	R_c (Å)	N	R^2	R_m (Å)	R_c (Å)	N	R^2
96	59	166	0.99909	95	61	156	0.99882
96	59	167	0.99909	96	60	161	0.99881
97	59	171	0.99906	97	61	164	0.99881
97	59	170	0.99906	95	60	161	0.99881
96	59	165	0.99902	95	61	157	0.99881
96	59	168	0.99902	97	61	165	0.99879
96	60	163	0.99900	96	61	162	0.99879
97	59	172	0.99900	95	58	163	0.99879
96	60	164	0.99899	96	62	157	0.99878
97	59	169	0.99899	96	60	166	0.99877
95	59	162	0.99896	97	61	163	0.99877
95	59	163	0.99896	97	60	165	0.99876
96	60	162	0.99895	95	61	155	0.99876
97	60	167	0.99895	95	59	165	0.99876
97	60	168	0.99893	96	62	158	0.99875
96	60	165	0.99891	95	59	160	0.99875
95	60	159	0.99890	96	62	156	0.99873
96	61	160	0.99890	95	62	153	0.99873
96	59	169	0.99890	97	60	170	0.99872
95	59	161	0.99890	98	60	171	0.99872
95	59	164	0.99889	96	61	158	0.99872
95	60	160	0.99889	94	58	162	0.99871
97	60	166	0.99889	95	61	158	0.99871
96	59	164	0.99889	96	59	170	0.99871
96	61	161	0.99888	98	60	172	0.99871
97	59	168	0.99886	94	58	161	0.99871
97	60	169	0.99886	95	62	154	0.99871
96	61	159	0.99885	97	61	166	0.99870
95	60	158	0.99884				

These modelled fits result in the following determination for the parameters, all of which are similar to those obtained for ω = 3000 rpm; $R_m = 97 \pm 1$ Å, $R_c = 60 \pm 1.5$ Å, $N = 171 \pm 4$, $t_s = 37 \pm 1$ Å, $a_1 = 0.93 \pm 0.07$, $a_2 = 0.208 \pm 0.005$.

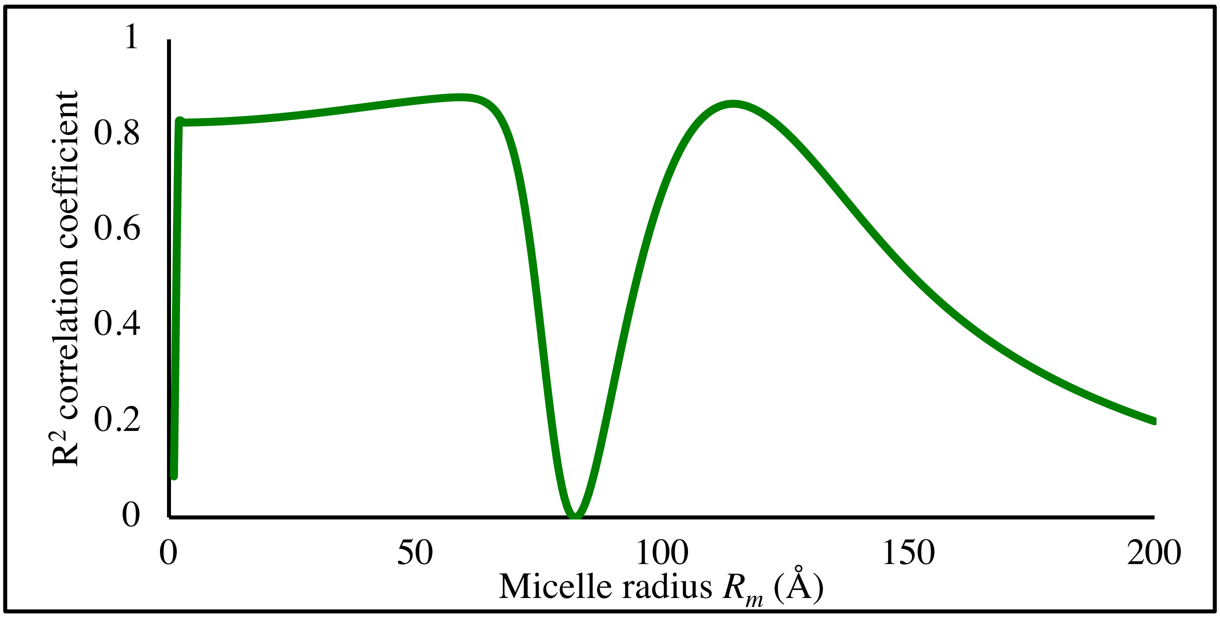

Fig. C.5: R^2 values of Model 1 fitted to SANS data of 5% w/w Pluronic P123 in D_2O in the VFD at ω = 7000 rpm.

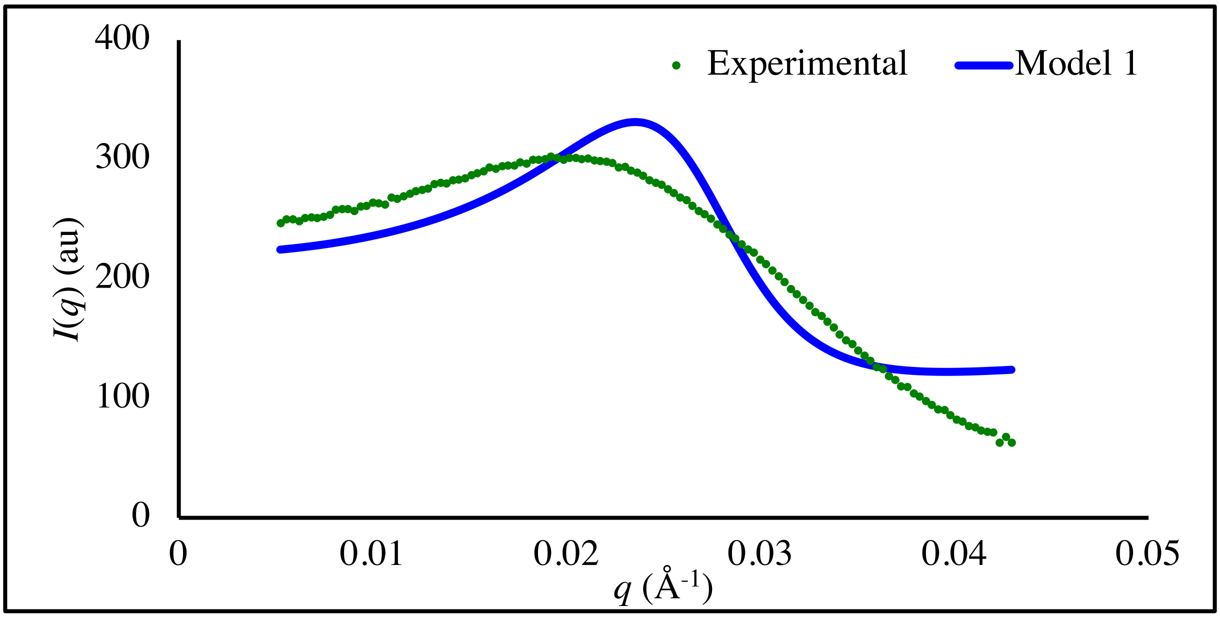

Fig. C.6: Best fit of Model 1 (R_m = 114 Å) for 5% w/w Pluronic P123 in D_2O in the VFD at ω = 7000 rpm, compared to experimental data.

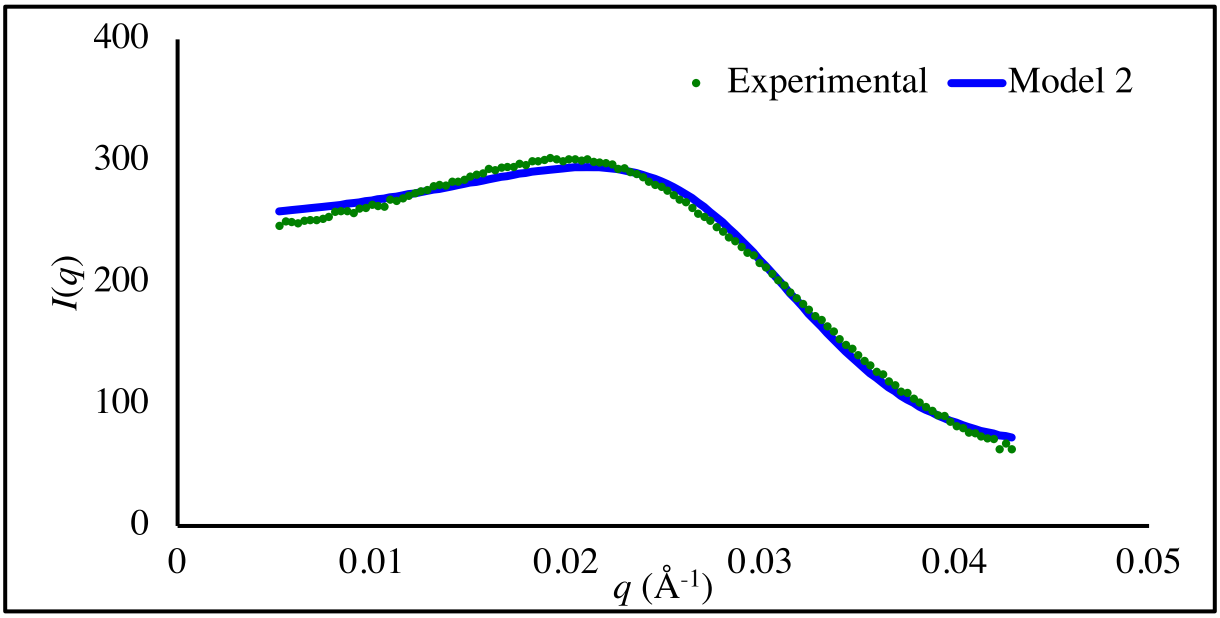

Fig. C.7: Best fit of Model 2 (R_m = 93 Å, N = 105) for 5% w/w Pluronic P123 in D_2O in the VFD at ω = 7000 rpm, compared to experimental data.

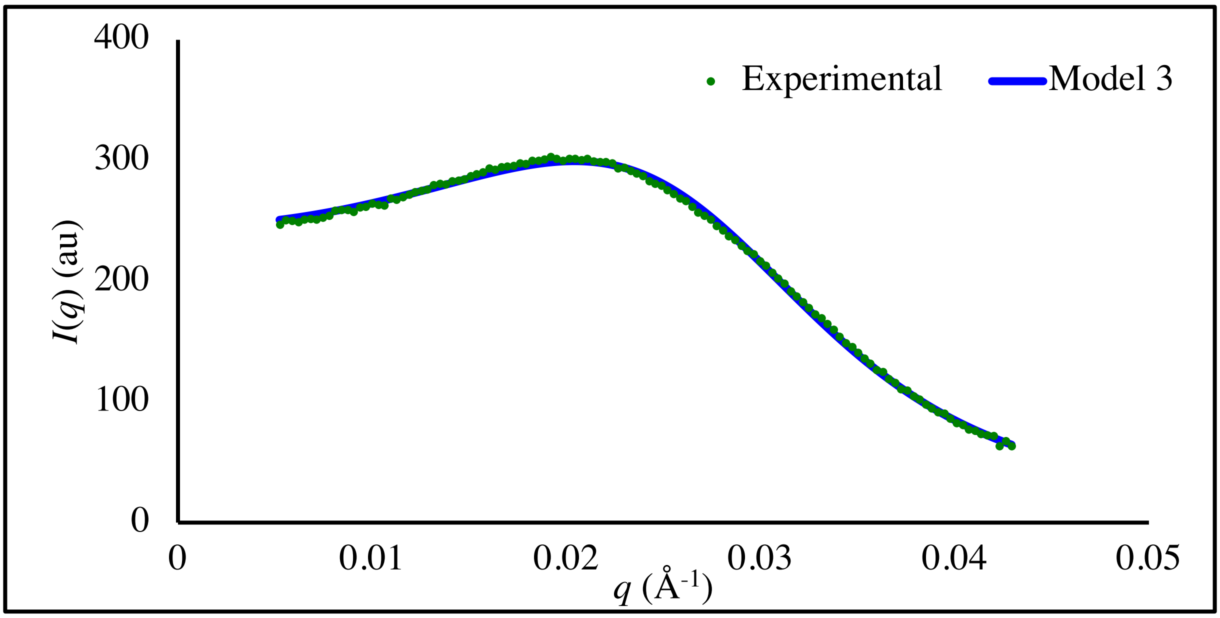

Fig. C.8: Best fit of Model 3 (R_m = 97 Å, N = 170) for 5% w/w Pluronic P123 in D_2O, in the VFD at ω = 7000 rpm, compared to experimental data.

Table C.3: Table of Model 3 parameter combinations for ω = 7000 rpm which give $R^2 > 0.998$. Parameter combinations which give a reasonable fit are highlighted.

R_m (Å)	N	R^2	R_m (Å)	N	R^2
97	170	0.99917	95	163	0.99858
98	173	0.99915	98	176	0.99857
97	169	0.99912	100	179	0.99852
98	172	0.99911	100	178	0.99851
97	171	0.9991	99	173	0.9985
98	174	0.99906	96	170	0.99847
96	167	0.99901	95	166	0.99845
98	171	0.99895	100	180	0.99842
96	168	0.99895	96	164	0.9984
97	168	0.99894	100	177	0.99838
96	166	0.99894	95	162	0.99835
99	176	0.99893	99	179	0.99834
97	172	0.99891	98	169	0.99824
99	175	0.99891	100	181	0.99822
98	175	0.99887	97	174	0.99821
99	177	0.99884	97	166	0.99817
99	174	0.99877	98	177	0.99817
96	169	0.99877	95	167	0.99816
96	165	0.99874	94	161	0.99815
95	164	0.99866	100	176	0.99814
98	170	0.99866	94	162	0.99812
99	178	0.99864	99	172	0.99811
97	167	0.99863	96	171	0.99807
95	165	0.99862	94	160	0.99804
97	173	0.99861			

Table C.4: Table of Model 4 parameter combinations for ω = 7000 rpm which give $R^2 > 0.9986$. Parameter combinations which give a reasonable fit are highlighted.

R_m (Å)	R_c (Å)	N	R^2	R_m (Å)	R_c (Å)	N	R^2
97	59	169	0.99915	96	61	160	0.99880
97	59	170	0.99913	96	61	158	0.99880
98	59	172	0.99911	98	61	165	0.99879
97	59	168	0.99910	97	62	161	0.99879
97	60	166	0.99906	96	60	164	0.99878
98	60	170	0.99904	97	60	169	0.99877
97	59	171	0.99904	98	62	164	0.99876
97	60	167	0.99903	98	61	169	0.99875
97	60	165	0.99903	96	60	160	0.99875
98	60	169	0.99901	98	60	173	0.99875
98	60	171	0.99901	96	62	156	0.99875
98	59	171	0.99901	98	62	163	0.99874
97	59	167	0.99899	98	60	167	0.99874
96	59	165	0.99897	97	60	163	0.99873
97	61	163	0.99896	99	60	172	0.99873
96	59	166	0.99895	99	60	176	0.99872
97	61	162	0.99893	96	59	168	0.99871
97	60	168	0.99893	96	62	155	0.99871
96	59	164	0.99893	98	62	165	0.99871
97	60	164	0.99892	97	62	158	0.99871
97	61	164	0.99892	96	62	157	0.99870
96	60	162	0.99891	97	63	157	0.99870
98	61	167	0.99891	96	61	161	0.99869
98	60	168	0.99891	99	61	171	0.99869
98	60	172	0.99891	96	61	157	0.99868
97	59	172	0.99889	97	63	156	0.99868
98	61	166	0.99889	97	62	162	0.99867
96	60	163	0.99888	99	61	170	0.99867
96	60	161	0.99887	98	62	162	0.99865
98	61	168	0.99887	97	63	158	0.99865
96	59	167	0.99887	99	61	172	0.99864
99	60	174	0.99885	97	61	160	0.99864
97	62	160	0.99884	95	59	161	0.99864
96	61	159	0.99884	96	63	153	0.99864
98	59	170	0.99883	97	61	166	0.99863
97	61	161	0.99882	98	61	164	0.99862
99	60	173	0.99882	95	59	162	0.99862
97	62	159	0.99881	96	60	165	0.99862
99	60	175	0.99881	96	59	162	0.99861

97	61	165	0.99881	95	60	158	0.99860
96	59	163	0.99880	95	58	163	0.99860
97	59	166	0.99880				

These modelled fits result in the following determination for the parameters, all of which are similar to those obtained for ω = 3000 rpm; $R_m = 98 \pm 1$ Å, $R_c = 60 \pm 1$ Å, $N = 172 \pm 6$, $t_s = 38 \pm 2$ Å, $a_1 = 0.94 \pm 0.07$, $a_2 = 0.204 \pm 0.005$.

Appendix D – NMR spectra

N-benzylbenzylimine – ^{1}H NMR

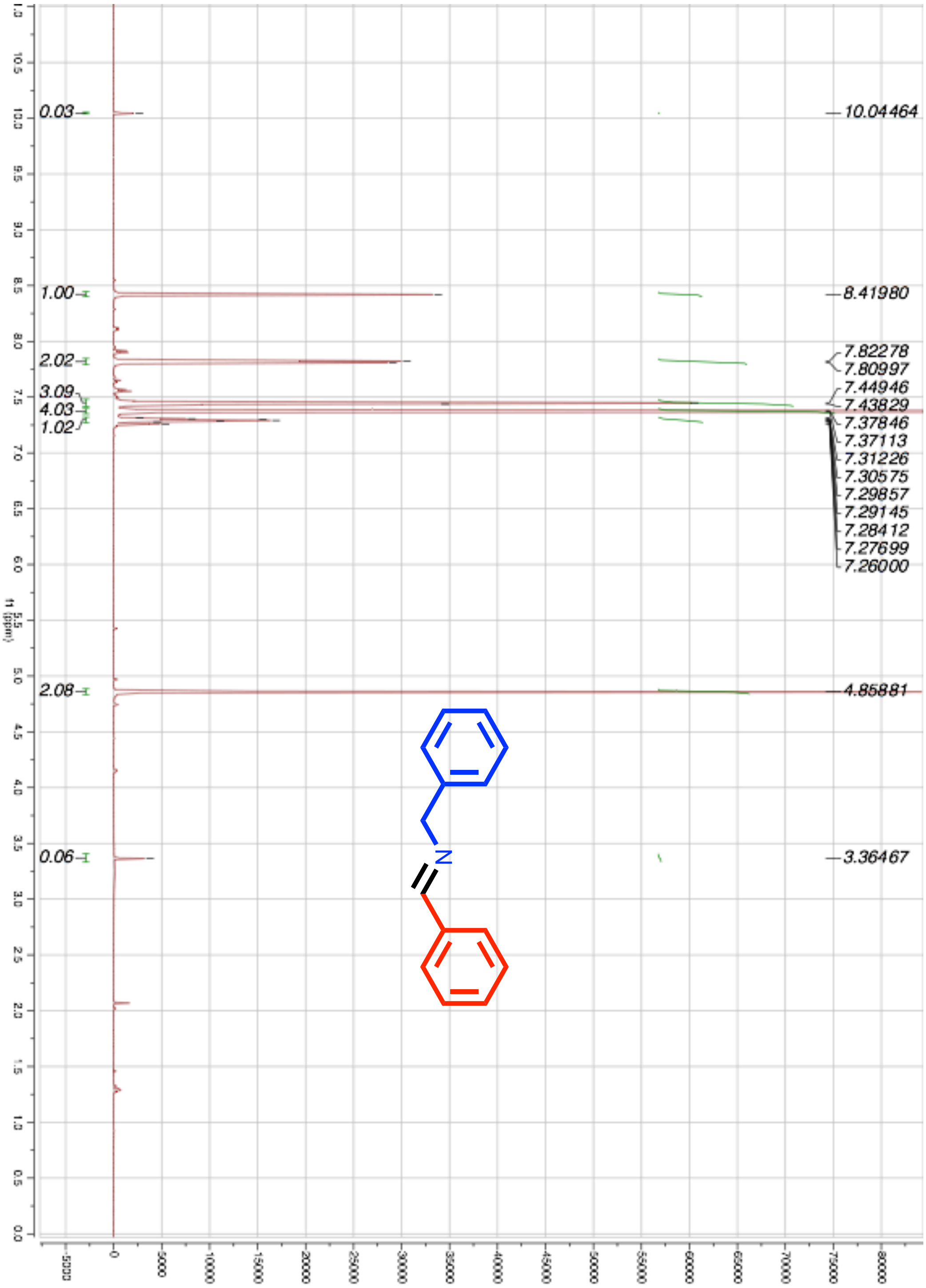

The singlets at 10.04 and 3.36 ppm indicate the presence of trace amounts of benzaldehyde and benzylamine respectively, and are taken into account in the yield calculation.

N-benzylbenzylimine – ^{13}C NMR

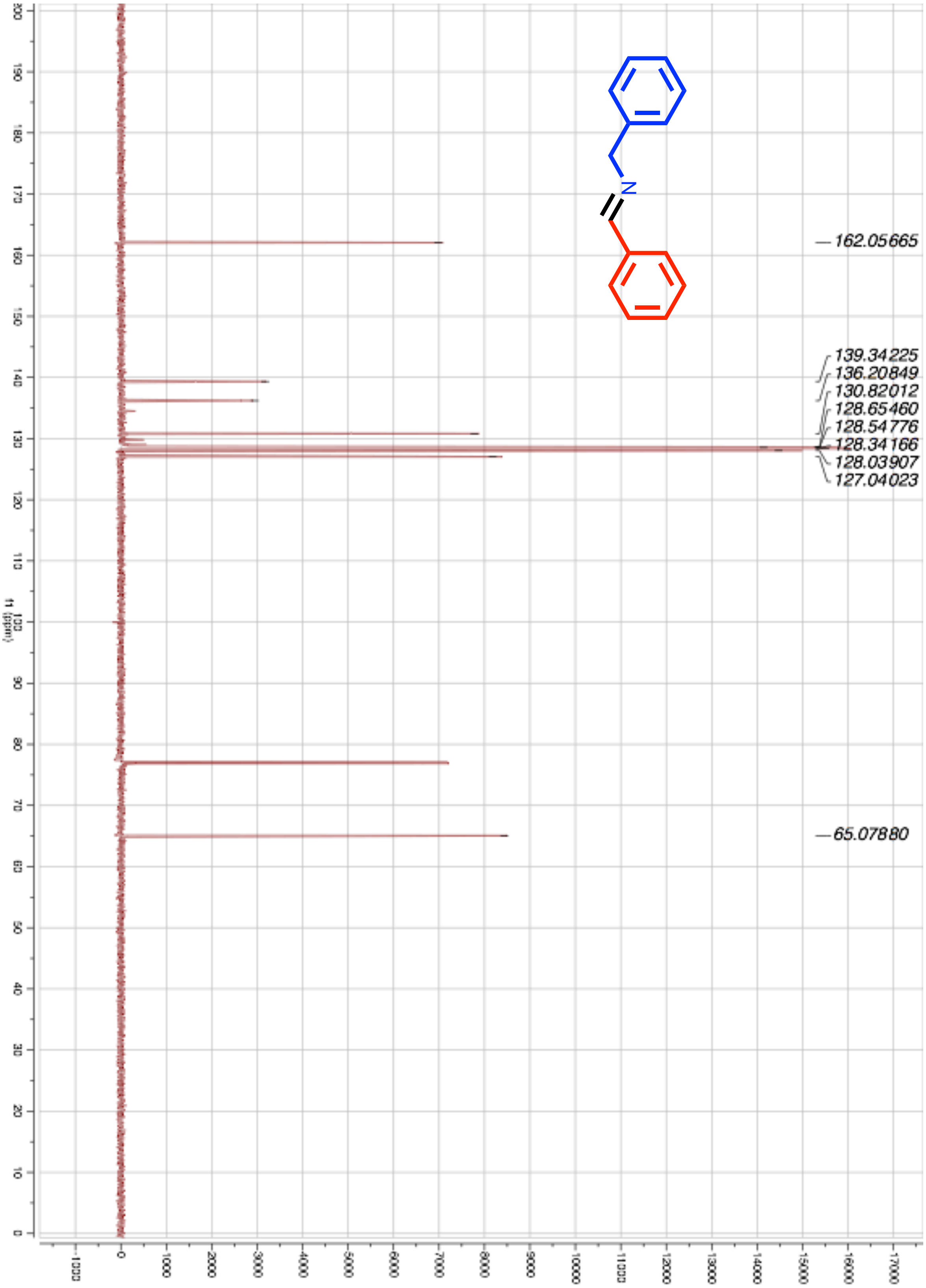

N-(1-naphthyl)cyclohexylimine – ^{1}H NMR

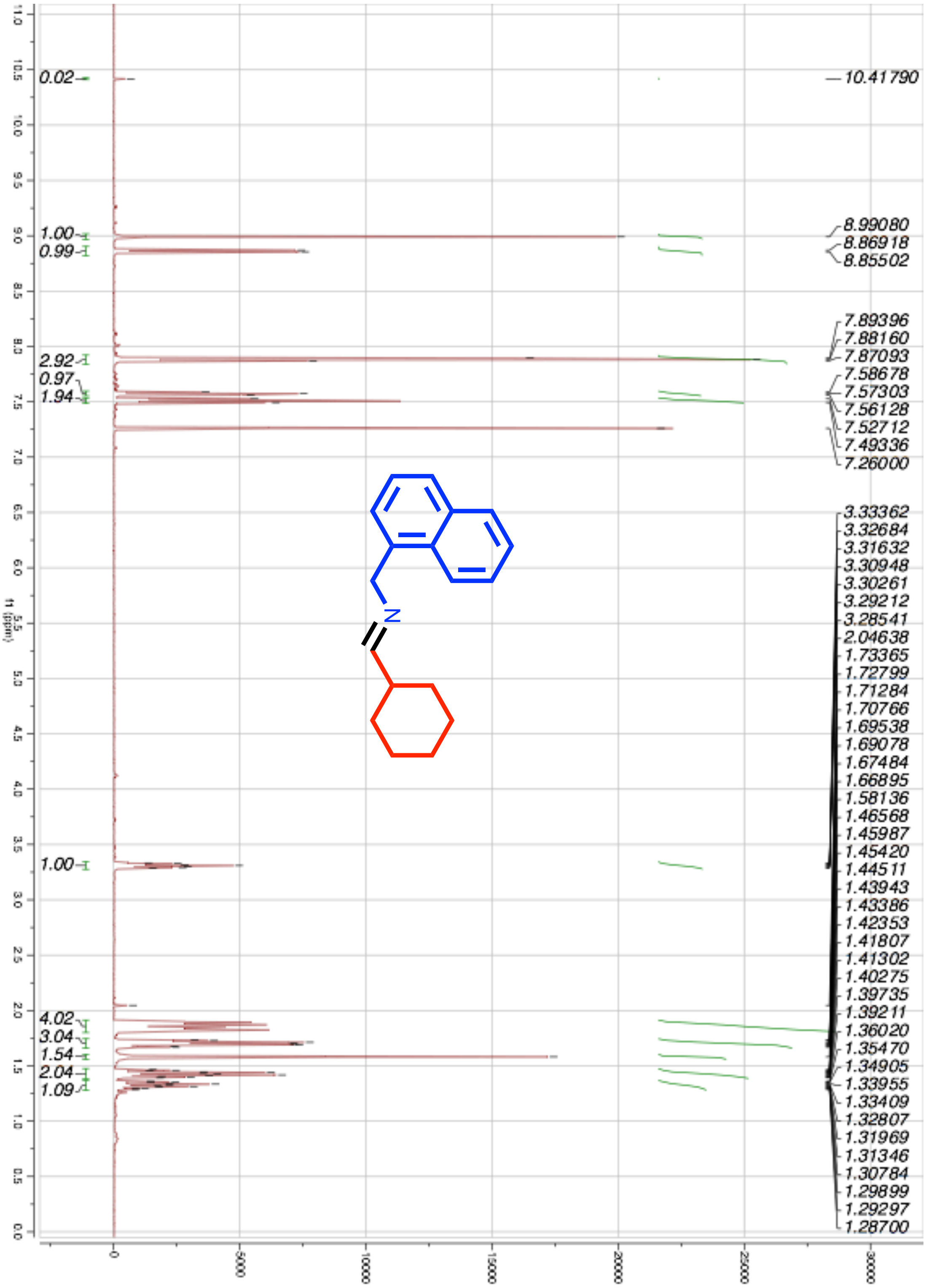

The singlet at 10.42 ppm indicates the presence of trace amounts of residual 1-naphthaldehyde, and the broad peak at 1.58 ppm is from by HDO in the NMR solvent.

N-(1-naphthyl)cyclohexylimine – ^{13}C NMR

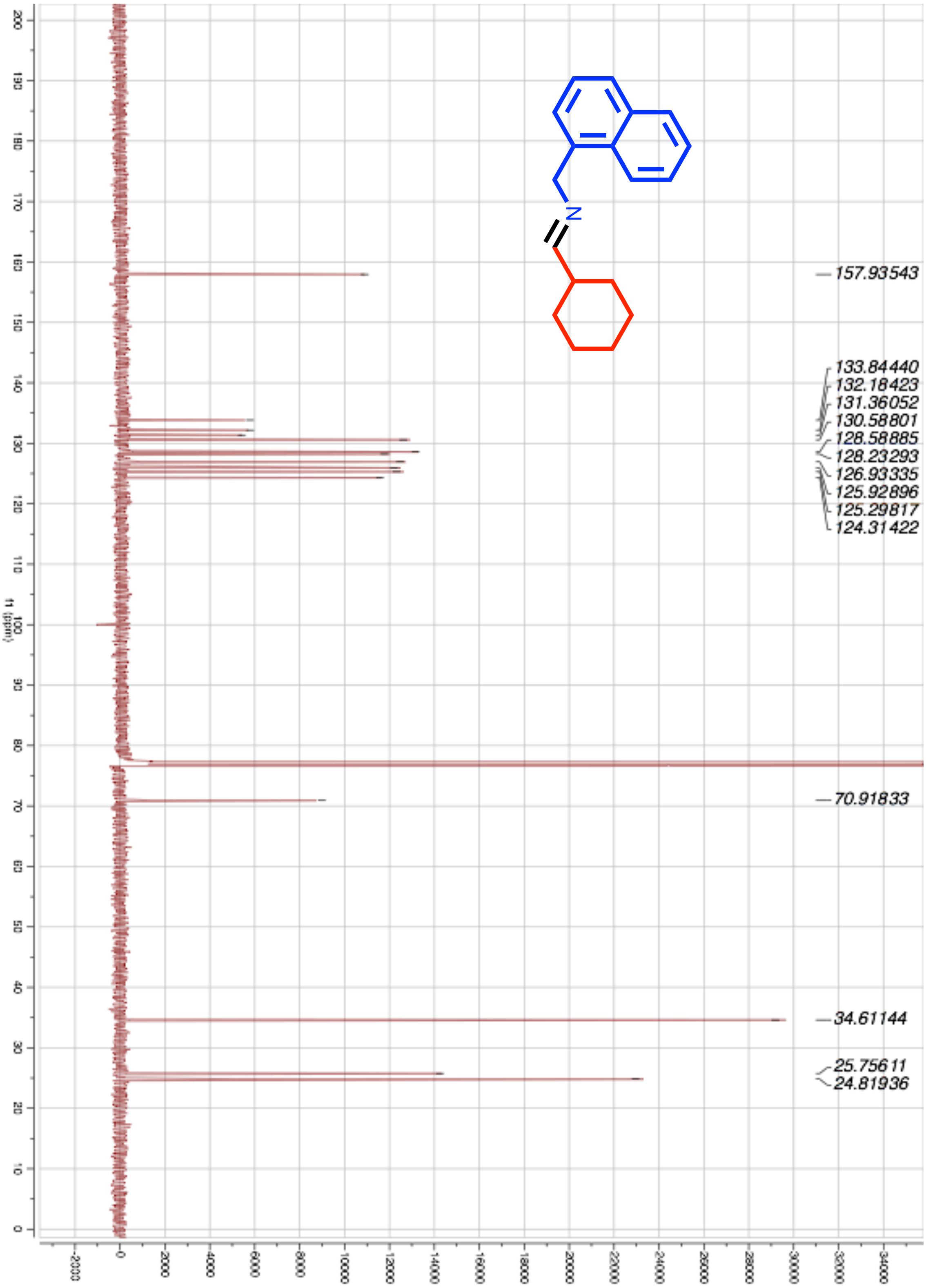

N-phenylbenzylimine – ¹H NMR

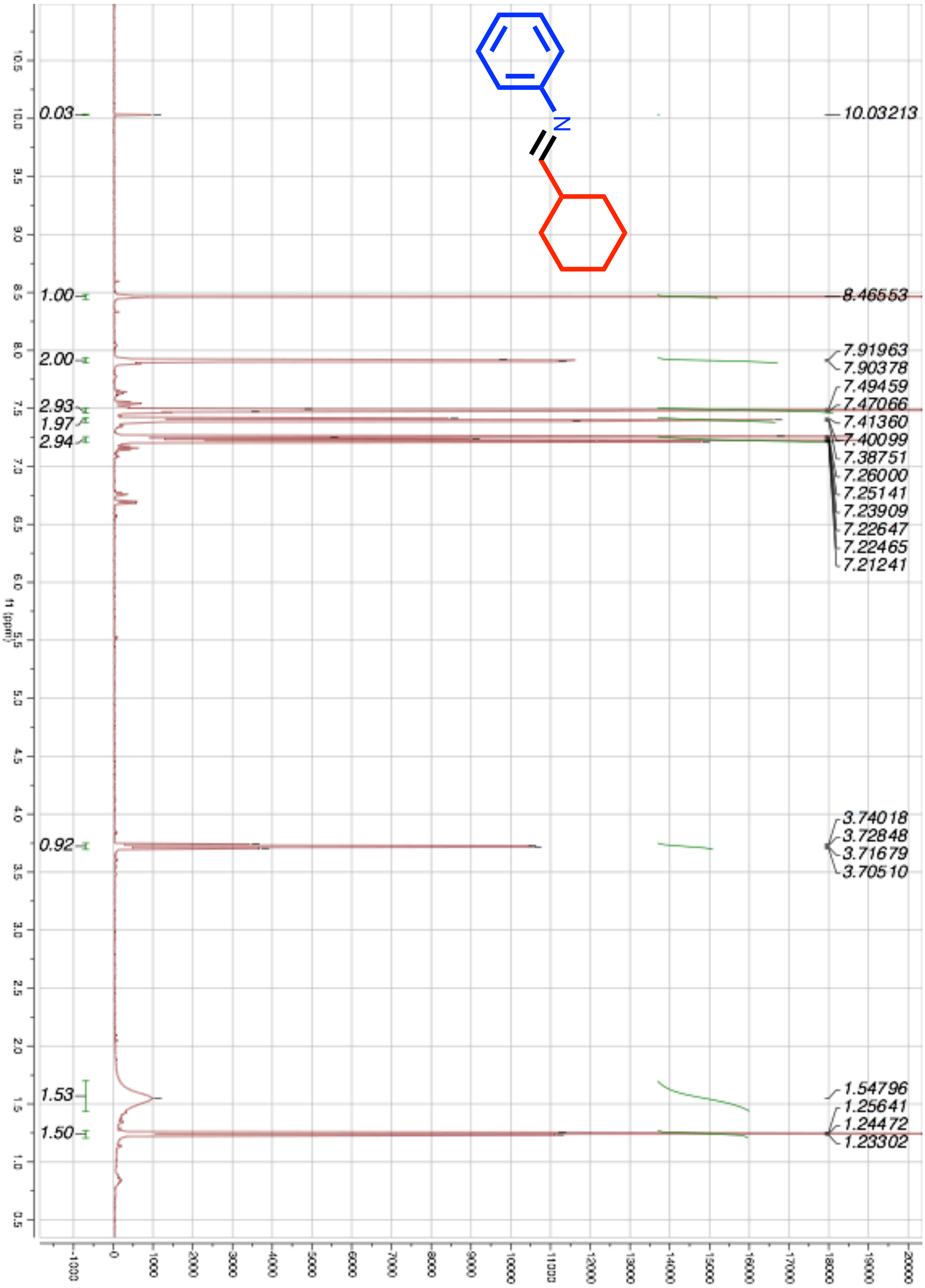

The singlet at 10.03 ppm indicates trace amounts of residual benzaldehyde. The peaks at 3.72, 1.55 and 1.24 ppm indicate the presence of residual ethanol from recrystallization (at 11% w/w), which is taken into account in the yield calculation.

N-phenylcyclohexylimine – ^{13}C NMR

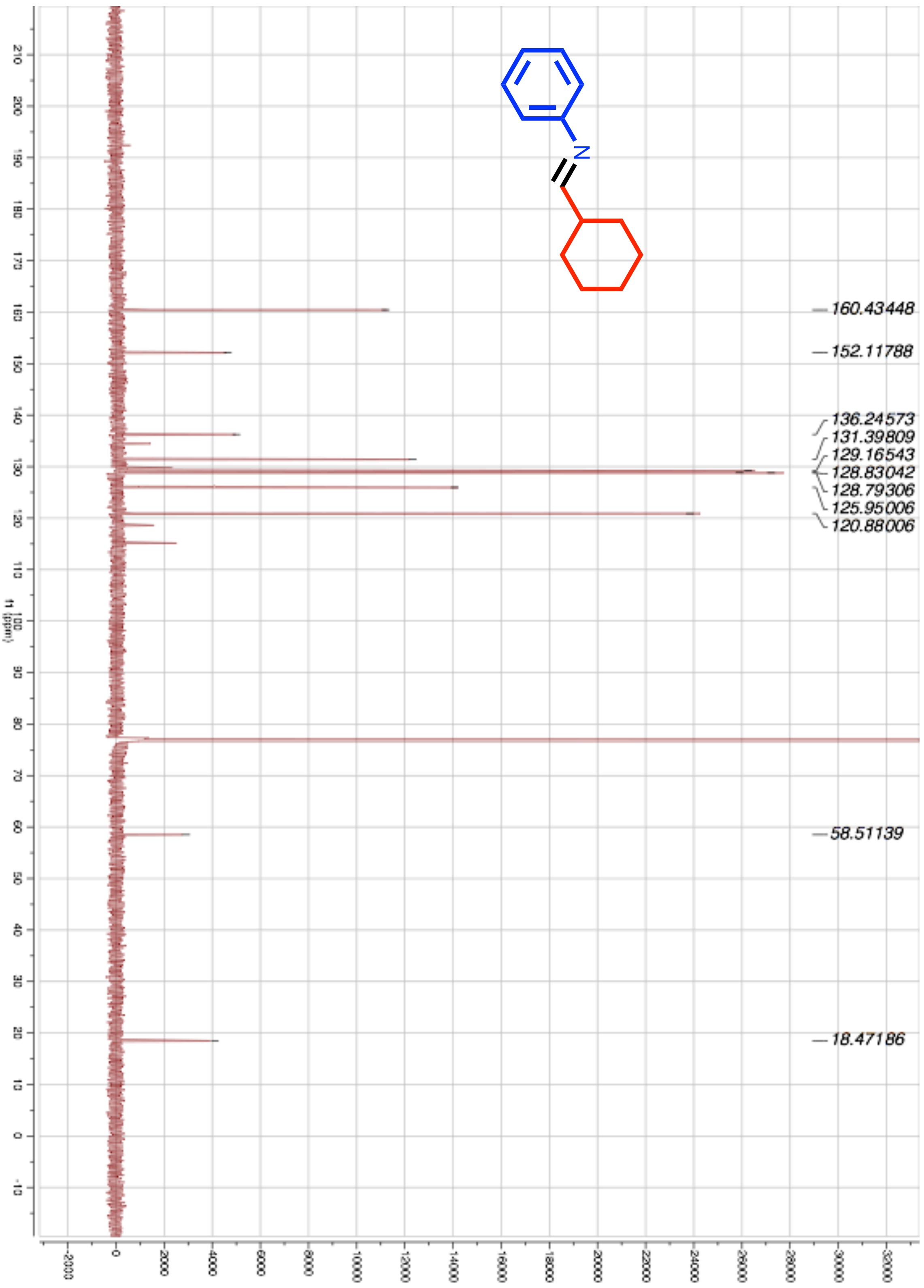

The peaks at 58.5 and 18.5 ppm are caused by the residual ethanol as noted above.

N-phenylbutanamide – ^{1}H NMR

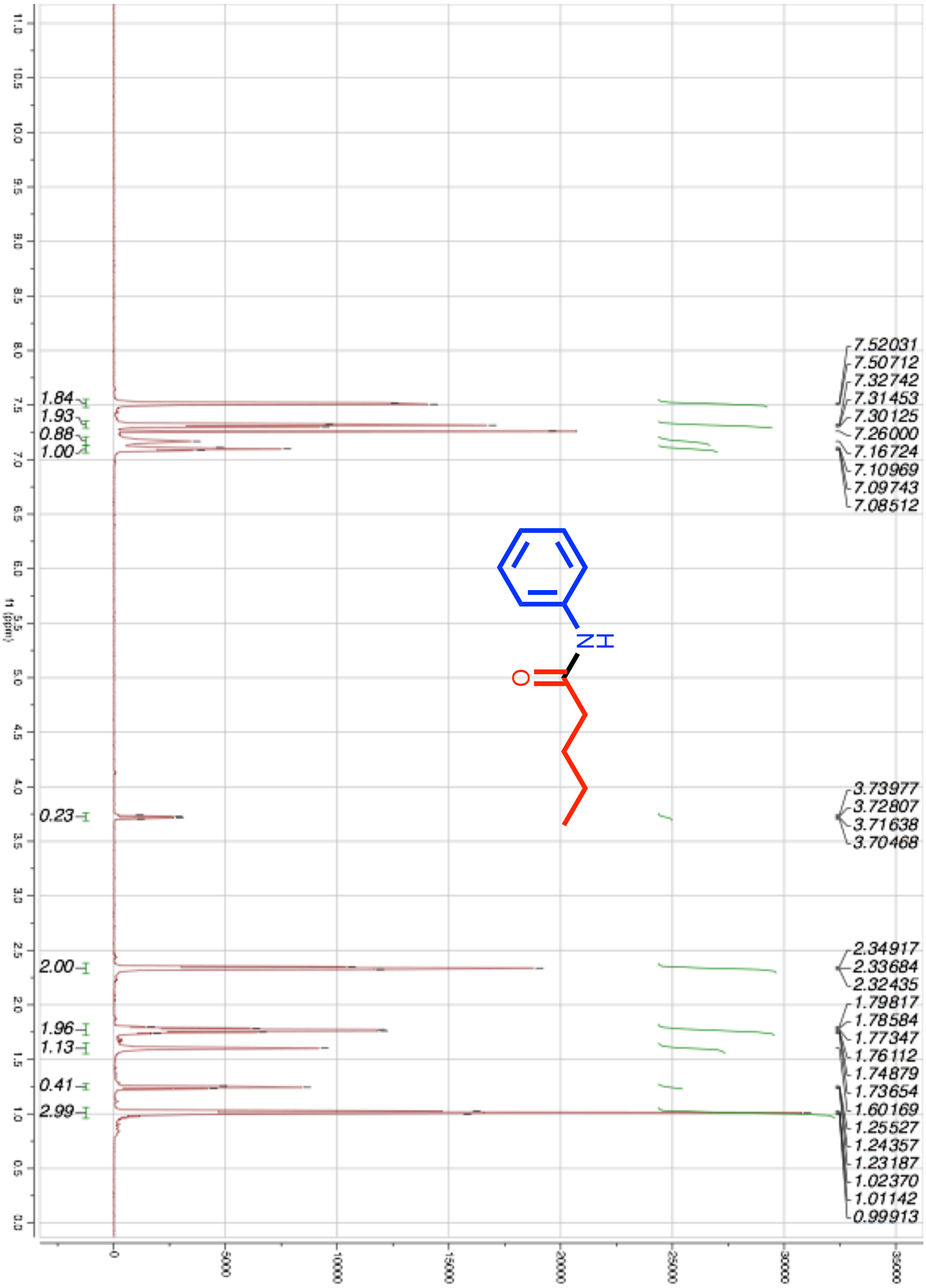

The peaks at 3.72 and 1.24 ppm indicate the presence of residual ethanol from the recrystallization (at 3% w/w), which is taken into account in the yield calculation. The peak at 1.60 ppm is from by HDO in the NMR solvent.

N-phenylbutanamide – ^{13}C NMR

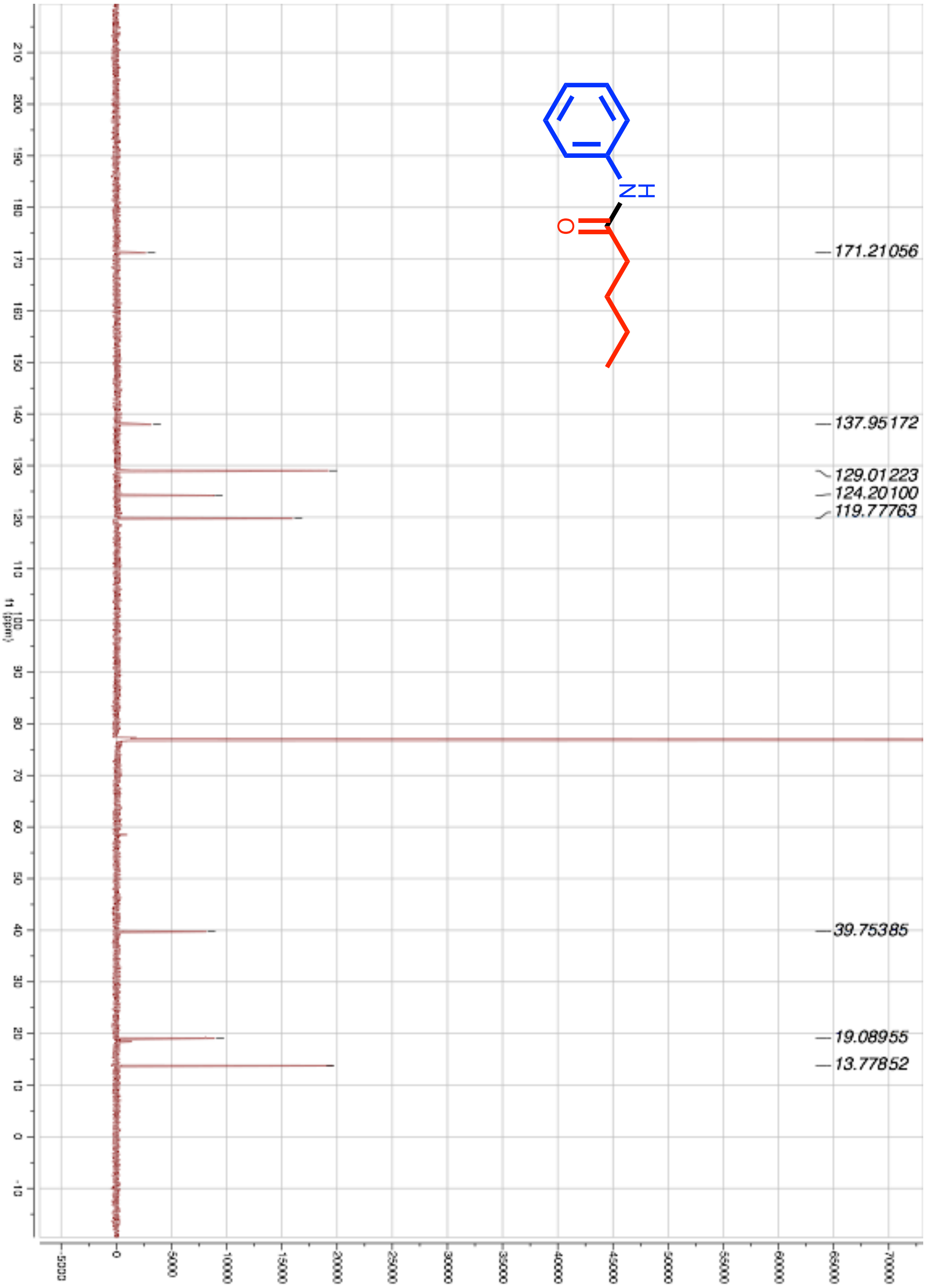

N-benzylbutanamide – ^{1}H NMR

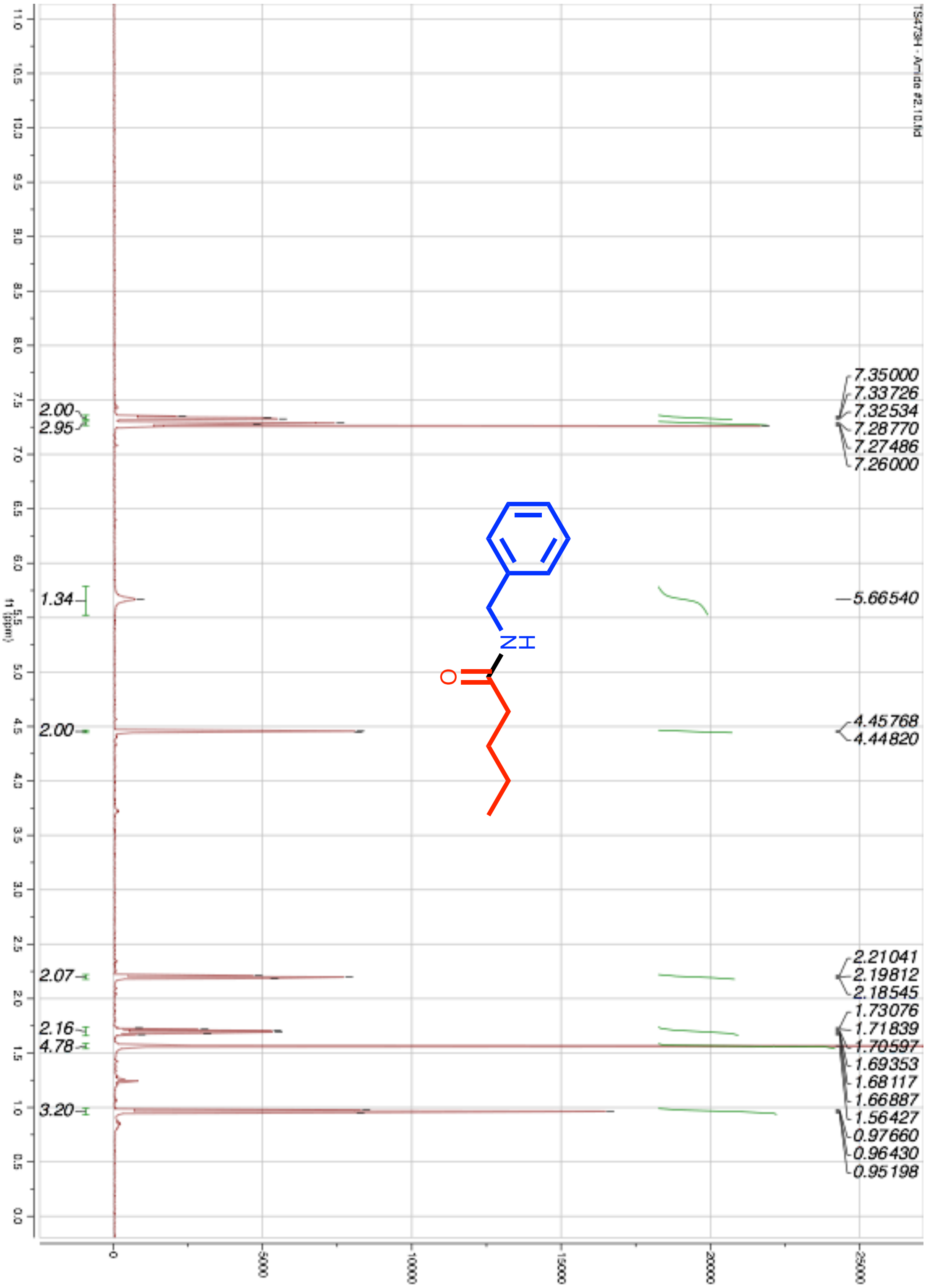

The peak at 1.56 ppm is from by HDO in the NMR solvent.

N-benzylbutanamide – ^{13}C NMR

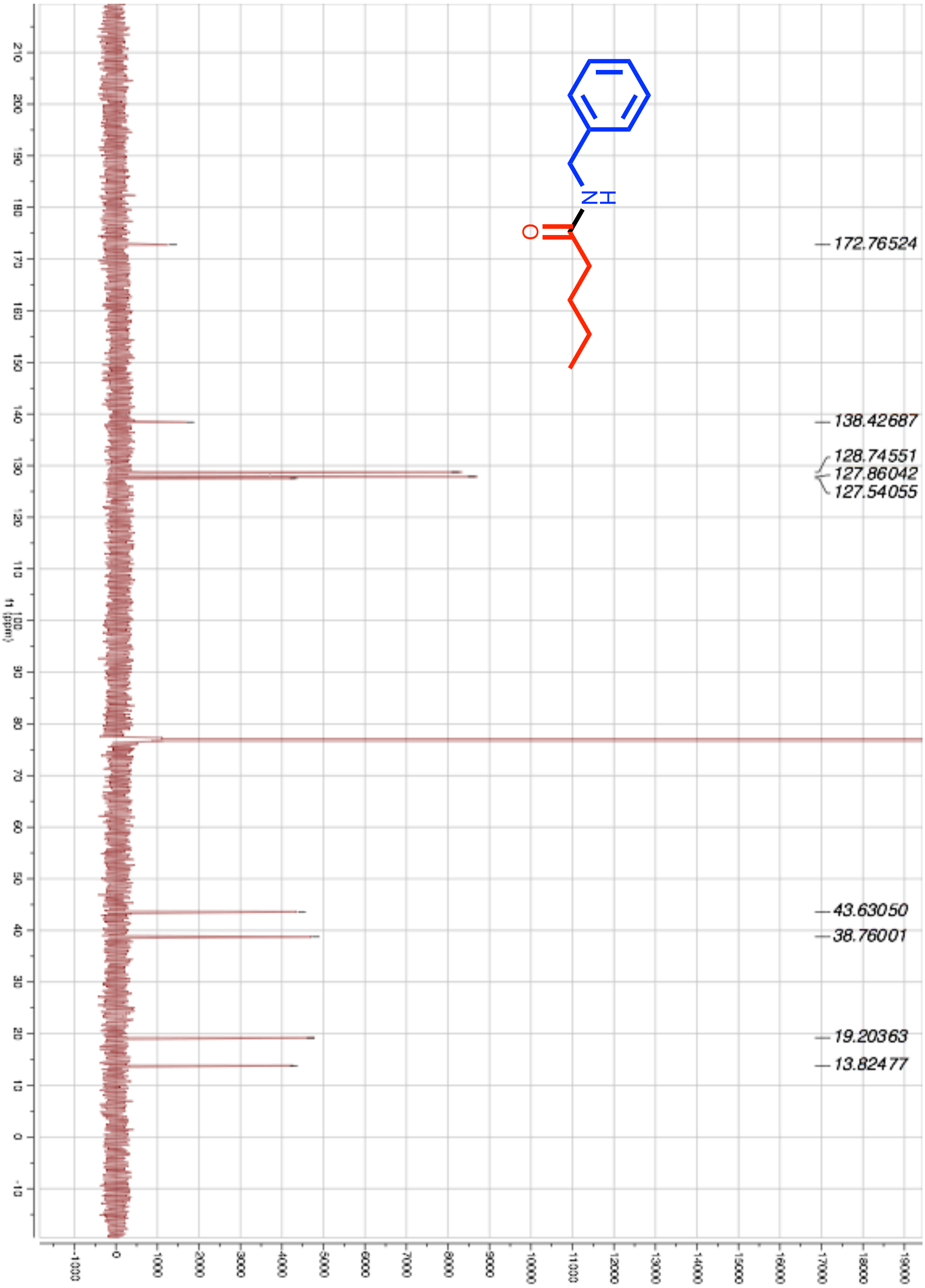

N-cyclohexylbutanamide – ¹H NMR

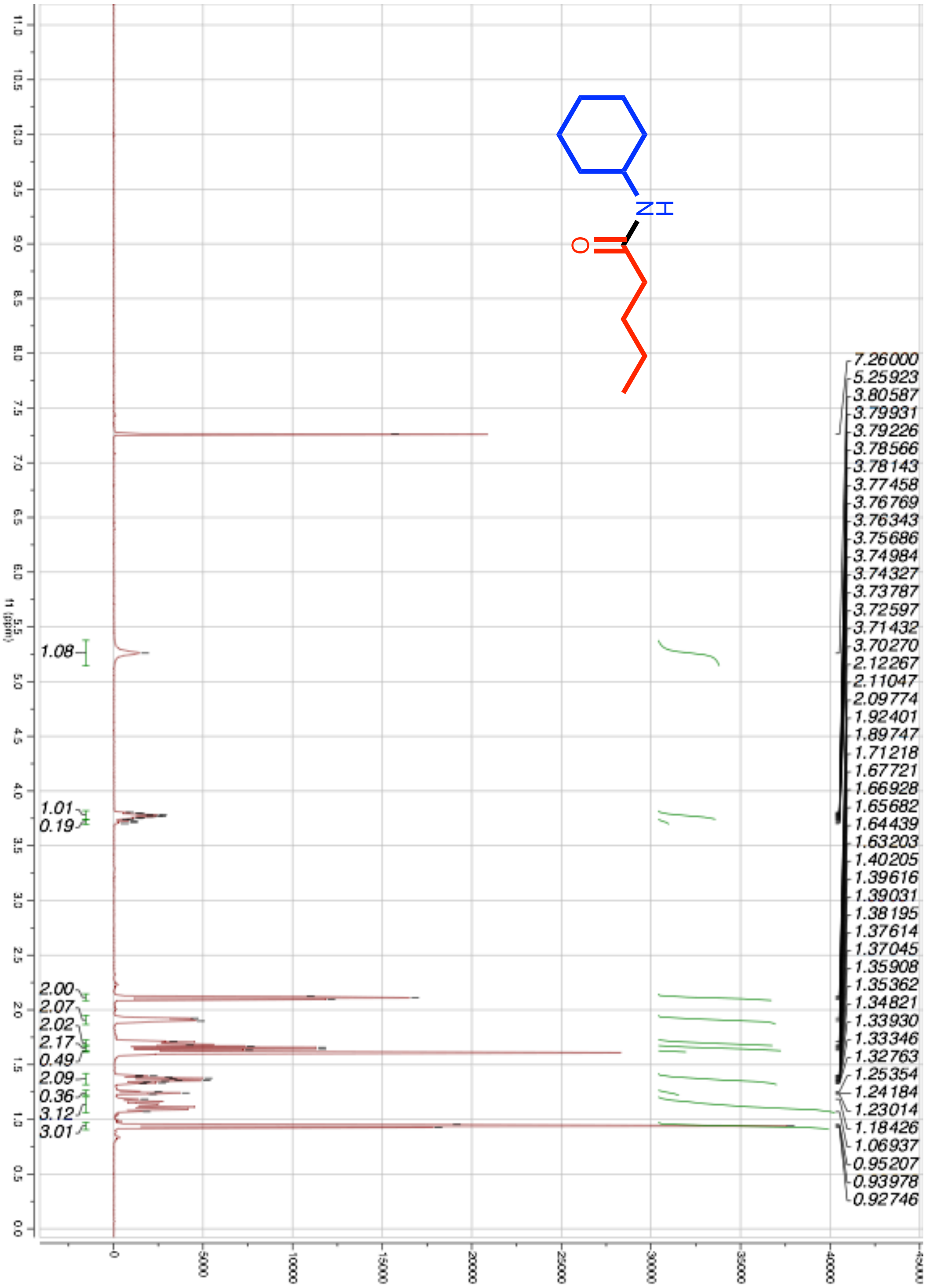

The peaks at 3.72 and 1.24 ppm indicate the presence of residual ethanol from the recrystallization (at 3% w/w), which is taken into account in the yield calculation. The peak at 1.60 ppm is from by HDO in the NMR solvent and overlaps a multiplet.

N-cyclohexylbutanamide – ^{13}C NMR

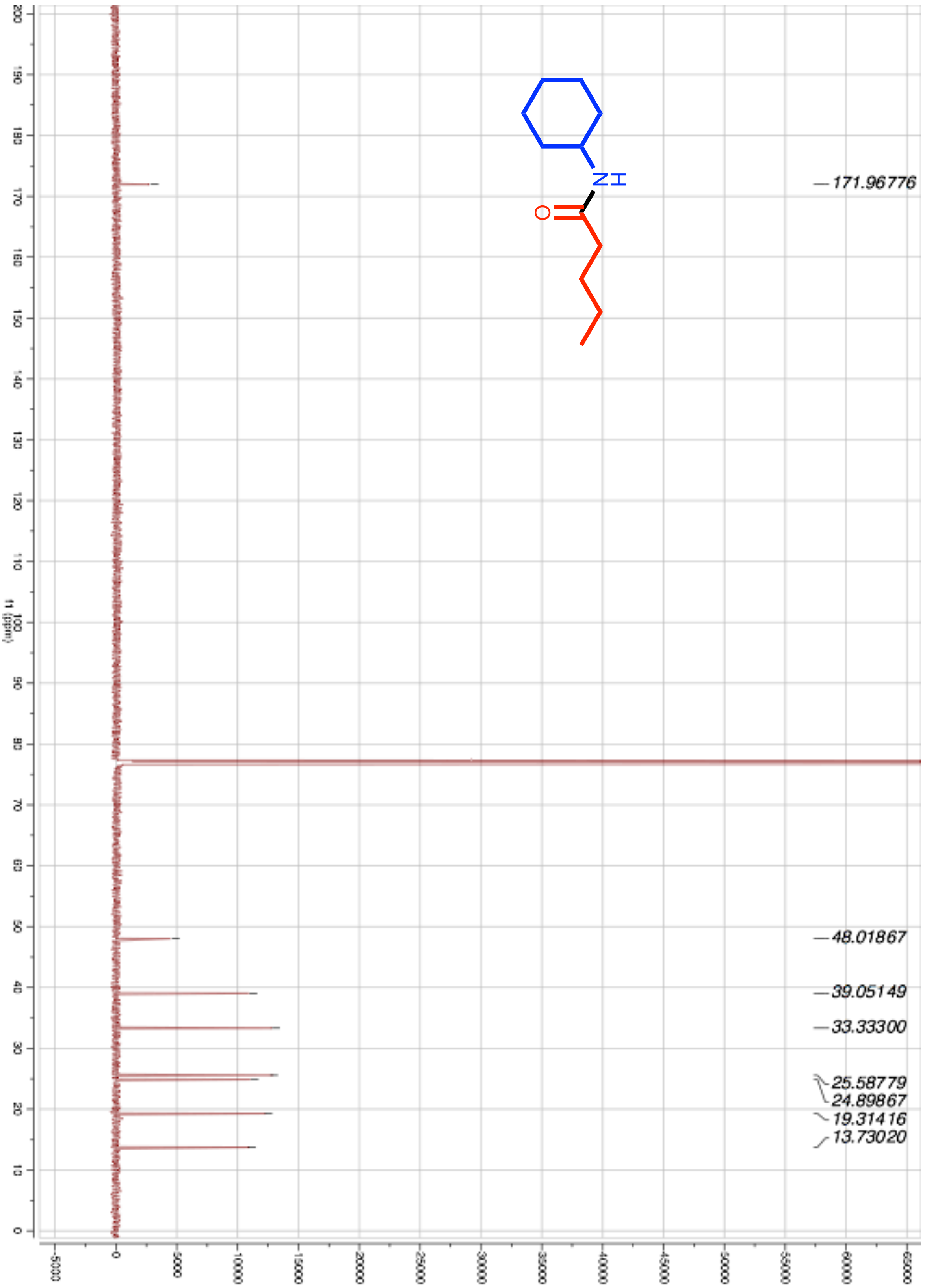

N-benzylpiperazine – ^{1}H NMR

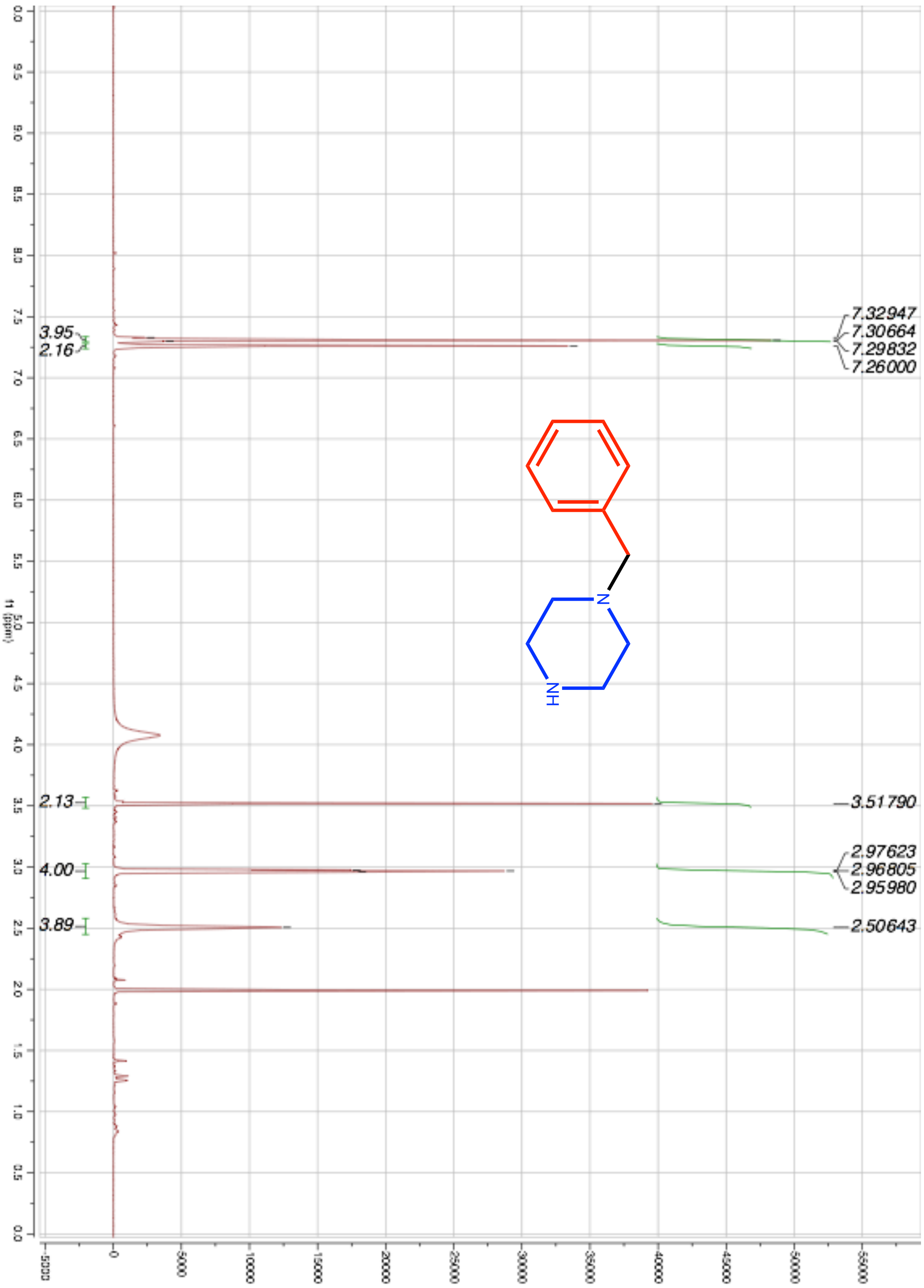

The peak at 2 ppm is caused by small amounts of residual acetone from cleaning the nmr tube.

N-benzylpiperazine – ^{13}C NMR